CHEMICAL AND OPTICAL PROPERTIES OF ATMOSPHERIC AEROSOL IRON SOURCES: COAL FLY ASH AND ICELANDIC DUST

by

School of Geography, Earth and Environmental Science

College of Life and Environmental Sciences

University of Birmingham

A thesis submitted to the University of Birmingham for the degree of

DOCTOR OF PHILOSOPHY

February 2022

Abstract

This thesis describes laboratory measurements of the chemical and physical properties of coal fly ash (CFA) and volcanic dust from Iceland which are important sources of atmospheric aerosol iron (Fe). These measurements are needed to determine the impacts of Fe-containing aerosols on the radiative balance and marine biogeochemistry and to reduce the uncertainty in model predictions. The spectral optical properties and size distribution of Icelandic dust were measured using the multi-instrument atmospheric simulation chamber CESAM (based at LISA CNRS, France). The Fe dissolution kinetics of CFA samples were determined by time-dependent leaching experiments that simulated atmospheric processing. A wide range of analytical techniques including X-ray diffraction (XRD) analysis, X-ray fluorescence (XRF) analysis, X-ray absorption near edge structure (XANES) analysis, and sequential extractions were used to determine the chemical and mineralogical composition in the samples with particular focus on the Fe mineralogy/speciation.

Our laboratory measurements indicate that the high ionic strength in the atmospheric aerosol water can strongly influence the Fe dissolution rates of CFA during the atmospheric transport. Our results also suggest that the Fe speciation is a key factor in determining the Fe solubility of CFA which varied considerably in different types of CFA. We also showed that CFA dissolves faster (up to 7 times) than mineral dust at similar experimental conditions. Based on these results, we developed a new Fe release scheme for coal combustion sources which has been implemented into the global atmospheric chemical transport model IMPACT to estimate the deposition flux of aerosol dissolved Fe to the ocean.

In addition, we built a new dataset on chemical composition, mineralogy, Fe solubility, size distribution, and optical properties of Icelandic dust and quantified the differences from typical low-latitude dust (e.g., from northern African and eastern Asian). Our results indicate that Icelandic dust could make a substantial contribution to dissolved Fe to the subpolar North Atlantic Ocean in particular in the Iceland Basin. Our results also suggest that in Icelandic dust magnetite is a major contribution to light absorption particularly between 660 and 950 nm, which can be 2-8 times higher than in low-latitude dust. This new

dataset of chemical and physical parameters can be used in global models to estimate the deposition fluxes of aerosol dissolved Fe to the North Atlantic Ocean and to determine the radiative impact of Icelandic dust in the Arctic.

Acknowledgments

First and foremost, I would like to thank my supervisors at the University of Birmingham, Prof. Zongbo Shi and Prof. Rob Mackenzie for their guidance and encouragement during my PhD journey. I am grateful for all their time, effort and support, and the opportunities and experiences provided. And I am thankful to Dr Paola Formenti from CNRS-LISA who has patiently contributed to the supervision of the work on the optical properties.

In addition to my supervisors, I would also like to thank Dr Claudia Di Biagio from CNRS-LISA, and Dr Akinori Ito from JAMSTEC for their wonderful collaboration and support, and Prof. Mike Krom from University of Leeds for all the insightful comments, advice, and suggestions. I would like to express my gratitude to all my collaborators at the University of Birmingham, CNRS-LISA, Université Paris-Est Créteil, Université Paris Cité, Diamond Light Source, Agricultural University of Iceland, JAMSTEC, Zhejiang University, Cardiff University, King's College London, and University of Leeds. I am grateful to NERC CENTA, COST Action inDust, and EUROCHAMP for funding this research.

Thank you to Nick for all the assistance in the lab. Thank you to Gretchel, Mica, Jamie, and Claire for all the help with admin-related tasks. Thank you to the library service, IT-Service, and BEAR staff for all the technical assistance. Thank you to my friends and colleagues at University of Birmingham in particular, Gongda, Alfred, Ana, Chai, Dewi, Karn, and Richard for always being around to share highs and lows of PhD life.

I am thankful to my friends Chiara, Matteo, Silvia, Susanna, Rita, and Jose back in Rome for all the phone calls, advice, and the laughter.

Lastly and most importantly, I am grateful to my parents, my sister, and my niece for always being so supportive, encouraging me and believing in me.

Thank you all.

Author's contribution

This thesis is based on four manuscripts, two manuscripts have already undergone peer-review, one manuscript is currently under review, and another one is in preparation for submission.

CHAPTER 1: INTRODUCTION (unique to this thesis)

CHAPTER 2: FIELD OBSERVATIONS AND LABORATORY MEASUREMENTS OF PYROGENIC IRON AEROSOL

published in npj Climate and Atmospheric Science as:

Ito, A., Ye, Y., Baldo, C., and Shi, Z.: Ocean fertilization by pyrogenic aerosol iron, npj Clim. Atmos. Sci., 4, 30, doi: 10.1038/s41612-021-00185-8, 2021.

Author contribution: AI proposed the concept, hosted a workshop at Nagoya University in 2019 (AI, YY, and ZS), and wrote the draft of the introduction and atmospheric iron-containing chemistry models. CB and ZS wrote the draft of observations and laboratory measurements. YY wrote the draft of ocean biogeochemistry models. All authors contributed to revising and finalizing the manuscript.

CHAPTER 3: IRON FROM COAL COMBUSTION PARTICLES DISSOLVES MUCH FASTER THAN MINERAL DUST UNDER SIMULATED ATMOSPHERIC ACID CONDITIONS

published in Atmospheric Chemistry and Physics as:

Baldo, C., Ito, A., Krom, M. D., Li, W., Jones, T., Drake, N., Ignatyev, K., Davidson, N., and Shi, Z.: Iron from coal combustion particles dissolves much faster than mineral dust under simulated atmospheric acid conditions, Atmos. Chem. Phys., 22, 6045-6066, doi: 10.5194/acp-22-6045-2022, 2022.

Author contribution: CB, ZS, and AI designed the experiments and discussed the results. ZS supervised the experimental and data analyses. CB conducted the experiments and the data analysis with contributions from ZS, AI, MDK and NDa. NDa, ZS and KI performed the XANES measurements. AI developed the model of the dissolution kinetics and performed the model simulations. Krakow and Aberthaw ash were provided by TJ, while Shandong ash was provided by WL. Soil 5 from Libya was collected by NDr. CB prepared the article with contributions from MDK and all the other co-authors.

CHAPTER 4: DISTINCT CHEMICAL AND MINERALOGICAL COMPOSITION OF ICELANDIC DUST COMPARED TO NORTH AFRICAN AND ASIAN DUST

published in Atmospheric Chemistry and Physics as:

Baldo, C., Formenti, P., Nowak, S., Chevaillier, S., Cazaunau, M., Pangui, E., Di Biagio, C., Doussin, J. F., Ignatyev, K., Dagsson-Waldhauserova, P., Arnalds, O., MacKenzie, A. R., and Shi, Z.: Distinct chemical and mineralogical composition of Icelandic dust compared to northern African and Asian dust, Atmos. Chem. Phys., 20, 13521-13539, doi: 10.5194/acp-20-13521-2020, 2020.

Author contribution: CB, ZS, CDB, PF and JFD designed the experiments and discussed the results. ZS supervised the experimental and data analyses. CB performed the experiments at CESAM and the data analysis with contributions from ZS, ARM, CDB, PF, MC, EP, and JFD. The soil samples used for the experiments were collected by OA and PDW. CB and SN performed the XRD measurements. SC and PF performed the XRF measurements. CB, ZS and KI performed the XANES measurements. CB performed the Fe extractions and solubility measurements. CB and ZS prepared the manuscript with contributions from all co-authors.

CHAPTER 5: COMPLEX REFRACTIVE INDEX AND SINGLE SCATTERING ALBEDO OF ICELANDIC DUST IN THE SHORTWAVE SPECTRUM

in preparation for submission to a peer-reviewed journal as:

Baldo, C., Formenti, P., Di Biagio, C., Lu, G., Song, C., Cazaunau, M., Pangui, E., Doussin, J. F., Dagsson-Waldhauserova, P., Arnalds, O., MacKenzie, A. R., and Shi, Z.: Complex refractive index and single scattering albedo of Icelandic dust in the shortwave spectrum.

Author contribution: CB, ZS, CDB, PF and JFD designed the experiments and discussed the results. ZS supervised the experimental and data analyses. CB performed the experiments at CESAM with support from ZS, CDB, PF, MC, EP, and JFD, and the data analysis with contributions from ZS, ARM, GL, CS, CDB, and PF. GL refined the research codes. The soil samples used for the experiments were collected by OA and PDW. CB prepared the manuscript with contributions from all co-authors.

CHAPTER 6: CONCLUSIONS AND FUTURE RESEARCH (unique to this thesis)

Tables of contents

List of figures

List of tables

List of abbreviations

Absorption coefficient	β_{abs}
Aerosol Robotic Network	AERONET
Anthropogenic combustion	ANTHRO
Arizona Test Dust	AZTD/ATD
Attenuation	ATTN
Biomass Burning	BB
Black Carbon	BC
Bottom of the Atmosphere	BOA
Chemical Index of Alteration	CIA
Coal Fly Ash	CFA
Community Atmosphere Model, version 5	CAM5
Complex refractive index	m
Condensation Particle Counter	CPC
Crystallography Open Database	COD
Differential Mobility Analyzer	DMA
Dissolved iron	DFe
Dynamic shape factor	χ
Extinction coefficient	β_{ext}
Experimental Multiphasic Atmospheric Simulation Chamber	CESAM chamber
Extended Aerosol Inorganics Model	E-AIM
Geometric diameter	D_g
Greenhouse Gases	GHG
Imaginary part of the complex refractive index	k
Inductively coupled plasma mass spectrometry analysis	ICP-MS analysis

Inductively coupled plasma optical emission spectrometry analysis	ICP-OES analysis
Inorganic Crystal Structure Database	ICSD-Pan
Integrated Massively Parallel Atmospheric Chemical Transport model	IMPACT model
Intergovernmental Panel on Climate Change	IPCC
Iron extracted in ammonium oxalate solution at pH 3.2	FeM
Iron extracted in ascorbate solution at pH 7.5	FeA
Iron extracted in dithionite solution at pH 4.8	FeD
Iron oxides	FeOx
Material Analysis Using Diffraction	MAUD
Mobility diameter	D_m
Optical diameter	D_{op}
Optical particle counters	OPC
Particles with an aerodynamic diameter smaller than 10 µm	PM_{10}
Particles with an aerodynamic diameter smaller than 2.5 µm	$PM_{2.5}$
Particles with an aerodynamic diameter smaller than 20 µm	PM_{20}
Real part of the complex refractive index	n
Reduced Major Axis regression	RMA regression
Relative Standard Deviation	RSD
Root Mean Square Error	RMSE
Scanning Mobility Particle Sizer	SMPS
Scattering coefficient	β_{sca}
Shortwave	SW
Single Scattering Albedo	SSA
Standard deviation	SD
Top of the atmosphere	TOA
Total iron	FeT

Ultraviolet	UV
Wavelength	λ
X-ray Absorption Near Edge Structure analysis	XANES analysis
X-ray Diffraction analysis	XRD analysis
X-ray Fluorescence analysis	XRF analysis

CHAPTER 1: INTRODUCTION

1.1 Atmospheric aerosols and climate

Atmospheric aerosol is a mixture of fine solid particles and liquid droplets suspended in air (Seinfeld and Pandis, 2016). Aerosols play an important role in the climate and biogeochemical systems (Boucher, 2015; Mahowald et al., 2011; Pöschl, 2005). Airborne particles affect the Earth's energy balance directly by scattering and absorbing the solar radiation and by scattering, absorbing and emitting terrestrial radiation (e.g., Haywood et al., 2003; Sokolik and Toon, 1999), and indirectly by acting as cloud condensation and ice nuclei thereby affecting the microphysical properties and lifetime of clouds (e.g., Boucher et al., 2013; Carslaw et al., 2010; Choobari et al., 2014; Lohmann and Feichter, 2005). While in the atmosphere, particles participate in heterogeneous chemical reactions which influence the abundance and distribution of atmospheric trace gases (Arimoto, 2001; Dentener et al., 1996). In the cryosphere, the deposition of aerosols onto snow or ice reduces the surface albedo (e.g., Dumont et al., 2014; Peltoniemi et al., 2015; Qian et al., 2015). Furthermore, the atmospheric deposition of nutrients carried by aerosols can affect the biogeochemistry of terrestrial and marine ecosystems (e.g., Jickells and Moore, 2015; Jickells et al., 2005; Kanakidou et al., 2018; Mahowald et al., 2010; Stockdale et al., 2016).

Aerosols are directly emitted into the atmosphere from a wide variety of sources including natural sources such as lithogenic sources, sea spray, volcanoes, wildfires, and biogenic sources, and anthropogenic activities such as agricultural practices, industrial activities, fossil fuels combustions, and biomass burning (Boucher, 2015; Seinfeld and Pandis, 2016). Secondary aerosols are also formed in the atmosphere through gas-to-particle conversion processes (Seinfeld and Pandis, 2016). Airborne particles are transported by winds over long distances and undergo chemical and physical transformations (atmospheric aging) such as mixing with other aerosols, uptake of atmospheric trace gases, evaporation-condensation cycles, and chemical reactions, which affect aerosol properties (Boucher, 2015; Mahowald

et al., 2011; Pöschl, 2005; Seinfeld and Pandis, 2016). Eventually, particles are removed from the atmosphere primarily via wet deposition through precipitations but also via dry deposition at the surface (Boucher, 2015; Mahowald et al., 2011; Pöschl, 2005; Seinfeld and Pandis, 2016). The tropospheric lifetime of aerosols is closely linked to the particle size which varies in the range from few nanometers to tens of micrometers. The lifetime of fine particle (from 0.1 to 2.5 μm in diameter) is generally in the order of days to weeks, while smaller and coarser particles have lifetimes of hours to days as these are lost principally through coagulation and gravitational settling, respectively (Boucher, 2015; Seinfeld and Pandis, 2016). Although aerosols are always present in the atmosphere, their spatial and temporal distribution is extremely variable along with their chemical, physical and optical properties which depend on the sources, transformation processes, transport, and sinks of aerosols and their precursors (Boucher, 2015; Seinfeld and Pandis, 2016). Consequently, the effects of aerosols on climate vary also in time and space (Boucher, 2015).

The climate response to aerosol perturbations is quantified by climate models which require a parametrization of the emission, transport, deposition, and properties of aerosols, but these factors have currently large uncertainties and the interactions between aerosols and climate are complex and yet not completely understood (Boucher, 2015; Mahowald et al., 2011; Mahowald et al., 2017). The radiative forcing is commonly used to quantify and compare the change in the Earth's energy balance caused by various climatic factors leading to warming or cooling the atmosphere. The Intergovernmental Panel on Climate Change (IPCC) 6th assessment report (Forster et al., 2021) estimated that the aerosol forcing via aerosol-cloud interaction and aerosol radiation interaction is from -2.0 to -0.6 W m^{-2} which represent the largest uncertainty in the Earth's energy budget during the Industrial Era. The net cooling effect of aerosols partly offset the warming effect of greenhouse gases (GHGs) which has produced a positive radiative forcing of around +3.8 W m^{-2}. However, individual aerosol species cause a range of radiative forcing with mineral dust, sulphates, nitrates, and organic carbon having a cooling effect, while black carbon having a warming effect. Black carbon and light absorbing aerosols cause an additional positive forcing when deposited onto snow and ice (Boucher et al., 2013; Forster et al., 2021). The climate

forcing resulting from aerosol-carbon cycle feedbacks is still uncertain (Mahowald et al., 2011; Mahowald et al., 2017). However, model estimates indicate that the atmospheric deposition of nutrients to terrestrial and marine ecosystems has determined an increase in carbon dioxide (CO_2) concentration between 0.2 and 1.5 PgC yr^{-1} (Mahowald et al., 2017).

1.2 The importance of atmospheric aerosol iron

Iron (Fe) is an important component of atmospheric aerosol. Dust aerosol particles produced by wind erosion in arid and semi-arid regions dominate the total aerosol Fe load and contribute around 95% of the total Fe emissions corresponding to 37-140 Tg yr^{-1} (Ito, 2013; Ito et al., 2018; Luo et al., 2008; Myriokefalitakis et al., 2015; Rathod et al., 2020; Wang et al., 2015). Other sources of aerosol Fe are from combustion processes including fossil fuel combustion, biomass burning and metal smelting (Ito et al., 2018; Luo et al., 2008; Myriokefalitakis et al., 2018; Rathod et al., 2020; Wang et al., 2015). The total aerosol Fe load can vary by several order of magnitudes from tens μg m^{-3} close to major dust source regions such as the Sahara Desert or heavily polluted area like East Asia to few ng m^{-3} over the remote oceans (e.g., Baker et al., 2006; Kumar et al., 2010; Longo et al., 2016; Sholkovitz et al., 2012; Srinivas et al., 2012).

Fe-containing aerosols have significant impacts on the radiation balance and marine biogeochemistry (Figure 1.1). Certain Fe oxide minerals such as hematite and magnetite strongly absorb the solar radiation and directly contribute to warming the atmosphere (Di Biagio et al., 2019; Engelbrecht et al., 2016; Lafon et al., 2006; Moosmuller et al., 2012; Sokolik and Toon, 1999), which indirectly affect atmospheric circulation, cloud formation, and precipitations (Carslaw et al., 2010; Choobari et al., 2014; Maher et al., 2010). The deposition of light-absorbing Fe oxide particles onto snow and ice accelerates the melting of snow and ice by reducing the surface albedo (Meinander et al., 2014; Painter et al., 2007; Peltoniemi et al., 2015). During atmospheric transport, Fe-containing particles undergo atmospheric aging processes which allow the dissolution of refractory Fe-bearing phase such crystalline iron oxides and aluminosilicate minerals (Baker et al., 2020; Li et al., 2017; Shi et al., 2015). The deposition of dissolved Fe which is bio-accessible for marine ecosystems can stimulate phytoplankton growth in Fe-

limited oceans (Martin, 1990; Tagliabue et al., 2017), and enhance nitrogen (N_2) fixation in N_2-limited oceans (Mills et al., 2004; Moore et al., 2006). This promotes the sequestration of carbon dioxide (CO_2) from the atmosphere to the deep ocean, consequently affecting the global carbon cycle and climate (Martin, 1990).

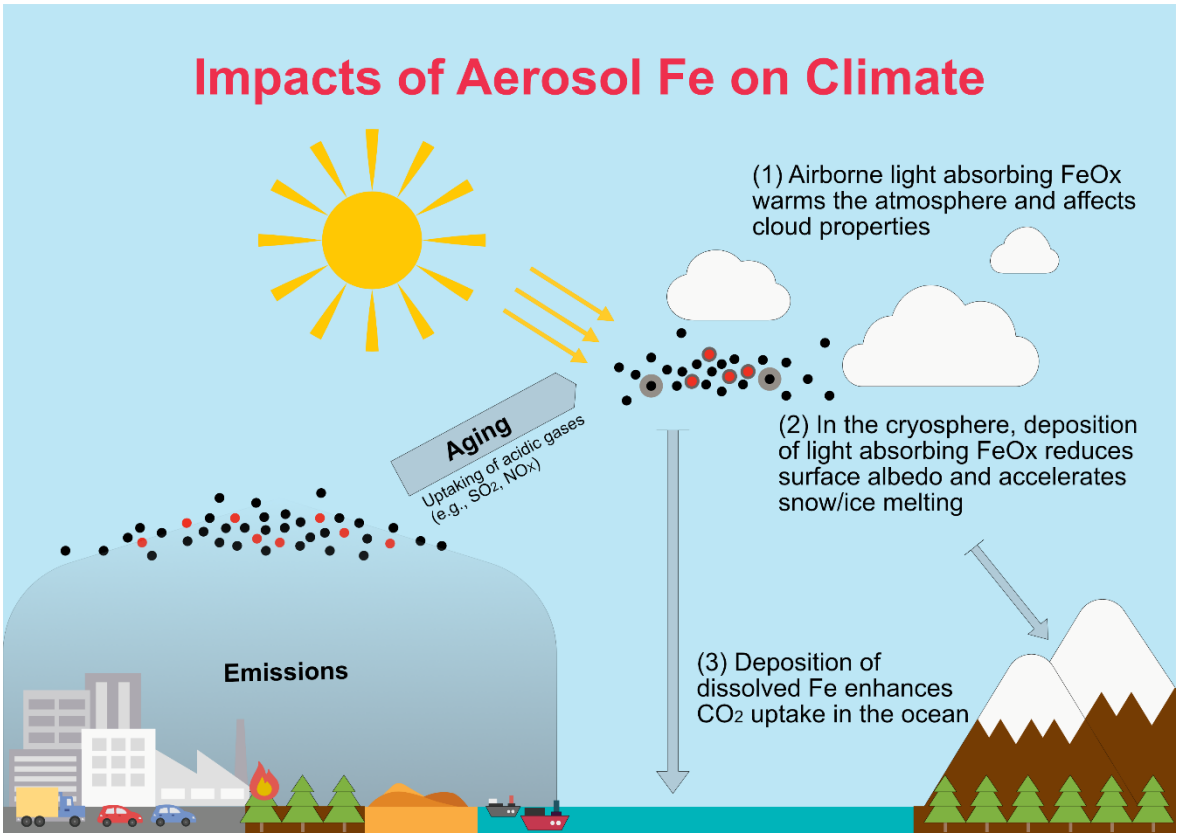

Figure 1.1: Impacts of atmospheric aerosol Fe. Fe-containing aerosols are emitted by coal combustion, oil combustion, metal smelting industry, and biomass burning sources in addition to mineral dust emissions. 1) Light absorbing iron oxides (FeO_x) contribute to warming the atmosphere and affect cloud properties. 2) The deposition of light absorbing FeO_x particles onto snow and ice accelerates the melting of snow and ice by reducing the surface albedo. During atmospheric transport, aging processes favors the dissolution of refractory Fe-containing phases. 3) The deposition of dissolved Fe fertilizes the ocean and enhances CO_2 uptake.

The chemical and physical properties of Fe-containing aerosols depend on their sources, transport, and transformations in the atmosphere, and will determine their ability to influence the climate and biogeochemical processes. However, a large number of assumptions are currently used in models to predict the impacts of atmospheric aerosol Fe on climate, such as the content of Fe oxide minerals, Fe solubility and optical properties. Thus, model predictions have big uncertainties.

1.3 Aerosol optical properties and iron oxide content

The optical properties of dust aerosols are strongly affected by the mineralogical composition of the dust particles, along with the mixing state, shape, and size distribution (e.g., Caponi et al., 2017; Di Biagio et al., 2019; Di Biagio et al., 2017; Formenti et al., 2014b; Kandler et al., 2011). Fe oxide minerals control absorption in the shortwave spectrum (Di Biagio et al., 2019; Engelbrecht et al., 2016; Lafon et al., 2006; Moosmuller et al., 2012; Sokolik and Toon, 1999), while minerals such as clay, quartz and calcite regulate the optical properties in the longwave spectrum (Di Biagio et al., 2017; Sokolik and Toon, 1999; Sokolik et al., 1998). The chemical and physical properties of Fe oxides in dust vary depending on individual source regions and the processes occurring during the atmospheric transport. The distribution of Fe oxide minerals in soils is extremely heterogeneous and is related to the parent rock and weathering regime (Cornell and Schwertmann, 2003). Hematite and goethite are the most common Fe oxide species in soils and contribute respectively around 10%-40% and 20-60% of the total Fe in northern African dust (Di Biagio et al., 2019; Formenti et al., 2014a; Shi et al., 2011b). Volcanic dust from Iceland is enriched in Fe (Baldo et al., 2020; Dagsson-Waldhauserova et al., 2014; Moroni et al., 2018) and showed low degree of chemical weathering and higher magnetite content but lower hematite and goethite than northern African dust (Baldo et al., 2020). As iron oxide minerals have different optical properties, for example, goethite is less absorbing than hematite and magnetite in the visible wavelengths (Bedidi and Cervelle, 1993; Huffman and Stapp, 1973; Longtin et al., 1988; Querry, 1985; Sokolik and Toon, 1999), determining the content and physicochemical properties of Fe oxide species in dust is necessary to accurately estimate the radiative effect of dust aerosols. Global aerosol models predict the concentration of Fe oxide in dust aerosols based on maps of soil mineralogy, some studies only consider iron oxide in the form of hematite (Claquin et al., 1999; Nickovic et al., 2012), while others distinguish hematite and goethite (Journet et al., 2014). A recent modelling studies estimated that the uncertainty related to the abundance of different Fe oxide minerals in soil contributes around 97% of the uncertainty of the direct radiative effect of dust aerosols (Li et al., 2021).

Several studies have demonstrated that magnetite from anthropogenic combustion sources is an important short-lived climate forcer. Moteki et al. (2017) estimated that the shortwave absorption by anthropogenic magnetite is at least 4%-7% of that of the highly absorbing black carbon (BC) over East Asia based on aircraft measurements. Incorporating these new measurements into a global aerosol model, Matsui et al. (2018) calculated that the direct radiative forcing of anthropogenic magnetite is +0.021 W m^{-2} globally and +0.22 W m^{-2} over East Asia. An emission inventory for anthropogenic combustion Fe has been recently developed by Rathod et al. (2020). They estimated anthropogenic Fe oxide emissions using available observations in particles from fuel combustion. Fe oxide emissions were also modelled using the initial fuel Fe mineralogy and temperature dependent mineral transformations, but the uncertainty in the modelled Fe oxide mineralogy can be over 100%. With the above assumptions, Rathod et al. (2020) concluded that magnetite and hematite contribute respectively ~70% and ~15% of the total anthropogenic combustion Fe, with metal smelting accounting for over 60% of pyrogenic Fe (1.35 Tg yr^{-1}).

1.4 Aerosol fractional Fe solubility

Global aerosol models are used to estimate the deposition of aerosol Fe to the ocean. In particular, the aerosol fractional Fe solubility is a key parameter to predict the deposition fluxes of Fe bio-accessible for marine ecosystems. The aerosol fractional Fe solubility (%) is operationally defined as the ratio of dissolved Fe (typically passing through 0.2 or 0.45 μm pore size filters) to the total Fe content in the bulk aerosol (e.g., Meskhidze et al., 2019; Shi et al., 2012). Mineral dust, which is the dominant source of total Fe in aerosols, has low Fe solubility at emission, generally below 1% (e.g., Baker et al., 2006; Chuang et al., 2005; Schroth et al., 2009; Sedwick et al., 2007; Shi et al., 2011c; Sholkovitz et al., 2009; Sholkovitz et al., 2012), that is related to the physicochemical properties of Fe-bearing phases in the mineral particles. In northern African dust, Fe is mostly contained in refractory phases such as crystalline iron oxides and clay minerals (Di Biagio et al., 2019; Formenti et al., 2014a; Shi et al., 2011b), while a smaller proportion of Fe is as highly reactive forms like amorphous Fe and ferrihydrite (0.3%-7% of the total Fe) which can vary depending on the degree of chemical weathering of the parent soils (Shi et al.,

2011b). Observations have demonstrated that the Fe solubility of dust aerosols increase somewhat during the atmospheric transport as a result of atmospheric aging processes (Baker et al., 2020; Li et al., 2017; Shi et al., 2015), and laboratory studies have currently identified three principal mechanisms of Fe dissolution in aerosols including the proton-promoted, ligand-promoted, and photo-reductive dissolution of Fe (Chen et al., 2012; Chen and Grassian, 2013; Cwiertny et al., 2008a; Cwiertny et al., 2008b; Desboeufs et al., 2005; Fu et al., 2010; Fu et al., 2012; Ito and Shi, 2016; Paris and Desboeufs, 2013; Paris et al., 2011; Shi et al., 2011a; Shi et al., 2011b; Shi et al., 2009; Shi et al., 2015). The Fe solubility in anthropogenic combustion sources vary considerably depending on the source and can be several orders of magnitude higher than that of mineral dust (Bowie et al., 2009; Desboeufs et al., 2005; Guieu et al., 2005; Ito et al., 2021; Oakes et al., 2012; Paris et al., 2010; Schroth et al., 2009; Shi et al., 2009) and further increase during atmospheric transport. Pyrogenic Fe contributes only few percent of the total Fe emissions but may result in a disproportionally higher contribution of bio-accessible Fe for marine ecosystems. Model estimates suggest that pyrogenic Fe accounts for around 20% of aerosol dissolved Fe deposited into the ocean (Ito et al., 2019; Ito et al., 2021; Myriokefalitakis et al., 2018).

Observations show a wide variety of aerosol Fe solubilities from around 0.01% to 100% with high Fe solubility at low total Fe concentrations for example in aerosols transported away from the dust source regions (e.g., Baker and Jickells, 2006; Jickells et al., 2016; Shelley et al., 2018; Sholkovitz et al., 2012). Global aerosol models predict the aerosol Fe solubility accounting for the Fe solubilities measured at emission and dissolution mechanisms during atmospheric transport. An intercomparison study of four widely used models highlighted the importance of pyrogenic Fe as a source of bio-accessible Fe to the remote ocean (Ito et al., 2019; Myriokefalitakis et al., 2018). However, pyrogenic Fe sources and their dissolution processes are still not well represented in models, which contributes to the large discrepancy between model and observations particularly over the Southern Ocean which is influenced by mixed aerosols far from the sources (Ito et al., 2019; Ito et al., 2021; Myriokefalitakis et al., 2018).

1.5 Thesis aim and research objectives

The overall aim of this thesis is to determine the chemical and physical properties of important sources of aerosol Fe such as coal combustion particles (i.e., coal fly ash, CFA) and volcanic dust from Iceland. These are needed to determine the impacts of Fe-containing aerosols on the radiative balance and marine biogeochemistry and to reduce the uncertainty in model predictions.

The specific research objectives are: (1) To determine the Fe dissolution kinetic of CFA under simulated aerosol conditions. (2) To determine the mineralogical and optical properties of Icelandic dust.

1.6 Thesis outline

This thesis is organized in the following way. Chapter 2 provides a review of field observations and laboratory measurements of pyrogenic Fe in aerosols. Chapters 3-5 describe and discuss experimental results. Chapter 3 examines the dissolution kinetics of Fe in CFA particles under simulated acidic processing. Chapter 4 investigates the chemical and mineralogical properties of Icelandic dust. Chapter 5 explores the optical properties of Icelandic dust. Chapter 6 summarizes key findings from the thesis and future research.

Chapters 3-5 have the format of journal articles for publication including abstract, introduction, methodology, discussions, and conclusions. Supporting information for these chapters are also provided in the thesis. Example research codes are available at the following GitHub repository: https://github.com/ClarissaBaldo/Research_codes_examples.

1.7 References

Arimoto, R.: Eolian dust and climate: relationships to sources, tropospheric chemistry, transport and deposition, Earth-Sci. Rev., 54, 29-42, doi: 10.1016/s0012-8252(01)00040-x, 2001.

Baker, A. R., French, M., and Linge, K. L.: Trends in aerosol nutrient solubility along a west-east transect of the Saharan dust plume, Geophys. Res. Lett., 33, doi: 10.1029/2005gl024764, 2006.

Baker, A. R., and Jickells, T. D.: Mineral particle size as a control on aerosol iron solubility, Geophys. Res. Lett., 33, doi: 10.1029/2006gl026557, 2006.

Baker, A. R., Li, M., and Chance, R.: Trace Metal Fractional Solubility in Size-Segregated Aerosols From the Tropical Eastern Atlantic Ocean, Global Biogeochem. Cy., 34, e2019GB006510, doi: 10.1029/2019GB006510, 2020.

Baldo, C., Formenti, P., Nowak, S., Chevaillier, S., Cazaunau, M., Pangui, E., Di Biagio, C., Doussin, J. F., Ignatyev, K., Dagsson-Waldhauserova, P., Arnalds, O., MacKenzie, A. R., and Shi, Z.: Distinct chemical and mineralogical composition of Icelandic dust compared to northern African and Asian dust, Atmos. Chem. Phys., 20, 13521-13539, doi: 10.5194/acp-20-13521-2020, 2020.

Bedidi, A., and Cervelle, B.: Light scattering by spherical particles with hematite and goethitelike optical properties: effect of water impregnation, J. Geophys. Res. -Solid Earth, 98, 11941-11952, doi: 10.1029/93JB00188, 1993.

Boucher, O., Randall, D., Artaxo, P., Bretherton, C., Feingold, G., Forster, P., Kerminen, V.-M., Kondo, Y., Liao, H., Lohmann, U., Rasch, P., Satheesh, S., Sherwood, S., Stevens, B., and Zhang, X.-Y.: Clouds and aerosols, in: Climate change 2013: the physical science basis. Contribution of Working Group I to the Fifth Assessment Report of the Intergovernmental Panel on Climate Change, edited by: Stocker, T. F., Qin, D., Plattner, G.-K., Tignor, M., Allen, S. K., Doschung, J., Nauels, A., Xia, Y., Bex, V., and Midgley, P. M., Cambridge University Press, United Kingdom and New York USA, 571-657, 2013.

Boucher, O.: Atmospheric Aerosols, in: Atmospheric Aerosols: Properties and Climate Impacts, Springer Netherlands, Dordrecht, 9-24, 2015.

Bowie, A. R., Lannuzel, D., Remenyi, T. A., Wagener, T., Lam, P. J., Boyd, P. W., Guieu, C., Townsend, A. T., and Trull, T. W.: Biogeochemical iron budgets of the Southern Ocean south of Australia: Decoupling of iron and nutrient cycles in the subantarctic zone by the summertime supply, Global Biogeochem. Cy., 23, GB4034, doi: 10.1029/2009gb003500, 2009.

Caponi, L., Formenti, P., Massabo, D., Di Biagio, C., Cazaunau, M., Pangui, E., Chevaillier, S., Landrot, G., Andreae, M. O., Kandler, K., Piketh, S., Saeed, T., Seibert, D., Williams, E., Balkanski, Y., Prati, P., and Doussin, J. F.: Spectral- and size-resolved mass absorption efficiency of mineral dust aerosols in the shortwave spectrum: a simulation chamber study, Atmos. Chem. Phys., 17, 7175-7191, doi: 10.5194/acp-17-7175-2017, 2017.

Carslaw, K. S., Boucher, O., Spracklen, D. V., Mann, G. W., Rae, J. G. L., Woodward, S., and Kulmala, M.: A review of natural aerosol interactions and feedbacks within the Earth system, Atmos. Chem. Phys., 10, 1701-1737, doi: 10.5194/acp-10-1701-2010, 2010.

Chen, H., Laskin, A., Baltrusaitis, J., Gorski, C. A., Scherer, M. M., and Grassian, V. H.: Coal fly ash as a source of iron in atmospheric dust, Environ. Sci. Technol., 46, 2112-2120, doi: 10.1021/es204102f, 2012.

Chen, H. H., and Grassian, V. H.: Iron Dissolution of Dust Source Materials during Simulated Acidic Processing: The Effect of Sulfuric, Acetic, and Oxalic Acids, Environ. Sci. Technol., 47, 10312-10321, doi: 10.1021/es401285s, 2013.

Choobari, O. A., Zawar-Reza, P., and Sturman, A.: The global distribution of mineral dust and its impacts on the climate system: A review, Atmos. Res., 138, 152-165, doi: 10.1016/j.atmosres.2013.11.007, 2014.

Chuang, P. Y., Duvall, R. M., Shafer, M. M., and Schauer, J. J.: The origin of water soluble particulate iron in the Asian atmospheric outflow, Geophys. Res. Lett., 32, L07813, doi: 10.1029/2004gl021946, 2005.

Claquin, T., Schulz, M., and Balkanski, Y. J.: Modeling the mineralogy of atmospheric dust sources, J. Geophys. Res.-Atmos, 104, 22243-22256, doi: 10.1029/1999jd900416, 1999.

Cornell, R. M., and Schwertmann, U.: The Iron Oxides: Structure, Properties, Reactions, Occurrence and Uses, Wiley-VCH, New York 2003.

Cwiertny, D. M., Baltrusaitis, J., Hunter, G. J., Laskin, A., Scherer, M. M., and Grassian, V. H.: Characterization and acid-mobilization study of iron-containing mineral dust source materials, J. Geophys. Res.-Atmos, 113, D05202, doi: 10.1029/2007jd009332, 2008a.

Cwiertny, D. M., Young, M. A., and Grassian, V. H.: Chemistry and photochemistry of mineral dust aerosol, Annu. Rev. Phys. Chem., 59, 27-51, doi: 10.1146/annurev.physchem.59.032607.093630, 2008b.

Dagsson-Waldhauserova, P., Arnalds, O., Olafsson, H., Skrabalova, L., Sigurdardottir, G. M., Branis, M., Hladil, J., Skala, R., Navratil, T., Chadimova, L., Menar, S. V. O., Thorsteinsson, T., Carlsen, H. K., and Jonsdottir, I.: Physical properties of suspended dust during moist and low wind conditions in Iceland, Icel. Agric. Sci., 27, 25-39, 2014.

Dentener, F. J., Carmichael, G. R., Zhang, Y., Lelieveld, J., and Crutzen, P. J.: Role of mineral aerosol as a reactive surface in the global troposphere, J. Geophys. Res.-Atmos, 101, 22869-22889, doi: 10.1029/96JD01818, 1996.

Desboeufs, K. V., Sofikitis, A., Losno, R., Colin, J. L., and Ausset, P.: Dissolution and solubility of trace metals from natural and anthropogenic aerosol particulate matter, Chemosphere, 58, 195-203, doi: 10.1016/j.chemosphere.2004.02.025, 2005.

Di Biagio, C., Formenti, P., Balkanski, Y., Caponi, L., Cazaunau, M., Pangui, E., Journet, E., Nowak, S., Caquineau, S., Andreae, M. O., Kandler, K., Saeed, T., Piketh, S., Seibert, D., Williams, E., and Doussin, J. F.: Global scale variability of the mineral dust long-wave refractive index: a new dataset of in situ measurements for climate modeling and remote sensing, Atmos. Chem. Phys., 17, 1901-1929, doi: 10.5194/acp-17-1901-2017, 2017.

Di Biagio, C., Formenti, P., Balkanski, Y., Caponi, L., Cazaunau, M., Pangui, E., Journet, E., Nowak, S., Andreae, M. O., Kandler, K., Saeed, T., Piketh, S., Seibert, D., Williams, E., and Doussin, J. F.: Complex refractive indices and single-scattering albedo of global dust aerosols in the shortwave spectrum and relationship to size and iron content, Atmos. Chem. Phys., 19, 15503-15531, doi: 10.5194/acp-19-15503-2019, 2019.

Dumont, M., Brun, E., Picard, G., Michou, M., Libois, Q., Petit, J. R., Geyer, M., Morin, S., and Josse, B.: Contribution of light-absorbing impurities in snow to Greenland's darkening since 2009, Nat. Geosci., 7, 509-512, doi: 10.1038/ngeo2180, 2014.

Engelbrecht, J. P., Moosmuller, H., Pincock, S., Jayanty, R. K. M., Lersch, T., and Casuccio, G.: Technical note: Mineralogical, chemical, morphological, and optical interrelationships of mineral dust re-suspensions, Atmos. Chem. Phys., 16, 10809-10830, doi: 10.5194/acp-16-10809-2016, 2016.

Formenti, P., Caquineau, S., Chevaillier, S., Klaver, A., Desboeufs, K., Rajot, J. L., Belin, S., and Briois, V.: Dominance of goethite over hematite in iron oxides of mineral dust from Western Africa: Quantitative partitioning by X-ray absorption spectroscopy, J. Geophys. Res.-Atmos, 119, 12740-12754, doi: 10.1002/2014jd021668, 2014a.

Formenti, P., Caquineau, S., Desboeufs, K., Klaver, A., Chevaillier, S., Journet, E., and Rajot, J. L.: Mapping the physico-chemical properties of mineral dust in western Africa: mineralogical composition, Atmos. Chem. Phys., 14, 10663-10686, doi: 10.5194/acp-14-10663-2014, 2014b.

Forster, P., Storelvmo, T., Armour, K., Collins, W., Dufresne, J.-L., Frame, D., Lunt, D. J., Mauritsen, T., Palmer, M. D., Watanabe, M., Wild, M., and Zhang, H.: The Earth's Energy Budget, Climate Feedbacks, and Climate Sensitivity., in: Climate Change 2021: The Physical Science Basis. Contribution of Working Group I to the Sixth Assessment Report of the Intergovernmental Panel on Climate Change edited by: Masson-Delmotte, V., P. Zhai, A. Pirani, S.L. Connors, C. Péan, S. Berger, N. Caud, Y. Chen, L. Goldfarb, M.I. Gomis, M. Huang, K. Leitzell, E. Lonnoy, J.B.R. Matthews, T.K. Maycock, T. Waterfield, O. Yelekçi, R. Yu, and B. Zhou, 923–1054, 2021.

Fu, H., Cwiertny, D. M., Carmichael, G. R., Scherer, M. M., and Grassian, V. H.: Photoreductive dissolution of Fe-containing mineral dust particles in acidic media, J. Geophys. Res., 115, D11304, doi: 10.1029/2009jd012702, 2010.

Fu, H. B., Lin, J., Shang, G. F., Dong, W. B., Grassian, V. H., Carmichael, G. R., Li, Y., and Chen, J. M.: Solubility of Iron from Combustion Source Particles in Acidic Media Linked to Iron Speciation, Environ. Sci. Technol., 46, 11119-11127, doi: 10.1021/es302558m, 2012.

Guieu, C., Bonnet, S., Wagener, T., and Loye-Pilot, M. D.: Biomass burning as a source of dissolved iron to the open ocean?, Geophys. Res. Lett., 32, L19608, doi: 10.1029/2005gl022962, 2005.

Haywood, J., Francis, P., Osborne, S., Glew, M., Loeb, N., Highwood, E., Tanre, D., Myhre, G., Formenti, P., and Hirst, E.: Radiative properties and direct radiative effect of Saharan dust measured by the C-130 aircraft during SHADE: 1. Solar spectrum, J. Geophys. Res.-Atmos, 108, 8577, doi: 10.1029/2002jd002687, 2003.

Huffman, D. R., and Stapp, J. L.: Optical measurements on solids of possible interstellar importance, in: Interstellar dust and related topics, Springer, 297-301, 1973.

Ito, A.: Global modeling study of potentially bioavailable iron input from shipboard aerosol sources to the ocean, Global Biogeochem. Cy., 27, 1-10, doi: 10.1029/2012gb004378, 2013.

Ito, A., and Shi, Z.: Delivery of anthropogenic bioavailable iron from mineral dust and combustion aerosols to the ocean, Atmos. Chem. Phys., 16, 85-99, doi: 10.5194/acp-16-85-2016, 2016.

Ito, A., Lin, G. X., and Penner, J. E.: Radiative forcing by light-absorbing aerosols of pyrogenetic iron oxides, Sci. Rep., 8, 7347, doi: 10.1038/s41598-018-25756-3, 2018.

Ito, A., Myriokefalitakis, S., Kanakidou, M., Mahowald, N. M., Scanza, R. A., Hamilton, D. S., Baker, A. R., Jickells, T., Sarin, M., Bikkina, S., Gao, Y., Shelley, R. U., Buck, C. S., Landing, W. M., Bowie, A. R., Perron, M. M. G., Guieu, C., Meskhidze, N., Johnson, M. S., Feng, Y., Kok, J. F., Nenes, A., and Duce, R. A.: Pyrogenic iron: The missing link to high iron solubility in aerosols, Sci. Adv., 5, eaau7671 doi: 10.1126/sciadv.aau7671, 2019.

Ito, A., Ye, Y., Baldo, C., and Shi, Z.: Ocean fertilization by pyrogenic aerosol iron, npj Clim. Atmos. Sci., 4, 30, doi: 10.1038/s41612-021-00185-8, 2021.

Jickells, T., and Moore, C. M.: The importance of Atmospheric Deposition for Ocean Productivity, Annu. Rev. Ecol. Evol. Syst., 46, 481-501, doi: 10.1146/annurev-ecolsys-112414-054118, 2015.

Jickells, T. D., An, Z. S., Andersen, K. K., Baker, A. R., Bergametti, G., Brooks, N., Cao, J. J., Boyd, P. W., Duce, R. A., Hunter, K. A., Kawahata, H., Kubilay, N., laRoche, J., Liss, P. S., Mahowald, N., Prospero, J. M., Ridgwell, A. J., Tegen, I., and Torres, R.: Global iron connections between desert dust, ocean biogeochemistry, and climate, Science, 308, 67-71, doi: 10.1126/science.1105959, 2005.

Jickells, T. D., Baker, A. R., and Chance, R.: Atmospheric transport of trace elements and nutrients to the oceans, Phil. Trans. R. Soc. A, 374, 20150286, doi: 10.1098/rsta.2015.0286, 2016.

Journet, E., Balkanski, Y., and Harrison, S. P.: A new data set of soil mineralogy for dust-cycle modeling, Atmos. Chem. Phys., 14, 3801-3816, doi: 10.5194/acp-14-3801-2014, 2014.

Kanakidou, M., Myriokefalitakis, S., and Tsigaridis, K.: Aerosols in atmospheric chemistry and biogeochemical cycles of nutrients, Environ. Res. Lett., 13, 063004, doi: 10.1088/1748-9326/aabcdb, 2018.

Kandler, K., Lieke, K., Benker, N., Emmel, C., Kupper, M., Muller-Ebert, D., Ebert, M., Scheuvens, D., Schladitz, A., Schutz, L., and Weinbruch, S.: Electron microscopy of particles collected at Praia, Cape Verde, during the Saharan Mineral Dust Experiment: particle chemistry, shape, mixing state and complex refractive index, Tellus B: Chem. Phys. Meteorol., 63, 475-496, doi: 10.1111/j.1600-0889.2011.00550.x, 2011.

Kumar, A., Sarin, M. M., and Srinivas, B.: Aerosol iron solubility over Bay of Bengal: Role of anthropogenic sources and chemical processing, Mar. Chem., 121, 167-175, doi: 10.1016/j.marchem.2010.04.005, 2010.

Lafon, S., Sokolik, I. N., Rajot, J. L., Caquineau, S., and Gaudichet, A.: Characterization of iron oxides in mineral dust aerosols: Implications for light absorption, J. Geophys. Res.-Atmos, 111, D21207, doi: 10.1029/2005jd007016, 2006.

Li, L., Mahowald, N. M., Miller, R. L., Pérez García-Pando, C., Klose, M., Hamilton, D. S., Gonçalves Ageitos, M., Ginoux, P., Balkanski, Y., Green, R. O., Kalashnikova, O., Kok, J. F., Obiso, V., Paynter, D., and Thompson, D. R.: Quantifying the range of the dust direct radiative effect due to source mineralogy uncertainty, Atmos. Chem. Phys., 21, 3973-4005, doi: 10.5194/acp-21-3973-2021, 2021.

Li, W. J., Xu, L., Liu, X. H., Zhang, J. C., Lin, Y. T., Yao, X. H., Gao, H. W., Zhang, D. Z., Chen, J. M., Wang, W. X., Harrison, R. M., Zhang, X. Y., Shao, L. Y., Fu, P. Q., Nenes, A., and Shi, Z. B.: Air pollution-aerosol interactions produce more bioavailable iron for ocean ecosystems, Sci. Adv., 3, e1601749, doi: 10.1126/sciadv.1601749, 2017.

Lohmann, U., and Feichter, J.: Global indirect aerosol effects: a review, Atmos. Chem. Phys., 5, 715-737, doi: 10.5194/acp-5-715-2005, 2005.

Longo, A. F., Feng, Y., Lai, B., Landing, W. M., Shelley, R. U., Nenes, A., Mihalopoulos, N., Violaki, K., and Ingall, E. D.: Influence of Atmospheric Processes on the Solubility and Composition of Iron in Saharan Dust, Environ. Sci. Technol., 50, 6912-6920, doi: 10.1021/acs.est.6b02605, 2016.

Longtin, D. R., Shettle, E. P., Hummel, J. R., and Pryce, J. D.: A wind dependent desert aerosol model: Radiative properties, AFGLTR-88-0112, Air Force Geophysics Laboratory, Hanscom AFB, MA, 1988.

Luo, C., Mahowald, N., Bond, T., Chuang, P. Y., Artaxo, P., Siefert, R., Chen, Y., and Schauer, J.: Combustion iron distribution and deposition, Global Biogeochem. Cy., 22, GB1012, doi: 10.1029/2007gb002964, 2008.

Maher, B. A., Prospero, J. M., Mackie, D., Gaiero, D., Hesse, P. P., and Balkanski, Y.: Global connections between aeolian dust, climate and ocean biogeochemistry at the present day and at the last glacial maximum, Earth-Sci. Rev., 99, 61-97, doi: 10.1016/j.earscirev.2009.12.001, 2010.

Mahowald, N., Ward, D. S., Kloster, S., Flanner, M. G., Heald, C. L., Heavens, N. G., Hess, P. G., Lamarque, J.-F., and Chuang, P. Y.: Aerosol Impacts on Climate and Biogeochemistry, Annu. Rev. Environ. Resour., 36, 45-74, doi: 10.1146/annurev-environ-042009-094507, 2011.

Mahowald, N. M., Kloster, S., Engelstaedter, S., Moore, J. K., Mukhopadhyay, S., McConnell, J. R., Albani, S., Doney, S. C., Bhattacharya, A., Curran, M. A. J., Flanner, M. G., Hoffman, F. M., Lawrence, D. M., Lindsay, K., Mayewski, P. A., Neff, J., Rothenberg, D., Thomas, E., Thornton, P. E., and Zender, C. S.: Observed 20th century desert dust variability: impact on climate and biogeochemistry, Atmos. Chem. Phys., 10, 10875-10893, doi: 10.5194/acp-10-10875-2010, 2010.

Mahowald, N. M., Scanza, R., Brahney, J., Goodale, C. L., Hess, P. G., Moore, J. K., and Neff, J.: Aerosol Deposition Impacts on Land and Ocean Carbon Cycles, Curr. Clim. Change Rep., 3, 16-31, doi: 10.1007/s40641-017-0056-z, 2017.

Martin, J. H.: Glacial-interglacial CO_2 change: The Iron Hypothesis, Paleoceanography, 5, 1-13, doi: 10.1029/PA005i001p00001, 1990.

Matsui, H., Mahowald, N. M., Moteki, N., Hamilton, D. S., Ohata, S., Yoshida, A., Koike, M., Scanza, R. A., and Flanner, M. G.: Anthropogenic combustion iron as a complex climate forcer, Nat. Commun., 9, 1593, doi: 10.1038/s41467-018-03997-0, 2018.

Meinander, O., Kontu, A., Virkkula, A., Arola, A., Backman, L., Dagsson-Waldhauserová, P., Järvinen, O., Manninen, T., Svensson, J., de Leeuw, G., and Leppäranta, M.: Brief communication: Light-absorbing impurities can reduce the density of melting snow, Cryosphere, 8, 991-995, doi: 10.5194/tc-8-991-2014, 2014.

Meskhidze, N., Volker, C., Al-Abadleh, H. A., Barbeau, K., Bressac, M., Buck, C., Bundy, R. M., Croot, P., Feng, Y., Ito, A., Johansen, A. M., Landing, W. M., Mao, J. Q., Myriokefalitakis, S., Ohnemus, D., Pasquier, B., and Ye, Y.: Perspective on identifying and characterizing the processes controlling iron speciation and residence time at the atmosphere-ocean interface, Mar. Chem., 217, 103704, doi: 10.1016/j.marchem.2019.103704, 2019.

Mills, M. M., Ridame, C., Davey, M., La Roche, J., and Geider, R. J.: Iron and phosphorus co-limit nitrogen fixation in the eastern tropical North Atlantic, Nature, 429, 292-294, doi: 10.1038/nature02550, 2004.

Moore, C. M., Mills, M. M., Milne, A., Langlois, R., Achterberg, E. P., Lochte, K., Geider, R. J., and La Roche, J.: Iron limits primary productivity during spring bloom development in the central North Atlantic, Glob. Change Biol., 12, 626-634, doi: 10.1111/j.1365-2486.2006.01122.x, 2006.

Moosmuller, H., Engelbrecht, J. P., Skiba, M., Frey, G., Chakrabarty, R. K., and Arnott, W. P.: Single scattering albedo of fine mineral dust aerosols controlled by iron concentration, J. Geophys. Res.-Atmos, 117, D11210, doi: 10.1029/2011jd016909, 2012.

Moroni, B., Arnalds, O., Dagsson-Waldhauserova, P., Crocchianti, S., Vivani, R., and Cappelletti, D.: Mineralogical and Chemical Records of Icelandic Dust Sources Upon Ny-angstrom lesund (Svalbard Islands), Front. Earth Sci., 6, UNSP 187, doi: 10.3389/feart.2018.00187, 2018.

Moteki, N., Adachi, K., Ohata, S., Yoshida, A., Harigaya, T., Koike, M., and Kondo, Y.: Anthropogenic iron oxide aerosols enhance atmospheric heating, Nat. Commun., 8, 15329, doi: 10.1038/ncomms15329, 2017.

Myriokefalitakis, S., Daskalakis, N., Mihalopoulos, N., Baker, A. R., Nenes, A., and Kanakidou, M.: Changes in dissolved iron deposition to the oceans driven by human activity: a 3-D global modelling study, Biogeosciences, 12, 3973-3992, doi: 10.5194/bg-12-3973-2015, 2015.

Myriokefalitakis, S., Ito, A., Kanakidou, M., Nenes, A., Krol, M. C., Mahowald, N. M., Scanza, R. A., Hamilton, D. S., Johnson, M. S., Meskhidze, N., Kok, J. F., Guieu, C., Baker, A. R., Jickells, T. D., Sarin, M. M., Bikkina, S., Shelley, R., Bowie, A., Perron, M. M. G., and Duce, R. A.: Reviews and syntheses: the GESAMP atmospheric iron deposition model intercomparison study, Biogeosciences, 15, 6659-6684, doi: 10.5194/bg-15-6659-2018, 2018.

Nickovic, S., Vukovic, A., Vujadinovic, M., Djurdjevic, V., and Pejanovic, G.: Technical Note: High-resolution mineralogical database of dust-productive soils for atmospheric dust modeling, Atmos. Chem. Phys., 12, 845-855, doi: 10.5194/acp-12-845-2012, 2012.

Oakes, M., Ingall, E. D., Lai, B., Shafer, M. M., Hays, M. D., Liu, Z. G., Russell, A. G., and Weber, R. J.: Iron Solubility Related to Particle Sulfur Content in Source Emission and Ambient Fine Particles, Environ. Sci. Technol., 46, 6637-6644, doi: 10.1021/es300701c, 2012.

Painter, T. H., Barrett, A. P., Landry, C. C., Neff, J. C., Cassidy, M. P., Lawrence, C. R., McBride, K. E., and Farmer, G. L.: Impact of disturbed desert soils on duration of mountain snow cover, Geophys. Res. Lett., 34, L12502, doi: 10.1029/2007gl030284, 2007.

Paris, R., Desboeufs, K. V., Formenti, P., Nava, S., and Chou, C.: Chemical characterisation of iron in dust and biomass burning aerosols during AMMA-SOP0/DABEX: implication for iron solubility, Atmos. Chem. Phys., 10, 4273-4282, doi: 10.5194/acp-10-4273-2010, 2010.

Paris, R., Desboeufs, K. V., and Journet, E.: Variability of dust iron solubility in atmospheric waters: Investigation of the role of oxalate organic complexation, Atmos. Environ., 45, 6510-6517, doi: 10.1016/j.atmosenv.2011.08.068, 2011.

Paris, R., and Desboeufs, K. V.: Effect of atmospheric organic complexation on iron-bearing dust solubility, Atmos. Chem. Phys., 13, 4895-4905, doi: 10.5194/acp-13-4895-2013, 2013.

Peltoniemi, J. I., Gritsevich, M., Hakala, T., Dagsson-Waldhauserova, P., Arnalds, O., Anttila, K., Hannula, H. R., Kivekas, N., Lihavainen, H., Meinander, O., Svensson, J., Virkkula, A., and de Leeuw, G.: Soot on Snow experiment: bidirectional reflectance factor measurements of contaminated snow, Cryosphere, 9, 2323-2337, doi: 10.5194/tc-9-2323-2015, 2015.

Pöschl, U.: Atmospheric Aerosols: Composition, Transformation, Climate and Health Effects, Angew. Chem. Int. Ed., 44, 7520-7540, doi: 10.1002/anie.200501122, 2005.

Qian, Y., Yasunari, T. J., Doherty, S. J., Flanner, M. G., Lau, W. K. M., Ming, J., Wang, H. L., Wang, M., Warren, S. G., and Zhang, R. D.: Light-absorbing Particles in Snow and Ice: Measurement and Modeling of Climatic and Hydrological impact, Adv. Atmos. Sci., 32, 64-91, doi: 10.1007/s00376-014-0010-0, 2015.

Magnetite, Refractive index database, available at https://refractiveindex.info/?shelf=main&book=Fe3O4& (last access: 02 January 2020), 1985.

Rathod, S. D., Hamilton, D. S., Mahowald, N. M., Klimont, Z., Corbett, J. J., and Bond, T. C.: A Mineralogy ‐ Based Anthropogenic Combustion ‐ Iron Emission Inventory, J. Geophys. Res.-Atmos, 125, e2019JD032114, doi: 10.1029/2019jd032114, 2020.

Schroth, A. W., Crusius, J., Sholkovitz, E. R., and Bostick, B. C.: Iron solubility driven by speciation in dust sources to the ocean, Nat. Geosci., 2, 337-340, doi: 10.1038/ngeo501, 2009.

Sedwick, P. N., Sholkovitz, E. R., and Church, T. M.: Impact of anthropogenic combustion emissions on the fractional solubility of aerosol iron: Evidence from the Sargasso Sea, Geochem. Geophys., 8, Q10Q06, doi: 10.1029/2007gc001586, 2007.

Seinfeld, J. H., and Pandis, S. N.: Atmospheric chemistry and physics: from air pollution to climate change, John Wiley & Sons, 2016.

Shelley, R. U., Landing, W. M., Ussher, S. J., Planquette, H., and Sarthou, G.: Regional trends in the fractional solubility of Fe and other metals from North Atlantic aerosols (GEOTRACES cruises GA01 and GA03) following a two-stage leach, Biogeosciences, 15, 2271-2288, doi: 10.5194/bg-15-2271-2018, 2018.

Shi, Z., Krom, M. D., Bonneville, S., Baker, A. R., Jickells, T. D., and Benning, L. G.: Formation of iron nanoparticles and increase in iron reactivity in the mineral dust during simulated cloud processing, Environ. Sci. Technol., 43, 6592-6596, doi: 10.1021/es901294g, 2009.

Shi, Z., Bonneville, S., Krom, M. D., Carslaw, K. S., Jickells, T. D., Baker, A. R., and Benning, L. G.: Iron dissolution kinetics of mineral dust at low pH during simulated atmospheric processing, Atmos. Chem. Phys., 11, 995-1007, doi: 10.5194/acp-11-995-2011, 2011a.

Shi, Z., Krom, M. D., Bonneville, S., Baker, A. R., Bristow, C., Drake, N., Mann, G., Carslaw, K., McQuaid, J. B., Jickells, T., and Benning, L. G.: Influence of chemical weathering and aging of iron oxides on the potential iron solubility of Saharan dust during simulated atmospheric processing, Global Biogeochem. Cy., 25, GB2010, doi: 10.1029/2010gb003837, 2011b.

Shi, Z., Krom, M. D., Jickells, T. D., Bonneville, S., Carslaw, K. S., Mihalopoulos, N., Baker, A. R., and Benning, L. G.: Impacts on iron solubility in the mineral dust by processes in the source region and the atmosphere: A review, Aeolian Res., 5, 21-42, doi: 10.1016/j.aeolia.2012.03.001, 2012.

Shi, Z., Krom, M. D., Bonneville, S., and Benning, L. G.: Atmospheric processing outside clouds increases soluble iron in mineral dust, Environ. Sci. Technol., 49, 1472-1477, doi: 10.1021/es504623x, 2015.

Shi, Z. B., Woodhouse, M. T., Carslaw, K. S., Krom, M. D., Mann, G. W., Baker, A. R., Savov, I., Fones, G. R., Brooks, B., Drake, N., Jickells, T. D., and Benning, L. G.: Minor effect of physical size sorting on iron solubility of transported mineral dust, Atmos. Chem. Phys., 11, 8459-8469, doi: 10.5194/acp-11-8459-2011, 2011c.

Sholkovitz, E. R., Sedwick, P. N., and Church, T. M.: Influence of anthropogenic combustion emissions on the deposition of soluble aerosol iron to the ocean: Empirical estimates for island sites in the North Atlantic, Geochim. Cosmochim. Ac., 73, 3981-4003, doi: 10.1016/j.gca.2009.04.029, 2009.

Sholkovitz, E. R., Sedwick, P. N., Church, T. M., Baker, A. R., and Powell, C. F.: Fractional solubility of aerosol iron: Synthesis of a global-scale data set, Geochim. Cosmochim. Ac., 89, 173-189, doi: 10.1016/j.gca.2012.04.022, 2012.

Sokolik, I. N., Toon, O. B., and Bergstrom, R. W.: Modeling the radiative characteristics of airborne mineral aerosols at infrared wavelengths, J. Geophys. Res.-Atmos, 103, 8813-8826, doi: 10.1029/98JD00049, 1998.

Sokolik, I. N., and Toon, O. B.: Incorporation of mineralogical composition into models of the radiative properties of mineral aerosol from UV to IR wavelengths, J. Geophys. Res.-Atmos, 104, 9423-9444, doi: 10.1029/1998jd200048, 1999.

Srinivas, B., Sarin, M. M., and Kumar, A.: Impact of anthropogenic sources on aerosol iron solubility over the Bay of Bengal and the Arabian Sea, Biogeochemistry, 110, 257-268, doi: 10.1007/s10533-011-9680-1, 2012.

Stockdale, A., Krom, M. D., Mortimer, R. J., Benning, L. G., Carslaw, K. S., Herbert, R. J., Shi, Z., Myriokefalitakis, S., Kanakidou, M., and Nenes, A.: Understanding the nature of atmospheric acid processing of mineral dusts in supplying bioavailable phosphorus to the oceans, P. Natl. Acad. Sci. USA, 113, 14639-14644, doi: 10.1073/pnas.1608136113, 2016.

Tagliabue, A., Bowie, A. R., Boyd, P. W., Buck, K. N., Johnson, K. S., and Saito, M. A.: The integral role of iron in ocean biogeochemistry, Nature, 543, 51-59, doi: 10.1038/nature21058, 2017.

Wang, R., Balkanski, Y., Boucher, O., Bopp, L., Chappell, A., Ciais, P., Hauglustaine, D., Penuelas, J., and Tao, S.: Sources, transport and deposition of iron in the global atmosphere, Atmos. Chem. Phys., 15, 6247-6270, doi: 10.5194/acp-15-6247-2015, 2015.

CHAPTER 2: FIELD OBSERVATIONS AND LABORATORY MEASUREMENTS OF PYROGENIC IRON AEROSOL

In this section, we will review the key observational and laboratory evidence of the direct emissions and secondary production of dissolved iron (DFe).

2.1 Aerosol Fe emission and solubility

The estimated global total Fe emission to the atmosphere is 37-140 Tg Fe yr^{-1}, around 95% originating from lithogenic sources, while the rest coming from pyrogenic sources including open biomass burning, coal combustion, shipping emissions, and metal smelting industry (Ito, 2013; Ito et al., 2018; Luo et al., 2008; Myriokefalitakis et al., 2015; Rathod et al., 2020; Wang et al., 2015). Even though mineral dust represents the largest contribution to atmospheric Fe, their solubility over low latitude source regions is low, usually <0.5% (Baker et al., 2006; Chuang et al., 2005; Schroth et al., 2009; Sedwick et al., 2007). On the other hand, the pyrogenic aerosol Fe solubility varies considerably depending on the sources and can be 1–2 orders of magnitude higher than mineral dust (Table 2.1).

Table 2.1 summarizes the Fe solubilities (%) in aerosols of pyrogenic origins, including solid fuel combustion, biomass burning, and liquid fuel combustion. Solid fuel combustion includes biofuel wood and waste burning, coal combustion, and metal smelting process. The total Fe content and the estimated contribution of each source to the total Fe emissions are also reported. The total Fe emissions from solid fuel combustion and biomass burning are 0.5-1.9 Tg Fe yr^{-1} and 0.5-1.2 Tg Fe yr^{-1}, respectively (Ito, 2013; Ito et al., 2018; Luo et al., 2008; Myriokefalitakis et al., 2015; Rathod et al., 2020; Wang et al., 2015). Minor contribution derives from liquid fuel combustion such as ship emissions, which is around 0.02% (Ito, 2013; Ito et al., 2018; Myriokefalitakis et al., 2015; Rathod et al., 2020; Wang et al., 2015).

The total Fe content is 0.1-12% in coal fly ash (Borgatta et al., 2016; Chen et al., 2012; Desboeufs et al., 2005; Fu et al., 2012; Ito and Feng, 2010; Ito et al., 2018; Rathod et al., 2020; Sholkovitz et al., 2009), 0.02-5.5% in biomass burning aerosol (Fu et al., 2012; Ito, 2011; Ito and Feng, 2010; Paris et al., 2010), and 0.1-9% in oil fly ash (Desboeufs et al., 2005; Fu et al., 2012; Ito et al., 2018; Rathod et al., 2020; Schroth et al., 2009; Sholkovitz et al., 2009). Emission inventories apply much higher Fe content to iron and steel smelting-related processes (26%-44%) (Ito et al., 2018; Rathod et al., 2020).

Schroth et al. (2009) found a very high aerosol Fe solubility in oil fly ash (77%-81%), where Fe is likely in the form of ferric sulfate salt ($Fe_2(SO_4)_3 \cdot 9(H_2O)$). A laboratory study reported 36% aerosol Fe solubility for oil fly ash, which is significantly higher than the 0.2% aerosol Fe solubility for coal fly ash (Desboeufs et al., 2005). The dominant component of coal fly ash is the aluminosilicate glass with aggregates of Fe (oxyhydr)oxide (Chen et al., 2012; Desboeufs et al., 2005; Fu et al., 2012), which is less soluble than ferric sulfate salt. Oakes et al. (2012) also estimated a considerably lower aerosol Fe solubility for coal fly ash (0.06%), compared to 51-75% and 46% Fe solubilities in vehicle exhaust and biomass burning, respectively. Guieu et al. (2005) and Paris et al. (2010) reported much lower aerosol Fe solubility for biomass burning near the source (around 2%) than the 18% aerosol Fe solubility over the ocean for aerosols mainly influenced by bushfire plumes (not at source) (Bowie et al., 2009). Field observations and laboratory measurements suggest that Fe solubilities near the source regions vary significantly, with lower values observed near dust source regions but higher values near oil combustion and biomass burning sources (Table 2.1). The high Fe solubilities in aerosols from the oil and biomass combustion are attributed to the presence of Fe sulfate instead of Fe oxides or Fe-bearing silicate minerals in dust (Oakes et al., 2012; Schroth et al., 2009). Long-range transport can alter the Fe properties and enhance Fe solubilities. It appears that current observations are inadequate to trace the aerosols from different sources and capture the variabilities in their Fe solubilities during atmospheric processing after atmospheric mixing between air masses of various origins.

Table 2.1: Estimated total Fe emissions, total Fe content, and aerosol Fe solubility largely influenced by pyrogenic aerosol sources: solid fuel combustion, biomass burning, and liquid fuel combustion. The solid fuel combustion includes biofuel wood and waste burning, coal combustion, and metal smelting process.

	Total Fe content (% particle mass)		Estimated total Fe emissions (Tg Fe yr^{-1})		Aerosol Fe solubility (%) for specific sources		
Solid fuel combustion	8.8	Desboeufs et al. (2005)	0.66	Luo et al. (2008)	0.2	2 h leaching in pH 4.7 sulfuric acid	Desboeufs et al. (2005)
	1-11	Sholkovitz et al. (2009)	0.51	Ito (2013)	0.06	30 min leaching in de-ionized water	Oakes et al. (2012)
	0.02-16	Ito and Feng (2010)	0.77	Myriokefalitakis et al. (2015)			
	3.57-9.32	Chen et al. (2012)	1.04	Wang et al. (2015)			
	3.7-11.9	Fu et al. (2012)	1.91	Ito et al. (2018)			
	0.9-3.8	Borgatta et al. (2006)	2.16	Rathod et al. (2020)			
	0.1-26	Ito et al. (2018)					
	0.12-44	Rathod et al. (2020)					
Biomass burning	0.02-3.4	Ito and Feng (2010)	1.07	Luo et al. (2008)	2	7 days leaching in seawater	Guieu et al. (2005)
	5.4-5.5	Paris (2010)	1.15	Ito (2013)	18	Instantaneous leaching in seawater	Bowie et al. (2009)
	0.06-3.4	Ito (2011)	0.79	Ito et al. (2018)	2.19	30 min leaching in de-ionized water	Paris et al. (2010)
	0.4-3.3	Fu et al. (2012)	1.2	Myriokefalitakis et al. (2015)	46	30 min leaching in de-ionized water	Oakes et al. (2012)
			0.5	Wang et al. (2015)			
Liquid fuel combustion	9.3	Fu et al. (2012)	0.016	Ito (2013)	36	2 h leaching in pH 4.7 sulfuric acid	Desboeufs et al. (2005)
	0.9-3.78	Schroth et al. (2009)	0.015	Myriokefalitakis et al. (2015)	77–81	Successive leaching in de-ionized water	Schroth et al. (2009)
	3.5	Desboeufs et al. (2005)	0.022	Wang et al. (2015)	51–75	30 min leaching in de-ionized water	Oakes et al. (2012)
	0.2-4	Sholkovitz et al. (2009)	0.019	Ito et al. (2018)			
	0.96-1.7	Ito et al. (2018)	0.034	Rathod et al. (2020)			
	0.11-4.37	Rathod et al. (2020)					

2.2 Field observation on pyrogenic Fe aerosol

The most direct evidence of anthropogenic emissions of Fe-containing aerosols comes from the single-particle analysis. Anthropogenic Fe-rich particles were directly identified close to the source, (i.e., steel plants), by both single-particle mass spectrometer (Taiwo et al., 2014) and microscopic analysis (Moreno et al., 2003; Zhang et al., 2014). They were also identified in the marine atmosphere, for instance, over the English Channel (Choel et al., 2007), Western Pacific Ocean (Furutani et al., 2011; Li et al., 2017; Moffet et al., 2012), and in the urban atmosphere (Ault et al., 2012; Zhang et al., 2014). Figure 2.1a shows spherical Fe-rich particles, which are likely formed under high-temperature processes, such as in steel plants.

Field observations have reported that magnetite is ubiquitous in anthropogenic aerosols (Moteki et al., 2017; Ohata et al., 2018; Tavares et al., 2017; Yoshida et al., 2018), as it crystallizes from the aluminosilicate glass during the ash formation. Since magnetite (Fe_3O_4) and hematite (α-Fe_2O_3) strongly absorb sunlight, a modified single-particle soot photometer (SP2) was employed to identify light-absorbing Fe oxide (FeOx) particles originating from anthropogenic combustion processes (Lamb, 2019; Moteki et al., 2017). The field measurements over both East Asia and the Arctic reported that mass concentrations of anthropogenic FeOx were at least 20% of those of black carbon (BC) (Yoshida et al., 2020). On the other hand, a limited number of observations suggests that magnetite is low or negligible in mineral dust from low latitude regions such as northern Africa and Asia, e.g., from not detectable to 0.1% in Saharan dust (Moskowitz et al., 2016) to 0.1-0.8 wt% in source regions of Asian dust (Jia et al., 2019; Maher et al., 2009; Song et al., 2014). Magnetite in high-latitude dust could be higher, for example, 1-2 wt% in Icelandic dust (Baldo et al., 2020). The content of magnetite in anthropogenic aerosols and their contribution to ambient bulk aerosols remain largely unknown. Therefore, more research is needed to quantify the content of magnetite in the sources and the Fe dissolution in aerosols (Hettiarachchi et al., 2019; Ito et al., 2018).

Several observational studies have attempted to link the aerosol Fe solubility to the aerosol chemical components. These studies suggest that the tendency of high Fe solubilities with low Fe concentrations

is influenced by pyrogenic sources and/or atmospheric processing (Chuang et al., 2005; Kumar et al., 2010; Sedwick et al., 2007; Zhang et al., 2013). It is, however, difficult to quantitatively disentangle these two factors from the atmospheric observations of the elemental composition alone (McDaniel et al., 2019; Sholkovitz et al., 2012).

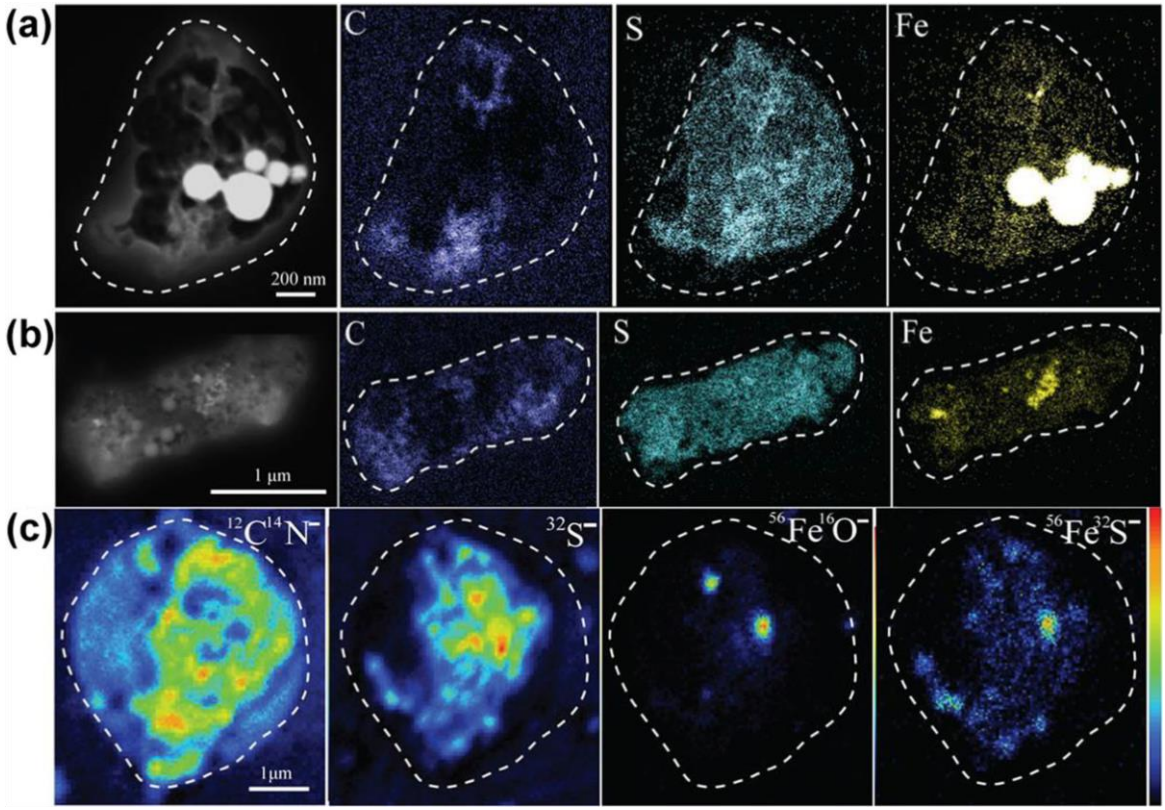

Figure 2.1: Dark-field TEM images and elemental maps of C, S, and Fe and NanoSIMS ion intensity maps of CN^-, S^-, FeO^-, and FeS^- of individual Fe-bearing particles. a-b) Elemental maps showing two individual sulfate particles with Fe-rich particles (as hotspots). C) Ion intensity maps showing the presence of organic matter, sulfate, Fe oxide, and Fe sulfate (reproduced from Li et al. 2017).

2.3 Field observations on the atmospheric processing of pyrogenic Fe aerosol

Zhu et al. (1992) proposed that the low pH predicted in aerosol water under polluted conditions could lead to the dissolution of ferric Fe from α-Fe_2O_3, FeO(OH) and $Fe(OH)_3$ minerals. Many laboratory, modelling and observation studies aimed to confirm the acid Fe dissolution hypothesis (Meskhidze et al., 2003). Laboratory experiments showed the insoluble Fe in aerosols is dissolved at low pH conditions (pH 1–3) (Chen et al., 2012; Fu et al., 2012; Shi et al., 2015; Spokes et al., 1994), lending some indirect evidence to this hypothesis. However, field observations have been less conclusive (Baker et al., 2006;

Buck et al., 2013; Buck et al., 2010; Kumar et al., 2010; McDaniel et al., 2019; Trapp et al., 2010). Recently, Li et al. (2017) provided convincing evidence of the acid dissolution of Fe in aerosol water. They observed Fe-containing particles in samples collected over the Yellow Sea, likely from coal combustion and steel industries, which were coated with sulfate. The single-particle analysis suggested that Fe was detected not only as "hotspots" (i.e., primary particles) but also in the sulfate coating as (water-soluble) Fe sulfate (Figure 2.1b-c). Since water-soluble Fe was not detected in the freshly emitted particles, this could only be formed via the acid dissolution of the primary particles.

2.4 Laboratory experiments of Fe dissolution kinetics

Aerosol particles are subject to both physical and chemical processes during long-range transport. The chemically and photochemically based processing have been shown to have the potential to convert relatively insoluble Fe to more labile Fe forms (Kumar et al., 2010; Li et al., 2017; Srinivas et al., 2012; Srinivas et al., 2014; Takahashi et al., 2011; Zhang et al., 2013). Several studies focused on the acid and photochemical processes involved in the Fe dissolution in lithogenic and pyrogenic aerosol sources. Laboratory simulations have currently identified three principal mechanisms for the Fe dissolution: proton-promoted, ligand-promoted, and photo-reductive dissolution of Fe (Chen et al., 2012; Chen and Grassian, 2013; Cwiertny et al., 2008a; Cwiertny et al., 2008b; Desboeufs et al., 2005; Fu et al., 2010; Fu et al., 2012; Ito and Shi, 2016; Paris and Desboeufs, 2013; Paris et al., 2011; Shi et al., 2011a; Shi et al., 2011b; Shi et al., 2009; Shi et al., 2015).

The aerosol Fe solubility primarily depends on the pH of the leaching media and is enhanced as the pH decreases. At low pH, the increasing concentrations of H^+ contribute to the protonation process which weakens the Fe-O bond on the particle surface favoring the detachment of Fe from the bulk oxides into solution (Cornell and Schwertmann, 2003). Shi et al. (2009, 2011b, 2015) investigated the effect of the proton-promoted dissolution on mineral dust during laboratory experiments to simulate acid and cloud processing, where the dust particles were subjected to multiple cycling between acidic (24 h at pH 1-2) and circumneutral pH (24 h at pH 5-6) up to 3 days. Low pH (pH 1-2), a condition relevant to fine aerosols, enhances the dissolution of metals including Fe and copper (Cu) (Fang et al., 2017). Under

cloud conditions (pH 5-6), the Fe dissolution is suppressed, and the formation of Fe-rich nanoparticle aggregates was observed when with no organic ligand in solution (Shi et al., 2009, 2011b, 2015).

Chen et al. (2012) simulated the acid and cloud processing of three certified coal fly ash samples, where the suspension of coal fly ash was cycled between pH 2 and pH 5 over periods of 24 h. The aerosol Fe solubility was ~20–70% after three pH cycles (Chen et al., 2012), which was considerably higher than that one found in mineral dust (Shi et al., 2011b). Subsequently, a laboratory study (Chen and Grassian, 2013) investigated the impact of organic ligands (i.e., oxalate) on the Fe dissolution behavior at low pH of the certified coal fly ash samples in comparison with the Arizona test dust (AZTD). Chen and Grassian (2013) reported that at low pH the aerosol Fe solubility of the fly ash could almost double in presence of oxalic acid. The aerosol Fe solubility for the fly ash samples (~40-80%) were similar to ~60% for the AZTD after 45 h at pH 2 in presence of oxalate. Oxalate can form bidentate complexes with Fe on the particle surface, and thus it promotes the Fe dissolution process when in excess. In addition, the light-induced reduction of the structural Fe(III) to Fe(II) along with the oxidation of Fe(II)-oxalate complexes can further enhance the detachment of Fe(II) from the surface to yield dissolved Fe(II) (photo-reductive dissolution) (Chen and Grassian, 2013).

Fu et al. (2012) assessed the Fe dissolution kinetics of lithogenic and pyrogenic aerosol sources at pH 2. The leaching experiments were carried out in hydrochloric acid solutions in either dark conditions or the presence of light (Figure 2.2). The aerosol Fe solubility after 12 h was 2.9-4.2% for coal fly ash, 74% for oil fly ash, 8.9-26.4% for biomass burning aerosols, and 4.3% for the Chinese loess. Slightly higher Fe solubilities were observed in presence of light (with no organic ligands) compared to dark conditions, due to the photochemical reduction of surface Fe(III) to Fe(II).

Borgatta et al. (2016) conducted laboratory experiments on coal fly ash samples collected from three distinctive locations: the USA Midwest, North-East India, and Europe. Sodium chloride (NaCl) was used to adjust the activity of proton in the acidic solutions (pH 1-2) to represent the high ionic strength in marine aerosol water. The resulting total Fe solubility at pH 2 after 24 h was 15-70%. The high variability in Fe dissolution behavior is attributed to the different physicochemical properties of the three

coal fly ash samples. For example, Fe speciation, surface area, and morphology are dependent on the source region and the coal combustion process (Borgatta et al., 2016). This is consistent with the findings in previous studies (Chen et al., 2012; Chen and Grassian, 2013). The high ionic strength influences the activity of protons and ligands in solution, hence it can affect the Fe dissolution behavior. However, currently, only a limited number of studies have considered the effect of the high ionic strength on the aerosol Fe solubility (Borgatta et al., 2016; Cwiertny et al., 2008a; Ito and Shi, 2016).

Overall, oil fly ash and biomass burning aerosols showed high Fe solubilities at acidic conditions, while the coal fly ash had variable Fe solubility, similar or considerably higher than mineral dust (Figure 2.2) (Fu et al., 2010; Fu et al., 2012). The Fe dissolution rates determined through laboratory experiments were used to parameterize atmospheric processing and the transformation of relatively insoluble Fe into DFe according to the proton-promoted, oxalate-promoted, and photo-reductive dissolution processes in global models (Table 2.2). The source type is also considered, as the release rate of DFe is faster in combustion aerosols compared to mineral dust (Figure 2.3) (Ito, 2015; Ito and Shi, 2016).

Table 2.2: Constants used to calculate Fe dissolution rates for pyrogenic aerosols in IMPACT model (Ito, 2015) and CAM5 (Hamilton et al., 2019).

Dissolution scheme	Model	Rate constant - k(pH, T)[a]	m[c]	A_j[d]
Proton-promoted	IMPACT	$3.05 \times 10^{-9}\exp[E(pH)^b \times (1/298 - 1/T)]$	0.36	0.8
	CAM5	$1.3 \times 10^{-11}\exp[9.2 \times 10^3 \times (1/298 - 1/T)]$	0.39	90
Oxalate-promoted	IMPACT	$2.24 \times 10^{-7}\exp[E(pH)^b \times (1/298 - 1/T)]$	1	0.8
	CAM5	$2.3 \times 10^{-7} \times [\text{oxalate}] + 4.8$		
Photoinduced	IMPACT	$2.39 \times 10^{-7}\exp[E(pH)^b \times (1/298 - 1/T)]$	1	0.8

[a] $K_i(T)$ is the reaction coefficient (moles m^{-2} s^{-1}) for each dissolution scheme i.
[b] $E(pH) = -1.56 \times 10^3 \times pH + 1.08 \times 10^4$.
[c] m_i is the reaction order with respect to aqueous phase protons.
[d] A_j is the specific surface area of Fe species in units of m^2 g^{-1}.
[e] The photoinduced dissolution rate of Fe compounds is scaled to the photolysis rate of H2O2 calculated in the model.

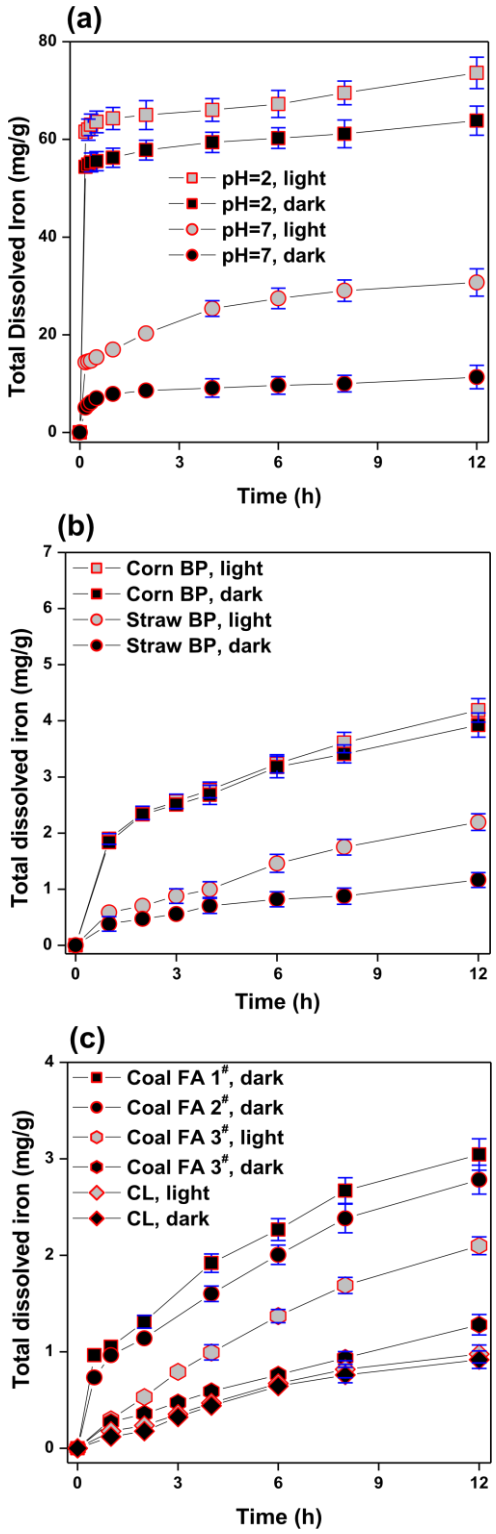

Figure 2.2: Comparison of total dissolved Fe concentration (mg g^{-1}) between pyrogenic and lithogenic aerosol sources at pH = 2 or 7. Total dissolved Fe concentration in a) oil fly ash, b) biomass burning particle, and c) coal fly ash and Chinese Loess (CL) in dark conditions or under irradiation in HCl suspensions, solids loading of 1.5 g L^{-1} (reproduced from Fu et al. 2012). The error bars represent one standard deviation from triplicate experiments.

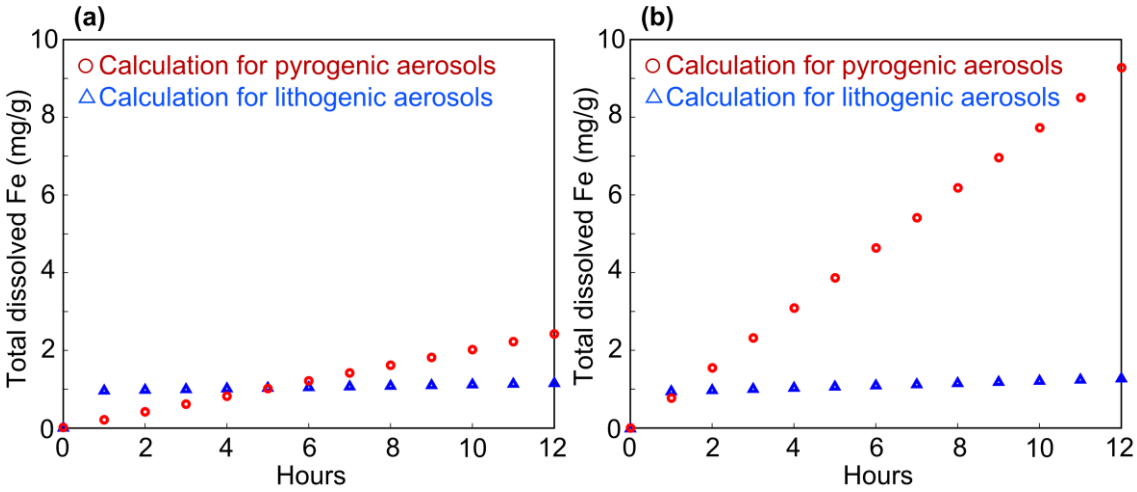

Figure 2.3: Comparison of total dissolved Fe concentration (mg g^{-1}) between pyrogenic and lithogenic aerosol sources at pH = 2. The estimates of total dissolved Fe concentration (mg g^{-1}) used in the IMPACT model a) with no organic ligand and b) with oxalate under dark conditions. The red curve was calculated for combustion aerosols (Ito, 2015). The blue curve was calculated for mineral aerosols (Ito and Shi, 2016). The total dissolved Fe concentration was calculated as mg of DFe per g of the solid particle.

2.5 References

Ault, A. P., Peters, T. M., Sawvel, E. J., Casuccio, G. S., Willis, R. D., Norris, G. A., and Grassian, V. H.: Single-Particle SEM-EDX Analysis of Iron-Containing Coarse Particulate Matter in an Urban Environment: Sources and Distribution of Iron within Cleveland, Ohio, Environ. Sci. Technol., 46, 4331-4339, doi: 10.1021/es204006k, 2012.

Baker, A. R., Jickells, T. D., Witt, M., and Linge, K. L.: Trends in the solubility of iron, aluminium, manganese and phosphorus in aerosol collected over the Atlantic Ocean, Mar. Chem., 98, 43-58, doi: 10.1016/j.marchem.2005.06.004, 2006.

Baldo, C., Formenti, P., Nowak, S., Chevaillier, S., Cazaunau, M., Pangui, E., Di Biagio, C., Doussin, J. F., Ignatyev, K., Dagsson-Waldhauserova, P., Arnalds, O., MacKenzie, A. R., and Shi, Z.: Distinct chemical and mineralogical composition of Icelandic dust compared to northern African and Asian dust, Atmos. Chem. Phys., 20, 13521-13539, doi: 10.5194/acp-20-13521-2020, 2020.

Borgatta, J., Paskavitz, A., Kim, D., and Navea, J. G.: Comparative evaluation of iron leach from different sources of fly ash under atmospherically relevant conditions, Environ. Chem., 13, 902-912, doi: 10.1071/en16046, 2016.

Bowie, A. R., Lannuzel, D., Remenyi, T. A., Wagener, T., Lam, P. J., Boyd, P. W., Guieu, C., Townsend, A. T., and Trull, T. W.: Biogeochemical iron budgets of the Southern Ocean south of Australia: Decoupling of iron and nutrient cycles in the subantarctic zone by the summertime supply, Global Biogeochem. Cy., 23, GB4034, doi: 10.1029/2009gb003500, 2009.

Buck, C. S., Landing, W. M., Resing, J. A., and Measures, C. I.: The solubility and deposition of aerosol Fe and other trace elements in the North Atlantic Ocean: Observations from the A16N CLIVAR/CO2 repeat hydrography section, Mar. Chem., 120, 57-70, doi: 10.1016/j.marchem.2008.08.003, 2010.

Buck, C. S., Landing, W. M., and Resing, J.: Pacific Ocean aerosols: Deposition and solubility of iron, aluminum, and other trace elements, Mar. Chem., 157, 117-130, doi: 10.1016/j.marchem.2013.09.005, 2013.

Chen, H., Laskin, A., Baltrusaitis, J., Gorski, C. A., Scherer, M. M., and Grassian, V. H.: Coal fly ash as a source of iron in atmospheric dust, Environ. Sci. Technol., 46, 2112-2120, doi: 10.1021/es204102f, 2012.

Chen, H. H., and Grassian, V. H.: Iron Dissolution of Dust Source Materials during Simulated Acidic Processing: The Effect of Sulfuric, Acetic, and Oxalic Acids, Environ. Sci. Technol., 47, 10312-10321, doi: 10.1021/es401285s, 2013.

Choel, M., Deboudt, K., Flament, P., Aimoz, L., and Meriaux, X.: Single-particle analysis of atmospheric aerosols at Cape Gris-Nez, English Channel: Influence of steel works on iron apportionment, Atmos. Environ., 41, 2820-2830, doi: 10.1016/j.atmosenv.2006.11.038, 2007.

Chuang, P. Y., Duvall, R. M., Shafer, M. M., and Schauer, J. J.: The origin of water soluble particulate iron in the Asian atmospheric outflow, Geophys. Res. Lett., 32, L07813, doi: 10.1029/2004gl021946, 2005.

Cornell, R. M., and Schwertmann, U.: The Iron Oxides: Structure, Properties, Reactions, Occurrence and Uses, Wiley-VCH, New York 2003.

Cwiertny, D. M., Baltrusaitis, J., Hunter, G. J., Laskin, A., Scherer, M. M., and Grassian, V. H.: Characterization and acid-mobilization study of iron-containing mineral dust source materials, J. Geophys. Res.-Atmos, 113, D05202, doi: 10.1029/2007jd009332, 2008a.

Cwiertny, D. M., Young, M. A., and Grassian, V. H.: Chemistry and photochemistry of mineral dust aerosol, Annu. Rev. Phys. Chem., 59, 27-51, doi: 10.1146/annurev.physchem.59.032607.093630, 2008b.

Desboeufs, K. V., Sofikitis, A., Losno, R., Colin, J. L., and Ausset, P.: Dissolution and solubility of trace metals from natural and anthropogenic aerosol particulate matter, Chemosphere, 58, 195-203, doi: 10.1016/j.chemosphere.2004.02.025, 2005.

Fang, T., Guo, H., Zeng, L., Verma, V., Nenes, A., and Weber, R. J.: Highly Acidic Ambient Particles, Soluble Metals, and Oxidative Potential: A Link between Sulfate and Aerosol Toxicity, Environ. Sci. Technol., 51, 2611-2620, doi: 10.1021/acs.est.6b06151, 2017.

Fu, H., Cwiertny, D. M., Carmichael, G. R., Scherer, M. M., and Grassian, V. H.: Photoreductive dissolution of Fe-containing mineral dust particles in acidic media, J. Geophys. Res., 115, D11304, doi: 10.1029/2009jd012702, 2010.

Fu, H. B., Lin, J., Shang, G. F., Dong, W. B., Grassian, V. H., Carmichael, G. R., Li, Y., and Chen, J. M.: Solubility of Iron from Combustion Source Particles in Acidic Media Linked to Iron Speciation, Environ. Sci. Technol., 46, 11119-11127, doi: 10.1021/es302558m, 2012.

Furutani, H., Jung, J. Y., Miura, K., Takami, A., Kato, S., Kajii, Y., and Uematsu, M.: Single-particle chemical characterization and source apportionment of iron-containing atmospheric aerosols in Asian outflow, J. Geophys. Res.-Atmos, 116, D18204, doi: 10.1029/2011jd015867, 2011.

Guieu, C., Bonnet, S., Wagener, T., and Loye-Pilot, M. D.: Biomass burning as a source of dissolved iron to the open ocean?, Geophys. Res. Lett., 32, L19608, doi: 10.1029/2005gl022962, 2005.

Hamilton, D. S., Scanza, R. A., Feng, Y., Guinness, J., Kok, J. F., Li, L., Liu, X., Rathod, S. D., Wan, J. S., Wu, M., and Mahowald, N. M.: Improved methodologies for Earth system modelling of atmospheric soluble iron and observation comparisons using the Mechanism of Intermediate complexity for Modelling Iron (MIMI v1.0), Geosci. Model Dev., 12, 3835-3862, doi: 10.5194/gmd-12-3835-2019, 2019.

Hettiarachchi, E., Reynolds, R. L., Goldstein, H. L., Moskowitz, B., and Rubasinghege, G.: Bioavailable iron production in airborne mineral dust:Control by chemical composition and solar flux, Atmos. Environ., 205, 90-102, doi: 10.1016/j.atmosenv.2019.02.037, 2019.

Ito, A., and Feng, Y.: Role of dust alkalinity in acid mobilization of iron, Atmos. Chem. Phys., 10, 9237-9250, doi: 10.5194/acp-10-9237-2010, 2010.

Ito, A.: Mega fire emissions in Siberia: potential supply of bioavailable iron from forests to the ocean, Biogeosciences, 8, 1679-1697, doi: 10.5194/bg-8-1679-2011, 2011.

Ito, A.: Global modeling study of potentially bioavailable iron input from shipboard aerosol sources to the ocean, Global Biogeochem. Cy., 27, 1-10, doi: 10.1029/2012gb004378, 2013.

Ito, A.: Atmospheric Processing of Combustion Aerosols as a Source of Bioavailable Iron, Environ. Sci. Technol. Lett., 2, 70-75, doi: 10.1021/acs.estlett.5b00007, 2015.

Ito, A., and Shi, Z.: Delivery of anthropogenic bioavailable iron from mineral dust and combustion aerosols to the ocean, Atmos. Chem. Phys., 16, 85-99, doi: 10.5194/acp-16-85-2016, 2016.

Ito, A., Lin, G. X., and Penner, J. E.: Radiative forcing by light-absorbing aerosols of pyrogenetic iron oxides, Sci. Rep., 8, 7347, doi: 10.1038/s41598-018-25756-3, 2018.

Jia, J., Wang, Y. J., Xia, D. S., Lu, H., and Gao, F. Y.: Dust Sources of Last Glacial Chinese Loess Based on the Iron Mineralogy of Fractionated Source Samples, Geophys. Res. Lett., 46, 2103-2110, doi: 10.1029/2018gl080909, 2019.

Kumar, A., Sarin, M. M., and Srinivas, B.: Aerosol iron solubility over Bay of Bengal: Role of anthropogenic sources and chemical processing, Mar. Chem., 121, 167-175, doi: 10.1016/j.marchem.2010.04.005, 2010.

Lamb, K. D.: Classification of iron oxide aerosols by a single particle soot photometer using supervised machine learning, Atmos. Meas. Tech., 12, 3885-3906, doi: 10.5194/amt-12-3885-2019, 2019.

Li, W. J., Xu, L., Liu, X. H., Zhang, J. C., Lin, Y. T., Yao, X. H., Gao, H. W., Zhang, D. Z., Chen, J. M., Wang, W. X., Harrison, R. M., Zhang, X. Y., Shao, L. Y., Fu, P. Q., Nenes, A., and Shi, Z. B.: Air pollution-aerosol interactions produce more bioavailable iron for ocean ecosystems, Sci. Adv., 3, e1601749, doi: 10.1126/sciadv.1601749, 2017.

Luo, C., Mahowald, N., Bond, T., Chuang, P. Y., Artaxo, P., Siefert, R., Chen, Y., and Schauer, J.: Combustion iron distribution and deposition, Global Biogeochem. Cy., 22, GB1012, doi: 10.1029/2007gb002964, 2008.

Maher, B. A., Mutch, T. J., and Cunningham, D.: Magnetic and geochemical characteristics of Gobi Desert surface sediments: Implications for provenance of the Chinese Loess Plateau, Geology, 37, 279-282, doi: 10.1130/g25293a.1, 2009.

McDaniel, M. F. M., Ingall, E. D., Morton, P. L., Castorina, E., Weber, R. J., Shelley, R. U., Landing, W. M., Longo, A. F., Feng, Y., and Lai, B.: Relationship between Atmospheric Aerosol Mineral Surface Area and Iron Solubility, ACS Earth Space Chem., 3, 2443-2451, doi: 10.1021/acsearthspacechem.9b00152, 2019.

Meskhidze, N., Chameides, W. L., Nenes, A., and Chen, G.: Iron mobilization in mineral dust: Can anthropogenic SO_2 emissions affect ocean productivity?, Geophys. Res. Lett., 30, 2085, doi: 10.1029/2003gl018035, 2003.

Moffet, R. C., Furutani, H., Rodel, T. C., Henn, T. R., Sprau, P. O., Laskin, A., Uematsu, M., and Gilles, M. K.: Iron speciation and mixing in single aerosol particles from the Asian continental outflow, J. Geophys. Res.-Atmos, 117, D07204, doi: 10.1029/2011jd016746, 2012.

Moreno, T., Gibbons, W., Jones, T., and Richards, R.: The geology of ambient aerosols: characterising urban and rural/coastal silicate PM10-2.5 and PM2.5 using high-volume cascade collection and scanning electron microscopy, Atmos. Environ., 37, 4265-4276, doi: 10.1016/s1352-2310(03)00534-x, 2003.

Moskowitz, B. M., Reynolds, R. L., Goldstein, H. L., Berquo, T. S., Kokaly, R. F., and Bristow, C. S.: Iron oxide minerals in dust-source sediments from the Bodele Depression, Chad: Implications for radiative properties and Fe bioavailability of dust plumes from the Sahara, Aeolian Res., 22, 93-106, doi: 10.1016/j.aeolia.2016.07.001, 2016.

Moteki, N., Adachi, K., Ohata, S., Yoshida, A., Harigaya, T., Koike, M., and Kondo, Y.: Anthropogenic iron oxide aerosols enhance atmospheric heating, Nat. Commun., 8, 15329, doi: 10.1038/ncomms15329, 2017.

Myriokefalitakis, S., Daskalakis, N., Mihalopoulos, N., Baker, A. R., Nenes, A., and Kanakidou, M.: Changes in dissolved iron deposition to the oceans driven by human activity: a 3-D global modelling study, Biogeosciences, 12, 3973-3992, doi: 10.5194/bg-12-3973-2015, 2015.

Oakes, M., Ingall, E. D., Lai, B., Shafer, M. M., Hays, M. D., Liu, Z. G., Russell, A. G., and Weber, R. J.: Iron Solubility Related to Particle Sulfur Content in Source Emission and Ambient Fine Particles, Environ. Sci. Technol., 46, 6637-6644, doi: 10.1021/es300701c, 2012.

Ohata, S., Yoshida, A., Moteki, N., Adachi, K., Takahashi, Y., Kurisu, M., and Koike, M.: Abundance of Light-Absorbing Anthropogenic Iron Oxide Aerosols in the Urban Atmosphere and Their Emission Sources, J. Geophys. Res.-Atmos, 123, 8115-8134, doi: 10.1029/2018jd028363, 2018.

Paris, R., Desboeufs, K. V., Formenti, P., Nava, S., and Chou, C.: Chemical characterisation of iron in dust and biomass burning aerosols during AMMA-SOP0/DABEX: implication for iron solubility, Atmos. Chem. Phys., 10, 4273-4282, doi: 10.5194/acp-10-4273-2010, 2010.

Paris, R., Desboeufs, K. V., and Journet, E.: Variability of dust iron solubility in atmospheric waters: Investigation of the role of oxalate organic complexation, Atmos. Environ., 45, 6510-6517, doi: 10.1016/j.atmosenv.2011.08.068, 2011.

Paris, R., and Desboeufs, K. V.: Effect of atmospheric organic complexation on iron-bearing dust solubility, Atmos. Chem. Phys., 13, 4895-4905, doi: 10.5194/acp-13-4895-2013, 2013.

Rathod, S. D., Hamilton, D. S., Mahowald, N. M., Klimont, Z., Corbett, J. J., and Bond, T. C.: A Mineralogy‐Based Anthropogenic Combustion‐Iron Emission Inventory, J. Geophys. Res.-Atmos, 125, e2019JD032114, doi: 10.1029/2019jd032114, 2020.

Schroth, A. W., Crusius, J., Sholkovitz, E. R., and Bostick, B. C.: Iron solubility driven by speciation in dust sources to the ocean, Nat. Geosci., 2, 337-340, doi: 10.1038/ngeo501, 2009.

Sedwick, P. N., Sholkovitz, E. R., and Church, T. M.: Impact of anthropogenic combustion emissions on the fractional solubility of aerosol iron: Evidence from the Sargasso Sea, Geochem. Geophys., 8, Q10Q06, doi: 10.1029/2007gc001586, 2007.

Shi, Z., Krom, M. D., Bonneville, S., Baker, A. R., Jickells, T. D., and Benning, L. G.: Formation of iron nanoparticles and increase in iron reactivity in the mineral dust during simulated cloud processing, Environ. Sci. Technol., 43, 6592-6596, doi: 10.1021/es901294g, 2009.

Shi, Z., Bonneville, S., Krom, M. D., Carslaw, K. S., Jickells, T. D., Baker, A. R., and Benning, L. G.: Iron dissolution kinetics of mineral dust at low pH during simulated atmospheric processing, Atmos. Chem. Phys., 11, 995-1007, doi: 10.5194/acp-11-995-2011, 2011a.

Shi, Z., Krom, M. D., Bonneville, S., Baker, A. R., Bristow, C., Drake, N., Mann, G., Carslaw, K., McQuaid, J. B., Jickells, T., and Benning, L. G.: Influence of chemical weathering and aging of iron oxides on the potential iron solubility of Saharan dust during simulated atmospheric processing, Global Biogeochem. Cy., 25, GB2010, doi: 10.1029/2010gb003837, 2011b.

Shi, Z., Krom, M. D., Bonneville, S., and Benning, L. G.: Atmospheric processing outside clouds increases soluble iron in mineral dust, Environ. Sci. Technol., 49, 1472-1477, doi: 10.1021/es504623x, 2015.

Sholkovitz, E. R., Sedwick, P. N., and Church, T. M.: Influence of anthropogenic combustion emissions on the deposition of soluble aerosol iron to the ocean: Empirical estimates for island sites in the North Atlantic, Geochim. Cosmochim. Ac., 73, 3981-4003, doi: 10.1016/j.gca.2009.04.029, 2009.

Sholkovitz, E. R., Sedwick, P. N., Church, T. M., Baker, A. R., and Powell, C. F.: Fractional solubility of aerosol iron: Synthesis of a global-scale data set, Geochim. Cosmochim. Ac., 89, 173-189, doi: 10.1016/j.gca.2012.04.022, 2012.

Song, Y. G., Chen, X. L., Qian, L. B., Li, C. X., Li, Y., Li, X. X., Chang, H., and An, Z. S.: Distribution and composition of loess sediments in the Ili Basin, Central Asia, Quat. Int., 334, 61-73, doi: 10.1016/j.quaint.2013.12.053, 2014.

Spokes, L. J., Jickells, T. D., and Lim, B.: Solubilization of aerosol trace-metals by cloud processing - a laboratory study, Geochim. Cosmochim. Ac., 58, 3281-3287, doi: 10.1016/0016-7037(94)90056-6, 1994.

Srinivas, B., Sarin, M. M., and Kumar, A.: Impact of anthropogenic sources on aerosol iron solubility over the Bay of Bengal and the Arabian Sea, Biogeochemistry, 110, 257-268, doi: 10.1007/s10533-011-9680-1, 2012.

Srinivas, B., Sarin, M. M., and Rengarajan, R.: Atmospheric transport of mineral dust from the Indo-Gangetic Plain: Temporal variability, acid processing, and iron solubility, Geochem. Geophys., 15, 3226-3243, doi: 10.1002/2014gc005395, 2014.

Taiwo, A. M., Beddows, D. C. S., Shi, Z. B., and Harrison, R. M.: Mass and number size distributions of particulate matter components: Comparison of an industrial site and an urban background site, Sci. Total Environ., 475, 29-38, doi: 10.1016/j.scitotenv.2013.12.076, 2014.

Takahashi, Y., Higashi, M., Furukawa, T., and Mitsunobu, S.: Change of iron species and iron solubility in Asian dust during the long-range transport from western China to Japan, Atmos. Chem. Phys., 11, 11237-11252, doi: 10.5194/acp-11-11237-2011, 2011.

Tavares, F. V. F., Ardisson, J. D., Rodrigues, P. C. H., Fabris, J. D., Fernandez-Outon, L. E., and Feliciano, V. M. D.: Ferruginous compounds in the airborne particulate matter of the metropolitan area of Belo Horizonte, Minas Gerais, Brazil, Environmental Science and Pollution Research, 24, 19683-19692, doi: 10.1007/s11356-017-9613-1, 2017.

Trapp, J. M., Millero, F. J., and Prospero, J. M.: Trends in the solubility of iron in dust-dominated aerosols in the equatorial Atlantic trade winds: Importance of iron speciation and sources, Geochem. Geophys., 11, doi: 10.1029/2009gc002651, 2010.

Wang, R., Balkanski, Y., Boucher, O., Bopp, L., Chappell, A., Ciais, P., Hauglustaine, D., Penuelas, J., and Tao, S.: Sources, transport and deposition of iron in the global atmosphere, Atmos. Chem. Phys., 15, 6247-6270, doi: 10.5194/acp-15-6247-2015, 2015.

Yoshida, A., Ohata, S., Moteki, N., Adachi, K., Mori, T., Koike, M., and Takami, A.: Abundance and Emission Flux of the Anthropogenic Iron Oxide Aerosols From the East Asian Continental Outflow, Journal of Geophysical Research-Atmospheres, 123, 11194-11209, doi: 10.1029/2018jd028665, 2018.

Yoshida, A., Moteki, N., Ohata, S., Mori, T., Koike, M., Kondo, Y., Matsui, H., Oshima, N., Takami, A., and Kita, K.: Abundances and Microphysical Properties of Light-Absorbing Iron Oxide and Black Carbon Aerosols Over East Asia and the Arctic, J. Geophys. Res.-Atmos, 125, e2019JD032301, doi: 10.1029/2019JD032301, 2020.

Zhang, G. H., Bi, X. H., Lou, S. R., Li, L., Wang, H. L., Wang, X. M., Zhou, Z., Sheng, G. Y., Fu, J. M., and Chen, C. H.: Source and mixing state of iron-containing particles in Shanghai by individual particle analysis, Chemosphere, 95, 9-16, doi: 10.1016/j.chemosphere.2013.04.046, 2014.

Zhang, T. R., Shi, J. H., Gao, H. W., Zhang, J., and Yao, X. H.: Impact of source and atmospheric processing on Fe solubility in aerosols over the Yellow Sea, China, Atmos. Environ., 75, 249-256, doi: 10.1016/j.atmosenv.2013.04.021, 2013.

Zhu, X. R., Prospero, J. M., Millero, F. J., Savoie, D. L., and Brass, G. W.: The solubility of ferric ion in marine mineral aerosol solutions at ambient relative humidities Mar. Chem., 38, 91-107, doi: 10.1016/0304-4203(92)90069-m, 1992.

CHAPTER 3: IRON FROM COAL COMBUSTION PARTICLES DISSOLVES MUCH FASTER THAN MINERAL DUST UNDER SIMULATED ATMOSPHERIC ACID CONDITIONS

3.1 Abstract

Mineral dust is the largest source of aerosol iron (Fe) to the offshore global ocean, but acidic processing of coal fly ash (CFA) in the atmosphere could be an important source of soluble aerosol Fe. Here, we determined the Fe speciation and dissolution kinetics of CFA from Aberthaw (United Kingdom), Krakow (Poland), and Shandong (China) in solutions which simulate atmospheric acidic processing. In CFA-PM_{10} fractions, 8%-21.5% of the total Fe was as hematite and goethite (dithionite extracted Fe), 2%-6.5 % as amorphous Fe (ascorbate extracted Fe), while magnetite (oxalate extracted Fe) varied from 3%-22%. The remaining 50%-87 % of Fe was associated with other Fe-bearing phases, possibly aluminosilicates. High concentrations of ammonium sulfate ($(NH_4)_2SO_4$), often found in wet aerosols, increased Fe solubility of CFA up to 7 times at low pH (2-3). The oxalate effect on the Fe dissolution rates at pH 2 varied considerably depending on the samples, from no impact for Shandong ash to doubled dissolution for Krakow ash. However, this enhancement was suppressed in the presence of high concentrations of $(NH_4)_2SO_4$. Dissolution of highly reactive (amorphous) Fe was insufficient to explain the high Fe solubility at low pH in CFA, and the modelled dissolution kinetics suggest that other Fe-bearing phases such as magnetite may also dissolve relatively rapidly under acidic conditions. Overall, Fe in CFA dissolved up to 7 times faster than in a Saharan dust precursor sample at pH 2. Based on these laboratory data, we developed a new scheme for the proton- and oxalate- promoted Fe dissolution of CFA, which was implemented into the global atmospheric chemical transport model IMPACT. The

revised model showed a better agreement with observations of Fe solubility in aerosol particles over the Bay of Bengal, due to the initial rapid release of Fe and the suppression of the oxalate-promoted dissolution at low pH. The improved model enabled us to predict sensitivity to a more dynamic range of pH changes, particularly between anthropogenic combustion and biomass burning aerosols.

3.2 Introduction

The availability of iron (Fe) limits primary productivity in high-nutrient low-chlorophyll (HNLC) regions of the global ocean including the subarctic North Pacific, the East Equatorial Pacific, and the Southern Ocean (Boyd et al., 2007; Martin, 1990). In other regions of the global ocean such as the subtropical North Atlantic, the Fe input may affect primary productivity by stimulating nitrogen fixation (Mills et al., 2004; Moore et al., 2006). These areas are particularly sensitive to changes in the supply of bioavailable Fe. Atmospheric aerosols are an important source of soluble (and, thus potentially bio-accessible) Fe to the offshore global ocean. The deposition of bio-accessible Fe to the ocean can alter biogeochemical cycles and increase the carbon uptake, consequently affecting the climate (e.g., Jickells and Moore, 2015; Jickells et al., 2005; Kanakidou et al., 2018; Mahowald et al., 2010; Shi et al., 2012). In general, bio-accessible Fe consists of aerosol dissolved Fe, and Fe-nanoparticles which can be present in the original particulate matter and/or formed during atmospheric transport as a result of cycling into and out of clouds (Shi et al., 2009). It is in addition possible that other more refractory forms of Fe could be solubilized in the surface waters by zooplankton (Schlosser et al., 2018) or the microbial community (Rubin et al., 2011).

The Fe transported in the atmosphere is largely derived from lithogenic sources, which contribute around 95% of the total Fe in suspended particles (e.g.,Shelley et al., 2018) and most studies so far have concentrated on atmospheric processing of mineral dust (e.g., Cwiertny et al., 2008; Fu et al., 2010; Ito and Shi, 2016; Shi et al., 2011a; Shi et al., 2015). Mineral dust has low Fe solubility (dissolved Fe/ total Fe) near the source regions, generally below 1% (e.g., Shi et al., 2011c; Sholkovitz et al., 2009; Sholkovitz et al., 2012), increasing somewhat as a result of processes occurring during atmospheric transport (e.g., Baker et al., 2021; Baker et al., 2020). Other sources of bio-accessible Fe to the ocean are from combustion sources such as biomass burning, coal combustion, oil combustion, and metal smelting (e.g., Ito et al., 2018; Rathod et al., 2020). Although these sources are only a small fraction of the total Fe in atmospheric particulates, the Fe solubility of pyrogenic sources can be 1–2 orders of magnitude higher than in mineral dust (Ito et al., 2021b and references therein), and thus can be

important in promoting carbon uptake. However the Fe solubility of pyrogenic sources varies considerably depending on the particular sources with higher values observed for oil combustion and biomass burning than coal combustion sources (Ito et al., 2021b and references therein).

Wang et al. (2015) estimated that coal combustion emitted around ~0.9 Tg yr^{-1} of Fe into the atmosphere (on average for 1960–2007), contributing up to ~86% of the total anthropogenic Fe emissions. A more recent study, which has included metal smelting as an atmospheric Fe source, estimated that coal combustion emitted ~0.7 Tg yr^{-1} of Fe for the year 2010, contributing around 34% of the total anthropogenic Fe atmospheric loading (Rathod et al., 2020). Although the use of coal as a principal energy source has been recently reduced as a result of concern about air quality and global warming, coal is still an important energy source in a number of countries in particular in the Asia-Pacific region (BP, 2020). In China, most of the total energy is supplied by coal, contributing over 50% of the global coal consumption in 2019, followed by India (12%), and the US (8%). Germany and Poland are the largest coal consumers in Europe, accounting together for around 40% of the European usage (BP, 2020). South Africa is also among the principal countries for coal consumption (BP, 2020) and is a source of Fe-bearing particles to the anemic Southern Ocean (e.g., Ito et al., 2019).

Coal fly ash (CFA) is a by-product of coal combustion. This generally consists of glassy spherical particles (e.g., Brown et al., 2011), which are formed through different transformations (decomposition, fusion, agglomeration, volatilization) of mineral matter in coal during combustion (e.g., Jones, 1995), and are transported with the flue gases undergoing rapid solidification. CFA are co-emitted with acidic gases such as sulfur dioxide (SO_2), nitrogen oxides (NO_x) and carbon dioxide (CO_2) (e.g., Munawer, 2018).

During long-range transport, CFA particles undergo atmospheric processing with the CFA surface coated by acidic species such as sulfuric acid (H_2SO_4) and oxalic acid ($H_2C_2O_4$) in atmospheric aerosols. Aged CFA particles are hygroscopic and absorb water at typical relative humidity in the marine atmosphere. As a result, a thin layer of water with high acidity, low pH and high ionic strength is formed around the particles (Meskhidze et al., 2003; Spokes and Jickells, 1995; Zhu et al., 1992). In addition,

ammonia (NH_3) which is a highly hydrophilic gas, can also partition into the aerosol phase, react with H_2SO_4 and form ammonium sulfate ($(NH_4)_2SO_4$) an important inorganic salt contributing to the high ionic strength in aged atmospheric aerosols (Seinfeld and Pandis, 2016).

At low pH conditions, Fe solubility in aerosols increases, as the high concentration of protons (H^+) weakens the Fe-O bonds facilitating the detachment of Fe from the surface lattice (Furrer and Stumm, 1986). Li et al. (2017) provided the first observational evidence that acidification leads to the release of Fe from anthropogenic particles.

In addition to these inorganic processes, organic ligands can also enhance atmospheric Fe dissolution by forming soluble complexes with Fe (e.g., Cornell and Schwertmann, 2003). For example, $H_2C_2O_4$ is an important organic species in aerosols (e.g., Kawamura and Bikkina, 2016). Laboratory studies have demonstrated that $H_2C_2O_4$ increases Fe solubility of aerosol sources (Chen and Grassian, 2013; Johnson and Meskhidze, 2013; Paris and Desboeufs, 2013; Paris et al., 2011; Xu and Gao, 2008). Recently, observations over the Bay of Bengal indicate that $H_2C_2O_4$ contributes to the increase of dissolved Fe in atmospheric water (Bikkina et al., 2020).

To simulate the Fe dissolution in CFA, it is necessary to determine the dissolution kinetics under realistic conditions. Previous studies have investigated the Fe dissolution kinetics of CFA under acidic conditions. Chen et al. (2012) simulated acidic and cloud processing of certified CFA. Fu et al. (2012) determined the dissolution kinetics of CFA samples at pH 2, while Chen and Grassian (2013) investigated the effect of organic species (e.g., oxalate and acetate) at pH 2-3. These studies showed that high acidity and the presence of oxalate enhanced Fe dissolution at the surface of CFA particles, similar to those reported in mineral dust (Chen et al., 2012; Chen and Grassian, 2013; Fu et al., 2012; Ito and Shi, 2016; Shi et al., 2011a). They also demonstrated that there are large differences in dissolution rates in different types of CFA, likely related to Fe speciation.

Furthermore, high ionic strength, commonly seen in aerosol water, affects the activity of molecular species present in solution, consequently it can significantly impact the Fe dissolution behavior. Recent

studies have considered the effect of the high ionic strength on the Fe dissolution kinetics of CFA under acidic conditions. For example, the Fe solubility of CFA samples was measured at pH 1-2 with high sodium chloride (NaCl) concentrations (Borgatta et al., 2016), and with high sodium nitrate ($NaNO_3$) concentrations Kim et al. (2020). In real atmospheric conditions, NaCl or $NaNO_3$ are unlikely to be the main driver of high ionic strength in aged CFA. Although NaCl can coagulate with dust particles in the marine boundary layer (Zhang et al., 2003), the aging of CFA is primarily by the uptake of secondary species, particularly sulfate and ammonia (Li et al., 2003). Ito and Shi (2016) found that at low pH and high concentration of $(NH_4)_2SO_4$ the Fe solubility of mineral dust is likely to be enhanced by the adsorption of sulfate ions on the particle surface. However, to date the effect of high $(NH_4)_2SO_4$ concentrations on the Fe dissolution behavior in combustion sources in the presence or absence of oxalate remains unknow.

The dissolution kinetics measured by Chen and Grassian (2013) have been used to develop a modelled dissolution scheme for CFA, assuming a single Fe-bearing phase in CFA (Ito, 2015). However, there are multiple Fe-bearing phases in CFA, primarily hematite, magnetite and Fe in aluminum silicate glass (Brown et al., 2011; Chen et al., 2012; Fu et al., 2012; Kukier et al., 2003; Kutchko and Kim, 2006; Lawson et al., 2020; Sutto, 2018; Valeev et al., 2019; Waanders et al., 2003; Wang, 2014; Zhao et al., 2006), but also accessory Fe-bearing minerals for example silicates, carbonate, sulfides and sulfates (Zhao et al., 2006). These phases have a range of reactivities. Previous studies showed that CFA dissolves much faster during the first 1-2 hours than subsequently (Borgatta et al., 2016; Chen et al., 2012; Chen and Grassian, 2013; Fu et al., 2012; Kim et al., 2020), confirming the existence of multiple Fe-bearing phases within a single CFA sample with different dissolution behavior.

In this study, laboratory experiments were conducted to determine the dissolution kinetics of coal combustion emission products (i.e., CFA) during simulated atmospheric acidic processing in the presence of $(NH_4)_2SO_4$ and oxalate which are commonly found in atmospheric aerosols. In particular, we investigated the effect of high $(NH_4)_2SO_4$ concentrations on the proton-promoted and oxalate-promoted Fe dissolution at low pH conditions. Our study also determined the Fe-bearing phases present

in the CFA and compared them to those present in mineral dust. The experimental results enabled us to develop a new Fe release scheme for CFA sources which was then implemented into the global atmospheric chemical transport model IMPACT. The model results were compared with observations of Fe solubility in aerosol particles over the Bay of Bengal from Bikkina et al. (2020).

3.3 Materials and Methods

3.3.1 Sample collection and subsequent size fractionation

CFA samples were collected from the electrostatic precipitators at three coal-fired power stations at different locations: United Kingdom (Aberthaw ash), Poland (Krakow ash), and China (Shandong ash). The bulk samples were resuspended to obtain aerosol fractions representative of particles emitted into the atmosphere. A custom-made resuspension system was used to collect the PM_{10} fraction (particles with an aerodynamic diameter smaller than 10 μm), which is shown in Figure S1. Around 20 g of sample was placed into a glass bottle and injected at regular intervals (2-5 sec) into a glass reactor (~70 L) by flushing the bottle with pure nitrogen. The air in the reactor was pumped at a flow rate of 30 L min^{-1} into a PM_{10} sampling head. Particles were collected on 0.6 μm polycarbonate filters and transferred into centrifuge tubes. The system was cleaned manually and flushed for 10 min with pure nitrogen before loading a new sample. A soil sample from Libya (Soil 5, 32.29237N/22.30437E) was dry sieved to 63 μm and used as an analogue for a Saharan mineral dust precursor to make a comparison between CFA and mineral dust.

3.3.2 Fe dissolution kinetics

The Fe dissolution kinetics of the CFA samples were determined by time-dependent leaching experiments. We followed a similar methodology as in Ito and Shi (2016). PM_{10} fractions were exposed to H_2SO_4 solutions at pH 1, 2 or 3, in the presence of $H_2C_2O_4$ and/or $(NH_4)_2SO_4$ to simulate acidic processing in aerosol conditions. The concentration of $H_2C_2O_4$ in the experiment solutions was chosen based on the molar ratio of oxalate and sulfate in $PM_{2.5}$ (particles with an aerodynamic diameter smaller than 2.5 μm) from observations over the East Asia region (Yu et al., 2005). Around 50 mg of CFA was

leached in 50 ml of acidic solution to obtain a particles/liquid ratio of 1 g L^{-1}. The sample solution was mixed continuously on a rotary mixer, in the dark at room temperature. A volume of 0.5 mL was sampled at fixed time intervals (2.5, 15, 60 min and 2, 6, 24, 48, 72, and 168 hours after the CFA sample was added to the experiment solution) and filtered through 0.2 µm pore size syringe filters. The dissolved Fe concentration in the filtrate was determined using the ferrozine method (Viollier et al., 2000). Leaching experiments were also conducted on the Libyan dust precursor sample. The relative standard deviation (RSD) at each sampling time varied from 4 % to 15 % (n=7).

The pH of all the experiment solutions was calculated using the E-AIM model III for aqueous solutions (Wexler and Clegg, 2002). In part this was because the high ionic strength generated by the elevated concentration of $(NH_4)_2SO_4$ prevents electrochemical sensors from making accurate pH measurements. For the experiment solutions with no $(NH_4)_2SO_4$, the pH was measured by a pH meter before adding the ash and at the end of the experiments. The solution pH increased after adding the ash, and the change in pH was used to estimate the buffer capacity of alkaline minerals in the samples, including for example calcium carbonates ($CaCO_3$), lime (CaO), and portlandite ($Ca(OH)_2$). The estimated concentration of H^+ buffered was used to input the concentration of H^+ into the E-AIM model. For each experiment, the pH was calculated before adding the CFA samples and at the end of the experiments. The pH of the original solution before adding the samples was estimated from the molar concentrations (mol L^{-1}) of H_2SO_4, $H_2C_2O_4$ and $(NH_4)_2SO_4$ used to prepare the solution. The model inputs included the total concentrations of H^+ (without $H_2C_2O_4$ contribution), NH_4^+, SO_4^{2-} and $H_2C_2O_4$. For the experiment solutions with no $(NH_4)_2SO_4$, we calculated the final pH by reducing the total H^+ concentration input into the model to match the pH measured at the end of the experiments. The buffered H^+ was then estimated from the difference between the original and final H^+ concentration input into the model. To determine the final pH of the solutions with high ionic strength, the H^+ concentration input in the model was calculated as the difference between the H^+ concentration in the original solution and the buffered H^+ estimated at low ionic strength.

For the solution with no $(NH_4)_2SO_4$, the difference between calculated and measured pH is <7%. Table S1 reports the concentrations of H_2SO_4, $H_2C_2O_4$ and $(NH_4)_2SO_4$ in the experiment solutions, the original and final pH from model estimates (including H^+ concentrations and activities), and the pH measurements for the solution with low ionic strength.

3.3.3 Sequential extractions

The content of Fe oxide species in the samples was determined by Fe sequential extraction (Baldo et al., 2020; Poulton and Canfield, 2005; Raiswell et al., 2008; Shi et al., 2011b). The Fe oxide species included highly reactive amorphous Fe oxide-hydroxide (FeA), crystalline Fe oxide-hydroxide, mainly goethite and hematite (FeD), and Fe associated with magnetite (FeM).

To extract FeA, samples were leached in an ascorbate solution buffered at pH 7.5 (Raiswell et al., 2008; Shi et al., 2011b). The ascorbate solution contained a deoxygenated solution of 50 g L^{-1} sodium citrate, 50 g L^{-1} sodium bicarbonate, and 10 g L^{-1} of ascorbic acid. Around 30 mg of CFA was leached for 24 hours in 10 mL of ascorbate extractant, mixed continuously on a rotary mixer. The extraction solution was then filtered through a 0.2 µm membrane filter. In order to extract FeD, the residue was leached for 2 more hours in a dithionite solution buffered at pH 4.8 (50 g L^{-1} sodium dithionite in 0.35 M acetic acid and 0.2 M sodium citrate) (Raiswell et al., 2008; Shi et al., 2011b).

For the extraction of FeM, the CFA samples were first leached for 2 hours using a citrate-buffered dithionite solution to remove FeD. The residue collected after filtration was then leached for 6 hours in a solution of 0.2 M ammonium oxalate ($(NH_4)_2C_2O_4$) and 0.17 M $H_2C_2O_4$ at pH 3.2 (Poulton and Canfield, 2005). The Fe extractions were all carried out in the dark at room temperature. The Fe concentration in the filtered extraction solutions was measured using the ferrozine method (Viollier et al., 2000) or by inductively coupled plasma optical emission spectrometry (ICP-OES) analysis for the solutions containing high concentration of oxalate.

The total Fe content in the samples was determined by microwave digestion in concentrated nitric acid (HNO_3) followed by inductively coupled plasma mass spectrometry (ICP-MS) analysis. The recovery

of Fe assessed using a standard reference material for urban particulate matter (NIST SRM 1648A) was around 89%. Therefore, the total Fe in the Libyan dust precursor sample could be underestimated somewhat as crystalline aluminum silicate minerals may not be fully digested.

The sequential extraction techniques were tested using the Arizona Test Dust (ATD, Power Technology, Inc.). The RSD% obtained for each extract using the ATD was 3% for FeA, 11% for FeD, 12% for FeM (n=7) and 2% for the total Fe (n=3). A summary of the results for the ATD is reported in Table S2.

3.3.4 X-ray absorption near edge structure (XANES) analysis

We collected XANES spectra to qualitatively examine the Fe speciation in the CFA samples. The XANES spectra at the Fe K-edge were collected at the Diamond Light Source beamline I18. A Si(111) double-crystal monochromator was used in the experiments. The beam size was 400 μm×400 μm. The XANES spectra were collected from 7000 to 7300 eV at a resolution varying from 0.2 eV for 3 s in proximity to the Fe K-edge (7100–7125 eV) to 5 eV for 1 s from 7100 to 7300 eV. Powder samples were suspended in methanol and deposited on Kapton® tape. The analysis was repeated three times. We measured the XANES spectra of the CFA-PM_{10} fractions and mineral standards including hematite, magnetite, and illite. Data were processed using the Athena program, part of the software package Demeter (version 0.9.26) (Ravel and Newville, 2005).

3.3.5 Model description

This study used the Integrated Massively Parallel Atmospheric Chemical Transport (IMPACT) model (Ito et al., 2021a and references therein). The model simulates the emission, chemistry, transport, and deposition of Fe-containing aerosols and the precursor gases of inorganic and organic acids. The coating of acidic species on the surface of Fe-containing aerosols promotes the release of soluble Fe in the aerosol deliquescent layer and enhances the aerosol Fe solubility (Li et al., 2017). On the other hand, the external mixing of oxalate-rich aerosols with Fe-rich aerosols can suppress the oxalate-promoted Fe dissolution at low concentration of oxalate near the source regions (Ito, 2015). However, the internal mixing of alkaline minerals such as calcium carbonate with Fe-containing dust aerosols can suppress

the Fe dissolution (Ito and Feng, 2010). Since CFA particles are co-emitted with acidic species, the transformation of relatively insoluble Fe in coal combustion aerosols into dissolved Fe is generally much faster than that for mineral dust aerosols during their atmospheric lifetime (Ito, 2015; Ito and Shi, 2016). Additionally, the size of CFA particles is substantially smaller than that of mineral dust. Thus, we adopted an observationally constrained parameter for the dry deposition scheme (Emerson et al., 2020) to improve the simulation of dry deposition velocity of fine particles.

To improve the accuracy of our simulations of Fe-containing aerosols, we revised the on-line Fe dissolution schemes in the original model (Ito et al., 2021a) in conjunction with a more dynamic range of pH estimates. To apply the Fe dissolution schemes for high ionic strength in aerosols, we used the mean activity coefficient for pH estimate (Pye et al., 2020). Moreover, the dissolution rate was assumed to be dependent of pH for highly acidic solutions (pH < 2) unlike in the former dissolution scheme (Ito, 2015), which allowed us to predict the sensitivity of Fe dissolution to pH lower than 2.

To validate the new dissolution scheme, we compared our model results with observations of Fe solubility in $PM_{2.5}$ aerosol particles over the Bay of Bengal (Bikkina et al., 2020).

3.4 Experimental results

3.4.1 Fe dissolution kinetics

We determined that Krakow ash had the largest buffer capacity, around 0.008 moles of buffered H^+ per liter, which was related to the content of alkaline minerals in the sample. The buffer capacity of Aberthaw and Shandong ash was ~10 times smaller than that of Krakow ash, around 0.0007 moles of buffered H^+ per liter. Leaching Krakow ash in 0.005 M H_2SO_4, the initial concentration of H^+ was similar to the concentration of the H^+ buffered. As a result, the solution pH raised from approximatively 2.1 to 2.7 corresponding to a pH change of around 20% (Table S1). For all the other experimental conditions, the pH change was below 12% (Table S1). At the pH conditions used in this study (pH 1-3), acid buffering was fast and likely occurred within the first 1-2 hours. We assumed that the calculated final pH was representative of the solution pH over the duration of the experiments.

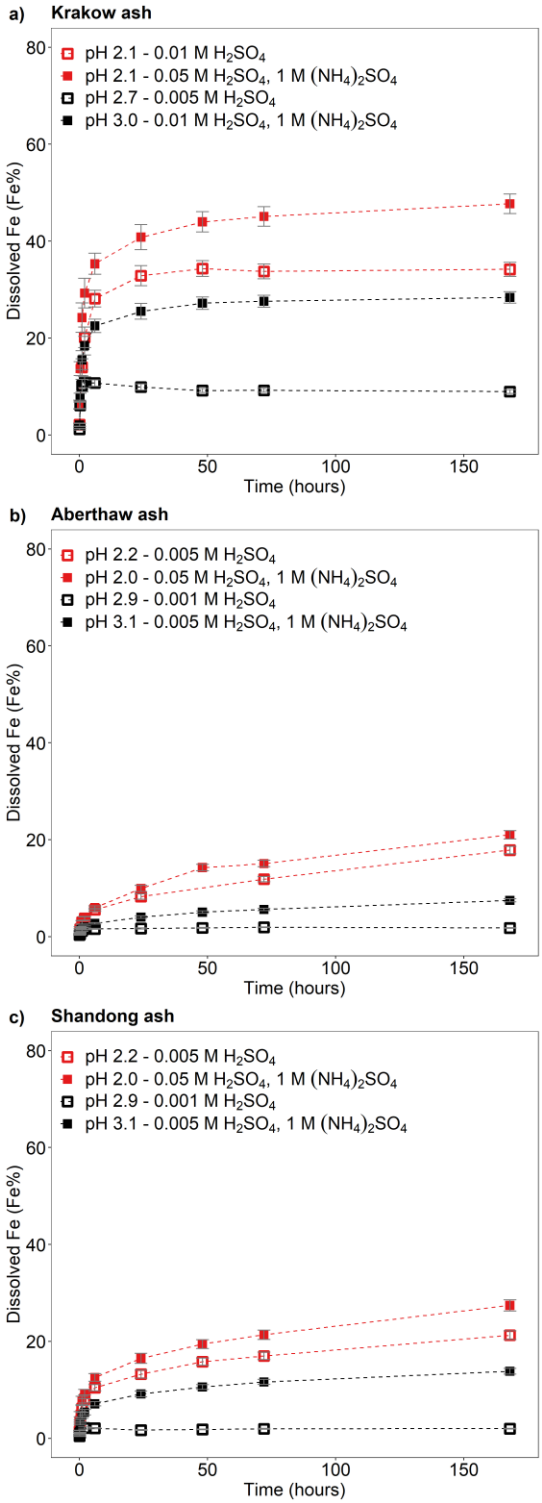

Figure 3.1: Fe dissolution kinetics of a) Krakow ash, b) Aberthaw ash and c) Shandong ash in H_2SO_4 solutions (open rectangles) and with 1 M $(NH_4)_2SO_4$ (filled rectangles). The molar concentrations of H_2SO_4 and $(NH_4)_2SO_4$ in the experiment solutions are shown. The final pH of the experiment solutions is also reported, which was calculated using the E-AIM model III for aqueous solution (Wexler and Clegg, 2002) accounting for the buffer capacity of the CFA samples (Experiments 1-2 in Table S1). The experiments conducted at around pH 2 are in red, while the experiments at around pH 3 are in black. The data uncertainty was estimated using the error propagation formula.

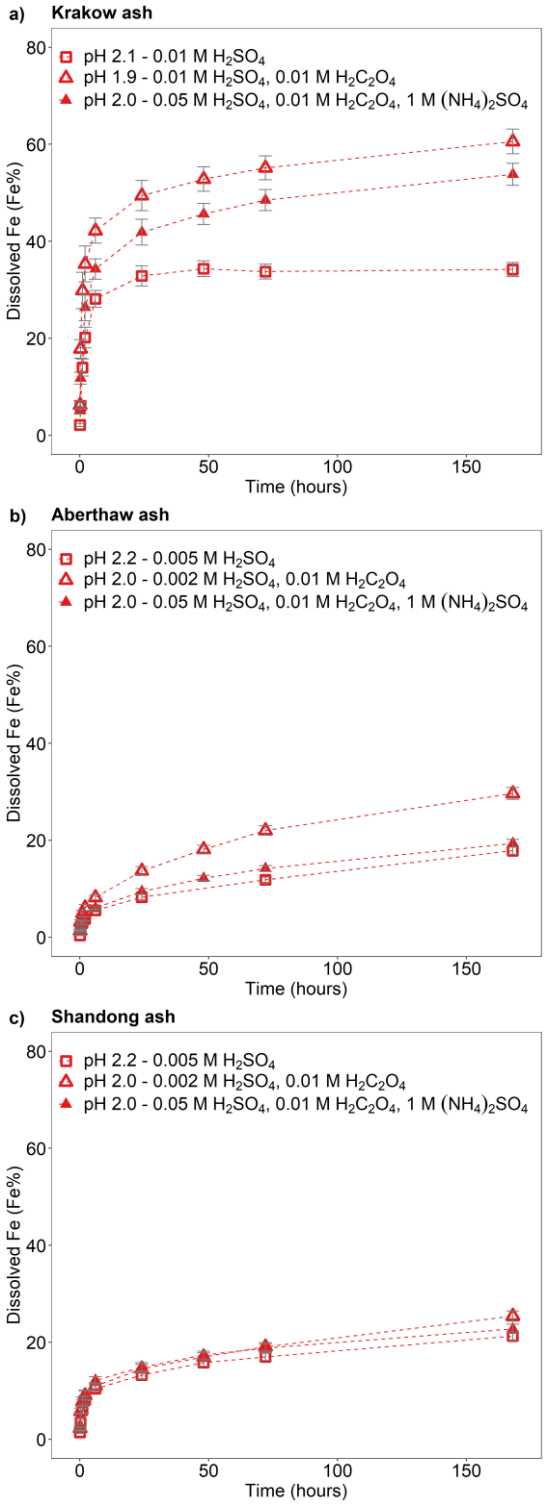

Figure 3.2: Fe dissolution kinetics of a) Krakow ash, b) Aberthaw ash, and c) Shandong ash in H_2SO_4 solutions at around pH 2 (red open rectangles), with 0.01 M $H_2C_2O_4$ (red open triangles), and 1 M $(NH_4)_2SO_4$ (red filled triangles). The molar concentrations of H_2SO_4, $H_2C_2O_4$ and $(NH_4)_2SO_4$ in the experiment solutions are shown. The final pH of the experiment solutions is also reported, which was calculated using the E-AIM model III for aqueous solution (Wexler and Clegg, 2002) accounting for the buffer capacity of the CFA samples (Experiments 1, 3-4 at around pH 2). The data uncertainty was estimated using the error propagation formula.

The leaching experiments were conducted up to 168 h to better capture the dissolution curve in the kinetic model but also considering the tropospheric lifetime of aerosol particles.

Dissolved Fe at different time intervals is reported as Fe%, which is the fraction of Fe dissolved to the total Fe content (FeT) in the CFA samples. For all samples, a fast dissolution rate was observed at the beginning of the experiment. In the case of Krakow ash, the dissolution plateau was reached after 2-hour leaching in 0.005 M H_2SO_4 as sufficient Fe may be dissolved from the highly reactive Fe species to suppress the dissolution of less reactive Fe. For that sample/initial condition the pH increased to 2.7, and no more Fe was dissolved, leading to a total Fe solubility of ~9% over the duration of the experiment (7 days) (Figure 3.1a). Dissolving Krakow ash in 0.01 M H_2SO_4 (Figure 3.1a), the experiment solution had a final calculated pH of 2.1. The total Fe solubility was 34% at pH 2.1, almost 4 times higher than that at pH 2.7 (in 0.005 M H_2SO_4). Dissolution of Aberthaw and Shandong ash was slower compared to Krakow ash (Figures 3.1b and 3.2c, respectively). Leaching Aberthaw and Shandong ash in 0.005 M H_2SO_4 resulted in solutions with a pH of around 2.2. At this pH, the total Fe solubility was 18% for Aberthaw ash and 21% for Shandong ash, which is 9-10 times higher than the total Fe solubility at pH 2.9 (in 0.001 M H_2SO_4), around 2% for both samples.

The experimental treatment of dissolved Fe from Krakow ash in 0.05 H_2SO_4 solution with 1 M $(NH_4)_2SO_4$ (Figure 3.1a) resulted in a final predicted pH of 2.1. At that pH, the total Fe solubility of Krakow ash increased from 34% with no $(NH_4)_2SO_4$ to 48% with high $(NH_4)_2SO_4$ concentration. The total Fe solubility of Krakow ash was around 28% at pH 3.0 with 1 M $(NH_4)_2SO_4$ (Figure 3.1a), 3 times higher than that at pH 2.7 with no $(NH_4)_2SO_4$. At around pH 2, the total Fe solubility of Aberthaw (Figure 3.1b) and Shandong ash (Figure 3.1c) increased by around 20% and 30% in the presence of $(NH_4)_2SO_4$. By contrast, the total Fe solubility at pH 3.1 with 1 M $(NH_4)_2SO_4$ was 7.5% for Aberthaw ash (Figure 3.1b) and 14% for Shandong ash (Figure 3.1c), respectively, which was around 4 and 7 times higher than in the experiments carried out at pH 2.9 without $(NH_4)_2SO_4$.

The Fe dissolution of the CFA samples in H_2SO_4 solutions with 0.01 M $H_2C_2O_4$ (at around pH 2) is shown in Figure 3.2. The total Fe solubility of Krakow ash at pH 1.9 with 0.01 M $H_2C_2O_4$ was 61%

(Figure 3.2a), which was almost 2 times higher than that at pH 2.1 but without $H_2C_2O_4$ (Figure 3.2a). For Aberthaw ash, oxalate contribution to the dissolution process led to a total Fe solubility of 30% at pH 2.0 (Figure 3.2b), which was 70% higher than in the experiment carried out in 0.005 M H_2SO_4 (~pH 2.2) Figure 3.2b). Shandong ash dissolution behavior was not affected by the presence of oxalate (Figure 3.2c).

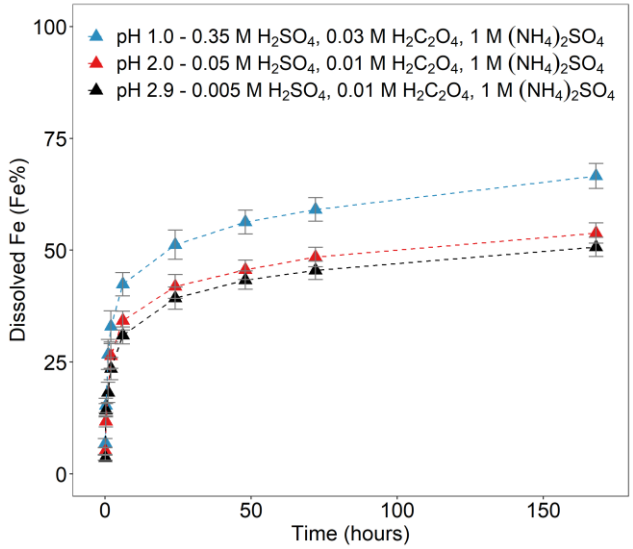

Figure 3.3: Fe dissolution kinetics of Krakow ash in H_2SO_4 solutions at pH 1.0 with 0.03 M $H_2C_2O_4$ and 1 M $(NH_4)_2SO_4$ (blue filled triangles), at pH 2.0 with 0.01 M $H_2C_2O_4$ and 1 M $(NH_4)_2SO_4$ (red filled triangles), and at pH 2.9 with 0.01 M $H_2C_2O_4$ and 1 M $(NH_4)_2SO_4$ (black filled triangles). The molar concentrations of H_2SO_4, $H_2C_2O_4$ and $(NH_4)_2SO_4$ in the experiment solutions are shown. The final pH of the experiment solutions is also reported, which was calculated using the E-AIM model III for aqueous solution (Wexler and Clegg, 2002) accounting for the buffer capacity of the CFA samples (Experiment 7 at pH 1.0, Experiment 3 at pH 2.0, and Experiment 3 at pH 2.9 in Table S1). The data uncertainty was estimated using the error propagation formula.

We also investigated the effect of high $(NH_4)_2SO_4$ concentration on oxalate-promoted dissolution. In Figure 3.2a, the total Fe solubility of Krakow ash decreased from 61% at pH 1.9 in the presence of oxalate to 54% at pH 2.0 with oxalate and $(NH_4)_2SO_4$. For Aberthaw ash, the total Fe solubility at pH 2.0 decreased from 30% in the presence of oxalate to 19% after the addition of $(NH_4)_2SO_4$ (Figure 3.2b).

Figure 3.3 shows the Fe dissolution behavior of Krakow ash at different pH conditions in the presence of 1 M $(NH_4)_2SO_4$ and $H_2C_2O_4$ (0.01-0.03 M depending on the solution pH). The total concentration of oxalate ions was calculated using the E-AIM model and was similar at different pH conditions, 0.015 at pH 1.0 (Experiment 7 Table S3), 0.009 at pH 2.0, and 0.01 at pH 2.9 (Experiments 3 Table S3). The

highest total Fe solubility was observed at pH 1.0 (~67%). At pH 2.0, the total Fe solubility decreased to 54%, and no substantial variations were observed between pH 2.0 and pH 2.9 (54%-51%). At pH 1.0, the concentration of H^+ was considerably higher compared to pH 2.0-2.9, leading to a faster dissolution rate. The total concentration of oxalate ions was 1.5-1.6 times higher in the solution at pH 1.0 than at pH 2.0-2.9, which may also contribute to the faster dissolution rate. $C_2O_4^{-2}$ concentration increased with rising pH. Although the concentration of H^+ was lower at pH 2.9 than at pH 2.0, the E-AIM model estimated that $C_2O_4^{-2}$ contributed around 35% of the total oxalate concentration at pH 2.9, which was 4.5 times higher than at pH 2.0 (Experiments 3 Table S3). The similar dissolution behavior at pH 2.0 and pH 2.9 conditions may reflect the combination of these two opposite factors, higher concentration of $C_2O_4^{-2}$ but lower concentration of H^+ at pH 2.9 compared to 2.0.

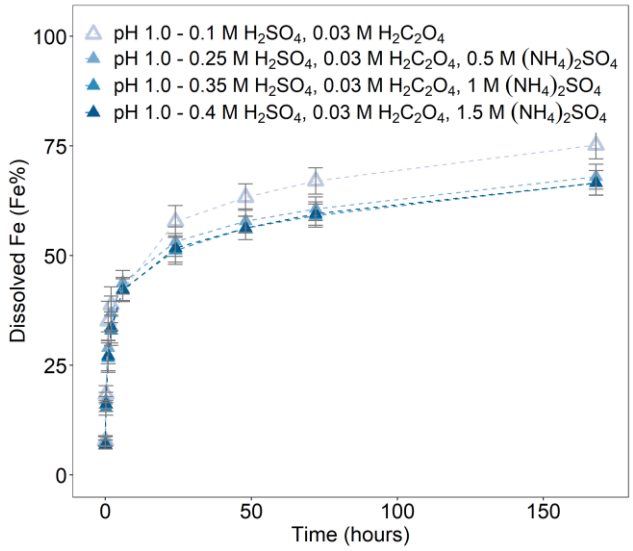

Figure 3.4: Fe dissolution kinetics of Krakow ash in H_2SO_4 solutions at pH 1.0 with 0.03 M $H_2C_2O_4$ and concentration of $(NH_4)_2SO_4$ from 0 to 1.5 M. The molar concentrations of H_2SO_4, $H_2C_2O_4$ and $(NH_4)_2SO_4$ in the experiment solutions are shown. The final pH of the experiment solutions is also reported, which was calculated using the E-AIM model III for aqueous solution (Wexler and Clegg, 2002) accounting for the buffer capacity of the CFA samples (Experiments 5-8 in Table S1). The data uncertainty was estimated using the error propagation formula.

We determined the Fe dissolution behavior of Krakow ash at pH 1.0 in the presence of oxalate and increasing concentrations of $(NH_4)_2SO_4$. The ash was leached in H_2SO_4 solutions with 0.03 M $H_2C_2O_4$ at pH 1.0, while the concentration of $(NH_4)_2SO_4$ varied from 0 to 1.5 M. In Figure 3.4, the total Fe solubility of Krakow ash in the presence of oxalate was 75% at pH 1.0 and decreased to 68% after the

addition of 0.5 M $(NH_4)_2SO_4$. Higher $(NH_4)_2SO_4$ concentrations did not affect the Fe dissolution behavior in the presence of oxalate at pH 1.0.

3.4.2 Fe speciation

The Fe-bearing phases in the CFA samples determined through sequential extractions are shown in Figure 3.5c. The Fe speciation in the Libyan dust precursor is added for comparison. Krakow ash had a total Fe (FeT) content of 5.2%, while FeT in Aberthaw and Shandong ash was 3.1% and 1.6% respectively. Amorphous Fe (FeA/FeT) was 6.5% in Krakow ash, 2% in Aberthaw ash, and 4.6% in Shandong ash. The CFA samples showed very different dithionite Fe (FeD/FeT) content, 21.5% in Krakow ash, 8% in Aberthaw ash and 14.8% in Shandong ash. The content of magnetite (FeM/FeT) was considerably higher in Krakow ash (22.4%) compared to Aberthaw (2.9%) and Shandong (4.5%) ash. About 50 %–87 % of Fe was contained in other phases most likely in aluminosilicates. Overall, CFA had more magnetite and highly reactive amorphous Fe and less dithionite Fe than the Libyan dust precursor sample.

In Figures. 3.5a-b, the Fe K-edge XANES spectra of Krakow and Aberthaw ash showed a single peak in the pre-edge region at around 7114.3 eV and 7114.6 eV, respectively. In the edge region, Aberthaw ash showed a broad peak at around 7132.2 eV, while the peak of Krakow ash was slightly shifted to 7132.9 eV and narrower. The pre-edge peak at around 7115.4 suggests that Fe was mainly as Fe(III). The spectral features of Aberthaw and Krakow ash are different from those of the hematite, magnetite and illite standards suggesting that the glass fraction was dominant and controlled their spectral characteristics, which is consistent with the results of the Fe sequential extractions. The XANES Fe K-edge spectra of the CFA samples have some common features with those of Icelandic dust but tend to differ from mineral dust sourced in the Saharan dust source region. In the pre-edge region of the spectrum, Icelandic dust (sample D3 in Figures 3.5a-b) showed a main peak at around 7114.4 eV and a second less intense peak at around 7112.7 eV, while a broad peak was observed at around 7131.9 eV in the edge region (Baldo et al., 2020). A mineral dust sample from western Sahara (WS dust in Figures 3.5a-b) showed a distinct double peak in the pre-edge region at around 7113.9 and 7115.2 eV, and a

main peak in the edge region at around 7133.3 eV (Baldo et al., 2020). The similarities between Icelandic ash and CFA could be because aluminum silicate glass is dominant in these samples (e.g., Baldo et al., 2020; Brown et al., 2011), while Fe-bearing phases in mineral dust from the Saharan region are primarily iron oxides minerals such as hematite and goethite, clay minerals and feldspars (e.g., Shi et al., 2011b).

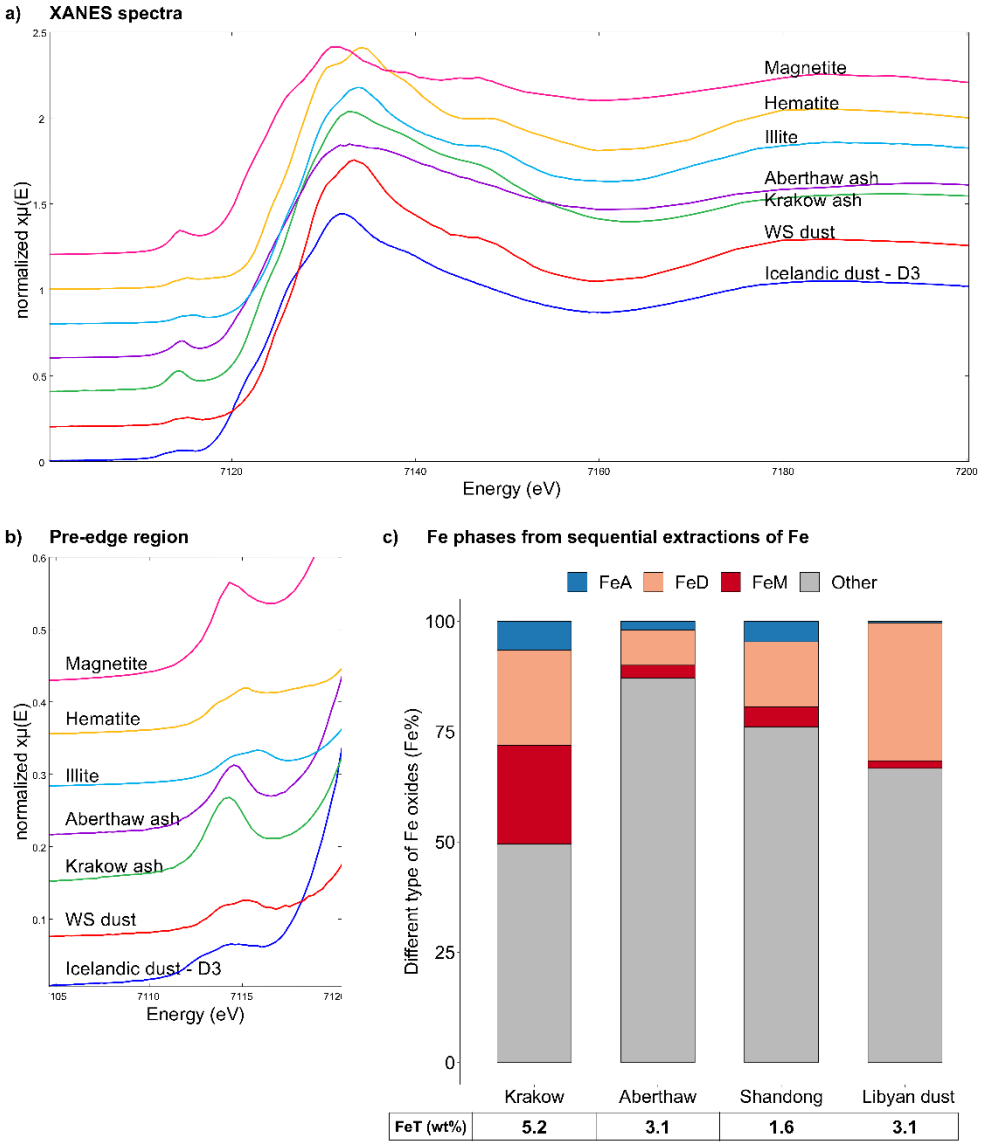

Figure 3.5: Fe speciation in CFA and mineral dust samples. a-b) Fe K-edge XANES spectra of Krakow ash, Aberthaw ash, magnetite, hematite, and illite standards, mineral dust from the Dyngjusandur dust hotspot in Iceland - D3 (Baldo et al., 2020), and mineral dust from western Sahara - WS dust (Shi et al., 2011b). c) Percentages of ascorbate Fe (amorphous Fe, FeA), dithionite Fe (goethite/hematite, FeD), magnetite Fe (FeM), and other Fe (including Fe in aluminosilicates) to the total Fe (FeT) in the CFA samples and Libyan dust precursor. The FeT (as %wt.) is given below each sample column. The data uncertainty was estimated using the error propagation formula: 4% for FeA/FeT, 11% for FeD/FeT, 12% for FeM/FeT, and 2 % for FeT.

3.5 Fe simulation from the IMPACT model

3.5.1 Fe dissolution scheme

Based on the laboratory experiments carried out on the CFA samples, we implemented a 3-step dissolution scheme for proton-promoted and oxalate-promoted Fe dissolution (Table 3.1). The Fe dissolution kinetics were described as follows (Ito, 2015):

$$\sum_{i} \mathrm{RFe_i} = \mathrm{k_i(pH, T)} \times \mathrm{a(H^+)^{m_i}} \times \mathrm{f_i} \quad (1)$$

where RFe_i is the dissolution rate of individual mineral i, k_i is the rate constant (moles Fe g^{-1} s^{-1}), $a(H^+)$ is the H^+ activity in solution, m_i represents the empirical reaction order for protons. The function f_i ($0 \leq f_i \leq 1$) accounts for the suppression of mineral dissolution by competition for oxalate between surface Fe and dissolved Fe (Ito, 2015):

$$f_i = 0.17 \times \ln([\mathrm{lig}] \times [Fe]^{-1})_i + 0.63 \quad (2)$$

in which, [Fe] is the molar concentration (mol L^{-1}) of Fe^{3+} dissolved in solution, and [lig] is the molar concentration of ligand (e.g., oxalate). f_i was set to 1 for the proton-promoted dissolution.

The scheme assumes 3 rate constants "fast", "intermediate" and "slow" for the proton-promoted, and the proton + oxalate-promoted dissolution (Table 3.1). These were obtained by fitting the parameters to our measurements for Krakow ash in H_2SO_4 and $(NH_4)_2SO_4$ at pH 2-3, with and without oxalate (Experiments 2 and 3 in Table S1), which are shown in Figure 3.6. The fast rate constant represents highly reactive Fe species such as amorphous Fe oxyhydroxides, Fe carbonates and Fe sulfates. The intermediate rate constant can be applied to nano-particulate Fe oxides, while more stable phases including for example Fe-aluminosilicate and crystalline Fe oxides have generally slower rates (Ito and Shi, 2016; Shi et al., 2011a; Shi et al., 2011b; Shi et al., 2015). Similarly, we predicted the dissolution kinetics of Aberthaw ash and Shandong ash (Figure 3.7). The dissolution kinetics of Krakow ash were

calculated based also on the experimental results at pH 1.0, which is shown in Figure S2 in comparison with kinetics predicted at pH 2.0 and pH 2.9 conditions.

The contribution of the oxalate-promoted dissolution to dissolved Fe was derived as the difference between the estimated dissolution rates for the proton + oxalate-promoted dissolution and the proton-promoted dissolution:

$$\mathrm{RFe_{i(oxalate)}} = \mathrm{RFe_{i(proton + oxalate)}} - \mathrm{RFe_{i(proton)}} \quad (3)$$

The Fe dissolution rates were predicted at a wider range of pH using Eq. (1) and Eq. (3) and the parameters in Table 3.1:

$$\mathrm{RFe_i} = \mathrm{RFe_{i(proton + oxalate)}} \text{ when } \mathrm{RFe_{i(oxalate)}} < 0 \quad (4)$$

Since $\mathrm{RFe_{i(oxalate)}}$ is less than 0 at low pH (< 2), this equation applies to highly acidic conditions. As a result, the predicted amount of dissolved Fe was smaller when using the dissolution rate for the proton + oxalate-promoted dissolution, $\mathrm{RFe_{i(proton + oxalate)}}$, rather than the rate for the proton-promoted dissolution, $\mathrm{RFe_{i(proton)}}$, at pH < 2. Accordingly, the dissolution rate, $\mathrm{RFe_i}$, was less dependent on the pH compared to $\mathrm{RFe_{i(proton)}}$ at highly acidic conditions, possibly due to the competition for the formation of surface complexes.

At pH > 2 when oxalate does promote Fe dissolution, the following equation applies:

$$\mathrm{RFe_i} = \mathrm{RFe_{i(proton)}} + \mathrm{RFe_{i(oxalate)}} \text{ when } \mathrm{RFe_{i(oxalate)}} > 0 \quad (5)$$

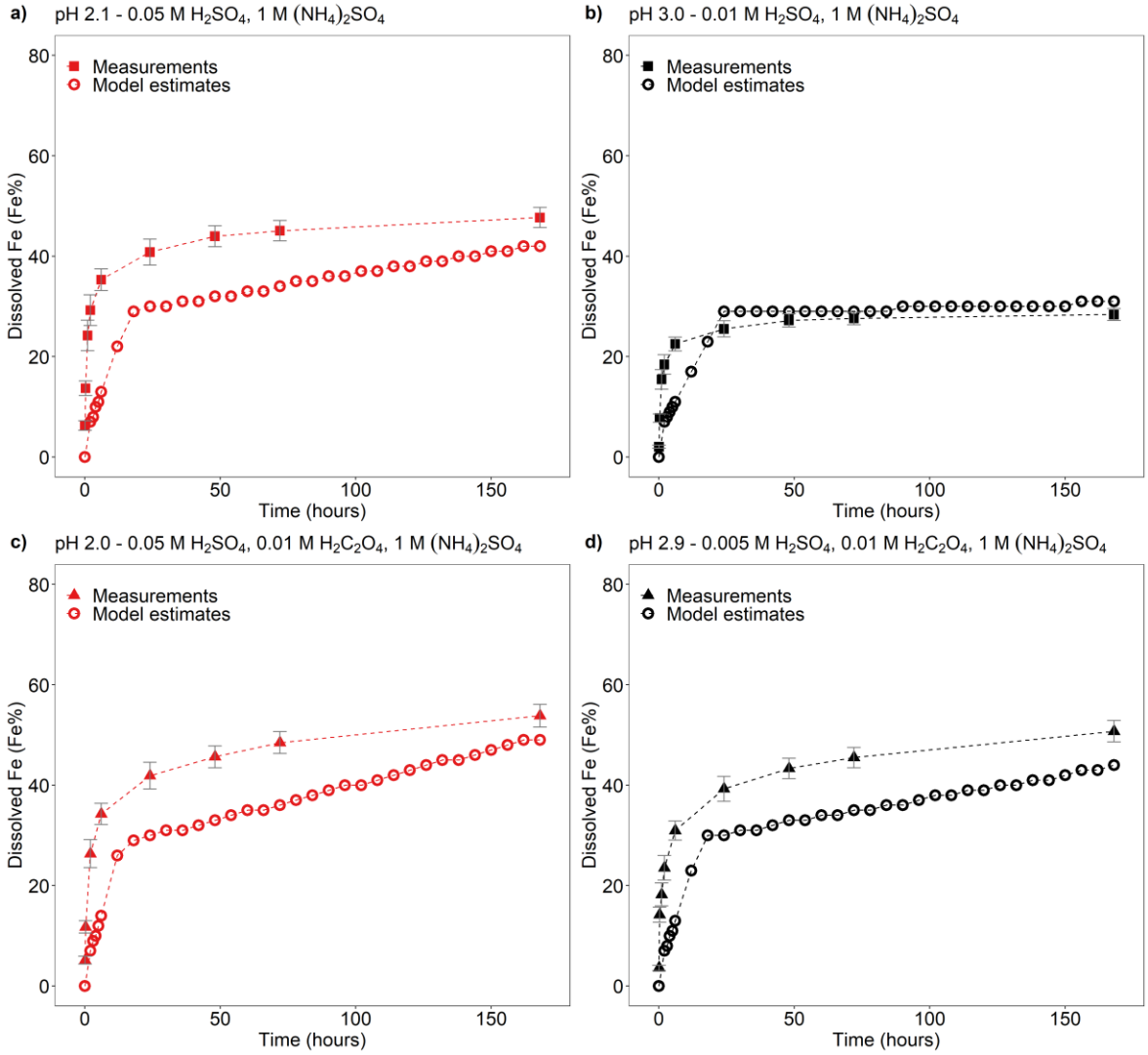

Figure 3.6: Comparison between the Fe dissolution kinetics of Krakow ash predicted using Eq. (1) and measured in H_2SO_4 solutions a-b) with 1 M $(NH_4)_2SO_4$, c-d) with 0.01 M $H_2C_2O_4$ and 1 M $(NH_4)_2SO_4$. The molar concentrations of H_2SO_4, $H_2C_2O_4$ and $(NH_4)_2SO_4$ in the experiment solutions are shown. The final pH of the experiment solutions is also reported, which was calculated using the E-AIM model III for aqueous solution (Wexler and Clegg, 2002) accounting for the buffer capacity of the CFA samples (Experiments 2-3 in Table S1). The experiments conducted at around pH 2 are in red, while the experiments at around pH 3 are in black. The data uncertainty was estimated using the error propagation formula.

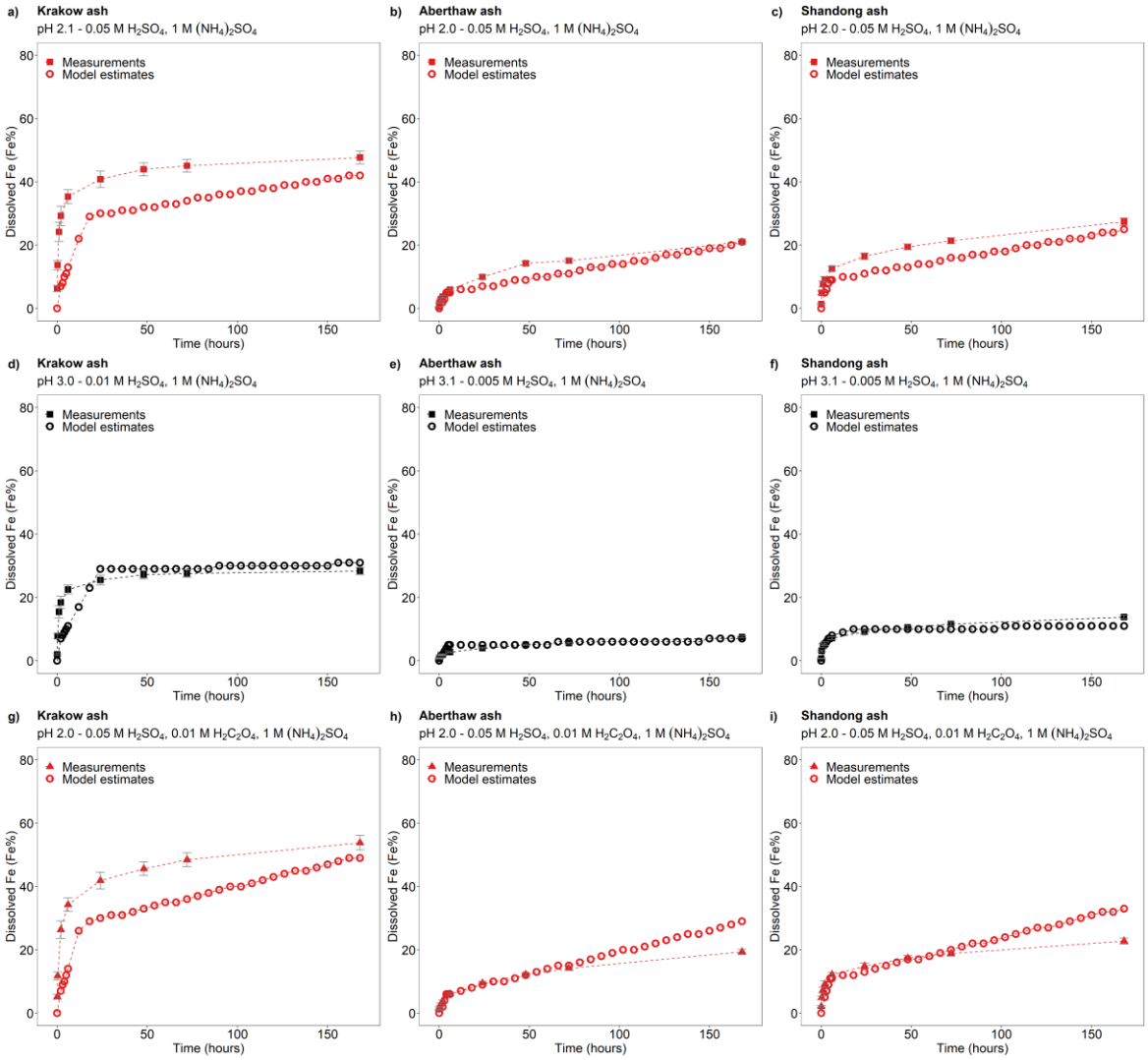

Figure 3.7: Comparison between the Fe dissolution kinetics of Krakow, Aberthaw, and Shandong ashes predicted using Eq. (1) and measured in a-c) H_2SO_4 solutions at around pH 2 with 1 M $(NH_4)_2SO_4$ (Experiments 2 at around pH 2 in Table S1), d-f) H_2SO_4 solutions at around pH 3 with 1 M $(NH_4)_2SO_4$ (Experiments 2 at around pH 3 in Table S1), g-i) H_2SO_4 solutions at pH 2.0 with 0.01 M $H_2C_2O_4$ and 1 M $(NH_4)_2SO_4$ (Experiments 3 at pH 2.0 in Table S1). The molar concentrations of H_2SO_4, $H_2C_2O_4$ and $(NH_4)_2SO_4$ in the experiment solutions are shown. The final pH of the experiment solutions is also reported, which was calculated using the E-AIM model III for aqueous solution (Wexler and Clegg, 2002) accounting for the buffer capacity of the CFA samples.

Table 3.1: Constants used to calculate Fe dissolution rates for fossil fuel combustion aerosols, based on laboratory experiments conducted at high ionic strength.

Stage	Kinetic	Scheme	Rate constant - k(pH, T)[a]	m[c]
I	Fast	Proton	$7.61 \times 10^{-6}\exp[E(pH)^{b} \times (1/298 - 1/T)]$	0.241
II	Intermediate	Proton	$1.91 \times 10^{-7}\exp[E(pH)^{b} \times (1/298 - 1/T)]$	0.195
III	Slow	Proton	$2.48 \times 10^{-7}\exp[E(pH)^{b} \times (1/298 - 1/T)]$	0.843
I	Fast	Proton + Oxalate	$5.54 \times 10^{-6}\exp[E(pH)^{b} \times (1/298 - 1/T)]$	0.209
II	Intermediate	Proton + Oxalate	$1.50 \times 10^{-7}\exp[E(pH)^{b} \times (1/298 - 1/T)]$	0.091
III	Slow	Proton + Oxalate	$1.77 \times 10^{-8}\exp[E(pH)^{b} \times (1/298 - 1/T)]$	0.204

[a] k(pH, T) is the pH and temperature dependent 'far-from-equilibrium' rate constant (moles Fe g^{-1} s^{-1}). The Fe dissolution scheme assumes 3 rate constants "fast", "intermediate" and "slow" for the proton- and oxalate-promoted dissolution. The parameters were fitted to our measurements for Krakow ash.
[b] $E(pH) = -1.56 \times 10^{3} \times pH + 1.08 \times 10^{4}$. The parameters were fitted to the measurements for soils (Bibi et al., 2014).
[c] m is the reaction order with respect to aqueous phase protons, which was determined by linear regression from our experimental data in the pH range between 2 and 3 for proton- and oxalate-promoted dissolution schemes.

3.5.2 Aerosol Fe solubility over the Bay of Bengal

The new dissolution scheme was applied in the IMPACT atmospheric chemistry transport model to predict the Fe solubility in atmospheric particles collected over the Bay of Bengal, which is an area for which there are detailed field measurements available (Bikkina et al., 2020; Kumar et al., 2010; Srinivas and Sarin, 2013; Srinivas et al., 2012) and multi-modelling analyses have been done (Ito et al., 2019). It thus represents a test for our experimental results in actual field conditions. Three sensitivity simulations were performed to explore the effects of the uncertainties associated with the dissolution schemes and mineralogical component of Fe. In addition, the former setting (Ito et al., 2021a) was used in the IMPACT model for comparison.

For all simulations, the total Fe emissions from anthropogenic combustion sources and biomass burning were estimated using the Fe emission inventory of Ito et al. (2018) including also emissions from the iron and steel industry, whereas Fe emissions from mineral dust sources were dynamically simulated

(Ito et al., 2021a). In Test 0, we ran the model without the upgrades of the dissolution scheme discussed in section 2.4, and apply in addition the photoinduced dissolution scheme for both combustion and dust aerosols (Ito, 2015; Ito and Shi, 2016), which was turned off in Test 1, Test 2, and Test 3 due to the lack of laboratory measurements under high ionic strength. To estimate the aerosol pH, we applied a H^+ activity coefficient of 1 for Test 0, while the mean activity coefficient from Pye et al. (2020) was used for the other tests. The dissolution rate was assumed as pH-independent for highly acidic solutions (pH < 2) (Ito, 2015) in Test 0, based on the laboratory measurements in Chen et al. (2012), while no pH threshold was considered in Test 1, Test 2, and Test 3 as the total dissolution (proton + oxalate) was suppressed at pH < 2 from the predicted dissolution rate.

In Test 1, we used the new dissolution scheme accounting for the proton- and oxalate- promoted dissolution of Krakow ash for all combustion aerosols in the model (Table 3.1). The dissolution kinetics were calculated using the base mineralogy for anthropogenic Fe emissions reported in Table S11 of Rathod et al. (2020). The Fe composition of wood was used for open biomass burning (Matsuo et al., 1992). In this simulation, three Fe pools were considered. Sulfate Fe in Rathod et al. (2020) was assumed as fast pool, magnetite Fe as intermediate pool, hematite, goethite and clay as slow pool. In Test 2, we calculated the dissolution kinetics only considering the proton-promoted dissolution. In Test 3, the Fe pools were as determined here for Krakow ash: ascorbate Fe (FeA) as fast pool, magnetite Fe (FeM) as intermediate pool, hematite plus goethite Fe (FeD) and other Fe as slow pool (Figure 3.5). FeA contains highly reactive Fe species with fast dissolution rates (Raiswell et al., 2008; Shi et al., 2011b). FeM appeared to work well for the different fly ash samples in the dissolution scheme as intermediate Fe pool. FeD is associated with crystalline Fe oxides which are mostly highly insoluble (Raiswell et al., 2008; Shi et al., 2011b), thus it was considered as slow pool in the dissolution scheme. We assumed other Fe to be mostly Fe-bearing aluminosilicates and considered this as slow Fe pool.

Observations of total Fe concentration and Fe solubility in $PM_{2.5}$ along the cruise tracks over the Bay of Bengal for the period extending from 27 December 2008 to 26 January 2009 (Bikkina et al., 2020) were compared with temporally and regionally averaged data from model estimates. The daily averages of

model results were calculated from hourly mass concentrations in the air over the surface ocean along the cruise tracks. The concentration of total Fe observed over the Bay of Bengal varies from 145 ± 144 ng m^{-3} over the North Bay of Bengal (27 December 2008 - 10 January 2009) to 55 ± 23 ng m^{-3} over the South Bay of Bengal (11-26 January 2009) (Bikkina et al., 2020). In Figure 3.8, the modelled concentrations of total Fe exhibit a similar variability to that of measurements with relatively higher values over the North Bay of Bengal (59 ± 29 ng m^{-3} in different sensitivity simulations) compared to the South Bay of Bengal (20 ± 12 ng m^{-3} in different sensitivity simulations). However, the modelled concentrations of total Fe were underestimated by a factor of 2.9 ± 1.5. The model reproduced the source apportion of Fe (Figure 3.8 - Table S4) which is qualitatively derived from previous observational studies indicating that the concentrations of total Fe in aerosols over the North Bay of Bengal are influenced by emissions of dust and combustion sources from the Indo-Gangetic Plain (Kumar et al., 2010), whereas combustion sources (e.g., biomass burning and fossil-fuel) from South-East Asia are dominant over the South Bay of Bengal (Kumar et al., 2010; Srinivas and Sarin, 2013). On the other hand, the model could not reproduce the peak in total Fe concentration (1.8% of Fe content in $PM_{2.5}$ sample) reported around 29 December 2008. The total Fe observed in PM_{10} (430 ng m^{-3}) on 29 December 2008 is lower than that measured on the day before (667 ng m^{-3}) and the day after (773 ng m^{-3}), whereas that in $PM_{2.5}$ peaked on 29 December 2008 (Srinivas et al., 2012). Thus, the extreme value recorded only for $PM_{2.5}$ on this date may be an outlier.

The comparison of Fe solubility using the same total Fe emissions directly represents the effect of the new dissolution scheme on $PM_{2.5}$. The aerosol Fe solubility measured over the South Bay of Bengal is higher than that over the North Bay of Bengal, respectively 32% ± 11% and 15% ± 7% (Bikkina et al., 2020), and model estimates showed a similar trend (Figure 3.9). In Figure 3.9 and Table S5, the calculated Fe solubilities over the North Bay of Bengal in Test 1 (11% ± 4%), Test 2 (17% ± 5%), and Test 3 (17% ± 6%) were in good agreement with observations. The aerosol Fe solubility over the South Bay of Bengal was better captured in Test 1 (30% ± 5%) and Test 3 (37% ± 7%), whereas Test 0 showed higher variability (37% ± 22%). The proton-promoted dissolution scheme in Test 2 significantly

overestimated the Fe solubility over the Bay of Bengal (Figure 3.9 and Table S5). The aerosol Fe solubility was largely overestimated in all scenarios after 22 January 2009, as open biomass burning sources become dominant (Figure 3.8 and Table S4).

The comparison between observations and model predictions of aerosol Fe solubility over the Bay of Bengal is shown in Figure S3. The agreement between measurements and model predictions was the best in Test 1 and Test 3. These exhibited good correlation with observations (R = 0.49 in Test 1 and R = 0.54 in Test 3), and the lowest root mean squared difference between the simulated and observed Fe solubilities (RMSE = 11 in Test 1 and RMSE = 12 in Test 3). In Test 0, the model estimates showed a greater difference from observations (RMSE = 21) and poor correlation (R = 0.26).

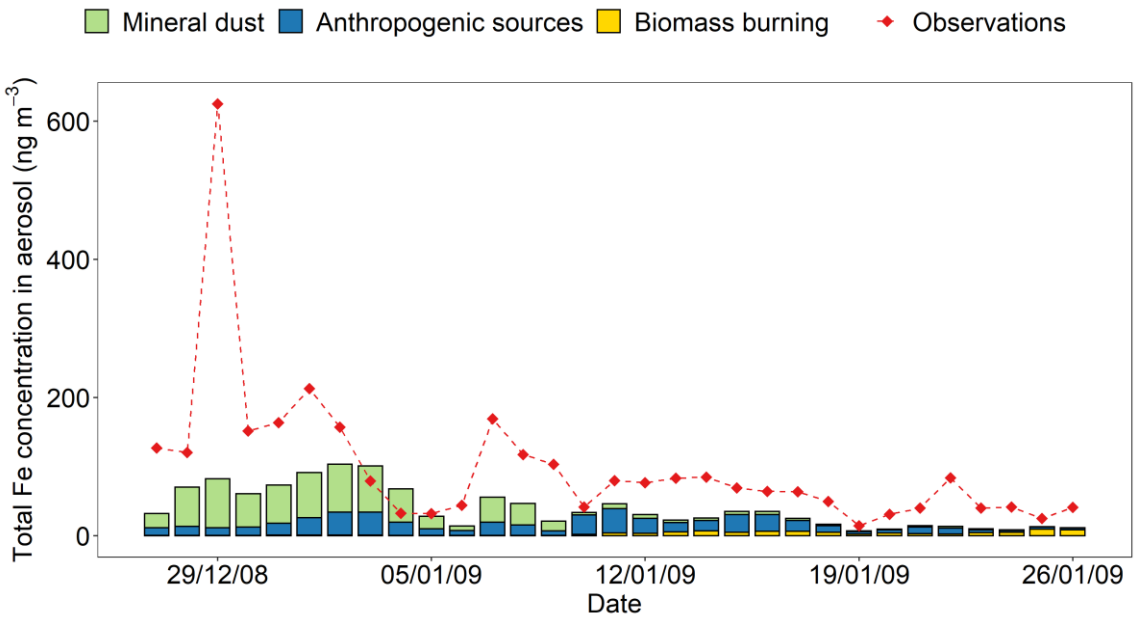

Figure 3.8: Mass concentration of total Fe in $PM_{2.5}$ aerosol particles over the Bay of Bengal from 27 December 2008 to 26 January 2009. Observations are from Bikkina et al. (2020) (red filled diamonds). The concentrations of total Fe were calculated along the cruise tracks in the North Bay of Bengal (27 December 2008 - 10 January 2009) and the South Bay of Bengal (11-26 January 2009) using the IMPACT model. The total Fe emissions from anthropogenic combustion sources (ANTHRO) and biomass burning (BB) were estimated using the emission inventory of Ito et al. (2018), whereas Fe emissions from mineral dust sources (DUST) were dynamically simulated (Ito et al., 2021a).

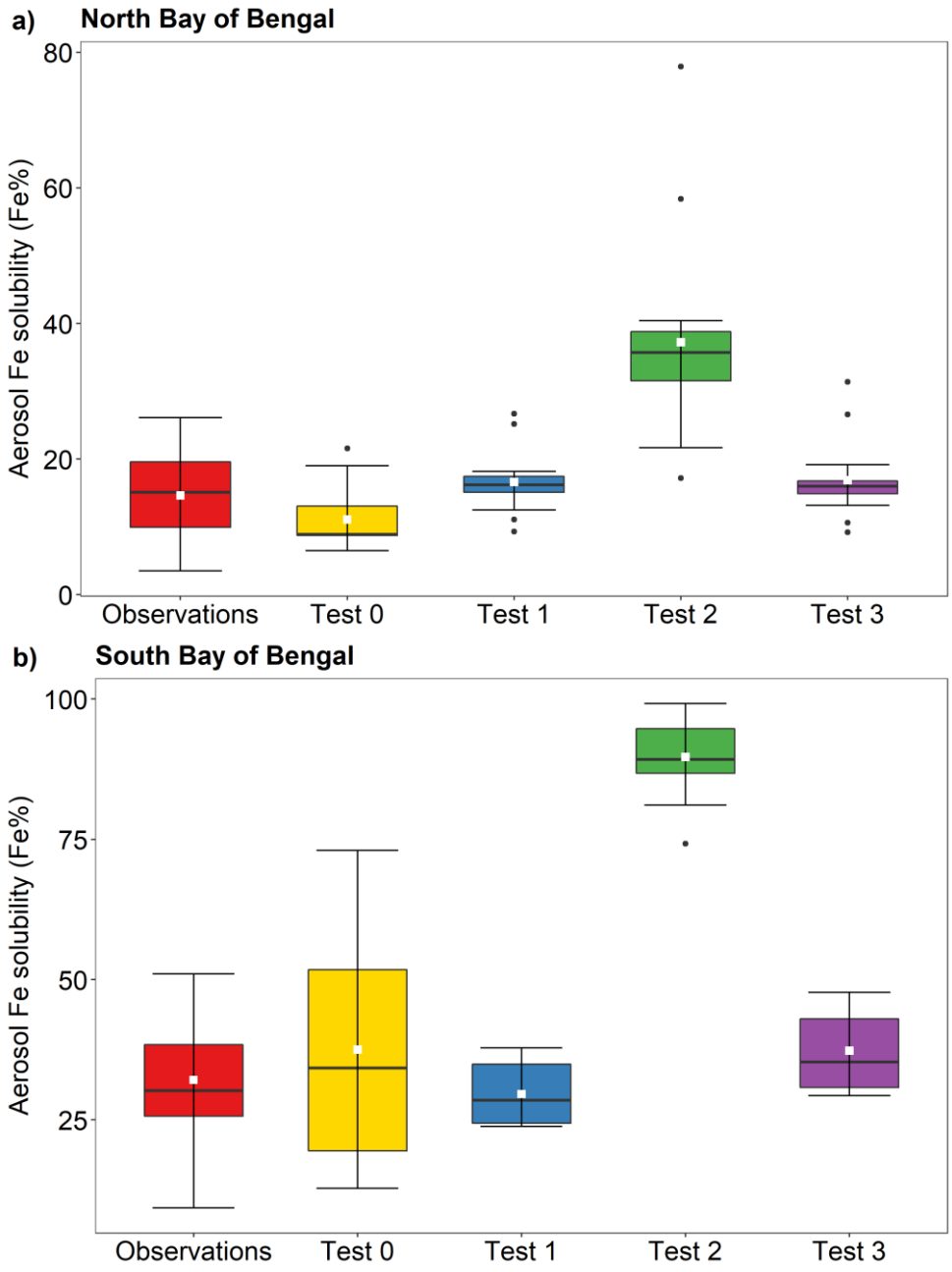

Figure 3.9: Fe solubility in $PM_{2.5}$ aerosol particles over a) the North Bay of Bengal, and b) the South Bay of Bengal from 27 December 2008 to 26 January 2009. Observations are from Bikkina et al. (2020). Model estimates of Test 0, Test 1, Test 2, and Test 3 were calculated along the cruise tracks using the IMPACT model. In Test 0, we run the model without upgrades (Ito et al., 2021a) and applying the proton-promoted, oxalate-promoted, and photoinduced dissolution schemes for combustion aerosols in Table S6 (Ito, 2015). The proton + oxalate dissolution scheme (Table 1) was applied in Test 1 and 3, while proton-promoted dissolution is used for Test 2. We adopted the base mineralogy for anthropogenic Fe emissions (Rathod et al., 2020) in Test 1 and 2. In Test 3, the Fe speciation of Krakow ash was used for all combustion sources. The small white square within the box shows the mean. The solid line within the box indicates the median. The lower and upper hinges correspond to the 25^{th} and 75^{th} percentiles. The whiskers above and below the box indicate the 1.5 × interquartile range, and the data outside this range are plotted individually.

3.6 Discussion

3.6.1 Dissolution behavior of Fe in CFA

In this study, the Fe dissolution kinetics of CFA samples from UK, Poland and China were investigated under simulated atmospheric acidic conditions. A key parameter in both the atmosphere and the simulation experiments is the pH of the water interacting with the CFA particles. The lower the pH of the experimental solution the faster the dissolution and eventually the higher the amount of Fe dissolved. Our results showed a strong pH dependence in low ionic strength conditions, with higher dissolution rates at lower pH. For example, reducing the solution pH from 2.7 to 2.1, the Fe solubility of Krakow ash in H_2SO_4 only increased by a factor of 4 (Figure 3.1a) over the duration of the experiments, while the Fe solubility of Aberthaw and Shandong ash increased by 9-10 times from pH 2.9 to pH 2.2 (Figures 3.1b-c). This enhancement is higher than that observed in studies conducted on mineral dust samples, which showed that one pH unit can lead to 3-4 times difference in dissolution rates (Ito and Shi, 2016; Shi et al., 2011a). Furthermore, Chen et al. (2012) reported that the Fe solubility of the certified CFA 2689 only increased by 10% from pH 2 to pH 1, after 50 hours of dissolution in acidic media. The Fe solubility of CFA (PM_{10} fractions) after 6 hours at pH 2 was 6%-10% for Aberthaw and Shandong ash respectively, and 28% for Krakow ash (Figure 3.1). The Fe in our CFA samples initially dissolved faster than those used by Fu et al. (2012), who reported 2.9%-4.2% Fe solubility in bulk CFA from three coal-fired power plants in China after 12-hour leaching at pH 2. These results suggest that there are considerable variabilities in the pH dependent dissolution of Fe in CFA. This could be due to differences in the Fe speciation between CFA samples and/or the different leaching media used.

Our results showed that high ionic strength has a major impact on dissolution rates of CFA at low pH (i.e., pH 2-3). The Fe solubility of CFA increased by approximatively 20%-40% in the presence of 1 M $(NH_4)_2SO_4$ at around pH 2 over the duration of the experiments, and by a factor from 3 to 7 at around pH 3 conditions (Figure 3.1). At high ionic strength, the activity of ions in solution is reduced, thus, in order to maintain similar pH conditions, the H^+ concentration has to be increased (Table S1). Although Fe dissolution was primarily controlled by the concentration of H^+, the high concentration of sulfate

ions could also be an important factor contributing to Fe dissolution, in particular when the concentration of H^+ in the system was low (e.g., pH 3). Previous research found that the high ability of anions to form soluble complexes with metals can enhance Fe dissolution (Cornell et al., 1976; Cornell and Schwertmann, 2003; Furrer and Stumm, 1986; Hamer et al., 2003; Rubasinghege et al., 2010; Sidhu et al., 1981; Surana and Warren, 1969). Sulfate ions adsorbed on the particles surface form complexes with Fe (e.g., Rubasinghege et al., 2010). This may increase the surface negative charge favoring the absorption of H^+ and thereby increase Fe dissolution at the particle surface. In addition, the formation of surface complexes may weaken the bonds between Fe and the neighboring ions (Cornell et al., 1976; Furrer and Stumm, 1986; Sidhu et al., 1981). Cwiertny et al. (2008) reported that at pH 1-2 the high ionic strength generated by NaCl up to 1 M did not influence Fe dissolution of mineral dust particles. However, Ito and Shi (2016) showed that the high ionic strength resulting from the addition of 1 M $(NH_4)_2SO_4$ in leaching solutions at pH 2-3 enhanced the Fe dissolution of dust particles, which was also observed here for the CFA samples. Borgatta et al. (2016) compared the Fe solubility of CFA from USA Midwest, North-East India, and Europe in acidic solution (pH 1-2) containing 1 M NaCl. The Fe solubility measured after 24 hours varied from 15% to 70% in different CFA (bulk samples) at pH 2 with 1 M NaCl, which was considerably higher than that observed at pH 2 with 1 M $NaNO_3$ (<20%) (Kim et al., 2020). Both studies did not investigate the impact of ionic strength on the dissolution behavior, i.e., by comparing the dissolution at low and high ionic strength. Note that both studies did not specify how the pH conditions were maintained at pH 2. Here, we considered the most important sources of high ionic strength in aerosol water and simulated Fe dissolution in the presence of $(NH_4)_2SO_4$ and $H_2C_2O_4$ under acidic conditions. We emphasize that the pH under high ionic strength here is estimated from a thermodynamic model, similar to those implemented in the IMPACT model.

The presence of oxalate enhanced Fe dissolution in Krakow and Aberthaw ash but not in Shandong ash at around pH 2 (Figure 3.2). The effect of oxalate on the Fe dissolution kinetics has also been studied by Chen and Grassian (2013) at pH 2 (11.6 mM $H_2C_2O_4$). After 45-hour leaching, the Fe solubility of the certified CFA 2689 increased from 16% in H_2SO_4 at pH 2 to 44% in $H_2C_2O_4$ at the same pH (Chen

and Grassian, 2013). Therefore, the enhancement in Fe solubility of CFA in the presence of oxalate observed in this study (from no impact in Shandong ash to doubled dissolution in Krakow ash) is lower than the 2.8 time increase in Fe solubility reported for the certified CFA 2689 (Chen and Grassian, 2013). Since no data are available in Chen and Grassian (2013), we are unable to make a comparison with the other two certified CFA samples. The Fe solubility of Krakow ash after 48-hour leaching at pH 1.9 with 0.01 M $H_2C_2O_4$ (Figure 3.2a) was 53%, which is within the range of Fe solubilities observed in Chen and Grassian (2013) for the certified CFA samples at similar pH and $H_2C_2O_4$ concentrations (from 44% to 78%), whereas the Fe solubility of Aberthaw and Shandong ash (Figures 3.2b-c, 18%-17% after 48-hour leaching at pH 2.0 with 0.01 M $H_2C_2O_4$) was considerably lower than that of certified CFA (Chen and Grassian, 2013). These results suggest a large variability in the effects of oxalate on the Fe dissolution rates in different types of CFA.

Our results also indicated that high $(NH_4)_2SO_4$ concentrations suppress oxalate-promoted Fe dissolution of CFA (Figure 3.2), which was not considered in previous research. At pH 1.9 in the presence of oxalate, the Fe solubility of Krakow ash decreased by around 10% after the addition of $(NH_4)_2SO_4$, while the Fe solubility of Aberthaw ash decreased by 35% (Figure 3.2). We used the E-AIM model to estimate the concentration of oxalate ions and their activity (Table S3). The pH influences the speciation of $H_2C_2O_4$ in solution (e.g., Lee et al., 2007). $H_2C_2O_4$ is the main species below pH 2, whereas $HC_2O_4^-$ is dominant between pH 2-4. Above pH 4, $C_2O_4^{-2}$ is the principal species. In our experiments, $H_2C_2O_4$ is mainly as $HC_2O_4^-$ at around pH 2 (Experiments 3-4 in Table S3). In the presence of $(NH_4)_2SO_4$, the activity coefficient of $HC_2O_4^-$ was reduced by approximatively 35-38% (Experiments 3 in Table S3). Increasing the ionic strength lowers the activity of the oxalate ions, but at the same time favors the dissociation of the acid. At around pH 2 conditions, the E-AIM model estimated that the activity of $C_2O_4^{-2}$ was reduced by around one order of magnitude in the presence of $(NH_4)_2SO_4$, while its concentration increased 12-15 times (Experiments 3 in Table S3). The adsorption of anions can reduce oxalate adsorption on the particle surface due to electrostatic repulsion which results in slower release of Fe (Eick et al., 1999). Precipitation of ammonium hydrogen oxalate ($NH_4HC_2O_4$) can also occur in the system, but this is very

soluble and easily re-dissolves forming soluble oxalate species (Lee et al., 2007). We speculate that the high concentration of sulfate ions is likely to be responsible for inhibiting the oxalate-promoted dissolution by reducing oxalate adsorption on the particle surface. At pH 1 in the presence of oxalate, increasing the concentration of $(NH_4)_2SO_4$ from 0.5 M to 1.5 M did not affect the Fe dissolution behavior of the CFA samples (Figure 3.4). As previously discussed, the adsorption of sulfate ions on the particle surface may inhibit oxalate-promoted dissolution. However, once the saturation coverage is reached, increasing the concentration of anions has no further effect on the dissolution rate (Cornell et al., 1976).

Fe speciation is an important factor affecting the Fe dissolution behavior. CFA particles have very different chemical and physical properties depending for example on the nature of coal burned, combustion conditions, cooling process and particle control devices implemented at the power stations (e.g., Blissett and Rowson, 2012; Yao et al., 2015). This is likely the reason why the Fe speciation observed in the CFA samples analyzed in this study from different locations varied considerably (Figure 3.5). In the CFA samples, the Fe dissolution curves for different pH and ionic strengths generally showed the greatest rate of Fe release within the first 2 hours, followed by a slower dissolution, reaching almost a plateau at the end of the experimental run. This indicates the presence of multiple Fe-bearing phases in CFA particles with a wide range of reactivity. Initially, highly reactive phases were the main contribution to dissolved Fe. As the dissolution continued, more refractory phases became the dominant source of dissolved Fe (Shi et al., 2011a). SEM analysis conducted on CFA samples showed that CFA particles are mostly spherical (e.g., Chen et al., 2012; Dudas and Warren, 1987; Valeev et al., 2018; Warren and Dudas, 1989) with Fe oxide aggregates on the surface (Chen et al., 2012; Valeev et al., 2018). The analysis of the CFA samples processed in aqueous solution at low pH suggests that initially Fe dissolved from the reactive external glass coating (Dudas and Warren, 1987; Warren and Dudas, 1989) and from the Fe oxide aggregates on the particle surface (Chen et al., 2012; Valeev et al., 2018). Subsequently, Fe is likely released from the structure of the aluminum silicate glass (Chen et al., 2012; Dudas and Warren, 1987; Valeev et al., 2018; Warren and Dudas, 1989), and crystalline Fe oxide phases (Warren and Dudas, 1989). Overall, Krakow ash showed the fastest dissolution rates, but the dissolution

of highly reactive Fe species as FeA is insufficient to account for the high Fe solubility observed at low pH. Our results showed that once the FeA dissolved, additional Fe was dissolved from more refractory Fe-bearing phases. The modelled dissolution kinetics obtained using FeM as intermediate pool were in good agreements with measurements (Figures 3.7-S2). FeM is likely to be primary magnetite but may contain a fraction of the more reactive aluminosilicate glass. Our model results suggest that magnetite in CFA particles may be more soluble than has been shown in Marcotte et al. (2020). It is possible that in real CFA samples the physicochemical properties of minerals including for example crystal size, degree of crystallinity, cationic and anionic substitution in the lattice which influence the Fe dissolution behavior (e.g., Schwertmann, 1991) are likely to be different from those of the reference minerals analyzed in Marcotte et al. (2020). In order to investigate the links between Fe solubility and Fe speciation/mineralogy, more work is needed to determine the Fe mineralogy in CFA samples at emission and after atmospheric processing, in combination with solubility experiments.

Finally, the modelled dissolution kinetics obtained using the new dissolution scheme for CFA (Table 3.1) showed better agreement with laboratory measurements than when using the original scheme (Ito, 2015) (Figure 3.10). In Figures. 3.10a-b, we compared the Fe dissolution kinetics of Krakow ash at around pH 2 and 3 with 1 M $(NH_4)_2SO_4$ calculated using the proton-promoted dissolution scheme in Table 3.1 with the dissolution kinetics calculated at similar pH but using the proton-promoted dissolution scheme for combustion aerosols in Ito (2015) (Table S6). The dissolution scheme in Ito (2015) was based on laboratory measurements conducted at low ionic strength (Chen et al., 2012) and assumed a single Fe-bearing phase in combustion aerosol particles, while the new dissolution scheme considered the high ionic strength of aerosol water and assumed three rate constants, for fast, intermediate and slow kinetics of the different Fe-bearing phases present in CFA particles. The Fe dissolution kinetics obtained using the new dissolution scheme showed a better agreement with measurements and was enhanced compared to the model estimates obtained using the original dissolution scheme (Ito, 2015) for low ionic strength conditions (Figures 3.10a-b). Figures 3.10c-d show the Fe dissolution kinetics of Krakow ash at pH 2.0 and 2.9 with 0.01 M $H_2C_2O_4$ and 1 M $(NH_4)_2SO_4$ calculated using the proton- and oxalate-promoted

dissolution scheme in Table 3.1 and the dissolution kinetics calculated at similar pH and $H_2C_2O_4$ concentration but using the scheme in Ito (2015) (i.e., single phase dissolution, see Table S6). The Fe dissolution kinetics predicted using the new dissolution scheme had a much better agreement with measurements. Figure 3.10e shows the suppression of the oxalate-promoted dissolution at pH 2.0 and high $(NH_4)_2SO_4$ concentrations. At pH 2, the proton-promoted dissolution was comparable to the proton + oxalate-promoted dissolution (Figure 3.10e), with $RFe_{(oxalate)}$ close to zero (see Eq. 3). At pH 2.9, the proton + oxalate-promoted dissolution was higher than the proton + oxalate-promoted dissolution (Figure 3.10f), with $RFe_{(oxalate)} > 0$ (Eq. 5).

Moreover, the new 3-step dissolution scheme better captured the initial fast dissolution of CFA (Figure 3.10) which was also observed in previous research (Borgatta et al., 2016; Chen et al., 2012; Chen and Grassian, 2013; Fu et al., 2012; Kim et al., 2020) (except for the certified CFA 2689 in Chen et al. (2012) which showed increasing dissolution rates over the duration of the experiment). Furthermore, the new scheme enabled us to account for the different Fe speciation determined in the CFA samples, which could be a key factor contributing to the different Fe dissolution behavior observed in the present study and in literature (Borgatta et al., 2016; Chen et al., 2012; Chen and Grassian, 2013; Fu et al., 2012; Kim et al., 2020). In Figure 3.7, the dissolution kinetics of Aberthaw and Shandong ash calculated using the dissolution rates in Table 3.1 and the Fe-bearing phases determined in the samples showed a good agreement with measurements.

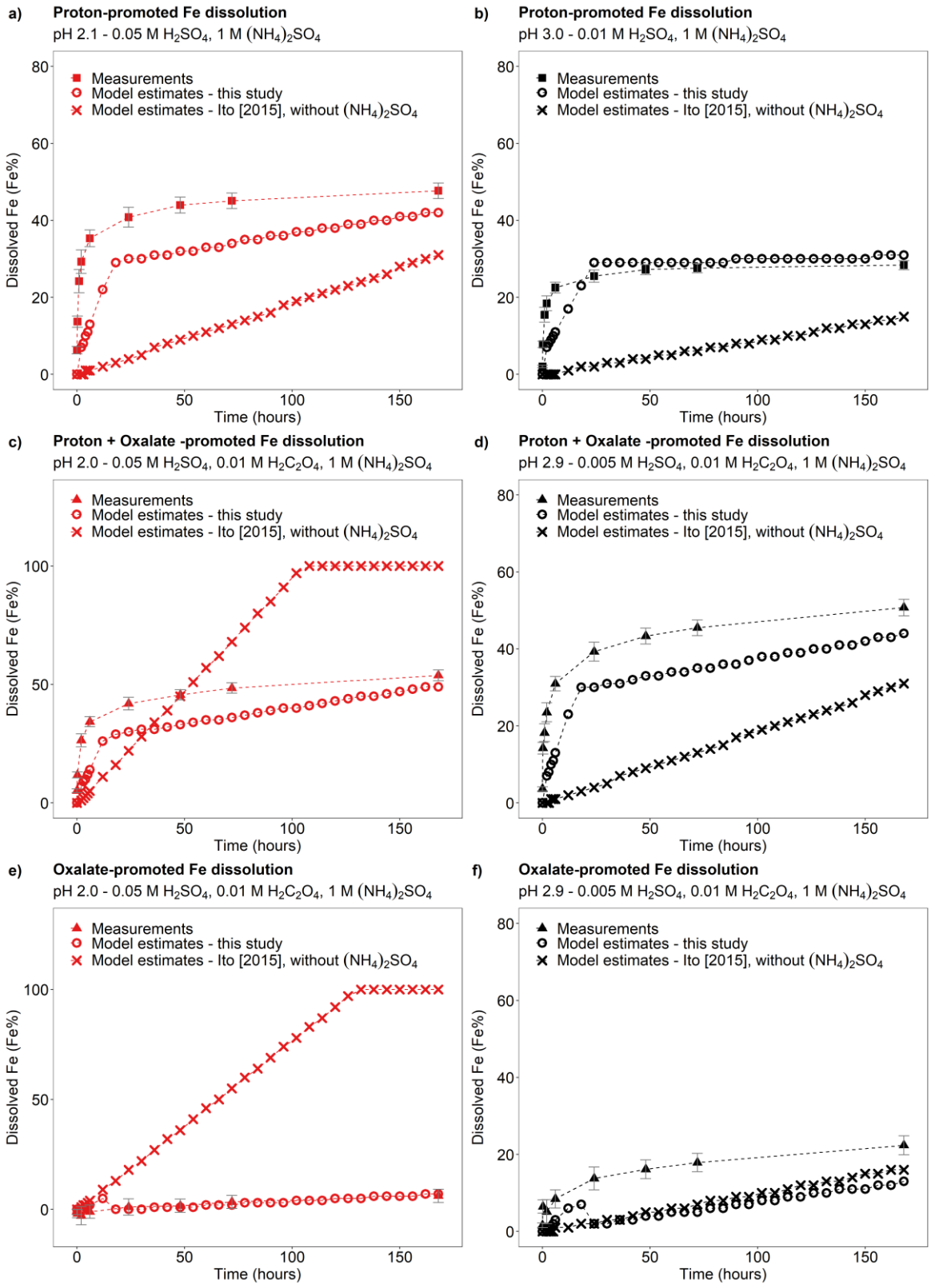

Figure 3.10: Comparison between the Fe dissolution kinetics of Krakow ash calculated using the original (Ito, 2015) and the new dissolution scheme (Tables 1 and S6). a-b) Proton-promoted Fe dissolution in H_2SO_4 solutions with 1 M $(NH_4)_2SO_4$ at pH 2.1 (a), and at pH 3.0 (b) (Experiment 2 at pH 2.1, and Experiment 2 at pH 3.0 in Table S1). c-d) Proton + oxalate promoted Fe dissolution in H_2SO_4 solutions

with 0.01 M $H_2C_2O_4$ and 1 M $(NH_4)_2SO_4$ at pH 2.0 (c), and at pH 2.9 (d) (Experiment 3 at pH 2.0, and Experiment 3 at pH 2.9 in Table S1). The Fe dissolution kinetics were predicted using the rate constants in Table 1 calculated in this study (open circles) and the dissolution scheme for combustion aerosols in Ito (2015) (cross marks). Note that the dissolution scheme in Ito (2015) was calculated based on laboratory measurements conducted at low ionic strength. e-f) Contribution of the oxalate-promoted dissolution to dissolved Fe estimated using Eq. (3). The molar concentrations of H_2SO_4, $H_2C_2O_4$ and $(NH_4)_2SO_4$ in the experiment solutions are shown. The final pH of the experiment solutions is also reported, which was calculated using the E-AIM model III for aqueous solution (Wexler and Clegg, 2002) accounting for the buffer capacity of the CFA samples.

3.6.2 Comparison with mineral dust

High ionic strength also impacted the dissolution rates of the Libyan dust precursor sample at low pH (Figure S4). At around pH 2 conditions, the proton-promoted Fe dissolution of Libyan dust was enhanced by ~40% after the addition of $(NH_4)_2SO_4$. At around pH 2 and with 0.01 M $H_2C_2O_4$, the Fe solubility of Libyan dust decreased by ~30% in the presence of $(NH_4)_2SO_4$. Overall, the Fe solubility of Libyan dust was lower compared to that observed in the CFA samples. After 168 hour-leaching at pH 2.1 with 1 M $(NH_4)_2SO_4$, the Fe solubility of Libyan dust was 7.2% (Figure S4), which was from around 3 to 7 times lower compared to that of the CFA samples (Figure 3.1). At around pH 2 conditions in the presence of oxalate and high $(NH_4)_2SO_4$ concentration, the Fe solubility of Libyan dust rose to ~13.6% (Figure S4), which is still 4 times lower than that of Krakow ash and around 1.5 lower than Aberthaw and Shandong ash (Figure 3.2). The Fe solubilities of the Libyan dust observed in this study are comparable with those of the Tibesti dust (Tibesti Mountains, Libya, 25.583333N/16.516667E) in Ito and Shi (2016) at similar experimental conditions.

The enhanced Fe solubility in CFA compared to mineral dust could be primarily related to the different Fe speciation (Figure 3.5). CFA contained more highly reactive Fe and magnetite but less hematite and goethite than mineral dust.

Although mineral dust is the largest contribution to aerosol Fe while CFA accounts for only a few percent, atmospheric processing of CFA may result in a larger than expected contribution of bio-accessible Fe deposited to the surface ocean. It is thus important to quantify the amount and nature of CFA in atmospheric particles.

3.6.3 Comparison of modelled Fe solubility with field measurements

The model results obtained using the new dissolution scheme for the proton + oxalate-promoted dissolution (Table 3.1) in Test 1 and Test 3 provided a better estimate of aerosol Fe solubility over the Bay of Bengal than the other tests (Figures 3.9 and S3). At the same time, the new model improved the agreement of aerosol Fe solubility from Test 0 (68% ± 5%) to Test 1 (35% ± 2%) and Test 3 (47% ± 1%) with the field data (25% ± 3%) but still overestimated it after 22 January 2009, when open biomass burning sources become dominant (Bikkina et al., 2020) as also shown in Figure 3.8 and Table S4. This could be due to the unrepresentative Fe speciation used in Test 1 and Test 3 for biomass burning over the Bay of Bengal. To reduce the uncertainty in model predictions, emission inventories could be improved through a comprehensive characterization of Fe species in combustion aerosol particles.

The revised model also enabled us to predict sensitivity to a more dynamic range of pH changes, particularly between anthropogenic combustion and biomass burning by the suppression of the oxalate-promoted dissolution at pH lower than 2. In Test 0, the dissolution rate was assumed to be independent from the pH for extremely acidic solutions (pH <2). The results show that the proton-promoted dissolution scheme in Test 2 significantly overestimated aerosol Fe solubility (Figures 3.9 and S3), which indicates the suppression of the proton + oxalate-promoted dissolution at pH < 2. In Figure S5, the model estimates of aerosol Fe solubility over the Bay of Bengal considerably improved in Test 1 (RMSE 11) compared to Test 0 (RMSE 21), but more work is needed to improve size-resolved Fe emission, transport, and deposition. The model results in Test 1 indicate a larger contribution of anthropogenic combustion sources to the atmospheric Fe loading over East Asia (Figure 3.11), but a smaller contribution of biomass burning sources downwind from tropical regions (Figure 3.12). We demonstrated that the implementation of the new Fe dissolution scheme, including a rapid Fe release at the initial stage and highly acidic conditions, enhanced the model estimates. However, in Test 1, we turned off the photo-reductive dissolution scheme (Ito, 2015), which was based on the laboratory measurements in Chen and Grassian (2013). To determine the photoinduced dissolution kinetics of CFA

particles it is necessary to account for the effect of high concentration of $(NH4)_2SO_4$ on photo-reductive dissolution rate which should be considered in future research.

3.7 Conclusion

This study investigated the dissolution kinetics of Fe in CFA samples under simulated atmospheric acidic processing, with particular focus on the effect of the high ionic strength in aerosol waters on the proton- and oxalate-promoted Fe dissolution. Our laboratory measurements indicate that the high ionic strength enhanced the proton-promoted Fe dissolution of CFA at low pH (2-3) but suppressed the oxalate-promoted Fe dissolution. However, the Fe dissolution behavior varied considerably depending on the type of CFA which exhibited different Fe speciation. Overall, CFA samples dissolved up to 7 times faster than a Saharan dust precursor at similar experimental conditions. The mineral dust precursor showed also lower highly reactive amorphous Fe and magnetite content compared to the CFA samples. Based on the experimental results, we developed a 3-step dissolution scheme for the proton- and oxalate-promoted Fe dissolution of combustion aerosols at high ionic strength which was implemented into the IMPACT model. Ultimately, the revised model showed a better agreement with observations of aerosol Fe solubility over the Bay of Bengal.

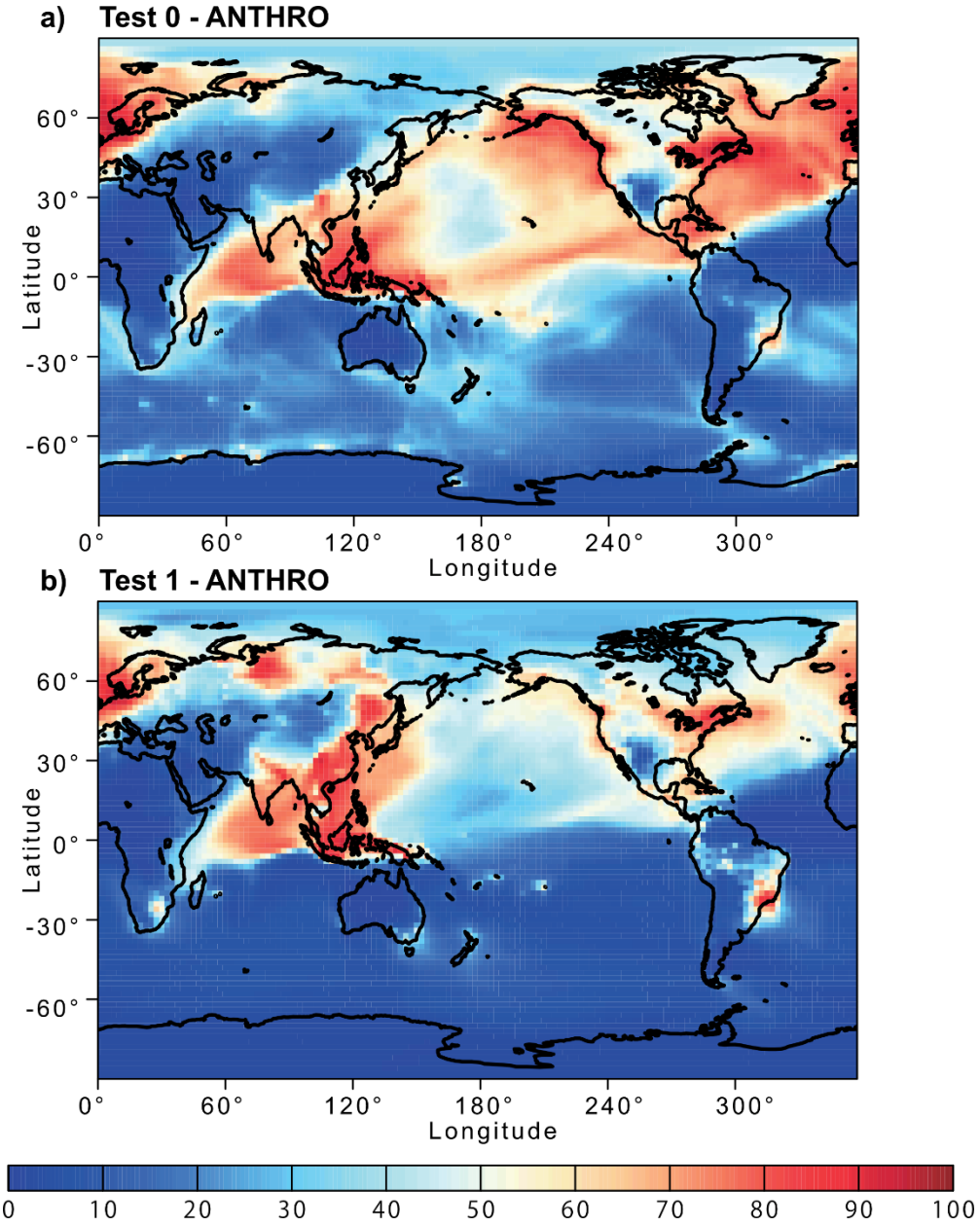

Figure 3.11: Percentage contribution of anthropogenic combustion (ANTHRO) aerosol to the atmospheric dissolved Fe concentration near the ground surface from a) Test 0 and b) Test 1 for December 2008 and January 2009. In Test 0, we ran the model without upgrades in the Fe dissolution scheme (Ito et al., 2021a) and applying the proton-promoted, oxalate-promoted and photoinduced dissolution schemes for combustion aerosols in Table S6 (Ito, 2015). The proton + oxalate dissolution scheme (Table 1) was applied in Test 1 and we adopted the base mineralogy for anthropogenic Fe emissions (Rathod et al., 2020).

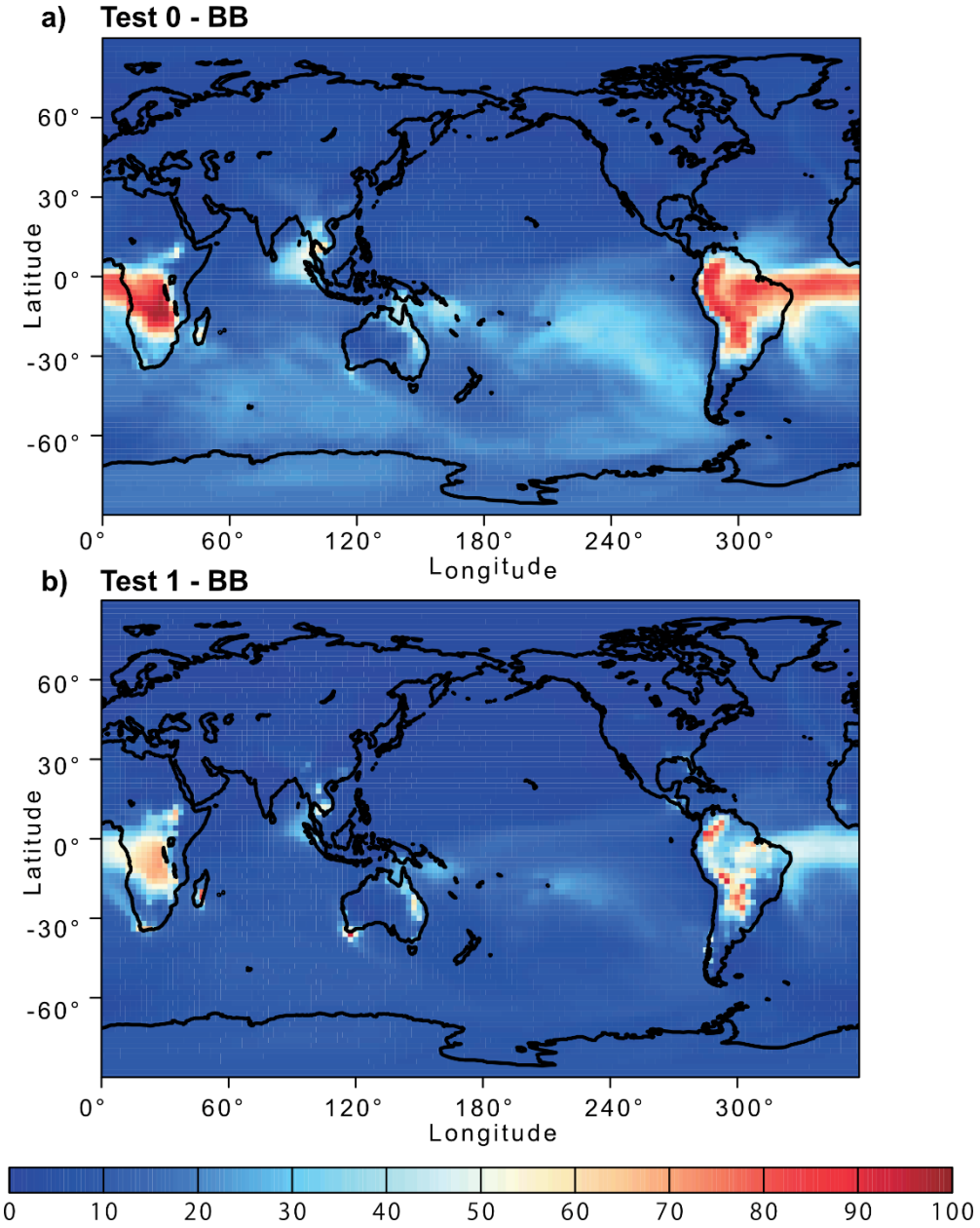

Figure 3.12: Percentage contribution of biomass burning (BB) aerosol to the atmospheric dissolved Fe concentration near the ground surface from a) Test 0 and b) Test 1 for December 2008 and January 2009. In Test 0, we ran the model without upgrades in the Fe dissolution scheme (Ito et al., 2021a) and applying the proton-promoted, oxalate-promoted and photoinduced dissolution schemes for combustion aerosols in Table S6 (Ito, 2015). The proton + oxalate dissolution scheme (Table 1) was applied in Test 1 and we adopted the base mineralogy for anthropogenic Fe emissions (Rathod et al., 2020).

3.8 References

Baker, A. R., Li, M., and Chance, R.: Trace Metal Fractional Solubility in Size-Segregated Aerosols From the Tropical Eastern Atlantic Ocean, Global Biogeochem. Cy., 34, e2019GB006510, doi: 10.1029/2019GB006510, 2020.

Baker, A. R., Kanakidou, M., Nenes, A., Myriokefalitakis, S., Croot, P. L., Duce, R. A., Gao, Y., Guieu, C., Ito, A., Jickells, T. D., Mahowald, N. M., Middag, R., Perron, M. M. G., Sarin, M. M., Shelley, R., and Turner, D. R.: Changing atmospheric acidity as a modulator of nutrient deposition and ocean biogeochemistry, Sci. Adv., 7, eabd8800, doi: 10.1126/sciadv.abd8800, 2021.

Baldo, C., Formenti, P., Nowak, S., Chevaillier, S., Cazaunau, M., Pangui, E., Di Biagio, C., Doussin, J. F., Ignatyev, K., Dagsson-Waldhauserova, P., Arnalds, O., MacKenzie, A. R., and Shi, Z.: Distinct chemical and mineralogical composition of Icelandic dust compared to northern African and Asian dust, Atmos. Chem. Phys., 20, 13521-13539, doi: 10.5194/acp-20-13521-2020, 2020.

Bibi, I., Singh, B., and Silvester, E.: Dissolution kinetics of soil clays in sulfuric acid solutions: Ionic strength and temperature effects, Appl. Geochem., 51, 170-183, doi: 10.1016/j.apgeochem.2014.10.004, 2014.

Bikkina, S., Kawamura, K., Sarin, M., and Tachibana, E.: ^{13}C Probing of Ambient Photo-Fenton Reactions Involving Iron and Oxalic Acid: Implications for Oceanic Biogeochemistry, ACS Earth Space Chem., 4, 964-976, doi: 10.1021/acsearthspacechem.0c00063, 2020.

Blissett, R. S., and Rowson, N. A.: A review of the multi-component utilisation of coal fly ash, Fuel, 97, 1-23, doi: 10.1016/j.fuel.2012.03.024, 2012.

Borgatta, J., Paskavitz, A., Kim, D., and Navea, J. G.: Comparative evaluation of iron leach from different sources of fly ash under atmospherically relevant conditions, Environ. Chem., 13, 902-912, doi: 10.1071/en16046, 2016.

Boyd, P. W., Jickells, T., Law, C. S., Blain, S., Boyle, E. A., Buesseler, K. O., Coale, K. H., Cullen, J. J., de Baar, H. J. W., Follows, M., Harvey, M., Lancelot, C., Levasseur, M., Owens, N. P. J., Pollard, R., Rivkin, R. B., Sarmiento, J., Schoemann, V., Smetacek, V., Takeda, S., Tsuda, A., Turner, S., and Watson, A. J.: Mesoscale Iron Enrichment Experiments 1993-2005: Synthesis and Future Directions, Science, 315, 612-617, doi: 10.1126/science.1131669, 2007.

British Petroleum (BP): Statistical Review of World Energy 2020, available at https://www.bp.com/en/global/corporate/energy-economics/statistical-review-of-world-energy.html, (last access: 10 April 2021), 2020.

Brown, P., Jones, T., and BéruBé, K.: The internal microstructure and fibrous mineralogy of fly ash from coal-burning power stations, Environ. Pollut., 159, 3324-3333, doi: 10.1016/j.envpol.2011.08.041, 2011.

Chen, H., Laskin, A., Baltrusaitis, J., Gorski, C. A., Scherer, M. M., and Grassian, V. H.: Coal fly ash as a source of iron in atmospheric dust, Environ. Sci. Technol., 46, 2112-2120, doi: 10.1021/es204102f, 2012.

Chen, H. H., and Grassian, V. H.: Iron Dissolution of Dust Source Materials during Simulated Acidic Processing: The Effect of Sulfuric, Acetic, and Oxalic Acids, Environ. Sci. Technol., 47, 10312-10321, doi: 10.1021/es401285s, 2013.

Cornell, R. M., Posner, A. M., and Quirk, J. P.: Kinetics and mechanisms of the acid dissolution of goethite (α-FeOOH), Journal of Inorganic and Nuclear Chemistry, 38, 563-567, doi: 10.1016/0022-1902(76)80305-3, 1976.

Cornell, R. M., and Schwertmann, U.: The Iron Oxides: Structure, Properties, Reactions, Occurrence and Uses, Wiley-VCH, New York 2003.

Cwiertny, D. M., Baltrusaitis, J., Hunter, G. J., Laskin, A., Scherer, M. M., and Grassian, V. H.: Characterization and acid-mobilization study of iron-containing mineral dust source materials, J. Geophys. Res.-Atmos, 113, D05202, doi: 10.1029/2007jd009332, 2008.

Dudas, M. J., and Warren, C. J.: Submicroscopic model of fly ash particles, Geoderma, 40, 101-114, doi: 10.1016/0016-7061(87)90016-4, 1987.

Eick, M. J., Peak, J. D., and Brady, W. D.: The Effect of Oxyanions on the Oxalate-Promoted Dissolution of Goethite, SSSAJ, 63, 1133-1141, doi: doi.org/10.2136/sssaj1999.6351133x, 1999.

Emerson, E. W., Hodshire, A. L., DeBolt, H. M., Bilsback, K. R., Pierce, J. R., McMeeking, G. R., and Farmer, D. K.: Revisiting particle dry deposition and its role in radiative effect estimates, P. Natl. Acad. Sci. USA, 117, 26076-26082, doi: 10.1073/pnas.2014761117, 2020.

Fu, H., Cwiertny, D. M., Carmichael, G. R., Scherer, M. M., and Grassian, V. H.: Photoreductive dissolution of Fe-containing mineral dust particles in acidic media, J. Geophys. Res., 115, D11304, doi: 10.1029/2009jd012702, 2010.

Fu, H. B., Lin, J., Shang, G. F., Dong, W. B., Grassian, V. H., Carmichael, G. R., Li, Y., and Chen, J. M.: Solubility of Iron from Combustion Source Particles in Acidic Media Linked to Iron Speciation, Environ. Sci. Technol., 46, 11119-11127, doi: 10.1021/es302558m, 2012.

Furrer, G., and Stumm, W.: The coordination chemistry of weathering: I. Dissolution kinetics of δ-Al_2O_3 and BeO, Geochim. Cosmochim. Ac., 50, 1847-1860, doi: 10.1016/0016-7037(86)90243-7, 1986.

Hamer, M., Graham, R. C., Amrheim, C., and Bozhilov, K. N.: Dissolution of ripidolite (Mg, Fe-chlorite) in organic and inorganic acid solutions, SSSAJ, 67, 654-661, doi: 10.2136/sssaj2003.6540, 2003.

Ito, A., and Feng, Y.: Role of dust alkalinity in acid mobilization of iron, Atmos. Chem. Phys., 10, 9237-9250, doi: 10.5194/acp-10-9237-2010, 2010.

Ito, A.: Atmospheric Processing of Combustion Aerosols as a Source of Bioavailable Iron, Environ. Sci. Technol. Lett., 2, 70-75, doi: 10.1021/acs.estlett.5b00007, 2015.

Ito, A., and Shi, Z.: Delivery of anthropogenic bioavailable iron from mineral dust and combustion aerosols to the ocean, Atmos. Chem. Phys., 16, 85-99, doi: 10.5194/acp-16-85-2016, 2016.

Ito, A., Lin, G. X., and Penner, J. E.: Radiative forcing by light-absorbing aerosols of pyrogenetic iron oxides, Sci. Rep., 8, 7347, doi: 10.1038/s41598-018-25756-3, 2018.

Ito, A., Myriokefalitakis, S., Kanakidou, M., Mahowald, N. M., Scanza, R. A., Hamilton, D. S., Baker, A. R., Jickells, T., Sarin, M., Bikkina, S., Gao, Y., Shelley, R. U., Buck, C. S., Landing, W. M., Bowie, A. R., Perron, M. M. G., Guieu, C., Meskhidze, N., Johnson, M. S., Feng, Y., Kok, J. F., Nenes, A., and Duce, R. A.: Pyrogenic iron: The missing link to high iron solubility in aerosols, Sci. Adv., 5, eaau7671 doi: 10.1126/sciadv.aau7671, 2019.

Ito, A., Adebiyi, A. A., Huang, Y., and Kok, J. F.: Less atmospheric radiative heating by dust due to the synergy of coarser size and aspherical shape, Atmos. Chem. Phys., 21, 16869–16891, doi: 10.5194/acp-21-16869-2021, 2021a.

Ito, A., Ye, Y., Baldo, C., and Shi, Z.: Ocean fertilization by pyrogenic aerosol iron, npj Clim. Atmos. Sci., 4, 30, doi: 10.1038/s41612-021-00185-8, 2021b.

Jickells, T., and Moore, C. M.: The importance of Atmospheric Deposition for Ocean Productivity, Annu. Rev. Ecol. Evol. Syst., 46, 481-501, doi: 10.1146/annurev-ecolsys-112414-054118, 2015.

Jickells, T. D., An, Z. S., Andersen, K. K., Baker, A. R., Bergametti, G., Brooks, N., Cao, J. J., Boyd, P. W., Duce, R. A., Hunter, K. A., Kawahata, H., Kubilay, N., laRoche, J., Liss, P. S., Mahowald, N., Prospero, J. M., Ridgwell, A. J., Tegen, I., and Torres, R.: Global iron connections between desert dust, ocean biogeochemistry, and climate, Science, 308, 67-71, doi: 10.1126/science.1105959, 2005.

Johnson, M. S., and Meskhidze, N.: Atmospheric dissolved iron deposition to the global oceans: effects of oxalate-promoted Fe dissolution, photochemical redox cycling, and dust mineralogy, Geoscientific Model Development, 6, 1137-1155, doi: 10.5194/gmd-6-1137-2013, 2013.

Jones, D. R.: The Leaching of Major and Trace Elements from Coal Ash, in: Environmental Aspects of Trace Elements in Coal, edited by: Swaine, D. J., and Goodarzi, F., Springer Netherlands, Dordrecht, 221-262, 1995.

Kanakidou, M., Myriokefalitakis, S., and Tsigaridis, K.: Aerosols in atmospheric chemistry and biogeochemical cycles of nutrients, Environ. Res. Lett., 13, 063004, doi: 10.1088/1748-9326/aabcdb, 2018.

Kawamura, K., and Bikkina, S.: A review of dicarboxylic acids and related compounds in atmospheric aerosols: Molecular distributions, sources and transformation, Atmos. Res., 170, 140-160, doi: 10.1016/j.atmosres.2015.11.018, 2016.

Kim, D., Xiao, Y., Karchere-Sun, R., Richmond, E., Ricker, H. M., Leonardi, A., and Navea, J. G.: Atmospheric Processing of Anthropogenic Combustion Particles: Effects of Acid Media and Solar Flux on the Iron Mobility from Fly Ash, ACS Earth Space Chem., 4, 750-761, doi: 10.1021/acsearthspacechem.0c00057, 2020.

Kukier, U., Ishak, C. F., Sumner, M. E., and Miller, W. P.: Composition and element solubility of magnetic and non-magnetic fly ash fractions, Environ. Pollut., 123, 255-266, doi: 10.1016/S0269-7491(02)00376-7, 2003.

Kumar, A., Sarin, M. M., and Srinivas, B.: Aerosol iron solubility over Bay of Bengal: Role of anthropogenic sources and chemical processing, Mar. Chem., 121, 167-175, doi: 10.1016/j.marchem.2010.04.005, 2010.

Kutchko, B. G., and Kim, A. G.: Fly ash characterization by SEM–EDS, Fuel, 85, 2537-2544, doi: 10.1016/j.fuel.2006.05.016, 2006.

Lawson, M. J., Prytherch, Z. C., Jones, T. P., Adams, R. A., and BéruBé, K. A.: Iron-Rich Magnetic Coal Fly Ash Particles Induce Apoptosis in Human Bronchial Cells, Appl. Sci., 10, 8368, doi: 10.3390/app10238368, 2020.

Lee, S. O., Tran, T., Jung, B. H., Kim, S. J., and Kim, M. J.: Dissolution of iron oxide using oxalic acid, Hydrometallurgy, 87, 91-99, doi: 10.1016/j.hydromet.2007.02.005, 2007.

Li, J., Anderson, J. R., and Buseck, P. R.: TEM study of aerosol particles from clean and polluted marine boundary layers over the North Atlantic, J. Geophys. Res.-Atmos, 108, doi: 10.1029/2002JD002106, 2003.

Li, W. J., Xu, L., Liu, X. H., Zhang, J. C., Lin, Y. T., Yao, X. H., Gao, H. W., Zhang, D. Z., Chen, J. M., Wang, W. X., Harrison, R. M., Zhang, X. Y., Shao, L. Y., Fu, P. Q., Nenes, A., and Shi, Z. B.: Air pollution-aerosol interactions produce more bioavailable iron for ocean ecosystems, Sci. Adv., 3, e1601749, doi: 10.1126/sciadv.1601749, 2017.

Mahowald, N. M., Kloster, S., Engelstaedter, S., Moore, J. K., Mukhopadhyay, S., McConnell, J. R., Albani, S., Doney, S. C., Bhattacharya, A., Curran, M. A. J., Flanner, M. G., Hoffman, F. M., Lawrence, D. M., Lindsay, K., Mayewski, P. A., Neff, J., Rothenberg, D., Thomas, E., Thornton, P. E., and Zender,

C. S.: Observed 20th century desert dust variability: impact on climate and biogeochemistry, Atmos. Chem. Phys., 10, 10875-10893, doi: 10.5194/acp-10-10875-2010, 2010.

Marcotte, A. R., Anbar, A. D., Majestic, B. J., and Herckes, P.: Mineral Dust and Iron Solubility: Effects of Composition, Particle Size, and Surface Area, Atmosphere, 11, 533, doi: 10.3390/atmos11050533, 2020.

Martin, J. H.: Glacial-interglacial CO_2 change: The Iron Hypothesis, Paleoceanography, 5, 1-13, doi: 10.1029/PA005i001p00001, 1990.

Matsuo, M., Kobayashi, T., Singh, T. B., Tsurumi, M., and Ichikuni, M.: ^{57}Fe Mössbauer spectroscopic study of Japanese cedar bark — The variation in chemical states of iron due to influence of human activities, Hyperfine Interact., 71, 1255-1258, doi: 10.1007/BF02397311, 1992.

Meskhidze, N., Chameides, W. L., Nenes, A., and Chen, G.: Iron mobilization in mineral dust: Can anthropogenic SO_2 emissions affect ocean productivity?, Geophys. Res. Lett., 30, 2085, doi: 10.1029/2003gl018035, 2003.

Mills, M. M., Ridame, C., Davey, M., La Roche, J., and Geider, R. J.: Iron and phosphorus co-limit nitrogen fixation in the eastern tropical North Atlantic, Nature, 429, 292-294, doi: 10.1038/nature02550, 2004.

Moore, C. M., Mills, M. M., Milne, A., Langlois, R., Achterberg, E. P., Lochte, K., Geider, R. J., and La Roche, J.: Iron limits primary productivity during spring bloom development in the central North Atlantic, Glob. Change Biol., 12, 626-634, doi: 10.1111/j.1365-2486.2006.01122.x, 2006.

Munawer, M. E.: Human health and environmental impacts of coal combustion and post-combustion wastes, J. Sustain. Min., 17, 87-96, doi: 10.1016/j.jsm.2017.12.007, 2018.

Paris, R., Desboeufs, K. V., and Journet, E.: Variability of dust iron solubility in atmospheric waters: Investigation of the role of oxalate organic complexation, Atmos. Environ., 45, 6510-6517, doi: 10.1016/j.atmosenv.2011.08.068, 2011.

Paris, R., and Desboeufs, K. V.: Effect of atmospheric organic complexation on iron-bearing dust solubility, Atmos. Chem. Phys., 13, 4895-4905, doi: 10.5194/acp-13-4895-2013, 2013.

Poulton, S. W., and Canfield, D. E.: Development of a sequential extraction procedure for iron: implications for iron partitioning in continentally derived particulates, Chem. Geol., 214, 209-221, doi: 10.1016/j.chemgeo.2004.09.003, 2005.

Pye, H. O. T., Nenes, A., Alexander, B., Ault, A. P., Barth, M. C., Clegg, S. L., Collett Jr, J. L., Fahey, K. M., Hennigan, C. J., Herrmann, H., Kanakidou, M., Kelly, J. T., Ku, I. T., McNeill, V. F., Riemer, N., Schaefer, T., Shi, G., Tilgner, A., Walker, J. T., Wang, T., Weber, R., Xing, J., Zaveri, R. A., and

Zuend, A.: The acidity of atmospheric particles and clouds, Atmos. Chem. Phys., 20, 4809-4888, doi: 10.5194/acp-20-4809-2020, 2020.

Raiswell, R., Benning, L. G., Tranter, M., and Tulaczyk, S.: Bioavailable iron in the Southern Ocean: the significance of the iceberg conveyor belt, Geochem. T., 9, 7, doi: 10.1186/1467-4866-9-7, 2008.

Rathod, S. D., Hamilton, D. S., Mahowald, N. M., Klimont, Z., Corbett, J. J., and Bond, T. C.: A Mineralogy‐Based Anthropogenic Combustion‐Iron Emission Inventory, J. Geophys. Res.-Atmos, 125, e2019JD032114, doi: 10.1029/2019jd032114, 2020.

Ravel, B., and Newville, M.: ATHENA, ARTEMIS, HEPHAESTUS: data analysis for X-ray absorption spectroscopy using IFEFFIT, J. Synchrotron Radiat., 12, 537-541, doi: 10.1107/S0909049505012719, 2005.

Rubasinghege, G., Lentz, R. W., Scherer, M. M., and Grassian, V. H.: Simulated atmospheric processing of iron oxyhydroxide minerals at low pH: roles of particle size and acid anion in iron dissolution, P. Natl. Acad. Sci. USA, 107, 6628-6633, doi: 10.1073/pnas.0910809107, 2010.

Rubin, M., Berman-Frank, I., and Shaked, Y.: Dust- and mineral-iron utilization by the marine dinitrogen-fixer Trichodesmium, Nat. Geosci., 4, 529-534, doi: 10.1038/ngeo1181, 2011.

Schlosser, C., Schmidt, K., Aquilina, A., Homoky, W. B., Castrillejo, M., Mills, R. A., Patey, M. D., Fielding, S., Atkinson, A., and Achterberg, E. P.: Mechanisms of dissolved and labile particulate iron supply to shelf waters and phytoplankton blooms off South Georgia, Southern Ocean, Biogeosciences, 15, 4973-4993, doi: 10.5194/bg-15-4973-2018, 2018.

Schwertmann, U.: Solubility and dissolution of iron oxides, Plant Soil, 130, 1-25, doi: 10.1007/BF00011851, 1991.

Seinfeld, J. H., and Pandis, S. N.: Atmospheric chemistry and physics: from air pollution to climate change, John Wiley & Sons, 2016.

Shelley, R. U., Landing, W. M., Ussher, S. J., Planquette, H., and Sarthou, G.: Regional trends in the fractional solubility of Fe and other metals from North Atlantic aerosols (GEOTRACES cruises GA01 and GA03) following a two-stage leach, Biogeosciences, 15, 2271-2288, doi: 10.5194/bg-15-2271-2018, 2018.

Shi, Z., Krom, M. D., Bonneville, S., Baker, A. R., Jickells, T. D., and Benning, L. G.: Formation of iron nanoparticles and increase in iron reactivity in the mineral dust during simulated cloud processing, Environ. Sci. Technol., 43, 6592-6596, doi: 10.1021/es901294g, 2009.

Shi, Z., Bonneville, S., Krom, M. D., Carslaw, K. S., Jickells, T. D., Baker, A. R., and Benning, L. G.: Iron dissolution kinetics of mineral dust at low pH during simulated atmospheric processing, Atmos. Chem. Phys., 11, 995-1007, doi: 10.5194/acp-11-995-2011, 2011a.

Shi, Z., Krom, M. D., Bonneville, S., Baker, A. R., Bristow, C., Drake, N., Mann, G., Carslaw, K., McQuaid, J. B., Jickells, T., and Benning, L. G.: Influence of chemical weathering and aging of iron oxides on the potential iron solubility of Saharan dust during simulated atmospheric processing, Global Biogeochem. Cy., 25, GB2010, doi: 10.1029/2010gb003837, 2011b.

Shi, Z., Krom, M. D., Jickells, T. D., Bonneville, S., Carslaw, K. S., Mihalopoulos, N., Baker, A. R., and Benning, L. G.: Impacts on iron solubility in the mineral dust by processes in the source region and the atmosphere: A review, Aeolian Res., 5, 21-42, doi: 10.1016/j.aeolia.2012.03.001, 2012.

Shi, Z., Krom, M. D., Bonneville, S., and Benning, L. G.: Atmospheric processing outside clouds increases soluble iron in mineral dust, Environ. Sci. Technol., 49, 1472-1477, doi: 10.1021/es504623x, 2015.

Shi, Z. B., Woodhouse, M. T., Carslaw, K. S., Krom, M. D., Mann, G. W., Baker, A. R., Savov, I., Fones, G. R., Brooks, B., Drake, N., Jickells, T. D., and Benning, L. G.: Minor effect of physical size sorting on iron solubility of transported mineral dust, Atmos. Chem. Phys., 11, 8459-8469, doi: 10.5194/acp-11-8459-2011, 2011c.

Sholkovitz, E. R., Sedwick, P. N., and Church, T. M.: Influence of anthropogenic combustion emissions on the deposition of soluble aerosol iron to the ocean: Empirical estimates for island sites in the North Atlantic, Geochim. Cosmochim. Ac., 73, 3981-4003, doi: 10.1016/j.gca.2009.04.029, 2009.

Sholkovitz, E. R., Sedwick, P. N., Church, T. M., Baker, A. R., and Powell, C. F.: Fractional solubility of aerosol iron: Synthesis of a global-scale data set, Geochim. Cosmochim. Ac., 89, 173-189, doi: 10.1016/j.gca.2012.04.022, 2012.

Sidhu, P. S., Gilkes, R. J., Cornell, R. M., Posner, A. M., and Quirk, J. P.: Dissolution of Iron Oxides and Oxyhydroxides in Hydrochloric and Perchloric Acids, Clays Clay Miner., 29, 269-276, doi: 10.1346/CCMN.1981.0290404, 1981.

Spokes, L. J., and Jickells, T. D.: Factors controlling the solubility of aerosol trace metals in the atmosphere and on mixing into seawater, Aquat. Geochem., 1, 355-374, doi: 10.1007/BF00702739, 1995.

Srinivas, B., Sarin, M. M., and Kumar, A.: Impact of anthropogenic sources on aerosol iron solubility over the Bay of Bengal and the Arabian Sea, Biogeochemistry, 110, 257-268, doi: 10.1007/s10533-011-9680-1, 2012.

Srinivas, B., and Sarin, M. M.: Atmospheric dry-deposition of mineral dust and anthropogenic trace metals to the Bay of Bengal, J. Mar. Syst., 126, 56-68, doi: 10.1016/j.jmarsys.2012.11.004, 2013.

Surana, V., and Warren, I.: The leaching of goethite, Transactions of the Institute of Mining and Metallurgy, 80, C152-155, 1969.

Sutto, T. E.: Magnetite fine particle and nanoparticle environmental contamination from industrial uses of coal, Environ. Pollut., 243, 528-533, doi: 10.1016/j.envpol.2018.08.080, 2018.

Valeev, D., Mikhailova, A., and Atmadzhidi, A.: Kinetics of Iron Extraction from Coal Fly Ash by Hydrochloric Acid Leaching, Metals, 8, 533, doi: 10.3390/met8070533, 2018.

Valeev, D., Kunilova, I., Alpatov, A., Varnavskaya, A., and Ju, D.: Magnetite and Carbon Extraction from Coal Fly Ash Using Magnetic Separation and Flotation Methods, Minerals, 9, 320, doi: 10.3390/min9050320, 2019.

Viollier, E., Inglett, P. W., Hunter, K., Roychoudhury, A. N., and Van Cappellen, P.: The ferrozine method revisited: Fe(II)/Fe(III) determination in natural waters, Appl. Geochem., 15, 785-790, doi: 10.1016/s0883-2927(99)00097-9, 2000.

Waanders, F. B., Vinken, E., Mans, A., and Mulaba-Bafubiandi, A. F.: Iron Minerals in Coal, Weathered Coal and Coal Ash – SEM and Mössbauer Results, Hyperfine Interact., 148, 21-29, doi: 10.1023/B:HYPE.0000003760.89706.f6, 2003.

Wang, R., Balkanski, Y., Boucher, O., Bopp, L., Chappell, A., Ciais, P., Hauglustaine, D., Penuelas, J., and Tao, S.: Sources, transport and deposition of iron in the global atmosphere, Atmos. Chem. Phys., 15, 6247-6270, doi: 10.5194/acp-15-6247-2015, 2015.

Wang, X. S.: Mineralogical and chemical composition of magnetic fly ash fraction, Environ. Earth Sci., 71, 1673-1681, doi: 10.1007/s12665-013-2571-0, 2014.

Warren, C. J., and Dudas, M. J.: Leachability and partitioning of elements in ferromagnetic fly ash particles, Sci. Total Environ., 84, 223-236, doi: 10.1016/0048-9697(89)90385-9, 1989.

Wexler, A. S., and Clegg, S. L.: Atmospheric aerosol models for systems including the ions H^+, NH_4^+, Na^+, SO_4^{2-}, NO_3^-, Cl^-, Br^-, and H_2O, J. Geophys. Res.-Atmos, 107, 4207, doi: 10.1029/2001JD000451, 2002.

Xu, N., and Gao, Y.: Characterization of hematite dissolution affected by oxalate coating, kinetics and pH, Appl. Geochem., 23, 783-793, doi: 10.1016/j.apgeochem.2007.12.026, 2008.

Yao, Z. T., Ji, X. S., Sarker, P. K., Tang, J. H., Ge, L. Q., Xia, M. S., and Xi, Y. Q.: A comprehensive review on the applications of coal fly ash, Earth-Sci. Rev., 141, 105-121, doi: 10.1016/j.earscirev.2014.11.016, 2015.

Yu, J. Z., Huang, X.-F., Xu, J., and Hu, M.: When Aerosol Sulfate Goes Up, So Does Oxalate: Implication for the Formation Mechanisms of Oxalate, Environ. Sci. Technol., 39, 128-133, doi: 10.1021/es049559f, 2005.

Zhang, D., Iwasaka, Y., Shi, G., Zang, J., Matsuki, A., and Trochkine, D.: Mixture state and size of Asian dust particles collected at southwestern Japan in spring 2000, J. Geophys. Res.-Atmos, 108, 4760, doi: 10.1029/2003JD003869, 2003.

Zhao, Y., Zhang, J., Sun, J., Bai, X., and Zheng, C.: Mineralogy, Chemical Composition, and Microstructure of Ferrospheres in Fly Ashes from Coal Combustion, Energy Fuels, 20, 1490-1497, doi: 10.1021/ef060008f, 2006.

Zhu, X. R., Prospero, J. M., Millero, F. J., Savoie, D. L., and Brass, G. W.: The solubility of ferric ion in marine mineral aerosol solutions at ambient relative humidities Mar. Chem., 38, 91-107, doi: 10.1016/0304-4203(92)90069-m, 1992.

CHAPTER 4: DISTINCT CHEMICAL AND MINERALOGICAL COMPOSITION OF ICELANDIC DUST COMPARED TO NORTHERN AFRICAN AND ASIAN DUST

4.1 Abstract

Iceland is a highly active source of natural dust. Icelandic dust has the potential to directly affect the climate via dust-radiation interaction, and indirectly via dust-cloud interaction, snow/ice albedo effect and impacts on biogeochemical cycles. The impacts of Icelandic dust depend on its mineralogical and chemical composition. However, lack of data has prevented an accurate assessment of the role of Icelandic dust in the Earth system. Here, we collected surface sediment samples from five major Icelandic dust hotspots. Dust aerosols were generated and suspended in atmospheric chambers, and PM_{10} and PM_{20} fractions were collected for further analysis. We found that the dust samples primarily consist of amorphous basaltic material ranging from 8 wt% (from the Hagavatn hotspot) to 60-90 wt% (other hotspots). Samples had relatively high total Fe content (10-13 wt%). Sequential extraction of Fe to determine its chemical form shows that dithionite Fe (Fe oxides such as hematite and goethite) and ascorbate Fe (amorphous Fe) contribute respectively 1-6%, and 0.3-1.4% of the total Fe in Icelandic dust. The magnetite fraction is 7-15% of total Fe and 1-2 wt% of PM_{10}, which is orders of magnitude higher than in mineral dust from North Africa. Nevertheless, about 80-90% of the Fe is contained in pyroxene and amorphous glass. The initial Fe solubility (ammonium acetate extraction at pH 4.7) is from 0.08-0.6%, which is comparable to low latitude dust such as that from North Africa. The Fe solubility at low pH (i.e., 2) is significantly higher than typical low latitude dust (up to 30% at pH 2 after 72 hrs). Our results revealed the fundamental differences in composition and mineralogy of Icelandic

dust from low latitude dust. We attribute these differences to the low degree of chemical weathering, the basaltic composition of the parent sediments, and glacial processes. Icelandic dust contributes to the atmospheric deposition of soluble Fe and can impact primary productivity in the North Atlantic Ocean. The distinct chemical and mineralogical composition, particularly the high magnetite content (1-2 wt%), indicates a potentially significant impact of Icelandic dust on the radiation balance in the sub-polar and polar regions.

4.2 Introduction

Airborne mineral dust has a major influence on the global climate. Depending on the chemical and mineralogical dust composition (together with the size distribution and shape), dust particles affect the radiation balance by scattering and absorbing the solar radiation, and by scattering, absorbing, and re-emitting terrestrial radiation (e.g., Haywood et al., 2003; Sokolik and Toon, 1999). This can produce cooling or warming of the atmosphere, and consequently alter the atmospheric circulation, stability, and cloud cover (e.g., Arimoto, 2001; Carslaw et al., 2010; Choobari et al., 2014; Maher et al., 2010). Dust can also act as cloud condensation and ice nuclei, influencing cloud properties and lifetime (e.g., Atkinson et al., 2013; Tang et al., 2016). In the cryosphere, dust deposition on snow and ice reduces the surface albedo, altering snow melting rate (e.g.,Dumont et al., 2014; Meinander et al., 2014; Peltoniemi et al., 2015; Qian et al., 2015). Finally, dust can also affect the biogeochemical cycles of terrestrial and marine ecosystems by deposition of nutrients and pollutants (e.g., Jickells and Moore, 2015; Jickells et al., 2005; Kanakidou et al., 2018; Mahowald et al., 2010; Shi et al., 2012; Stockdale et al., 2016).

Natural dust is emitted from soil surfaces through wind erosion and is generally associated with desert dust from arid and semiarid regions. However, significant dust events occur also in cold regions at high latitude (Bullard et al., 2016). In the Northern hemisphere, high latitude (>60°N) dust sources includes for example Alaska, Canada, Greenland, and Iceland, and contributes about 3% of global dust emissions (Groot Zwaaftink et al., 2016).

Iceland is among the most active dust source areas in the world. Iceland has extensive sandy deserts subjected to intense aeolian processes (Arnalds et al., 2001).The active aeolian areas cover 15,000 km^2 and include super active dust hotspots. These areas have the potential to generate millions of tons of dust during major dust storm events (Arnalds et al., 2016). Iceland experiences 34-135 dust events per year, which is comparable to dust-active area in arid regions including northern Africa and China (Dagsson-Waldhauserova et al., 2014a). The dust can travel long distance and reach Europe and the high

Artic (Baddock et al., 2017; Dordevic et al., 2019; Groot Zwaaftink et al., 2017; Groot Zwaaftink et al., 2016; Moroni et al., 2018; Prospero et al., 2012).

Iceland lies in the North Atlantic Ocean, just south of the Arctic Circle. Iceland is a volcanic hotspot along the northern end of the Mid-Atlantic ridge and has intensive volcanic activity (Oskarsson, 1980). Around 10% of Iceland is covered by glaciers (Björnsson and Palsson, 2008). Volcanic activity within glaciers is common in Iceland (Jakobsson and Gudmundsson, 2008). Glacial flood plains contain fine glacial volcanic sediments that supply the Icelandic dust hotspots (Arnalds, 2010; Arnalds et al., 2016; Jensen et al., 2018). Sandy areas in Iceland have a dark surface and are often dominated by amorphous basaltic glass (Arnalds et al., 2001). Therefore, Icelandic cold deserts are different from deserts in arid continental areas such as Africa and Asia.

Arnalds et al. (2014) estimated that 30-40 Tg of Icelandic dust are deposited annually on land, glaciers, and sea. The majority is deposited on land, and around 18-35% reach the ocean. Icelandic dust can affect the climate via dust deposition on glaciers. Wittmann et al. (2017) observed that the deposition of small amounts of dust on the Vatnajökull, the largest ice cap in Iceland, caused a positive radiative effect and enhanced the ice melting due to the reduced surface albedo. Outdoor experiments found that thin layers of volcanic deposits on the Vatnajökull ice cap accelerated snow melting as a result of the reduced surface albedo, while thick layers of volcanic deposits (1.5-15mm) had insulating effects because of reduced heat conduction to the glacier surface (Dragosics et al., 2016; Möller et al., 2016; Möller et al., 2018). The Soot on the Snow experiments in 2013 investigated the effect of black carbon (BC) and volcanic sand deposited on snow (Meinander et al., 2014; Peltoniemi et al., 2015). The results showed that the volcanic sand from Iceland reduces the surface albedo and increases the melting rate of snow similarly to black carbon. Icelandic dust is strongly light absorbing (Zubko et al., 2019). Icelandic dust is also rich in iron (Fe) (e.g., Arnalds et al., 2014). The Fe speciation regulates the light absorption properties of mineral dust in the shortwave spectrum, as Fe oxide minerals strongly absorb the solar radiation (Caponi et al., 2017; Derimian et al., 2008; Di Biagio et al., 2019; Engelbrecht et al., 2016;

Formenti et al., 2014a; Lafon et al., 2006; Moosmuller et al., 2012; Sokolik and Toon, 1999). In addition, atmospheric deposition of soluble Fe to the ocean can stimulate primary productivity and enhance the carbon uptake, consequently affecting the carbon budget and climate (e.g., Jickells et al., 2005). As a consequence, Icelandic dust contributes to the instantaneous radiative forcing (IRD) in the Artic (Kylling et al., 2018), and may influence the biogeochemical processes in the sub polar North Atlantic Ocean, which is seasonally Fe limited (Arnalds et al., 2014).

Icelandic dust scavenges effectively SO_2 and can possibly participate in a variety of heterogeneous reactions in the atmosphere, and thus influence the chemical balance of the atmosphere (Urupina et al., 2019). Icelandic dust is also a potential source of ice nucleating particles (Paramonov et al., 2018). The increase in ice nucleating particles may shorten the lifetime and lower the albedo of mixed-phase clouds (Vergara-Temprado et al., 2018), which have a significant impact on the energy budgets in the Arctic region (Boucher et al., 2013).

However, our knowledge on the chemical and mineralogical composition of Icelandic dust is very limited, which prevents us to provide a more realistic estimation on their local and regional impacts.

Here we determine the chemical and mineralogical composition of Icelandic dust from major dust source areas. In particular, we focus on the Fe speciation as it determines the light-absorption properties in the shortwave spectrum. The fractional Fe solubility of Icelandic dust is also determined. The Icelandic dust composition and Fe solubility are compared to northern African and Asian dust. The potential direct radiative effect and the implications for the primary productivity in the North Atlantic Ocean are also discussed.

4.3 Materials and methodology

4.3.1 Sample collection and experimental setup

Surface sediment samples were collected from five major dust hotspots in Iceland: D3 (Dyngjusandur), H55 (Hagavatn), Land1 (Landeyjarsandur), Maeli2 (Mælifellssandur), MIR45 (Myrdalssandur), which

are shown in Figure 4.1. The coordinates of the sampling sites are reported in Table S1 in the supporting information. A comprehensive description of the sites is given in Arnalds (2010) and Arnalds et al. (2016). These extensive areas (10–140 km^2) are subjected to intensive aeolian erosion due to frequent dust storms, and significantly contribute to the total dust emissions from Iceland, which is on the order of 30–40 million tons per year (Arnalds et al., 2016).

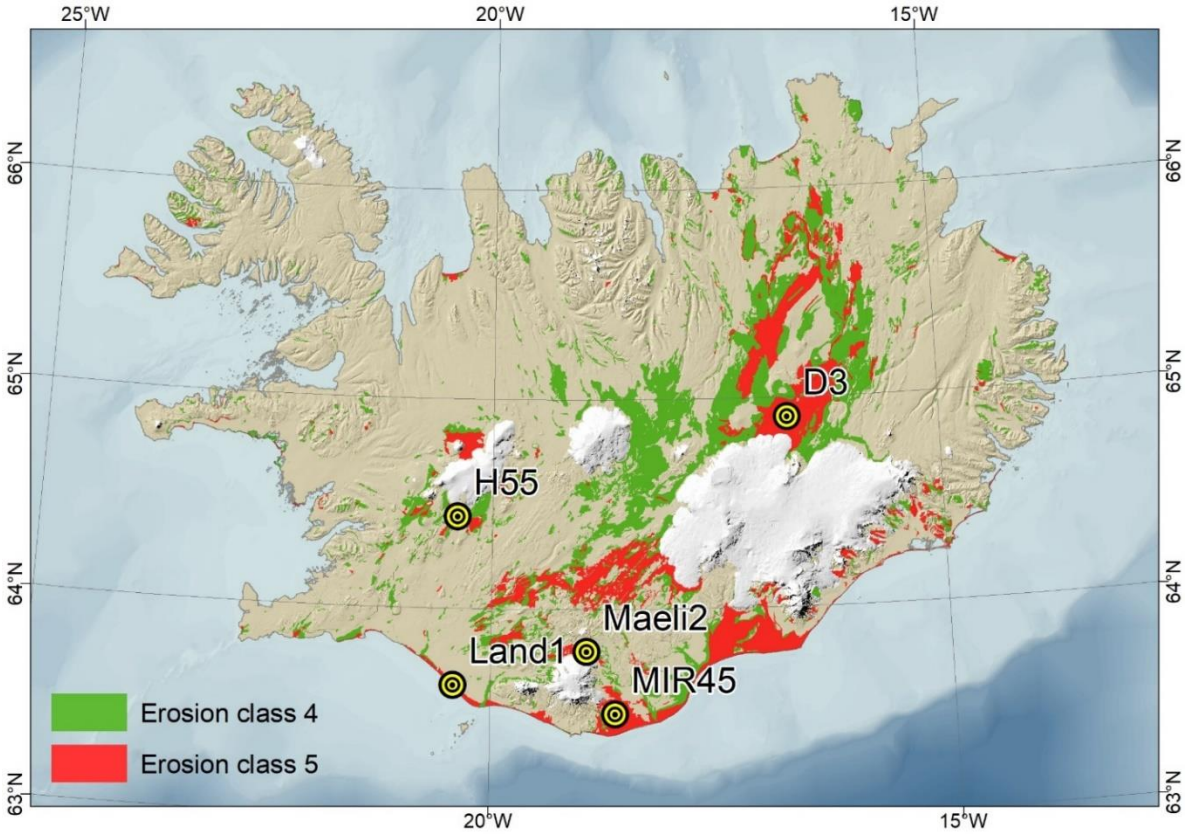

Figure 4.1: Surface sediment sampling sites and major dust hotspots. D3, Dyngjusandur hotspot; H55, Hagavatn hotspot; Land1, Landeyjarsandur; Maeli2, Mælifellssandur; MIR45, Myrdalssandur. In green, the unstable sandy areas. In red, the very unstable sandy areas.
Note: Map prepared by Ólafur Arnalds using data created and owned by him at the Agricultural University of Iceland, older works (database housed by the Agricultural University of Iceland).

In order to obtain dust particles which are representative of the particles emitted into the atmosphere, we re-suspended the surface sediment samples in atmospheric chambers and collected the PM_{10} and PM_{20} fractions (particulate matter with aerodynamic diameter < 10 µm and < 20 µm, respectively).

The PM_{10} samples were used for offline composition and mineralogy analyses. PM_{10} was collected using a custom-made reactor schematically represented in Figure S1. The method in Di Biagio et al. (2017)

was adopted to generate dust particles, allowing for the realistic generation of dust aerosols from parent soils. Firstly, the sediment samples were sieved to < 1 mm to remove the non-erodible fraction. 15 g of sediments were placed in a Büchner flask and flushed with pure nitrogen for 10 minutes to eliminate gaseous contamination and residual water vapor. The sample was then shaken for 5 minutes at 70 Hz on a sieve shaker (Retsch AS200) and injected in a glass manifold of approximately 1 L by nitrogen gas at 10 L min^{-1}, while the air was pumped at a flow rate of 30 L min^{-1} into a PM_{10} sampling head (custom-made). The PM_{10} fraction was collected on 0.4 µm polycarbonate filters and transferred into centrifuge tubes. The system was manually cleaned prior to each loading and flushed for 5 minutes with pure nitrogen to ensure an initial particle-free environment.

The PM_{20} fraction was collected using the large-scale atmospheric simulation chamber, CESAM (French acronym for Experimental Multiphasic Atmospheric Simulation Chamber) (Wang et al., 2011). The CESAM simulation facility, made of stainless steel, consists in a 4.2 m^3 multi-instrumented environmental chamber which allows to measure the size distribution and the optical properties of the generated dust aerosols while collecting filter samples for offline analysis (Di Biagio et al., 2017; 2019). Dust particles were generated with the sieve shaker (Retsch AS200) using the same protocol as for the small reactor as in Di Biagio et al. (2017), and injected in the CESAM chamber by flushing a Büchner flask with nitrogen gas carrier at 10 L min^{-1} for 10 minutes. The dust aerosol injected in CESAM was left suspended for about 10 minutes to allow the particle mass concentration inside the chamber to become spatially uniform. Dust particles corresponding to approximately the PM_{20} fraction were extracted from the chamber using custom-made filter samplers as in Caponi et al. (2017). Particles were collected by filtration on 0.4-µm pore size polycarbonate filters of 37 mm diameter at 7 L min^{-1} for approximately 1 hour. The residence time of particles in the chamber depends on their size. As shown in Di Biagio et al. (2017), particles larger than 1 µm have a lifetime of 20-30 minutes, while the lifetime of particles smaller than 1 µm can exceed a day. A second filter sample was collected subsequently to the first one to verify if the chemical composition of the dust was dependent on size. No significant difference was observed (not shown). The PM_{20} fraction was used for offline chemical analyses and to

investigate the relationship between chemical composition, size distribution, and optical properties of the aerosol dust, which will be the subject of a future paper.

4.3.2 X-ray diffraction (XRD) analysis

XRD was used to quantify the mineral phases present and to investigate the differences between the mineral fractions of dust aerosols (PM_{10}) and sediments. PM_{20} samples were not analyzed because the mass of dust particles collected from CESAM was not sufficient for the XRD analysis. This is because the mass concentrations in the CESAM chamber is much lower compared to the custom-made reactor used for the PM_{10} collection. The analysis was carried out at the Université de Paris, Plateforme RX UFR de Chimie, using a Panalytical Empyrean powder diffractometer equipped with a PIXcel detector fitted with a Cu anode tube (Kα1 = 1.5406 Å) operating at 45 kV and 40 mA. Diffractograms were recorded in the 5°–60° 2θ range. The samples were placed on a flat silicon monocrystalline wafer, which was loaded on the sample holder, a reflection spinner (1 s rotation time). The mineral identification was performed in Highscore Plus 3.0 (Degen et al., 2014) using the ICSD-Pan (Inorganic Crystal Structure Database) and COD (Crystallography Open Database) databases. The quantitative analysis of the mineral phases was conducted in MAUD (Material Analysis Using Diffraction). MAUD is an XRD program based on the Rietveld refinement method, which uses least square procedures to minimize the differences between the observed and calculated diffractograms (Lutterotti et al., 1999). The phase files identified with Highscore Plus were loaded as references in MAUD. It is also possible to determine the proportion of amorphous phase with the Rietveld method (Lutterotti et al., 1998). Augite was chosen as reference for the amorphous phase, having an Fe content close to MIR45, which is the samples with largest proportion of amorphous glass. The Rietveld model refines n -1 phases. As the total is fixed to100, the last phase results from the subtraction of the sum of the n refined phases. The analytical uncertainty is estimated by the software for the refined phases and represents the lower limit of the uncertainty of the proportion of each identified mineral phase.

The quality of the fitting was evaluated considering the χ^2 calculated by the model close to one, and by comparing visually the observed and calculated diffractograms to achieve a realistic chemical model (Toby, 2006). Small χ^2 values can be obtained when a large percentage of the intensity comes from the background (Toby, 2006). For example, the estimated χ^2 for H55 is relatively high (2.3-3.8) primarily due to missing minor mineral phases. However, H55 has the lowest fraction of amorphous material and compared to the other samples having χ^2 values very close to one, its diffraction intensities are considerably higher than the background signal.

4.3.3 X-ray fluorescence (XRF) analysis

PM_{10} and PM_{20} were analyzed by wavelength-dispersive X-ray fluorescence (WD-XRF) to determine the elemental composition of the dust aerosols. The WD-XRF analyses were performed using a PW-2404 spectrometer by Panalytical available at LISA. Excitation X-rays are produced by a Coolidge tube (I_{max} = 125 mA, V_{max} = 60 kV) with a Rh anode. The primary X-ray spectrum is controlled by inserting filters (Al, at different thickness) between the anode and the sample. Each element was analyzed three times, with specific conditions (voltage, tube filter, collimator, analyzing crystal and detector), lasting 8 to 10 s.

Data were collected for 24 elements (Cl, S, Ca, Fe, Na, Mg, Al, Si, P, K, Ti, Mn, Zn, Cr, V, Ba, Co, Cu, Nd, Ni, Sr, Cd, As, Pb) using the SuperQ software. The elemental mass thickness (μg cm^{-2}), which is the analyzed elemental mass per unit surface, was obtained by comparing the sample X-ray yields with those measured in the same geometry on a set of certified XRF calibration standards (Micromatter ™). The uncertainty of the measured elemental concentrations is around 10% (Caponi et al., 2017).

Data are reported as weight percentage of element oxides (wt%) calculated by dividing the elemental oxide mass (μg) by the total mass on filter (μg). The elemental mass on filter (μg) was first determined multiplying the measured mass thickness by the ratio between the analyzed surface area and the collection area, then converted into elemental oxide mass. The total mass on filter was calculated as the sum of the mass of the oxides of the major crustal elements reported in Table 4.1. Fe is assumed to be

as Fe_2O_3. We recognize that Fe(II) and Fe(III) can be found in the mineral phases (e.g., magnetite, augite) and in the amorphous glass, but the Fe(II)/Fe(III) ratio is not known.

In the XRF analysis, the concentration of light elements (atomic number Z < 19), such as Si and Al, can be underestimated due to the self-absorption of the emitted fluorescence X-Ray in the individual particles when these exceed approximately 1 μm in diameter. This is problematic when comparing elemental ratios such as Fe/Al (Formenti et al., 2010). In this study, the concentrations of light-weight elements were corrected for self-attenuation effects according to Formenti et al. (2010).

4.3.4 Chemical weathering index

The degree of chemical weathering of Icelandic dust was calculated based on the elemental composition. This is important to evaluate the presence in the samples of secondary minerals such as clays. The chemical index of alteration (CIA) (Nesbitt and Young, 1984) was considered most suitable for the present datasets based on the chemical compositions. The CIA is interpreted as a measure of the degree of weathering of aluminum silicate minerals, (in particular feldspars) into clay minerals. In this study, the CIA was calculated according to Price and Velbel (2003) using the molecular proportion of the element oxides which were obtained by dividing the weight percentage of each oxide by the molecular weight of the oxide:

$$\mathrm{CIA} = \frac{\mathrm{Al_2O_3}}{\mathrm{Al_2O_3} + \mathrm{CaO} + \mathrm{Na_2O} + \mathrm{K_2O}} \times 100 \quad (1)$$

CIA ≤ 50 represents the optimum fresh value, while 100 is the optimum weathered value. The CIA uncertainty was estimated using the error propagation formula and is ~14%.

4.3.5 X-ray absorption near edge structure (XANES) analysis

To examine qualitatively the Fe speciation in the dust samples, XANES spectra at the Fe K-edge were collected at the Diamond Light Source beamline I18. A Si(111) double-crystal monochromator was used in the experiments. The beam size was 400 × 400 μm^2. The XANES spectra were collected from 7000

to 7300 eV at a resolution varying from 0.2eV for 3 sec in proximity of the Fe K-edge (7100-7125 eV) to 5eV for 1 sec from 7100-7300eV. Powder samples were suspended in methanol and deposited on kapton® tape. Filter samples were loaded without prior preparation. The analysis was repeated three times. We measured the XANES spectra of PM_{20} fractions and mineral standards, including hematite and goethite standards, magnetite, feldspar standards (Clay Mineral Society), natural pyroxene and olivine. Data were processed using the Athena program, part of the software package Demeter (ver. 0.9.26) (Ravel and Newville, 2005). For comparison, we also collected the XANES spectra for mineral dust from western Sahara and Mali (Shi et al., 2011b).

4.3.6 Sequential extractions

Sequential extractions of Fe were used to determine the content of Fe oxides in the PM_{10} fractions. The samples were suspended in an ascorbate solution buffered at pH 7.5 to extract highly reactive amorphous Fe oxide-hydroxide (FeA) (Raiswell et al., 2008; Shi et al., 2011b; Shi et al., 2009). The ascorbate extractant was prepared by mixing a deoxygenated solution of 50 g L^{-1} sodium citrate and 50 g L^{-1} sodium bicarbonate, with 10 g L^{-1} ascorbic acid. 30 mg of dust was leached in 10 ml of ascorbate extractant continuously mixed for 24 hours. The solution was then filtered through 0.2 μm membrane filters. The residue was subsequently suspended in a dithionite solution (50 g L^{-1} sodium dithionite in 0.35 M acetic acid and 0.2 M sodium citrate) buffered at pH 4.8 for 2 hours to extract crystalline Fe oxide-hydroxide, mainly goethite and hematite (FeD).

The dithionite-oxalate sequential extraction was performed to determine the content of iron associated to magnetite (FeM) in the samples (Poulton and Canfield, 2005). First, the dust particles were treated for 2 hours with the citrate-buffered dithionite solution to remove crystalline Fe oxide-hydroxide. After filtration, the residue was leached for 6 hours in a solution of 0.2 M ammonium oxalate and 0.17 M oxalic acid at pH 3.2.

All the experiments were conducted at room temperature, in darkness. The sample solutions were continuously mixed on a rotary mixer, and then filtered through 0.2 μm membrane filters. The dissolved

Fe concentration in the filtrates was measured using the ferrozine method (Viollier et al., 2000) and ICP-OES analysis for the solution containing oxalate. Each experiment was repeated 3 times. The range of relative standard deviations (rsd) for each extract for each site are: FeA, 2-18%; FeD, 1-11%; FeM, 2-15%, which have been considered as the measurement uncertainty.

4.3.7 Fe solubility and dissolution kinetics

The initial Fe solubility (Fe_{isol}) of PM_{10} fractions was determined by extraction in 1.1 M ammonium acetate solution at pH 4.7 following the method in Baker et al. (2006). About 1 mg of dust was weighed on polycarbonate filters and leached for 2 hours in 10 ml of ammonium acetate solution. The solution was then filtered through 0.2 μm membrane filters and acidified to pH 2 before storage. Three replicates were performed for each sample, rsd 3-12%.

The potential Fe solubility (Fe_{psol}) was assessed through leaching experiments in sulfuric acid solution at pH2. Around 1.5 mg of dust were weighed on polycarbonate filters and leached in 50 ml of pH 2 sulfuric acid for 72 hours to simulate atmospheric acid processing similar to the method in Shi et al. (2011a, 2015). The solution was continuously stirred in darkness at room temperature. 0.5 ml of sample solution was collected at fixed time intervals (2.5 min, 15 min, 60 min, 2 hours, 6 hours, 24 hours, 48 hours and 72 hours after the dust sample was added) and filtered through 0.2 μm syringe filters into 1 ml centrifuge tubes. Dissolution kinetics of a dust sample from Africa (Libya) showed a very good repeatability with a relative standard deviation at each sampling time ranging from 4-15%.

All the experiments were conducted at room temperature, in darkness. The sample solutions were continuously mixed on a rotary mixer. The dissolved Fe concentration was measured using the ferrozine method (Viollier et al., 2000).

4.3.8 Volume average refractive index

The volume average refractive index was calculated to evaluate the effect of the dust compositions on the optical properties. Using the volume average refractive index, we assume that the mineral phases in

the dust samples are internally mixed, which can be different from the real conditions and may overestimate absorption (Formenti et al., 2014b):

$$\tilde{n}(\lambda) = \sum_{j} f_j \times n_j(\lambda) \quad (2)$$

where $f_j = \frac{v_j}{v_{tot}}$ is the volume fraction of individual j minerals in the dust samples, and n_j is the corresponding refractive index. The mineral volumes V_j (cm^3) are calculated as:

$$V_j = \frac{m_j}{\rho_j} \quad (3)$$

where $m_j = w_j \times m_{tot}$ is the mineral mass (g), w_j is the mineral mass fraction, m_{tot} is the total mass of the sample (g), and ρ_j is the mineral density (g cm^{-3}). The mineral mass fractions were obtained combining the content of the silicate minerals and glass from the XRD analysis with the contents of FeM and FeD in PM_{10}. The total mass is calculated as the sum of the element oxides mass from the XRF measurements. The densities of the crystalline phases are from http://webmineral.com/ (last access: 2 January 2020). The density of the amorphous glass was estimated for each sample as:

$$\rho_{glass} = \frac{\rho_{dust} - \sum_j w_{jCR} \times \rho_{jCR}}{w_{glass}} \quad (4)$$

where ρ_{dust} is the density of the sample, ρ_{jCR} and w_{jCR} are respectively the density and the mass fraction of the crystalline phases, while w_{glass} is the mass fraction of glass. The density of the samples (fraction <63 µm) was measured by a He-pycnometer and varied from 2.80 to 3.1 g cm^{-3}.

The volume average refractive index was calculated at selected wavelength (470 nm, 520 nm, 590 nm, and 660 nm). The reference complex refractive indices of the individual minerals are reported in Table S2, when necessary, the original data were interpolated at the selected wavelengths. Since it was

not possible to separate the relative contribution of hematite and goethite, we assumed two extreme scenarios: FeD = goethite, FeD = hematite. For hematite, we consider two reference complex refractive from Bedidi and Cervelle (1993) and Longtin et al. (1988) as in Formenti et al. (2014b). Also for magnetite we used two different reference indices from Querry (1985) and from Huffman and Stapp (1973).

4.4 Results

4.4.1 Elemental composition

Table 4.1 shows the results of the XRF analysis and includes also relevant elemental ratios. The PM_{10} fractions collected using the custom-made system and PM_{20} generated using CESAM have similar elemental composition (Figure S2). The difference between PM_{10} and PM_{20} in element oxide content > 1% including CaO, Fe_2O_3, Na_2O, MgO, Al_2O_3, SiO_2 and TiO_2 is within 16%. For Fe_2O_3, Al_2O_3, SiO_2 which are the major element oxides in the dust samples, the relative differences in content are <10%. The PM_{10} and PM_{20} fractions have basaltic compositions, like the parent material, with SiO_2 representing 46-52% of the total estimated mass, and the sum of the alkali oxides (Na_2O+K_2O) between 2% and 4% (see Figure S3 in the supporting information). Al_2O_3 ranges between 11% in MIR45 to 18% in H55. H55 has the lowest Si/Al ratio (2.3-2.4), while in the other samples Si/Al is 3.1-3.7. The content of Fe_2O_3 and TiO_2 is relatively high. Fe_2O_3 is 14-16% in H55 and D3, and 17-19% in Land1, Maeli2 and MIR45. The Fe/Al ratio is from 1 to 2.2. TiO_2 is around 2-3% in H55 and D3, and 2-5.5% in Land1, Maeli2 and MIR45. CaO is 6-9% in Land1, Maeli2 and MIR45, and 10-12% in H55 and D3. The Fe/Ca ratio is 1.2-1.4 in H55 and D3, and 2.1-2.8 in Land1, Maeli2 and MIR45. Compared to D3 and H55, Land 1, Maeli2 and MIR45 have more Fe and Ti (titanium) but less Ca.

Table 4.1: Elemental oxide mass percentages, chemical index of alteration (CIA), and relevant elemental ratios in PM_{10} (custom-made reactor) and PM_{20} (CESAM chamber).

Sample	Size	Element oxide mass wt%										CIA	Si/Al	Fe/Al	Ca/Fe
		CaO	Fe_2O_3	Na_2O	MgO	Al_2O_3	SiO_2	P_2O_5	K_2O	TiO_2	MnO				
D3	PM_{10}	11.6	16.3	2.3	4.9	13.7	47.5	0.2	0.5	2.7	0.3	35	3.06	1.58	1.38
H55	PM_{10}	12.4	15.1	1.9	5.1	16.9	46.0	0.1	0.2	2.2	0.2	39	2.41	1.19	1.19
Land1	PM_{10}	6.9	18.2	2.5	2.4	12.7	50.8	0.4	1.4	4.3	0.3	41	3.52	1.88	2.56
Maeli2	PM_{10}	8.5	18.4	2.4	3.9	12.7	47.7	0.3	0.9	4.9	0.3	38	3.31	1.92	2.13
MIR45	PM_{10}	8.6	18.8	2.6	4.0	11.4	47.4	0.4	0.9	5.5	0.4	35	3.68	2.18	2.14
D3	PM_{20}	10.3	14.8	2.3	5.0	13.7	50.7	0.2	0.4	2.4	0.2	37	3.26	1.42	1.41
H55	PM_{20}	11.3	13.8	2.2	5.1	18.1	47.1	0.1	0.1	2.0	0.2	43	2.30	1.01	1.20
Land1	PM_{20}	5.8	16.8	2.9	2.8	13.6	52.2	0.5	1.2	4.0	0.3	45	3.39	1.63	2.82
Maeli2	PM_{20}	7.6	17.6	2.5	3.9	13.1	49.2	0.3	0.8	4.7	0.2	41	3.32	1.78	2.26
MIR45	PM_{20}	8.3	18.8	2.8	4.0	11.7	47.9	0.4	0.9	5.0	0.3	36	3.61	2.11	2.22

Note: The data uncertainty was estimated using the error propagation formula: ~12% for the elemental oxide mass percentage, ~14% for CIA and the element ratios.

4.4.2 Mineralogical composition

Table 4.2 reports the results of the XRD analysis. The mineralogy of Icelandic dust is compatible with the parent basaltic material. The mineral composition of PM_{10} is similar to the bulk sediments. In H55, the amorphous fraction is 8% in PM_{10} and 15% in the bulk sediments. This is significantly lower than the amorphous content observed in the rest of the samples, ranging from 60 to 90%. MIR45 has the highest proportion of amorphous glass, around 90%.

Ca-rich plagioclase (anorthite) and pyroxene (augite) are the dominant mineral phases. The content of plagioclase varies respectively from around 4% in MIR45 to 46% in H55, while pyroxene is between 4% in MIR45 and 30% in H55. Olivine (forsterite) is only present in Land1 at around 7%, and in H55 1.5-1.6%. K-feldspar (microcline) is also found in Land1 and H55, but the content of K-feldspar is higher in the PM_{10} fractions, around 9% in Land1 and 10% in H55, compared to the bulk sediments 3% and 1%, respectively. XRD analysis identified (titano)magnetite in all the samples (>1%), except for D3 (see Figures S4-S8 in the supporting information).

Table 4.2: Mineralogical composition of PM_{10} and sediments. Standard deviation (sd) of the identified mineral phases is estimated by the MAUD software, except for anorthite which is calculated using the error propagation formula.

Samples	Size	Anorthite wt% (sd)	Augite wt% (sd)	Forsterite wt% (sd)	Microcline wt% (sd)	Quartz wt% (sd)	Ti-Magnetite wt% (sd)	Glass wt% (sd)	χ^2
D3	PM_{10}	14.9 (0.9)	13.4 (0.2)	-	-	-	-	71.7 (0.9)	1.0
H55	PM_{10}	43.3 (1.7)	29.7 (0.4)	7.3 (0.3)	10.3 (0.6)	-	1.3 (0.1)	8.1 (1.5)	2.3
Land1	PM_{10}	16.1 (0.9)	6.7 (0.1)	1.6 (0.1)	8.7 (0.3)	0.6 (0.04)	1.7 (0.1)	64.6 (0.9)	1.0
Maeli2	PM_{10}	8.9 (1.2)	8.2 (0.2)	-	-	-	1.6 (0.1)	81.3(1.2)	0.9
MIR45	PM_{10}	3.6 (2.3)	3.6 (0.1)	-	-	-	1.1 (0.1)	91.7 (2.4)	0.8
D3	Sediments	13.0 (0.9)	11.1 (0.2)	-	-	-	-	75.9 (0.9)	1.0
H55	Sediments	46.1 (1.5)	29.7 (0.4)	6.5 (0.3)	1.3 (0.3)	-	1.2 (0.1)	15.2 (1.3)	3.8
Land1	Sediments	14.6 (1.1)	10.2 (0.3)	1.5 (0.2)	3.1 (0.2)	1.5 (0.1)	1.2 (0.1)	68.1 (1)	1.1
Maeli2	Sediments	9.3 (1.3)	7.1 (0.2)	-	-	-	1.4 (0.1)	82.2 (1.3)	0.8
MIR45	Sediments	4.3 (2)	4.1 (0.2)	-	-	-	1.7 (0.1)	89.9 (2)	0.8

4.4.3 Fe speciation

Figure 4.2 shows Fe phases in Icelandic dust from the sequential extractions. The total Fe (FeT) content is 10-13%, consistent with XRF analyses. The content of amorphous Fe (FeA/FeT) is 0.3-0.4% in MIR45 and H55, and around 1% in D3, Land1 and Maeli2. Dithionite Fe (FeD/FeT) is 1% in MIR45, 3-4% in D3 and H55, and about 6% in Land1 and Maeli2. Magnetite (FeM/FeT) is 7-8% in Land1 and MIR45, and around 13-15% in D3, H55 and Maeli2. About 80-90% of Fe is contained in other phases including minerals and amorphous glass.

The Fe K-edge XANES spectra of Icelandic dust have some common features (Figure 4.3). In the pre-edge region, there is a main peak around 7114.4 eV and a second less intense peak around 7112.7 eV. In the edge region, a main peak is observed around 7131.9 eV, but in H55 it is slightly shifted to 7131.4 eV. The presence of large quantities of amorphous material makes the quantitative analysis of the XANES spectra challenging. The presence of two peaks at 7112.7 and 7114.4 in the pre-edge region suggests that Fe is present both as Fe^{2+} and Fe^{3+} (Wilke et al., 2001). This agrees with the fact that magnetite, pyroxene, and the glass phase contain Fe^{2+} and Fe^{3+}. The composition and Fe speciation of the amorphous glass varies in the different samples. H55 is the most crystalline samples (see above),

and its spectral features are similar to the pyroxene standard. For all the other samples, the glass fraction is dominant, and controls their spectral characteristics.

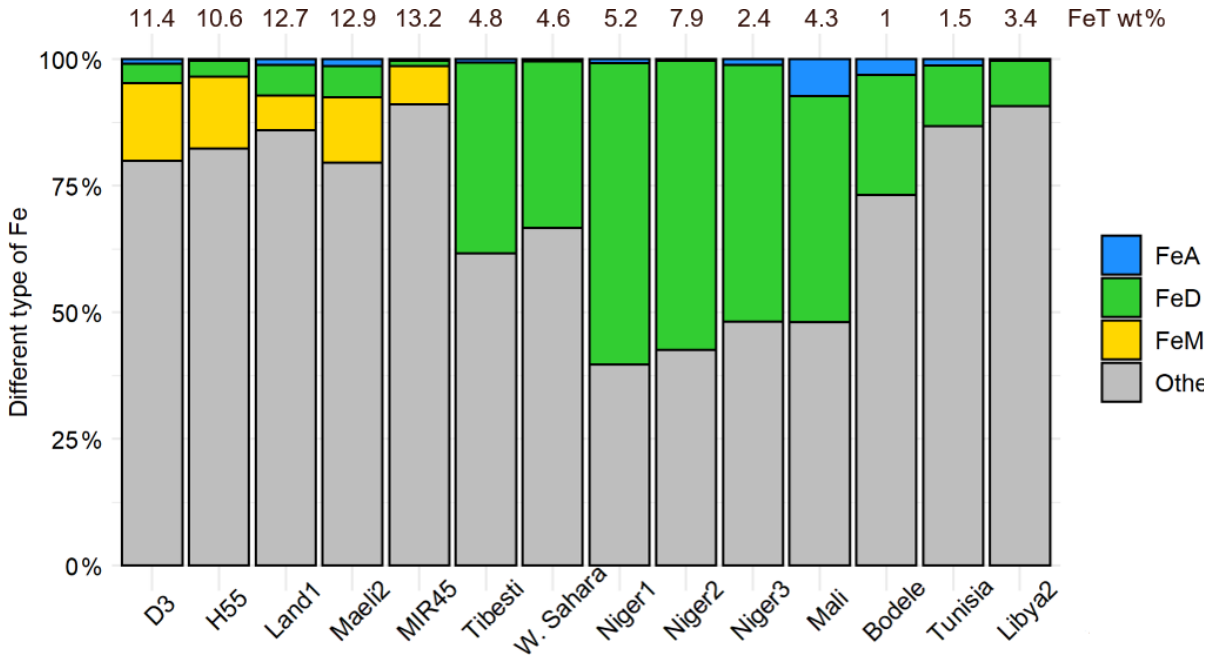

Figure 4.2: Percentages of ascorbate Fe (FeA), dithionite Fe (FeD), magnetite Fe (FeM) and other Fe to the total Fe (FeT) in Icelandic dust PM_{10} samples (this study) and African dust (Shi et al., 2011b). The data uncertainty was estimated using the error propagation formula: 12-22% FeA, 11-16% for FeD, 12-19% for FeM, ~11% for FeT. The original data are reported in Table S3 of the supporting information. Note that FeM was not measured in Shi et al. (2011b), but it is expected to be negligible in North African dust (Lazaro et al., 2008; Moskowitz et al., 2016).

4.4.4 Initial Fe solubility and dissolution kinetics

The initial Fe solubility (Fe_{isol}/FeT) is 0.08-0.2%, except in D3, which is as high as 0.6% (Figure 4.4). We assessed the Fe dissolution kinetic of Icelandic dust through leaching experiments in sulfuric acid at pH 2. Figure 4.5 shows a fast dissolution rate at the beginning, suggesting the release of Fe from highly reactive Fe phase. After 1-2 hours, the percentage of dissolved Fe increased at a slower rate, indicating that Fe solubilizes from more stable phases (Shi et al., 2011a). After 72 hour-leaching, the Fe solubility in D3 and Maeli2 was 30%, up to 2 times higher than what observed for the other Icelandic dust. The potential Fe solubility after 72 hours (Fe_{psol}/FeT) is around 13% in MIR45, 17% in H55 and Land1, 26% and 29% in Maeli2 and D3, respectively.

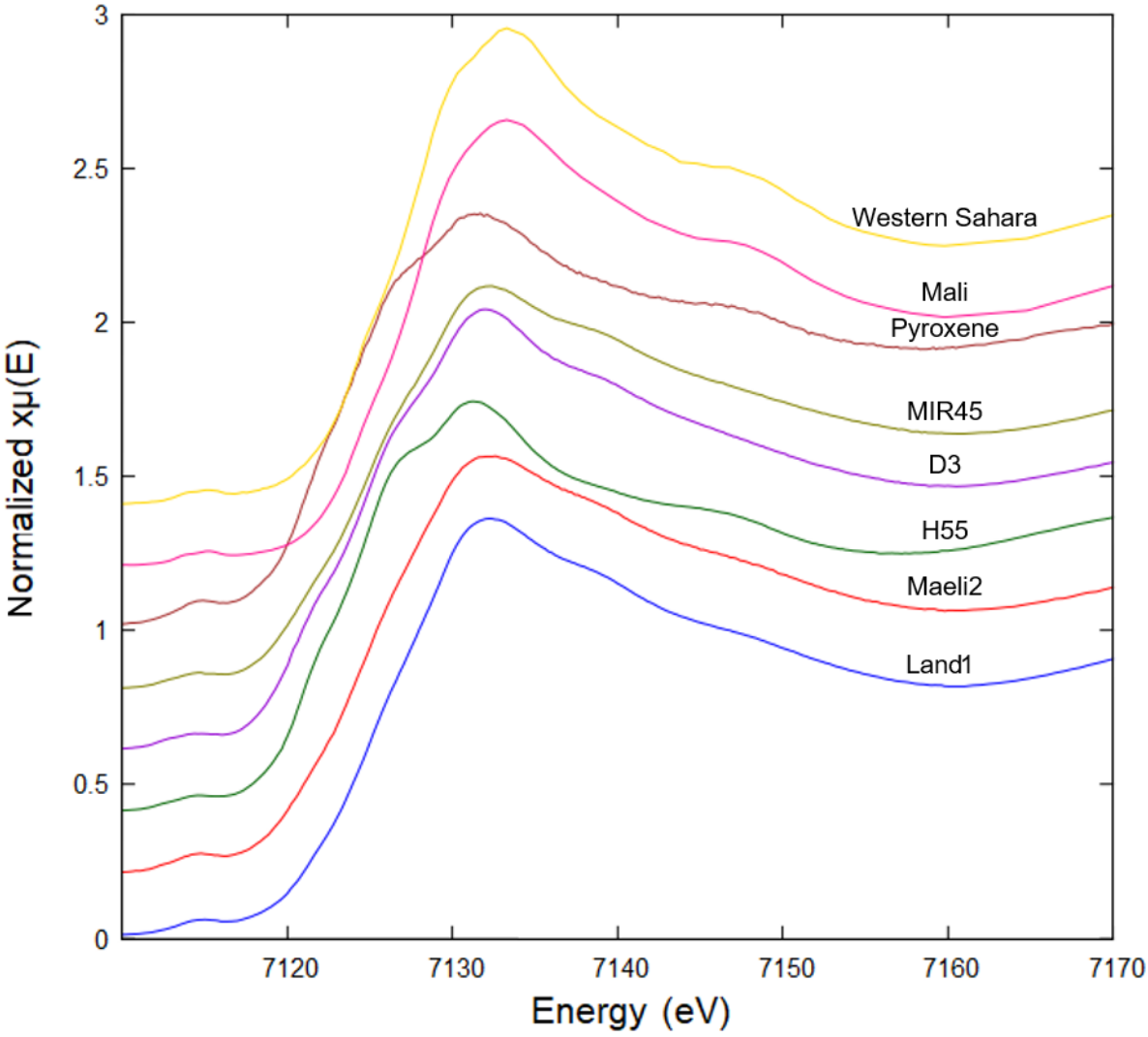

Figure 4.3: Fe Kedge XANES spectra of Icelandic Dust, natural pyroxene from Iceland, and African Dust. The Y-axis represents an arbitrary intensity.

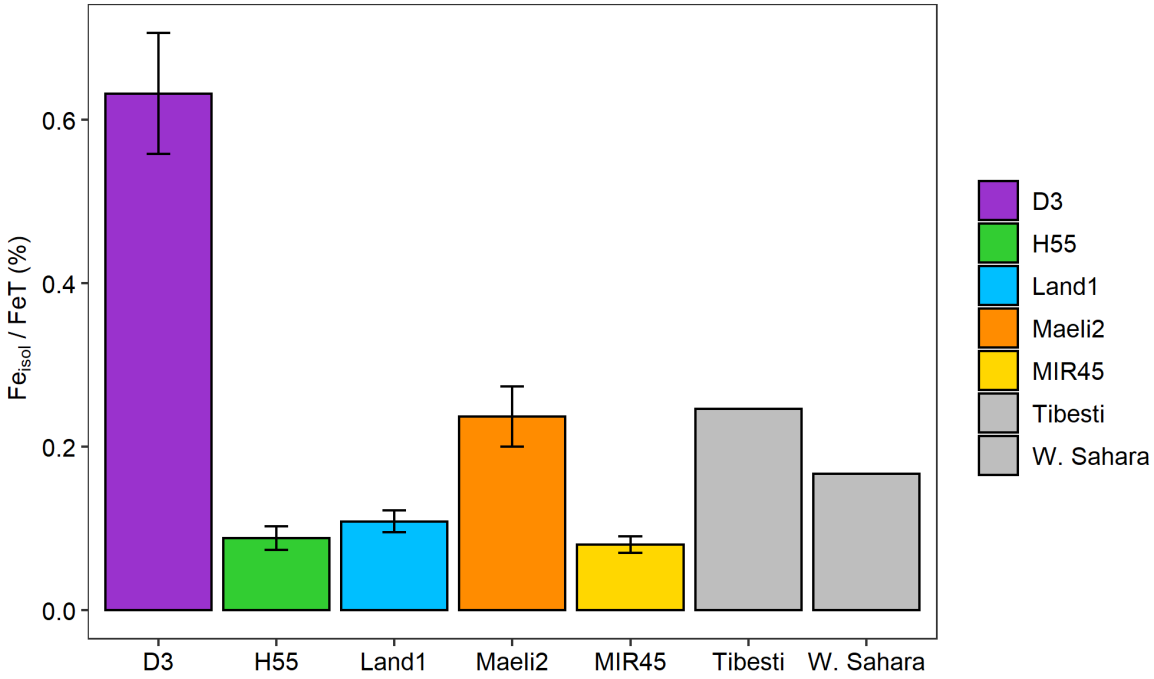

Figure 4.4: Initial Fe solubility (Fe_{isol} / FeT, %) of Icelandic dust (this study). The data uncertainty was estimated using the error propagation formula. Data for African dust samples (Tibesti and W. Sahara) were from Shi et al. (2011c).

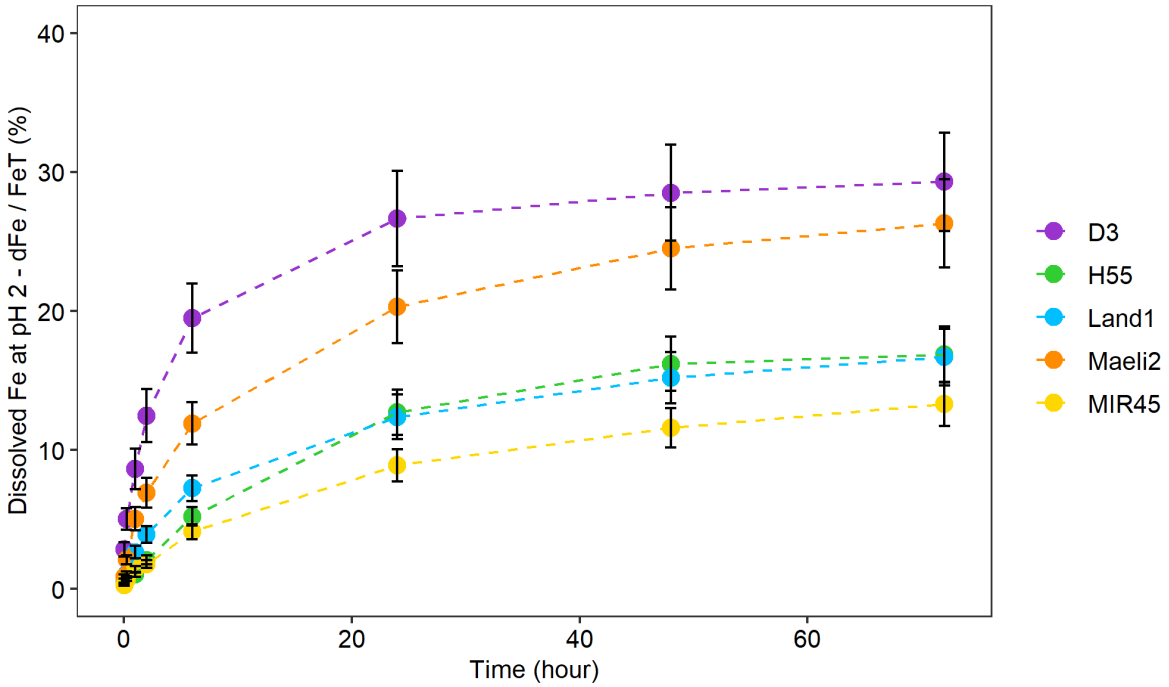

Figure 4.5: Fe dissolution kinetics at pH 2. The data uncertainty was estimated using the error propagation formula.

4.5 Discussion

Our data indicate that Icelandic dust has basaltic composition with relatively high Fe_2O_3 and TiO_2 content (Table 4.1, Figure S3). The principal crystalline mineral phases observed are Ca-rich plagioclase and pyroxene, while the amorphous fraction, mostly aluminosilicate glass, is 60-90% (except for the Hagavatn hotspot, which is only 15%). Glacial processes produce fine sediments (glacial flour), which accumulates into glacial-fluvial floodplains where the dust hotspots are located (Arnalds, 2010; Arnalds et al., 2016). Our results are consistent with the composition of the volcanic systems supplying the dust hotspots: Bárðarbunga and Kverkfjöll volcanic systems (Dyngjusandur), Katla volcanic system (Mýrdalssandur, Maelifellssandur and Landeyjasandur), Eldborgir and Skersli volcanic centers (Hagavatn) (Arnalds et al., 2016; Baratoux et al., 2011; Oladottir et al., 2008).

The large amorphous fraction found in Icelandic dust and in volcanic sandy deposits is related to the volcanic activity within glaciers (Baratoux et al., 2011). The rapid cooling of magma upon the interaction with water prevents crystallization and forms glass. Hyaloclastite deposits consisting of glass fragments are then eroded by the combined action of wind and glaciers. By contrast, sediments from the Hagavtan dust hotspots, at South of the Langjökull glacier, are from the glacial erosion of lava flows (Baratoux et al., 2011). This material is more crystalline than hyaloclastites as the rate of cooling of magma is relatively slower.

4.5.1 Mineralogical composition of Icelandic dust and parent sediments

Our results show that the mineralogical compositions of PM_{10} are similar to the bulk sediments from the five dust hotspots. Mineralogical fractionation is observed in African and Asian dust as a result of size segregation during emission (e.g., Claquin et al., 1999; Jeong, 2008). Quartz and K-feldspars are abundant in the soil silt fractions, while clay minerals are dominant in the clay fraction (Journet et al., 2014; Shi et al., 2005). Mineralogical fractionation is not evident in Icelandic dust, probably due to the low chemical weathering, and the lack of larger mineral grains such as quartz, K-feldspar, and clays. Only the more crystalline samples from Hagavatn showed some fractionation with respect to K-feldspar

and glass, while the sediments from the other sites are derived from the glacial abrasion of hyaloclastite and thus, they tend to be more uniform.

Dagsson-Waldhauserova et al. (2015) reported the composition of dust deposited on snow after a snow-dust storm in Reykjavik. Dust was transported from the Skeidararsandur and Hagavatn hotspots. About 75% of the dust particles were volcanic glass with basaltic composition. Dagsson-Waldhauserova et al. (2014b) investigated the composition of dust from the Mælifellssandur hotspot. The dust particles were primarily composed of basaltic glass (80 wt%). The main mineral phases included plagioclases (12 wt%), pyroxenes (4.6 wt%), and olivine (2 wt%). Volcanic deposits supplying the major dust hotspots Dyngjusandur, Hagavatn, Landeyjarsandur, Mælifellssandur, and Myrdalssandur has basaltic compositions and relatively high Fe content, over 10% (Baratoux et al., 2011; Oladottir et al., 2008). Basaltic glass is the major component (up to 90%) in sediments from Dyngjusandur, Mælifellssandur, and Myrdalssandur (Baratoux et al., 2011; Moroni et al., 2018). Baratoux et al. (2011) reported 10 wt% amorphous glass in volcanic sand from the Hagavatn hotspot area. Plagioclase, pyroxene and olivine are dominant minerals in sediments from Dyngjusandur, Hagavatn, Mælifellssandur and Myrdalssandur (Baratoux et al., 2011; Moroni et al., 2018). (Titano)magnetite has been also identified in dust and sediments (Baratoux et al., 2011; Dagsson-Waldhauserova et al., 2015; Dagsson-Waldhauserova et al., 2014b; Moroni et al., 2018; Oladottir et al., 2008)

The chemical and mineralogical compositions of Icelandic dust determined in this study are comparable to those of rocks and volcanic sands from the Dyngjusandur and Hagavatn areas (Baratoux et al., 2011). The mineral phases observed in the sediments from Dyngjusandur, Mælifellssandur, and Myrdalssandur are also similar to those reported by Moroni et al. (2018).

4.5.2 Comparison of Icelandic dust with northern African and Asian dust

In Icelandic dust the Si/Al ratio is 2.3-3.7 and the Fe/Al ratio is 1-2.2. In northern African and Asian dust, Si/Al ranges between 1 and 7 (Scheuvens and Kandler, 2014). Si/Al >10 is reported in dust from the Bodele depression, which originates from Si-rich diatomite deposits (Formenti et al., 2014b;

Scheuvens et al., 2013). In northern African dust, Fe/Al is mainly 0.4-0.8, with similar values reported for Asian dust (Formenti et al., 2011; Scheuvens and Kandler, 2014). Compared to northern African and Asian dust, Icelandic dust shows similar Si/Al, but higher Fe/Al ratio.

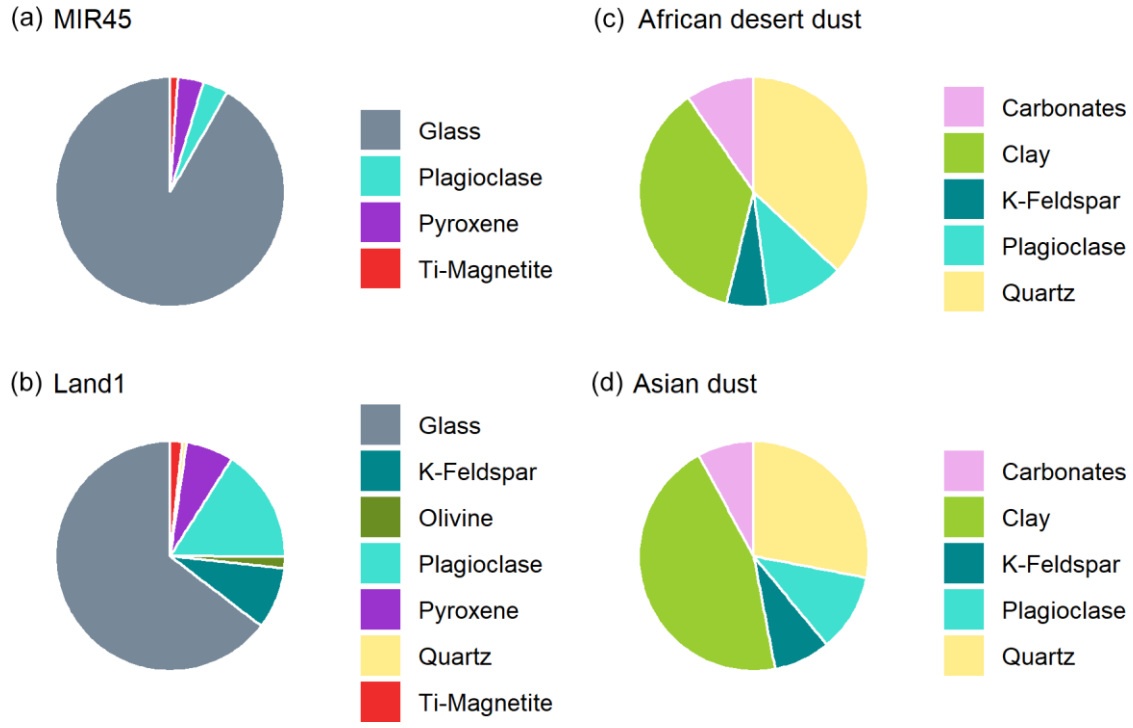

Figure 4.6: a-b) Mineralogy of Icelandic dust (MIR45 and Land1; PM10). c) Mineral composition of northern African desert dust (PM_{20}), representing the average bulk composition by X-ray diffraction of Tibesti, western Sahara, Niger and Mali samples (Shi et al., 2011b). d) Mineral composition of Asian dust (PM_{10}); average bulk composition by X-ray diffraction of dust from arid regions in Mongolia and northern China collected in Seoul (South Korea) during eight dust events in 2003–2005 (Jeong et al., 2008).

TiO_2 catalyzes heterogeneous photochemical reactions of atmospheric trace gases including SO_2, NO_2, VOC and O_3, and contributes to the chemical balance of the atmosphere (Chen et al., 2012). In northern African and Asian dust, TiO_2 is around 1% (e.g., Formenti et al., 2014b; Jeong, 2008; Shi et al., 2011b). In Icelandic dust, the element oxide concentration of Ti is relatively high 2-5.5%, although Ti can be not just as TiO_2 minerals (anatase and rutile). Ti may be present in magnetite and aluminosilicate minerals (e.g., augite) or in the amorphous glass.

A comparison of our results for the PM_{10} fraction to northern African desert dust (Shi et al., 2011b) and Asian dust (Jeong, 2008) is provided in Figure 4.6. The principal minerals in Icelandic dust are Ca-rich

plagioclase and pyroxene, with around 60-90% of aluminosilicate glass. The mineral composition of Icelandic dust is therefore very different from northern African dust or Asian dust that derives from very different environments, which are composed mainly of quartz, feldspars, calcite and clays (Avila et al., 1997; Formenti et al., 2014b; Jeong, 2008; Jeong et al., 2016; Kandler et al., 2009; Scheuvens et al., 2013; Shao et al., 2007; Shi et al., 2011b; Shi et al., 2005).

The Fe mineralogy of Icelandic dust also differs significantly from northern African and Asian dust (Figure 4.2). The total Fe content in Icelandic dust (10-13%) is higher than in northern African dust (1-8%). In northern African and Asian dust, Fe is primarily as clay minerals and Fe oxides (e.g., Formenti et al., 2014b; Lafon et al., 2006; Lu et al., 2017; Shi et al., 2011b; Takahashi et al., 2011); in particular, goethite is dominant among the crystalline Fe oxide-hydroxide (Formenti et al., 2014b; Lu et al., 2017). Icelandic dust has comparable amorphous Fe (FeA) content to northern African dust, but higher magnetite and lower goethite and hematite (FeD) content. Existing observations show that the magnetite content in African dust is generally below 0.1 wt% or not detectable (Lazaro et al., 2008; Moskowitz et al., 2016). Moskowitz et al. (2016) reported 0.6 wt% magnetite in surface sediments (PM_{63}) collected in proximity of the Tibesti volcanic based on magnetic measurements. The content of magnetite reported in Asian dust source regions is in the range 0.1-0.8 wt% from magnetitic measurements and XRD analysis (Jia et al., 2019; Maher et al., 2009; Song et al., 2014). Crusius et al. (2011) reported 0.2 wt% of magnetite in glacial dust from the Copper River Valley. In Icelandic dust, the magnetite content estimated from XRD measurements and sequential extractions is 1-2 wt%.

Magnetite and to a lesser extent hematite are common in magmatic rocks (Cornell and Schwertmann, 2003). Basalts have the highest magnetite content (Cornell and Schwertmann, 2003), which explains the high magnetite content in Icelandic dust. Hematite, goethite and ferrihydrite are more likely to form during weathering (Cornell and Schwertmann, 2003). Shi et al. (2011b) observed that the content of FeA and FeD in mineral dust from northern Africa was variable and dependent on the degree of weathering. The calculated CIA for Icelandic dust is below 50 (i.e., 35-45 in Table 4.1), indicating a

low degree of weathering. The dust hotspots in Iceland are characterized by the continuous input of material by glacial-fluvial processes that prevents the alteration of minerals and the formation of soil (Arnalds, 2015).

Figure 4.7 shows the variation of CIA against (FeA+FeD)/FeT for both Icelandic dust and northern African dust (Shi et al., 2011b). Icelandic dust is weakly weathered and has low CIA and (FeA+FeD)/FeT. By contrast, desert dust in northern Africa tends to be more weathered and consequently have higher CIA and (FeA+FeD)/FeT. Having plotted the data from Shi et al. (2011b) together with the data from this study, the positive correlation between CIA and (FeA+FeD)/FeT is maintained. In summary, our results are consistent with the findings in Shi et al. (2011b) and suggest that the low content of FeA and FeD observed in the samples is related to the low degree of weathering.

The XANES Fe Kedge spectra of Icelandic dust are also quite different from those of the northern African dust (Figure 4.3). The spectra of the two African samples (Western Sahara and Mali) have a clear double peak in the pre-edge region at around 7113.9 and 7115.2 eV, and a main peak in the edge region at around 7133.3 eV. This difference is consistent with the difference in Fe mineralogy reported above.

4.5.3 Factors controlling Fe solubility in Icelandic Dust

The initial fractional Fe solubility observed in mineral dust from northern Africa and Asia is generally below 0.5% (Desboeufs et al., 2005; Oakes et al., 2012; Schroth et al., 2009; Shi et al., 2011c). In this study, the initial Fe solubility (Fe_{isol}/FeT) of Icelandic dust is determined through ammonium acetate extraction at pH 4.7 (Baker et al., 2006), as in Shi et al. (2011c). Icelandic dust Fe_{isol}/FeT varies from 0.08-0.6%, which is comparable to Fe_{isol}/FeT in African dust (around 0.2%) in Shi et al. (2011c) (Figure 4.4).

Icelandic dust has similar origin to volcanic ash. Achterberg et al. (2013) observed an initial fractional Fe solubility of 0.04-0.14% for ash from the 2011 eruption of the volcano Eyjafjallajökull (leaching in

de-ionized water). Frogner et al. (2001) and Jones and Gislason (2008) reported relatively high initial fractional Fe solubility for ash from the 2000 eruption of the volcano Hekla, 2.5% for particle size 44-74 µm and 0.6% for particle size 45-125 µm (leaching in seawater). For the same volcano, Olgun et al. (2011) observed an initial fractional Fe solubility of 0.004% in the ash from the eruption in 1947 (leaching in seawater). The initial fractional Fe solubility of volcanic ash primarily depends on its surface properties determined by the eruption conditions, which can be very different from the bulk composition controlled by the source magma (Maters et al., 2017). The interaction of the ash with volcanic gases mainly HCl, SO_2 and HF within the eruption plume (plume processing) enhances the dissolution of the ash surface and the Fe mobilization (Ayris and Delmelle, 2012; Duggen et al., 2010). As the Fe speciation on the ash surface is determined by the eruption history, the Fe dissolution behavior can vary significantly, even for ash emitted from the same volcano (Maters et al., 2017). After deposition, the ash undergoes further processing, which modifies its surface properties, consequently the Fe speciation in freshly emitted ash may be different from the Icelandic volcanic dust. The range of initial fractional Fe solubility observed for volcanic ash from Iceland is quite large 0.004-2.5%. Although, both the volcanoes Hekla and Eyjafjallajökull have andesitic composition (e.g., Frogner et al., 2001; Olgun et al., 2011), the initial Fe solubility of Icelandic dust still lies within this range.

Icelandic dust is strongly influenced by glacial processes. The FeA and FeD content in Icelandic dust is similar to what was measured by Raiswell et al. (2016) in Ice-hosted sediments 0.03-0.2 wt% for FeA, and 0.04-0.7 wt% for FeD. Previous research investigated the initial fractional Fe solubility of dust from glacial sediments in the Copper River Valley, an important source of Fe for the Gulf of Alaska, which is Fe limited (Crusius et al., 2011; Schroth et al., 2017; Schroth et al., 2009). Glacial dust and sediments showed high initial fractional Fe solubility, which was associated to low degree of chemical weathering (Schroth et al., 2017; Schroth et al., 2009). The initial fractional Fe solubility reported for the glacial dust from the Copper River Valley is 1.4% (multiple leaches in Milli-Q water), 2-14 times higher than the initial Fe solubility observed for Icelandic dust. Mineralogy and Fe speciation control the Fe solubility in dust particles (Cwiertny et al., 2008; Fu et al., 2010; Journet et al., 2008; Schroth et al.,

2009; Shi et al., 2011a). Although different methods were used, leading to uncertainties when comparing the results (Meskhidze et al., 2016), the large differences in initial fractional Fe solubility observed between the Icelandic dust and the glacial dust from the Copper River Valley here is more likely due to the distinctive mineralogy and Fe speciation. Instead, measurements conducted on snow pits from the Roosevelt Island (Antarctica), reported similar initial fractional Fe solubility to the Icelandic dust samples, around 0.7% (dissolved Fe in snow melt) (Winton et al., 2016).

Icelandic dust composition is different from northern African and Asian dust, but they have similar initial Fe solubility. To better understand the factors controlling the Fe solubility in Icelandic dust we investigated the Fe dissolution kinetic at low pH. Icelandic dust showed a positive correlation between the potential Fe solubility (Fe_{psol}/FeT, defined as the fractional solubility after 72 hrs of dissolution at pH 2 sulfuric acid) and the content of pyroxene and magnetite, when the fraction of amorphous materials is significant (60-90%) (Figure S9 of the supporting information). But H55 weakens the overall correlation (Figure S9). This could be explained by the significantly higher degree of crystallinity (8-15%) observed in H55, which affects the reactivity and Fe speciation in the sample. The degree of crystallinity may directly impact the Fe solubility, as amorphous materials are generally more reactive than the crystalline forms with same composition (Wolff-Boenisch et al., 2006). However, there is no apparent correlation between the Fe_{psol} and the amorphous glass content, which was also observed for volcanic ash (Maters et al., 2017). This is because Icelandic dust consist of a mixture of crystalline minerals and glass, and the proportion of glass and its compositions vary in the different samples resulting in different solubility (Maters et al., 2017). The Fe minerals in Icelandic dust are mainly pyroxene and magnetite, and there is a minor contribution from olivine, hematite, goethite and ferrihydrite. Overall, the low degree of weathering and low crystallinity are responsible for the high potential Fe solubility in the samples.

Figure 4.8 shows that Icelandic dust Fe_{psol}/FeT is significantly higher than what was observed for intensively weathered desert dust such as Niger, Tibesti and Western Sahara (Shi et al., 2011b).

Fe_{psol}/FeT in D3 and Maeli2 is about 30%. In H55, Land1 and MIR45, Fe_{psol}/FeT is 13-16%, which is comparable to the African samples Bodele and Tunisia. These samples are from weakly weathered paleolake sediments. Adding all the new data in this study to the data from Shi et. al (2011b) generates an inverse relationship between the degree of weathering and Fe_{psol}/FeT (Figure 4.8), which is consistent with the finding in Shi et al. (2011b).

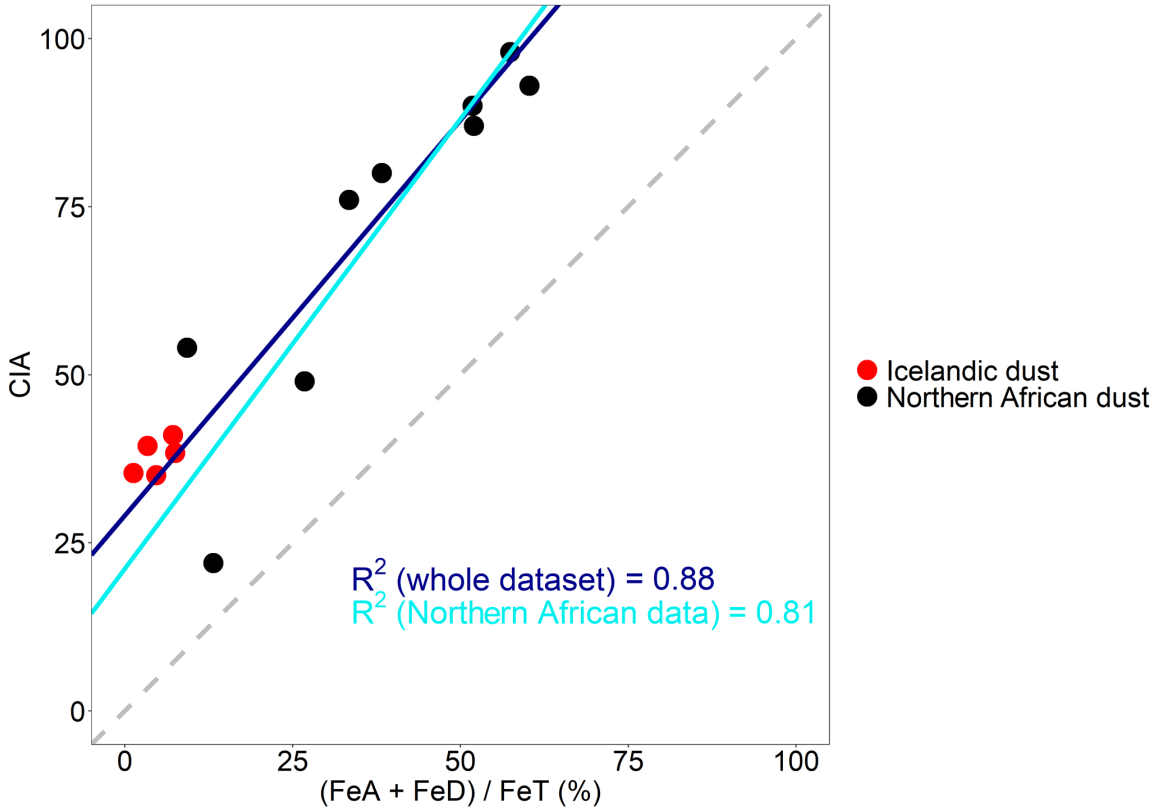

Figure 4.7: Correlation of the chemical index of alteration (CIA) with (FeA+FeD)/FeT (%) performed using the standard major axis regression. Data for African dust are from Shi et al. (2011b). The regression line in blue was calculated including the whole dataset: Icelandic dust (this study) and northern African dust (Shi et al., 2011b). The regression line in light blue was calculated using only the northern African dust data (Shi et al., 2011b).

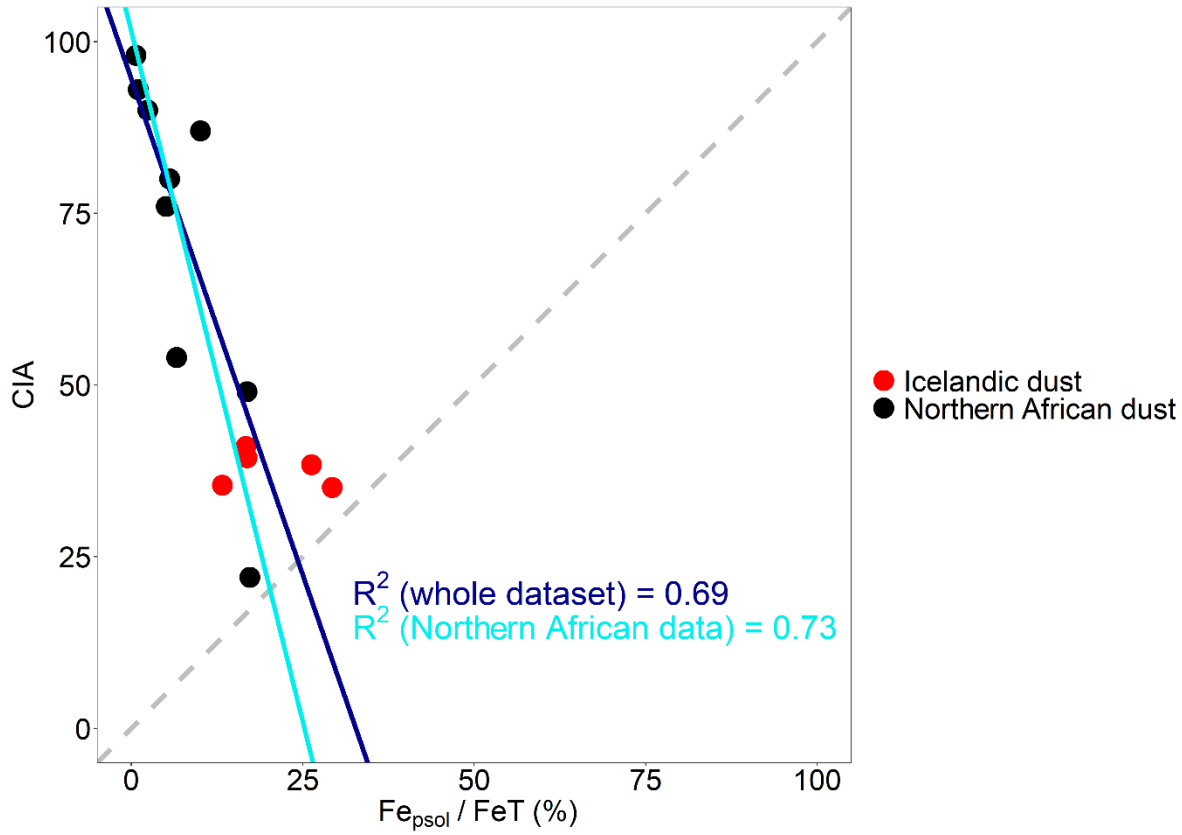

Figure 4.8: Correlation of the chemical index of alteration (CIA) with Fepsol/FeT (%) performed using the standard major axis regression. The regression line in blue was calculated including the whole dataset: Icelandic dust (this study) and northern African dust (Shi et al., 2011b). The regression line in light blue was calculated using only the northern African dust data (Shi et al., 2011b).

4.5.4 Implications for the soluble Fe deposition to the ocean

The sub polar North Atlantic Ocean including the Iceland Basin is seasonally Fe-limited (Moore et al., 2006; Nielsdottir et al., 2009; Ryan-Keogh et al., 2013). Achterberg et al. (2013) reported that deposition of volcanic ash from the 2010 Eyjafjallajökull eruption caused a significant perturbation to the biogeochemistry of the Iceland Basin. Elevated dissolved Fe concentration and nitrate depletion were observed locally followed by an early spring bloom (Achterberg et al., 2013). This suggests that additional Fe inputs to the sub polar North Atlantic Ocean has the potential to perturb the biogeochemical cycling of Fe and primary production in the surface ocean.

Here we calculated the deposition of soluble Fe to the North Atlantic Ocean based on the total Fe deposition estimated in Arnalds et al. (2014), which is 0.56-1.38 Tg yr^{-1}. The initial Fe solubility of Icelandic dust reported in this study varies from 0.08-0.2% for the dust hotspots in South and Central

Iceland to 0.6% for Dyngjusandur in NE Iceland. As 90% of the dust reaching the ocean is from the south coast of Iceland (Arnalds et al., 2014), a fractional Fe solubility of 0.13%, the average of the dust hotspots in South Iceland, is used in the calculation. The estimated soluble Fe deposition from Icelandic dust to the ocean is approximatively 0.73-1.79 Gg yr^{-1}. This suggests that Icelandic dust contributes to around 0.3-0.7 % of the global annual deposition flux of soluble Fe to the ocean (Myriokefalitakis et al., 2018).

4.5.5 Implications for the direct radiative effect

Kylling et al. (2018) estimated that in 2012 the instantaneous radiative forcing (IRF) of Icelandic dust in the Arctic was 0.02 W m^{-2} at the bottom of the atmosphere (BOA). They assumed the same optical properties for dust from different source regions, which is different from the real conditions. The mineralogical composition and the Fe speciation in Icelandic dust are different for examples from northern African and Asian dust (Figure 4.2, Table 4.2), leading to different spectral optical properties. Previous research investigated the absorption properties of volcanic sand deposited on snow, suggesting that the absorption properties of Icelandic dust from the Mýrdalssandur hotspot are similar to black carbon (Meinander et al., 2014; Peltoniemi et al., 2015). The spectral reflectance estimated for the pure volcanic sand was about 0.03, which is very similar to a black body (0.0) (Dagsson-Waldhauserova, 2014; Peltoniemi et al., 2015). Zubko et al. (2019) measured the complex refractive index of milled volcanic sand from the same area. The imaginary part of the complex refractive index (k), responsible for absorption, was 0.01 (λ = 647 nm), which is around one order of magnitude higher than the average values for natural dust from Sahel (0.002, λ = 660 nm), northern Africa-Sahara and Easter Asia (0.001, λ = 660 nm) (Di Biagio et al., 2019). In the shortwave spectrum, the k values reported in literature for volcanic ash from Iceland range from around 0.0001 to 0.02 (Ball et al., 2015; Bukowiecki et al., 2011; Derimian et al., 2012; Hervo et al., 2012; Reed et al., 2017; Rocha-Lima et al., 2014; Schumann et al., 2011; Toledano et al., 2012; Vogel et al., 2017; Weinzierl et al., 2012), which makes it difficult to evaluate the absorption properties of volcanic dust.

Here we present a first estimate of the complex refractive index of Icelandic dust based on the mineral volume fractions determined in this study. For the scenario assuming all FeD as hematite, the calculations were repeated using different reference refractive indices for hematite and magnetite, and four scenarios were considered. The real part of the volume-average refractive index (ñ) has an average value of 1.60 at the selected wavelengths consistently in the different scenarios. The imaginary part of the volume-average index ($\tilde{k}$) calculated using the refractive index of magnetite from Huffman and Stapp (1973) is up to one order of magnitude higher than when using the data from Querry (1985) (Table 4.3). No significant variations were observed applying the two different refractive indices for hematite (not shown). If using the data of magnetite from Querry (1985), $\tilde{k}$ showed little variations among the samples at the selected wavelengths, ranging from 0.001 to 0.003. While using the data from Huffman and Stapp (1973), $\tilde{k}$ generally decreased from 470 to 660 nm, and higher $\tilde{k}$ values were observed for D3, Maeli2 and H55 (0.006-0.01) compared to Land1 and MIR45 (0.004-0.006). Note that D3 has almost twice the magnetite content of Land1 and MIR45. Similar results are observed if assuming all FeD is goethite (Table 4.3). Overall, the estimated ñ and $\tilde{k}$ values are within the range of n and k reported for volcanic ash. The $\tilde{k}$ value of the dust samples from the Mýrdalssandur hotspot is 0.002-0.004 at λ = 660 nm which is 2-5 times lower than what observed in Zubko et al. (2019). The $\tilde{k}$ values estimated using the reference index of magnetite from Querry (1985) are comparable to the k values reported in Di Biagio et al. (2019) for Sahel, northern Africa-Sahara and eastern Asia. Using the magnetite refractive index from Huffman and Stapp (1973), the estimated $\tilde{k}$ values rise up to 12 times higher than the k of northern African and Asian dust from Di Biagio et al. (2019).

Our results indicate that magnetite can be a key factor contributing to the shortwave absorption of Icelandic dust, which is in agreement with the findings in Yoshida et al. (2016), who reported the presence of strongly light absorbing mineral in Icelandic dust which were identified as magnetite-like particles. Our analysis suggests that Icelandic dust may absorb solar radiation more than northern African and Asian natural dust, possibly leading to a stronger direct positive radiative effect in the Artic than the estimates by Kylling et al. (2018).

There is large uncertainty in the estimated volume-average refractive index, which is related to complex refractive index of the amorphous glass and Fe oxides (Zhang et al., 2015). In addition, the method used here may overestimate absorption as the mineral phases are considered internally mixed in the dust samples (Formenti et al., 2014b). Direct measurements are thus necessary to evaluate the optical properties of Icelandic dust, which will be reported in a separate manuscript.

Table 4.3: Estimated imaginary part of the volume average refractive index of Icelandic dust (PM_{10} fraction).

Assuming FeD = Hematite								
Samples	470 nm		520 nm		590 nm		660 nm	
	$\tilde{k}1$	$\tilde{k}2$	$\tilde{k}1$	$\tilde{k}2$	$\tilde{k}1$	$\tilde{k}2$	$\tilde{k}1$	$\tilde{k}2$
D3	0.010	0.002	0.009	0.002	0.008	0.002	0.007	0.002
H55	0.009	0.002	0.008	0.002	0.007	0.002	0.006	0.002
Land1	0.006	0.002	0.005	0.002	0.004	0.001	0.004	0.001
Maeli2	0.011	0.003	0.009	0.002	0.008	0.002	0.007	0.002
MIR45	0.006	0.001	0.006	0.001	0.005	0.001	0.004	0.002
Assuming FeD = Goethite								
Samples	470 nm		520 nm		590 nm		660 nm	
	$\tilde{k}1$	$\tilde{k}2$	$\tilde{k}1$	$\tilde{k}2$	$\tilde{k}1$	$\tilde{k}2$	$\tilde{k}1$	$\tilde{k}2$
D3	0.010	0.002	0.009	0.002	0.008	0.002	0.007	0.003
H55	0.009	0.001	0.008	0.002	0.007	0.002	0.007	0.002
Land1	0.005	0.001	0.005	0.002	0.005	0.002	0.004	0.002
Maeli2	0.010	0.002	0.009	0.003	0.008	0.003	0.008	0.003
MIR45	0.006	0.001	0.006	0.001	0.005	0.002	0.004	0.002

Note: The $\tilde{\mathbf{k}}1$ and $\tilde{\mathbf{k}}2$ values are calculated using two different complex refractive indices for magnetite, from Huffman and Stapp (1973) and Querry (1985), respectively. If assuming FeD is purely hematite, the data shown in the table are calculated using the data from Longtin et al. (1988).

4.6 Conclusions

In this study, we investigated the chemical composition and mineralogy of dust samples representative of five major dust hotspots in Iceland. Our results show that Icelandic dust is fundamentally different from low latitude dust. Icelandic dust has basaltic composition, and it is mainly composed of Ca-rich plagioclase, pyroxene, and amorphous glass. The amorphous materials account for 8% (Hagavatn dust hotspot) to 60-90% (Dyngjusandur, Landeyjarsandur, Mælifellssandur, Myrdalssandur hotspots) of total dust mass. Mineralogical fractionation was not observed between dust samples and sediments. Icelandic

dust has high magnetite content and low hematite and goethite (FeD) and amorphous Fe (FeA). The initial Fe solubility (pH 4.7) is 0.08-0.6 %. The low degree of weathering and low crystallinity are responsible for the high Fe solubility at low pH (up to 30%).

Here we provide a comprehensive dataset including chemical composition, mineralogy, Fe speciation and Fe solubility of Icelandic dust, which can be fed to global models to estimate the flux of atmospheric soluble Fe to the sub-Arctic and Artic Oceans and to assess the radiative effect of Icelandic dust. Our analysis suggest that the shortwave absorption properties of Icelandic dust are determined by the high magnetite content, possibly leading to a stronger direct positive radiative effect in the Artic than previous estimates. The original measurements of the spectral optical properties together with the size distribution conducted at CESAM will provide further insight on the absorption properties and long range transport of Icelandic dust, necessary to estimate the radiative impact of Icelandic dust and its contribution to the Arctic warming.

4.7 References

Achterberg, E. P., Moore, C. M., Henson, S. A., Steigenberger, S., Stohl, A., Eckhardt, S., Avendano, L. C., Cassidy, M., Hembury, D., Klar, J. K., Lucas, M. I., Macey, A. I., Marsay, C. M., and Ryan-Keogh, T. J.: Natural iron fertilization by the Eyjafjallajökull volcanic eruption, Geophys. Res. Lett., 40, 921-926, doi: 10.1002/grl.50221, 2013.

Arimoto, R.: Eolian dust and climate: relationships to sources, tropospheric chemistry, transport and deposition, Earth-Sci. Rev., 54, 29-42, doi: 10.1016/s0012-8252(01)00040-x, 2001.

Arnalds, O., Gisladottir, F. O., and Sigurjonsson, H.: Sandy deserts of Iceland: an overview, J. Arid Environ., 47, 359-371, doi: 10.1006/jare.2000.0680, 2001.

Arnalds, O.: Dust sources and deposition of aeolian materials in Iceland, Icel. Agric. Sci., 23, 3-21, 2010.

Arnalds, O., Olafsson, H., and Dagsson-Waldhauserova, P.: Quantification of iron-rich volcanogenic dust emissions and deposition over the ocean from Icelandic dust sources, Biogeosciences, 11, 6623-6632, doi: 10.5194/bg-11-6623-2014, 2014.

Arnalds, O.: The soils of Iceland, World Soils Book Series, Springer, Dordrecht, 2015.

Arnalds, O., Dagsson-Waldhauserova, P., and Olafsson, H.: The Icelandic volcanic aeolian environment: Processes and impacts — A review, Aeolian Res., 20, 176-195, doi: 10.1016/j.aeolia.2016.01.004, 2016.

Atkinson, J. D., Murray, B. J., Woodhouse, M. T., Whale, T. F., Baustian, K. J., Carslaw, K. S., Dobbie, S., O'Sullivan, D., and Malkin, T. L.: The importance of feldspar for ice nucleation by mineral dust in mixed-phase clouds, Nature, 498, 355-358, doi: 10.1038/nature12278, 2013.

Avila, A., QueraltMitjans, I., and Alarcon, M.: Mineralogical composition of African dust delivered by red rains over northeastern Spain, J. Geophys. Res.-Atmos, 102, 21977-21996, doi: 10.1029/97jd00485, 1997.

Ayris, P., and Delmelle, P.: Volcanic and atmospheric controls on ash iron solubility: A review, Phys. Chem. Earth, 45-46, 103-112, doi: 10.1016/j.pce.2011.04.013, 2012.

Baddock, M. C., Mockford, T., Bullard, J. E., and Thorsteinsson, T.: Pathways of high-latitude dust in the North Atlantic, Earth Planet. Sci. Lett., 459, 170-182, doi: 10.1016/j.epsl.2016.11.034, 2017.

Baker, A. R., Jickells, T. D., Witt, M., and Linge, K. L.: Trends in the solubility of iron, aluminium, manganese and phosphorus in aerosol collected over the Atlantic Ocean, Mar. Chem., 98, 43-58, doi: 10.1016/j.marchem.2005.06.004, 2006.

Ball, J. G. C., Reed, B. E., Grainger, R. G., Peters, D. M., Mather, T. A., and Pyle, D. M.: Measurements of the complex refractive index of volcanic ash at 450, 546.7, and 650nm, J. Geophys. Res.-Atmos, 120, 7747-7757, doi: 10.1002/2015jd023521, 2015.

Baratoux, D., Mangold, N., Arnalds, O., Bardintzeff, J. M., Platevoët, B., Grégoire, M., and Pinet, P.: Volcanic sands of Iceland - Diverse origins of aeolian sand deposits revealed at Dyngjusandur and Lambahraun, Earth Surf. Process. Landf., 36, 1789-1808, doi: 10.1002/esp.2201, 2011.

Bedidi, A., and Cervelle, B.: Light scattering by spherical particles with hematite and goethitelike optical properties: effect of water impregnation, J. Geophys. Res. -Solid Earth, 98, 11941-11952, doi: 10.1029/93JB00188, 1993.

Björnsson, H., and Palsson, F.: Icelandic glaciers, Jokull, 58, 365-386, 2008.

Boucher, O., Randall, D., Artaxo, P., Bretherton, C., Feingold, G., Forster, P., Kerminen, V.-M., Kondo, Y., Liao, H., Lohmann, U., Rasch, P., Satheesh, S., Sherwood, S., Stevens, B., and Zhang, X.-Y.: Clouds and aerosols, in: Climate change 2013: the physical science basis. Contribution of Working Group I to the Fifth Assessment Report of the Intergovernmental Panel on Climate Change, edited by: Stocker, T. F., Qin, D., Plattner, G.-K., Tignor, M., Allen, S. K., Doschung, J., Nauels, A., Xia, Y., Bex, V., and Midgley, P. M., Cambridge University Press, United Kingdom and New York USA, 571-657, 2013.

Bukowiecki, N., Zieger, P., Weingartner, E., Juranyi, Z., Gysel, M., Neininger, B., Schneider, B., Hueglin, C., Ulrich, A., Wichser, A., Henne, S., Brunner, D., Kaegi, R., Schwikowski, M., Tobler, L., Wienhold, F. G., Engel, I., Buchmann, B., Peter, T., and Baltensperger, U.: Ground-based and airborne in-situ measurements of the Eyjafjallajökull volcanic aerosol plume in Switzerland in spring 2010, Atmos. Chem. Phys., 11, 10011-10030, doi: 10.5194/acp-11-10011-2011, 2011.

Bullard, J. E., Baddock, M., Bradwell, T., Crusius, J., Darlington, E., Gaiero, D., Gasso, S., Gisladottir, G., Hodgkins, R., McCulloch, R., McKenna-Neuman, C., Mockford, T., Stewart, H., and Thorsteinsson, T.: High-latitude dust in the Earth system, Rev. Geophys., 54, 447-485, doi: 10.1002/2016rg000518, 2016.

Caponi, L., Formenti, P., Massabo, D., Di Biagio, C., Cazaunau, M., Pangui, E., Chevaillier, S., Landrot, G., Andreae, M. O., Kandler, K., Piketh, S., Saeed, T., Seibert, D., Williams, E., Balkanski, Y., Prati, P., and Doussin, J. F.: Spectral- and size-resolved mass absorption efficiency of mineral dust aerosols in the shortwave spectrum: a simulation chamber study, Atmos. Chem. Phys., 17, 7175-7191, doi: 10.5194/acp-17-7175-2017, 2017.

Carslaw, K. S., Boucher, O., Spracklen, D. V., Mann, G. W., Rae, J. G. L., Woodward, S., and Kulmala, M.: A review of natural aerosol interactions and feedbacks within the Earth system, Atmos. Chem. Phys., 10, 1701-1737, doi: 10.5194/acp-10-1701-2010, 2010.

Chen, H., Nanayakkara, C. E., and Grassian, V. H.: Titanium dioxide photocatalysis in atmospheric chemistry, Chem. Rev., 112, 5919-5948, doi: 10.1021/cr3002092, 2012.

Choobari, O. A., Zawar-Reza, P., and Sturman, A.: The global distribution of mineral dust and its impacts on the climate system: A review, Atmos. Res., 138, 152-165, doi: 10.1016/j.atmosres.2013.11.007, 2014.

Claquin, T., Schulz, M., and Balkanski, Y. J.: Modeling the mineralogy of atmospheric dust sources, J. Geophys. Res.-Atmos, 104, 22243-22256, doi: 10.1029/1999jd900416, 1999.

Cornell, R. M., and Schwertmann, U.: The Iron Oxides: Structure, Properties, Reactions, Occurrence and Uses, Wiley-VCH, New York 2003.

Crusius, J., Schroth, A. W., Gasso, S., Moy, C. M., Levy, R. C., and Gatica, M.: Glacial flour dust storms in the Gulf of Alaska: Hydrologic and meteorological controls and their importance as a source of bioavailable iron, Geophys. Res. Lett., 38, doi: 10.1029/2010gl046573, 2011.

Cwiertny, D. M., Baltrusaitis, J., Hunter, G. J., Laskin, A., Scherer, M. M., and Grassian, V. H.: Characterization and acid-mobilization study of iron-containing mineral dust source materials, J. Geophys. Res.-Atmos, 113, D05202, doi: 10.1029/2007jd009332, 2008.

Dagsson-Waldhauserova, P.: Variability, origin and physical characteristics of dust aerosol in Iceland (PhD dissertation), Faculty of Physical Sciences Agricultural University of Iceland, Reykjavik, 163 pp., 2014.

Dagsson-Waldhauserova, P., Arnalds, O., and Olafsson, H.: Long-term variability of dust events in Iceland (1949–2011), Atmos. Chem. Phys., 14, 13411-13422, doi: 10.5194/acp-14-13411-2014, 2014a.

Dagsson-Waldhauserova, P., Arnalds, O., Olafsson, H., Skrabalova, L., Sigurdardottir, G. M., Branis, M., Hladil, J., Skala, R., Navratil, T., Chadimova, L., Menar, S. V. O., Thorsteinsson, T., Carlsen, H. K., and Jonsdottir, I.: Physical properties of suspended dust during moist and low wind conditions in Iceland, Icel. Agric. Sci., 27, 25-39, 2014b.

Dagsson-Waldhauserova, P., Arnalds, O., Olafsson, H., Hladil, J., Skala, R., Navratil, T., Chadimova, L., and Meinander, O.: Snow–Dust Storm: Unique case study from Iceland, March 6–7, 2013, Aeolian Res., 16, 69-74, doi: 10.1016/j.aeolia.2014.11.001, 2015.

Degen, T., Sadki, M., Bron, E., König, U., and Nénert, G.: The highscore suite, Powder Diffr., 29, S13-S18, doi: 10.1017/S0885715614000840, 2014.

Derimian, Y., Karnieli, A., Kaufman, Y. J., Andreae, M. O., Andreae, T. W., Dubovik, O., Maenhaut, W., and Koren, I.: The role of iron and black carbon in aerosol light absorption, Atmos. Chem. Phys., 8, 3623-3637, doi: 10.5194/acp-8-3623-2008, 2008.

Derimian, Y., Dubovik, O., Tanre, D., Goloub, P., Lapyonok, T., and Mortier, A.: Optical properties and radiative forcing of the Eyjafjallajökull volcanic ash layer observed over Lille, France, in 2010, J. Geophys. Res.-Atmos, 117, D00U25, doi: 10.1029/2011jd016815, 2012.

Desboeufs, K. V., Sofikitis, A., Losno, R., Colin, J. L., and Ausset, P.: Dissolution and solubility of trace metals from natural and anthropogenic aerosol particulate matter, Chemosphere, 58, 195-203, doi: 10.1016/j.chemosphere.2004.02.025, 2005.

Di Biagio, C., Formenti, P., Balkanski, Y., Caponi, L., Cazaunau, M., Pangui, E., Journet, E., Nowak, S., Caquineau, S., Andreae, M. O., Kandler, K., Saeed, T., Piketh, S., Seibert, D., Williams, E., and Doussin, J. F.: Global scale variability of the mineral dust long-wave refractive index: a new dataset of in situ measurements for climate modeling and remote sensing, Atmos. Chem. Phys., 17, 1901-1929, doi: 10.5194/acp-17-1901-2017, 2017.

Di Biagio, C., Formenti, P., Balkanski, Y., Caponi, L., Cazaunau, M., Pangui, E., Journet, E., Nowak, S., Andreae, M. O., Kandler, K., Saeed, T., Piketh, S., Seibert, D., Williams, E., and Doussin, J. F.: Complex refractive indices and single-scattering albedo of global dust aerosols in the shortwave spectrum and relationship to size and iron content, Atmos. Chem. Phys., 19, 15503-15531, doi: 10.5194/acp-19-15503-2019, 2019.

Dordevic, D., Tosic, I., Sakan, S., Petrovic, S., Duricic-Milankovic, J., Finger, D. C., and Dagsson-Waldhauserova, P.: Can Volcanic Dust Suspended From Surface Soil and Deserts of Iceland Be Transferred to Central Balkan Similarly to African Dust (Sahara)?, Front. Earth Sci., 7, UNSP 142, doi: 10.3389/feart.2019.00142, 2019.

Dragosics, M., Meinander, O., Jónsdóttír, T., Dürig, T., De Leeuw, G., Pálsson, F., Dagsson-Waldhauserová, P., and Thorsteinsson, T.: Insulation effects of Icelandic dust and volcanic ash on snow and ice, Arab. J. Geosci., 9, 126, doi: 10.1007/s12517-015-2224-6, 2016.

Duggen, S., Olgun, N., Croot, P., Hoffmann, L., Dietze, H., Delmelle, P., and Teschner, C.: The role of airborne volcanic ash for the surface ocean biogeochemical iron-cycle: a review, Biogeosciences, 7, 827-844, doi: 10.5194/bg-7-827-2010, 2010.

Dumont, M., Brun, E., Picard, G., Michou, M., Libois, Q., Petit, J. R., Geyer, M., Morin, S., and Josse, B.: Contribution of light-absorbing impurities in snow to Greenland's darkening since 2009, Nat. Geosci., 7, 509-512, doi: 10.1038/ngeo2180, 2014.

Engelbrecht, J. P., Moosmuller, H., Pincock, S., Jayanty, R. K. M., Lersch, T., and Casuccio, G.: Technical note: Mineralogical, chemical, morphological, and optical interrelationships of mineral dust re-suspensions, Atmos. Chem. Phys., 16, 10809-10830, doi: 10.5194/acp-16-10809-2016, 2016.

Formenti, P., Nava, S., Prati, P., Chevaillier, S., Klaver, A., Lafon, S., Mazzei, F., Calzolai, G., and Chiari, M.: Self‐attenuation artifacts and correction factors of light element measurements by X‐ray

analysis: Implication for mineral dust composition studies, J. Geophys. Res.-Atmos, 115, D01203, doi: 10.1029/2009JD012701, 2010.

Formenti, P., Schutz, L., Balkanski, Y., Desboeufs, K., Ebert, M., Kandler, K., Petzold, A., Scheuvens, D., Weinbruch, S., and Zhang, D.: Recent progress in understanding physical and chemical properties of African and Asian mineral dust, Atmos. Chem. Phys., 11, 8231-8256, doi: 10.5194/acp-11-8231-2011, 2011.

Formenti, P., Caquineau, S., Chevaillier, S., Klaver, A., Desboeufs, K., Rajot, J. L., Belin, S., and Briois, V.: Dominance of goethite over hematite in iron oxides of mineral dust from Western Africa: Quantitative partitioning by X-ray absorption spectroscopy, J. Geophys. Res.-Atmos, 119, 12740-12754, doi: 10.1002/2014jd021668, 2014a.

Formenti, P., Caquineau, S., Desboeufs, K., Klaver, A., Chevaillier, S., Journet, E., and Rajot, J. L.: Mapping the physico-chemical properties of mineral dust in western Africa: mineralogical composition, Atmos. Chem. Phys., 14, 10663-10686, doi: 10.5194/acp-14-10663-2014, 2014b.

Frogner, P., Gislason, S. R., and Oskarsson, N.: Fertilizing potential of volcanic ash in ocean surface water, Geology, 29, 487-490, doi: 10.1130/0091-7613(2001)029<0487:Fpovai>2.0.Co;2, 2001.

Fu, H., Cwiertny, D. M., Carmichael, G. R., Scherer, M. M., and Grassian, V. H.: Photoreductive dissolution of Fe-containing mineral dust particles in acidic media, J. Geophys. Res., 115, D11304, doi: 10.1029/2009jd012702, 2010.

Groot Zwaaftink, C. D., Grythe, H., Skov, H., and Stohl, A.: Substantial contribution of northern high-latitude sources to mineral dust in the Arctic, J. Geophys. Res.-Atmos, 121, 13678-13697, doi: 10.1002/2016jd025482, 2016.

Groot Zwaaftink, C. D., Arnalds, O., Dagsson-Waldhauserova, P., Eckhardt, S., Prospero, J. M., and Stohl, A.: Temporal and spatial variability of Icelandic dust emissions and atmospheric transport, Atmos. Chem. Phys., 17, 10865-10878, doi: 10.5194/acp-17-10865-2017, 2017.

Haywood, J., Francis, P., Osborne, S., Glew, M., Loeb, N., Highwood, E., Tanre, D., Myhre, G., Formenti, P., and Hirst, E.: Radiative properties and direct radiative effect of Saharan dust measured by the C-130 aircraft during SHADE: 1. Solar spectrum, J. Geophys. Res.-Atmos, 108, 8577, doi: 10.1029/2002jd002687, 2003.

Hervo, M., Quennehen, B., Kristiansen, N. I., Boulon, J., Stohl, A., Freville, P., Pichon, J. M., Picard, D., Labazuy, P., Gouhier, M., Roger, J. C., Colomb, A., Schwarzenboeck, A., and Sellegri, K.: Physical and optical properties of 2010 Eyjafjallajökull volcanic eruption aerosol: ground-based, Lidar and airborne measurements in France, Atmos. Chem. Phys., 12, 1721-1736, doi: 10.5194/acp-12-1721-2012, 2012.

Huffman, D. R., and Stapp, J. L.: Optical measurements on solids of possible interstellar importance, in: Interstellar dust and related topics, Springer, 297-301, 1973.

Jakobsson, S. P., and Gudmundsson, M. T.: Subglacial and intraglacial volcanic formations in Iceland, Jokull, 58, 179-196, 2008.

Hættumat vegna jökulhlaupa í Skaftá [Danger of Skafta jokulhlaup]. Icelandic Meteorological Office Report VÍ 2018-0xx, available at http://www.vedur.is/media/Eplican%C3%A1mskei%C3%B0/2018_skaftarhlaup_soguleg_gogn_lokadrog_rs.pdf (last access: 04 January 2020), 2018.

Jeong, G. Y.: Bulk and single-particle mineralogy of Asian dust and a comparison with its source soils, J. Geophys. Res.-Atmos, 113, D02208, doi: 10.1029/2007jd008606, 2008.

Jeong, G. Y., Park, M. Y., Kandler, K., Nousiainen, T., and Kemppinen, O.: Mineralogical properties and internal structures of individual fine particles of Saharan dust, Atmos. Chem. Phys., 16, 12397-12410, doi: 10.5194/acp-16-12397-2016, 2016.

Jia, J., Wang, Y. J., Xia, D. S., Lu, H., and Gao, F. Y.: Dust Sources of Last Glacial Chinese Loess Based on the Iron Mineralogy of Fractionated Source Samples, Geophys. Res. Lett., 46, 2103-2110, doi: 10.1029/2018gl080909, 2019.

Jickells, T., and Moore, C. M.: The importance of Atmospheric Deposition for Ocean Productivity, Annu. Rev. Ecol. Evol. Syst., 46, 481-501, doi: 10.1146/annurev-ecolsys-112414-054118, 2015.

Jickells, T. D., An, Z. S., Andersen, K. K., Baker, A. R., Bergametti, G., Brooks, N., Cao, J. J., Boyd, P. W., Duce, R. A., Hunter, K. A., Kawahata, H., Kubilay, N., laRoche, J., Liss, P. S., Mahowald, N., Prospero, J. M., Ridgwell, A. J., Tegen, I., and Torres, R.: Global iron connections between desert dust, ocean biogeochemistry, and climate, Science, 308, 67-71, doi: 10.1126/science.1105959, 2005.

Jones, M. T., and Gislason, S. R.: Rapid releases of metal salts and nutrients following the deposition of volcanic ash into aqueous environments, Geochim. Cosmochim. Ac., 72, 3661-3680, doi: 10.1016/j.gca.2008.05.030, 2008.

Journet, E., Desboeufs, K. V., Caquineau, S., and Colin, J. L.: Mineralogy as a critical factor of dust iron solubility, Geophys. Res. Lett., 35, L07805, doi: 10.1029/2007gl031589, 2008.

Journet, E., Balkanski, Y., and Harrison, S. P.: A new data set of soil mineralogy for dust-cycle modeling, Atmos. Chem. Phys., 14, 3801-3816, doi: 10.5194/acp-14-3801-2014, 2014.

Kanakidou, M., Myriokefalitakis, S., and Tsigaridis, K.: Aerosols in atmospheric chemistry and biogeochemical cycles of nutrients, Environ. Res. Lett., 13, 063004, doi: 10.1088/1748-9326/aabcdb, 2018.

Kandler, K., Schutz, L., Deutscher, C., Ebert, M., Hofmann, H., Jackel, S., Jaenicke, R., Knippertz, P., Lieke, K., Massling, A., Petzold, A., Schladitz, A., Weinzierl, B., Wiedensohler, A., Zorn, S., and Weinbruch, S.: Size distribution, mass concentration, chemical and mineralogical composition and derived optical parameters of the boundary layer aerosol at Tinfou, Morocco, during SAMUM 2006, Tellus B: Chem. Phys. Meteorol., 61, 32-50, doi: 10.1111/j.1600-0889.2008.00385.x, 2009.

Kylling, A., Zwaaftink, C. D. G., and Stohl, A.: Mineral Dust Instantaneous Radiative Forcing in the Arctic, Geophys. Res. Lett., 45, 4290-4298, doi: 10.1029/2018gl077346, 2018.

Lafon, S., Sokolik, I. N., Rajot, J. L., Caquineau, S., and Gaudichet, A.: Characterization of iron oxides in mineral dust aerosols: Implications for light absorption, J. Geophys. Res.-Atmos, 111, D21207, doi: 10.1029/2005jd007016, 2006.

Lazaro, F. J., Gutierrez, L., Barron, V., and Gelado, M. D.: The speciation of iron in desert dust collected in Gran Canaria (Canary Islands): Combined chemical, magnetic and optical analysis, Atmos. Environ., 42, 8987-8996, doi: 10.1016/j.atmosenv.2008.09.035, 2008.

Longtin, D. R., Shettle, E. P., Hummel, J. R., and Pryce, J. D.: A wind dependent desert aerosol model: Radiative properties, AFGLTR-88-0112, Air Force Geophysics Laboratory, Hanscom AFB, MA, 1988.

Lu, W. Y., Zhao, W. C., Balsam, W., Lu, H., Liu, P., Lu, Z. L., and Ji, J. F.: Iron Mineralogy and Speciation in Clay-Sized Fractions of Chinese Desert Sediments, J. Geophys. Res.-Atmos, 122, 13458-13471, doi: 10.1002/2017jd027733, 2017.

Lutterotti, L., Ceccato, R., Dal Maschio, R., and Pagani, E.: Quantitative analysis of silicate glass in ceramic materials by the Rietveld method, Mater. Sci. Forum, 278, 87-92, 1998.

Lutterotti, L., Matthies, S., and Wenk, H.: MAUD: a friendly Java program for material analysis using diffraction, IUCr: Newsletter of the CPD, 21, 1999.

Maher, B. A., Mutch, T. J., and Cunningham, D.: Magnetic and geochemical characteristics of Gobi Desert surface sediments: Implications for provenance of the Chinese Loess Plateau, Geology, 37, 279-282, doi: 10.1130/g25293a.1, 2009.

Maher, B. A., Prospero, J. M., Mackie, D., Gaiero, D., Hesse, P. P., and Balkanski, Y.: Global connections between aeolian dust, climate and ocean biogeochemistry at the present day and at the last glacial maximum, Earth-Sci. Rev., 99, 61-97, doi: 10.1016/j.earscirev.2009.12.001, 2010.

Mahowald, N. M., Kloster, S., Engelstaedter, S., Moore, J. K., Mukhopadhyay, S., McConnell, J. R., Albani, S., Doney, S. C., Bhattacharya, A., Curran, M. A. J., Flanner, M. G., Hoffman, F. M., Lawrence, D. M., Lindsay, K., Mayewski, P. A., Neff, J., Rothenberg, D., Thomas, E., Thornton, P. E., and Zender, C. S.: Observed 20th century desert dust variability: impact on climate and biogeochemistry, Atmos. Chem. Phys., 10, 10875-10893, doi: 10.5194/acp-10-10875-2010, 2010.

Maters, E. C., Delmelle, P., and Gunnlaugsson, H. P.: Controls on iron mobilisation from volcanic ash at low pH: Insights from dissolution experiments and Mossbauer spectroscopy, Chem. Geol., 449, 73-81, doi: 10.1016/j.chemgeo.2016.11.036, 2017.

Meinander, O., Kontu, A., Virkkula, A., Arola, A., Backman, L., Dagsson-Waldhauserová, P., Järvinen, O., Manninen, T., Svensson, J., de Leeuw, G., and Leppäranta, M.: Brief communication: Light-absorbing impurities can reduce the density of melting snow, Cryosphere, 8, 991-995, doi: 10.5194/tc-8-991-2014, 2014.

Meskhidze, N., Johnson, M. S., Hurley, D., and Dawson, K.: Influence of measurement uncertainties on fractional solubility of iron in mineral aerosols over the oceans, Aeolian Res., 22, 85-92, doi: 10.1016/j.aeolia.2016.07.002, 2016.

Möller, R., Möller, M., Kukla, P. A., and Schneider, C.: Impact of supraglacial deposits of tephra from Grímsvötn volcano, Iceland, on glacier ablation, J. Glaciol., 62, 933-943, doi: 10.1017/jog.2016.82, 2016.

Möller, R., Möller, M., Kukla, P. A., and Schneider, C.: Modulation of glacier ablation by tephra coverage from Eyjafjallajökull and Grimsvötn volcanoes, Iceland: an automated field experiment, Earth Syst. Sci. Data, 10, 53-60, doi: 10.5194/essd-10-53-2018, 2018.

Moore, C. M., Mills, M. M., Milne, A., Langlois, R., Achterberg, E. P., Lochte, K., Geider, R. J., and La Roche, J.: Iron limits primary productivity during spring bloom development in the central North Atlantic, Glob. Change Biol., 12, 626-634, doi: 10.1111/j.1365-2486.2006.01122.x, 2006.

Moosmuller, H., Engelbrecht, J. P., Skiba, M., Frey, G., Chakrabarty, R. K., and Arnott, W. P.: Single scattering albedo of fine mineral dust aerosols controlled by iron concentration, J. Geophys. Res.-Atmos, 117, D11210, doi: 10.1029/2011jd016909, 2012.

Moroni, B., Arnalds, O., Dagsson-Waldhauserova, P., Crocchianti, S., Vivani, R., and Cappelletti, D.: Mineralogical and Chemical Records of Icelandic Dust Sources Upon Ny-angstrom lesund (Svalbard Islands), Front. Earth Sci., 6, UNSP 187, doi: 10.3389/feart.2018.00187, 2018.

Moskowitz, B. M., Reynolds, R. L., Goldstein, H. L., Berquo, T. S., Kokaly, R. F., and Bristow, C. S.: Iron oxide minerals in dust-source sediments from the Bodele Depression, Chad: Implications for radiative properties and Fe bioavailability of dust plumes from the Sahara, Aeolian Res., 22, 93-106, doi: 10.1016/j.aeolia.2016.07.001, 2016.

Myriokefalitakis, S., Ito, A., Kanakidou, M., Nenes, A., Krol, M. C., Mahowald, N. M., Scanza, R. A., Hamilton, D. S., Johnson, M. S., Meskhidze, N., Kok, J. F., Guieu, C., Baker, A. R., Jickells, T. D., Sarin, M. M., Bikkina, S., Shelley, R., Bowie, A., Perron, M. M. G., and Duce, R. A.: Reviews and syntheses: the GESAMP atmospheric iron deposition model intercomparison study, Biogeosciences, 15, 6659-6684, doi: 10.5194/bg-15-6659-2018, 2018.

Nesbitt, H. W., and Young, G. M.: Prediction of some weathering trends of plutonic and volcanic-rocks based on thermodynamic and kinetic considerations, Geochim. Cosmochim. Ac., 48, 1523-1534, doi: 10.1016/0016-7037(84)90408-3, 1984.

Nielsdottir, M. C., Moore, C. M., Sanders, R., Hinz, D. J., and Achterberg, E. P.: Iron limitation of the postbloom phytoplankton communities in the Iceland Basin, Global Biogeochem. Cy., 23, GB3001, doi: 10.1029/2008gb003410, 2009.

Oakes, M., Ingall, E. D., Lai, B., Shafer, M. M., Hays, M. D., Liu, Z. G., Russell, A. G., and Weber, R. J.: Iron Solubility Related to Particle Sulfur Content in Source Emission and Ambient Fine Particles, Environ. Sci. Technol., 46, 6637-6644, doi: 10.1021/es300701c, 2012.

Oladottir, B. A., Sigmarsson, O., Larsen, G., and Thordarson, T.: Katla volcano, Iceland: magma composition, dynamics and eruption frequency as recorded by Holocene tephra layers, B. Volcanol., 70, 475-493, doi: 10.1007/s00445-007-0150-5, 2008.

Olgun, N., Duggen, S., Croot, P. L., Delmelle, P., Dietze, H., Schacht, U., Oskarsson, N., Siebe, C., Auer, A., and Garbe-Schonberg, D.: Surface ocean iron fertilization: The role of airborne volcanic ash from subduction zone and hot spot volcanoes and related iron fluxes into the Pacific Ocean, Global Biogeochem. Cy., 25, GB4001, doi: 10.1029/2009gb003761, 2011.

Oskarsson, N.: The interaction between volcanic gases and tephra - fluorine adhering to tephra of the 1970 Hekla eruption, J. Volcanol. Geoth. Res., 8, 251-266, doi: 10.1016/0377-0273(80)90107-9, 1980.

Paramonov, M., David, R. O., Kretzschmar, R., and Kanji, Z. A.: A laboratory investigation of the ice nucleation efficiency of three types of mineral and soil dust, Atmos. Chem. Phys., 18, 16515-16536, doi: 10.5194/acp-18-16515-2018, 2018.

Peltoniemi, J. I., Gritsevich, M., Hakala, T., Dagsson-Waldhauserova, P., Arnalds, O., Anttila, K., Hannula, H. R., Kivekas, N., Lihavainen, H., Meinander, O., Svensson, J., Virkkula, A., and de Leeuw, G.: Soot on Snow experiment: bidirectional reflectance factor measurements of contaminated snow, Cryosphere, 9, 2323-2337, doi: 10.5194/tc-9-2323-2015, 2015.

Poulton, S. W., and Canfield, D. E.: Development of a sequential extraction procedure for iron: implications for iron partitioning in continentally derived particulates, Chem. Geol., 214, 209-221, doi: 10.1016/j.chemgeo.2004.09.003, 2005.

Price, J. R., and Velbel, M. A.: Chemical weathering indices applied to weathering profiles developed on heterogeneous felsic metamorphic parent rocks, Chem. Geol., 202, 397-416, doi: 10.1016/j.chemgeo.2002.11.001, 2003.

Prospero, J. M., Bullard, J. E., and Hodgkins, R.: High-Latitude Dust Over the North Atlantic: Inputs from Icelandic Proglacial Dust Storms, Science, 335, 1078-1082, doi: 10.1126/science.1217447, 2012.

Qian, Y., Yasunari, T. J., Doherty, S. J., Flanner, M. G., Lau, W. K. M., Ming, J., Wang, H. L., Wang, M., Warren, S. G., and Zhang, R. D.: Light-absorbing Particles in Snow and Ice: Measurement and Modeling of Climatic and Hydrological impact, Adv. Atmos. Sci., 32, 64-91, doi: 10.1007/s00376-014-0010-0, 2015.

Magnetite, Refractive index database, available at https://refractiveindex.info/?shelf=main&book=Fe3O4& (last access: 02 January 2020), 1985.

Raiswell, R., Benning, L. G., Tranter, M., and Tulaczyk, S.: Bioavailable iron in the Southern Ocean: the significance of the iceberg conveyor belt, Geochem. T., 9, 7, doi: 10.1186/1467-4866-9-7, 2008.

Raiswell, R., Hawkings, J. R., Benning, L. G., Baker, A. R., Death, R., Albani, S., Mahowald, N., Krom, M. D., Poulton, S. W., and Wadham, J.: Potentially bioavailable iron delivery by iceberg-hosted sediments and atmospheric dust to the polar oceans, Biogeosciences, 13, 3887-3900, doi: 10.5194/bg-13-3887-2016, 2016.

Ravel, B., and Newville, M.: ATHENA, ARTEMIS, HEPHAESTUS: data analysis for X-ray absorption spectroscopy using IFEFFIT, J. Synchrotron Radiat., 12, 537-541, doi: 10.1107/S0909049505012719, 2005.

Reed, B. E., Peters, D. M., McPheat, R., Smith, A. J. A., and Grainger, R. G.: Mass extinction spectra and size distribution measurements of quartz and amorphous silica aerosol at 0.33-19 mu m compared to modelled extinction using Mie, CDE, and T-matrix theories, J. Quant. Spectrosc. Ra., 199, 52-65, doi: 10.1016/j.jqsrt.2017.05.011, 2017.

Rocha-Lima, A., Martins, J. V., Remer, L. A., Krotkov, N. A., Tabacniks, M. H., Ben-Ami, Y., and Artaxo, P.: Optical, microphysical and compositional properties of the Eyjafjallajökull volcanic ash, Atmos. Chem. Phys., 14, 10649-10661, doi: 10.5194/acp-14-10649-2014, 2014.

Ryan-Keogh, T. J., Macey, A. I., Nielsdottir, M. C., Lucas, M. I., Steigenberger, S. S., Stinchcombe, M. C., Achterberg, E. P., Bibby, T. S., and Moore, C. M.: Spatial and temporal development of phytoplankton iron stress in relation to bloom dynamics in the high-latitude North Atlantic Ocean, Limnol. Oceanogr., 58, 533-545, doi: 10.4319/lo.2013.58.2.0533, 2013.

Scheuvens, D., Schutz, L., Kandler, K., Ebert, M., and Weinbruch, S.: Bulk composition of northern African dust and its source sediments - A compilation, Earth-Sci. Rev., 116, 170-194, doi: 10.1016/j.earscirev.2012.08.005, 2013.

Scheuvens, D., and Kandler, K.: On composition, morphology, and size distribution of airborne mineral dust, in: Mineral Dust, Springer, 15-49, 2014.

Schroth, A. W., Crusius, J., Sholkovitz, E. R., and Bostick, B. C.: Iron solubility driven by speciation in dust sources to the ocean, Nat. Geosci., 2, 337-340, doi: 10.1038/ngeo501, 2009.

Schroth, A. W., Crusius, J., Gasso, S., Moy, C. M., Buck, N. J., Resing, J. A., and Campbell, R. W.: Atmospheric deposition of glacial iron in the Gulf of Alaska impacted by the position of the Aleutian Low, Geophys. Res. Lett., 44, 5053-5061, doi: 10.1002/2017gl073565, 2017.

Schumann, U., Weinzierl, B., Reitebuch, O., Schlager, H., Minikin, A., Forster, C., Baumann, R., Sailer, T., Graf, K., Mannstein, H., Voigt, C., Rahm, S., Simmet, R., Scheibe, M., Lichtenstern, M., Stock, P., Ruba, H., Schauble, D., Tafferner, A., Rautenhaus, M., Gerz, T., Ziereis, H., Krautstrunk, M., Mallaun, C., Gayet, J. F., Lieke, K., Kandler, K., Ebert, M., Weinbruch, S., Stohl, A., Gasteiger, J., Gross, S., Freudenthaler, V., Wiegner, M., Ansmann, A., Tesche, M., Olafsson, H., and Sturm, K.: Airborne observations of the Eyjafjalla volcano ash cloud over Europe during air space closure in April and May 2010, Atmos. Chem. Phys., 11, 2245-2279, doi: 10.5194/acp-11-2245-2011, 2011.

Shao, L. Y., Li, W. J., Yang, S. S., Shi, Z., and Lu, S. L.: Mineralogical characteristics of airborne particles collected in Beijing during a severe Asian dust storm period in spring 2002, Sci. China Ser. D, 50, 953-959, doi: 10.1007/s11430-007-0035-7, 2007.

Shi, Z., Shao, L. T., Jones, T. P., and Lu, S. L.: Microscopy and mineralogy of airborne particles collected during severe dust storm episodes in Beijing, China, J. Geophys. Res.-Atmos, 110, D01303, doi: 10.1029/2004jd005073, 2005.

Shi, Z., Krom, M. D., Bonneville, S., Baker, A. R., Jickells, T. D., and Benning, L. G.: Formation of iron nanoparticles and increase in iron reactivity in the mineral dust during simulated cloud processing, Environ. Sci. Technol., 43, 6592-6596, doi: 10.1021/es901294g, 2009.

Shi, Z., Bonneville, S., Krom, M. D., Carslaw, K. S., Jickells, T. D., Baker, A. R., and Benning, L. G.: Iron dissolution kinetics of mineral dust at low pH during simulated atmospheric processing, Atmos. Chem. Phys., 11, 995-1007, doi: 10.5194/acp-11-995-2011, 2011a.

Shi, Z., Krom, M. D., Bonneville, S., Baker, A. R., Bristow, C., Drake, N., Mann, G., Carslaw, K., McQuaid, J. B., Jickells, T., and Benning, L. G.: Influence of chemical weathering and aging of iron oxides on the potential iron solubility of Saharan dust during simulated atmospheric processing, Global Biogeochem. Cy., 25, GB2010, doi: 10.1029/2010gb003837, 2011b.

Shi, Z., Krom, M. D., Jickells, T. D., Bonneville, S., Carslaw, K. S., Mihalopoulos, N., Baker, A. R., and Benning, L. G.: Impacts on iron solubility in the mineral dust by processes in the source region and the atmosphere: A review, Aeolian Res., 5, 21-42, doi: 10.1016/j.aeolia.2012.03.001, 2012.

Shi, Z., Krom, M. D., Bonneville, S., and Benning, L. G.: Atmospheric processing outside clouds increases soluble iron in mineral dust, Environ. Sci. Technol., 49, 1472-1477, doi: 10.1021/es504623x, 2015.

Shi, Z. B., Woodhouse, M. T., Carslaw, K. S., Krom, M. D., Mann, G. W., Baker, A. R., Savov, I., Fones, G. R., Brooks, B., Drake, N., Jickells, T. D., and Benning, L. G.: Minor effect of physical size sorting on iron solubility of transported mineral dust, Atmos. Chem. Phys., 11, 8459-8469, doi: 10.5194/acp-11-8459-2011, 2011c.

Sokolik, I. N., and Toon, O. B.: Incorporation of mineralogical composition into models of the radiative properties of mineral aerosol from UV to IR wavelengths, J. Geophys. Res.-Atmos, 104, 9423-9444, doi: 10.1029/1998jd200048, 1999.

Song, Y. G., Chen, X. L., Qian, L. B., Li, C. X., Li, Y., Li, X. X., Chang, H., and An, Z. S.: Distribution and composition of loess sediments in the Ili Basin, Central Asia, Quat. Int., 334, 61-73, doi: 10.1016/j.quaint.2013.12.053, 2014.

Stockdale, A., Krom, M. D., Mortimer, R. J., Benning, L. G., Carslaw, K. S., Herbert, R. J., Shi, Z., Myriokefalitakis, S., Kanakidou, M., and Nenes, A.: Understanding the nature of atmospheric acid processing of mineral dusts in supplying bioavailable phosphorus to the oceans, P. Natl. Acad. Sci. USA, 113, 14639-14644, doi: 10.1073/pnas.1608136113, 2016.

Takahashi, Y., Higashi, M., Furukawa, T., and Mitsunobu, S.: Change of iron species and iron solubility in Asian dust during the long-range transport from western China to Japan, Atmos. Chem. Phys., 11, 11237-11252, doi: 10.5194/acp-11-11237-2011, 2011.

Tang, M. J., Cziczo, D. J., and Grassian, V. H.: Interactions of Water with Mineral Dust Aerosol: Water Adsorption, Hygroscopicity, Cloud Condensation, and Ice Nucleation, Chem. Rev., 116, 4205-4259, doi: 10.1021/acs.chemrev.5b00529, 2016.

Toby, B. H.: R factors in Rietveld analysis: How good is good enough?, Powder Diffr., 21, 67-70, doi: 10.1154/1.2179804, 2006.

Toledano, C., Bennouna, Y., Cachorro, V., de Galisteo, J. P. O., Stohl, A., Stebel, K., Kristiansen, N. I., Olmo, F. J., Lyamani, H., Obregon, M. A., Estelles, V., Wagner, F., Baldasano, J. M., Gonzalez-Castanedo, Y., Clarisse, L., and de Frutos, A. M.: Aerosol properties of the Eyjafjallajökull ash derived from sun photometer and satellite observations over the Iberian Peninsula, Atmos. Environ., 48, 22-32, doi: 10.1016/j.atmosenv.2011.09.072, 2012.

Urupina, D., Lasne, J., Romanias, M. N., Thiery, V., Dagsson-Waldhauserova, P., and Thevenet, F.: Uptake and surface chemistry of SO2 on natural volcanic dusts, Atmos. Environ., 217, 116942, doi: 10.1016/j.atmosenv.2019.116942, 2019.

Vergara-Temprado, J., Miltenberger, A. K., Furtado, K., Grosvenor, D. P., Shipway, B. J., Hill, A. A., Wilkinson, J. M., Field, P. R., Murray, B. J., and Carslaw, K. S.: Strong control of Southern Ocean cloud reflectivity by ice-nucleating particles, P. Natl. Acad. Sci. USA, 115, 2687-2692, doi: 10.1073/pnas.1721627115, 2018.

Viollier, E., Inglett, P. W., Hunter, K., Roychoudhury, A. N., and Van Cappellen, P.: The ferrozine method revisited: Fe(II)/Fe(III) determination in natural waters, Appl. Geochem., 15, 785-790, doi: 10.1016/s0883-2927(99)00097-9, 2000.

Vogel, A., Diplas, S., Durant, A. J., Azar, A. S., Sunding, M. F., Rose, W. I., Sytchkova, A., Bonadonna, C., Kruger, K., and Stohl, A.: Reference data set of volcanic ash physicochemical and optical properties, J. Geophys. Res.-Atmos, 122, 9485-9514, doi: 10.1002/2016jd026328, 2017.

Wang, J., Doussin, J. F., Perrier, S., Perraudin, E., Katrib, Y., Pangui, E., and Picquet-Varrault, B.: Design of a new multi-phase experimental simulation chamber for atmospheric photosmog, aerosol and cloud chemistry research, Atmos. Meas. Tech., 4, 2465-2494, doi: 10.5194/amt-4-2465-2011, 2011.

Weinzierl, B., Sauer, D., Minikin, A., Reitebuch, O., Dahlkotter, F., Mayer, B., Emde, C., Tegen, I., Gasteiger, J., Petzold, A., Veira, A., Kueppers, U., and Schumann, U.: On the visibility of airborne volcanic ash and mineral dust from the pilot's perspective in flight, Phys. Chem. Earth, 45-46, 87-102, doi: 10.1016/j.pce.2012.04.003, 2012.

Wilke, M., Farges, F., Petit, P. E., Brown, G. E., and Martin, F.: Oxidation state and coordination of Fe in minerals: An FeK-XANES spectroscopic study, Am. Mineral., 86, 714-730, doi: 10.2138/am-2001-5-612, 2001.

Winton, V. H. L., Edwards, R., Delmonte, B., Ellis, A., Andersson, P. S., Bowie, A., Bertler, N. A. N., Neff, P., and Tuohy, A.: Multiple sources of soluble atmospheric iron to Antarctic waters, Global Biogeochem. Cy., 30, 421-437, doi: 10.1002/2015gb005265, 2016.

Wittmann, M., Zwaaftink, C. D. G., Schmidt, L. S., Gudmundsson, S., Palsson, F., Arnalds, O., Björnsson, H., Thorsteinsson, T., and Stohl, A.: Impact of dust deposition on the albedo of Vatnajökull ice cap, Iceland, Cryosphere, 11, 741-754, doi: 10.5194/tc-11-741-2017, 2017.

Wolff-Boenisch, D., Gislason, S. R., and Oelkers, E. H.: The effect of crystallinity on dissolution rates and CO2 consumption capacity of silicates, Geochim. Cosmochim. Ac., 70, 858-870, doi: 10.1016/j.gca.2005.10.016, 2006.

Yoshida, A., Moteki, N., Ohata, S., Mori, T., Tada, R., Dagsson-Waldhauserová, P., and Kondo, Y.: Detection of light-absorbing iron oxide particles using a modified single-particle soot photometer, Aerosol Sci. Tech., 50, 1-4, doi: 10.1080/02786826.2016.1146402, 2016.

Zhang, X. L., Wu, G. J., Zhang, C. L., Xu, T. L., and Zhou, Q. Q.: What is the real role of iron oxides in the optical properties of dust aerosols?, Atmos. Chem. Phys., 15, 12159-12177, doi: 10.5194/acp-15-12159-2015, 2015.

Zubko, N., Munoz, O., Zubko, E., Gritsevich, M., Escobar-Cerezo, J., Berg, M. J., and Peltoniemi, J.: Light scattering from volcanic-sand particles in deposited and aerosol form, Atmos. Environ., 215, 116813, doi: 10.1016/j.atmosenv.2019.06.051, 2019.

CHAPTER 5: COMPLEX REFRACTIVE INDEX AND SINGLE SCATTERING ALBEDO OF ICELANDIC DUST IN THE SHORTWAVE SPECTRUM

5.1 Abstract

There is growing evidence of the impacts of Icelandic dust on the climate, which tend to produce a positive radiative forcing. However, the current knowledge on the optical properties of Icelandic dust is limited which prevents an accurate assessment of the climate impacts of Icelandic dust in global models. In this study, we determined the spectral single scattering albedo and complex refractive index of Icelandic dust in the shortwave spectrum (λ from 370 to 950 nm). Icelandic dust was generated from parent soils from five major dust hotspots in Iceland. The single scattering albedo and complex refractive index were retrieved from the online measurements of the size distribution and spectral Mie coefficients of particles suspended in the atmospheric simulation chamber CESAM. The average single scattering albedo, $SSA_{avg}(\lambda)$, increased from 0.90-0.94 at 370 nm to 0.94-0.96 at 950 nm in different Icelandic samples, which is comparable to Iceland volcano plumes and mineral dust from northern Africa-Saharan, Sahel, and eastern Asian. The average real index, $n_{avg}(\lambda)$, did not show a clear dependence on λ and was 1.60-1.61 in different samples, while the imaginary index, $k_{avg}(\lambda)$, decreased from 0.004 at 370 nm to 0.002-0.003 at 950 nm. Although Icelandic dust has considerably different mineralogical composition compared to typical low-latitude dust, our results indicate that their spectral optical properties between 370 and 590 nm are similar. However, the imaginary index of Icelandic dust between 660 and 950 nm is 2-8 times higher than most of the dust samples sourced in northern Africa-Sahara, Sahel, and eastern Asia. Furthermore, $k_{avg}(\lambda)$ tend to be similar to the initial estimates calculated based on the mineralogical composition, suggesting that the high content of magnetite may have contributed to the high absorptive

capacity of Icelandic dust. Our results indicate that Icelandic dust may have a stronger positive direct radiative forcing on climate than previous thoughts.

5.2 Introduction

In the Northern Hemisphere, Iceland is an important contributor to the dust aerosol loading over high-latitude (>60º N) regions (Arnalds et al., 2016; Baddock et al., 2017; Bullard et al., 2016; Dagsson-Waldhauserova et al., 2019; Groot Zwaaftink et al., 2017; Groot Zwaaftink et al., 2016; Prospero et al., 2012). There is growing evidence of the impacts of Icelandic dust on climate at high latitudes, where the melting of sea ice is producing an accelerated warming rate of surface air temperature compared to the rest of the world (Dai et al., 2019; Serreze and Barry, 2011). Icelandic dust strongly absorbs solar radiation (Zubko et al., 2019), and can have major impacts on the cryosphere (Boy et al., 2019; Bullard et al., 2016; Dagsson-Waldhauserova and Meinander, 2019; Meinander et al., 2016). Experiments have shown that the deposition of volcanic dust particles from Iceland onto snow and ice can reduce the surface albedo and alter the melting process (Dragosics et al., 2016; Meinander et al., 2014; Möller et al., 2016; Möller et al., 2018; Peltoniemi et al., 2015; Wittmann et al., 2017). In the Arctic, the estimated instantaneous radiative forcing (IRF) of Icelandic dust is 0.005 W m^{-2} at the top of the atmosphere (TOA) via dust-radiation interaction, which is lower but still significant compared to the IRF at the bottom of the atmosphere (BOA) via dust deposition onto snow-covered areas, 0.02 W m^{-2} (Kylling et al., 2018).

In addition, Icelandic dust is a source of ice-nucleating particles (Sanchez-Marroquin et al., 2020). The increase in ice-nucleating particles can reduce the amount of supercooled liquid water and consequently the albedo of mixed-phase clouds (Vergara-Temprado et al., 2018), which have a large impact on the radiative budget in the Arctic (Morrison et al., 2012; Murray et al., 2021).

Furthermore, Icelandic dust contributes to the deposition of dissolved iron (Fe) to the subpolar North Atlantic Ocean (Arnalds et al., 2014; Baldo et al., 2020), which has the potential to alter nutrient biogeochemical cycling and primary production in the surface ocean (Achterberg et al., 2013; Achterberg et al., 2018). The deposition of nutrients such as phosphorus (P) and Fe from mineral dust can also promote the blooming of algae in ice, which consequently reduces the ice albedo and accelerates the surface melting (Cook et al., 2020; McCutcheon et al., 2021).

The mineralogical composition of Icelandic dust is considerably different from typical low-latitude dust such as northern African and Asian dust. Icelandic dust primarily consists of amorphous basaltic material with relatively high magnetite content. And, it is also enriched in Fe contributing to over 10% of the total dust mass (Baldo et al., 2020). The absorption of solar radiation by mineral dust is strongly related to the content of total Fe and Fe oxide minerals (Caponi et al., 2017; Derimian et al., 2008; Di Biagio et al., 2019; Engelbrecht et al., 2016; Formenti et al., 2014; Lafon et al., 2006; Moosmuller et al., 2012; Sokolik and Toon, 1999). This suggests that the optical properties of Icelandic dust may be also different from that of low-latitude dust. However, the current knowledge on the optical properties of Icelandic dust is limited. Peltoniemi et al. (2015) found that volcanic sand from the Mýrdalssandur hotspot in Iceland deposited onto snow reduced the snow albedo similarly to black carbon (BC) between 400-2500 nm. The laboratory measurements conducted on pure volcanic sand (deposited particles) showed a spectral reflectance < 0.04, which is close to a black body (0.0) (Dagsson-Waldhauserova, 2014; Peltoniemi et al., 2015). Zubko et al. (2019) determined that the imaginary part of the complex refractive index of suspended particles from the same area was 0.01 at 647 nm, which is around 1 order of magnitude higher than the average values for mineral dust from northern Africa and Asia reported by Di Biagio et al. (2019). However, due to the lack of regional-resolved measurements, the current model estimates of the direct radiative effects of Icelandic dust in the Arctic assumed the same complex refractive index for dust aerosols from different source regions (Kylling et al., 2018). Consequently, further measurements are necessary to reduce the uncertainty in the model predictions.

This study aims at filling these gaps by determining the shortwave (SW) optical properties of Icelandic dust from different major emission hotspots. Here, we determined the single scattering albedo (SSA) and complex refractive index of Icelandic dust in the SW range from 370 to 950 nm based on the measurements of the size distribution and optical properties of suspended particles generated from natural parent soils.

5.3 Methodology

This section illustrates the approach used to retrieve the SSA and complex refractive index of Icelandic dust in the SW range which was based on the method by Di Biagio et al. (2019). The spectral scattering coefficient (β_{sca}), absorption coefficient (β_{abs}), and size distribution of suspended dust particles were measured using the multi-instrument atmospheric simulation chamber CESAM (French acronym for Experimental Multiphasic Atmospheric Simulation Chamber) (Wang et al., 2011). SSA was estimated from β_{abs} and β_{sca} measured at CESAM. The complex refractive index was retrieved from the comparison between the spectral Mie coefficients β_{sca} and β_{abs} measured and computed using the size distribution data. The data were analyzed based on the Mie theory assuming that the particles are spherical and internally homogeneous. A schematic diagram of the method used to retrieve the complex refractive index is shown in Figure 5.1.

5.3.1 Experimental setup and instrumentations

The size distribution and optical properties of Icelandic dust were measured by the use of CESAM, a 4.2 m^3 stainless steel atmospheric simulation chamber (Wang et al., 2011). Icelandic dust was generated following the method in Di Biagio et al. (2017a) to produce mineral dust from parent soils. The experiments were conducted using surface sediment samples from five major dust hotspots in Iceland (Baldo et al., 2020): D3 (Dyngjusandur), H55 (Hagavatn), Land1 (Landeyjarsandur), Maeli2 (Mælifellssandur) and MIR45 (Mýrdalssandur). As described in Baldo et al. (2020), 15 g of sediments (previously sieved to <1 mm) was placed in a Büchner flask, this was shaken for 5 min at 70 Hz on a sieve shaker (Retsch AS200), then mixed with nitrogen carrier gas and injected into the CESAM chamber at 10 L min^{-1} for 10 min. Once injected in CESAM, the dust particles were allowed to mix for around 10 min inside the chamber. A four-blade stainless-steel fan located at the bottom of the chamber ensured that the particle mass concentration was homogeneous inside the chamber. The physical and chemical properties of the suspended dust were monitored over the duration of the experiments (approximatively 3 hours) using different instruments connected to the chamber (Figure 5.2).

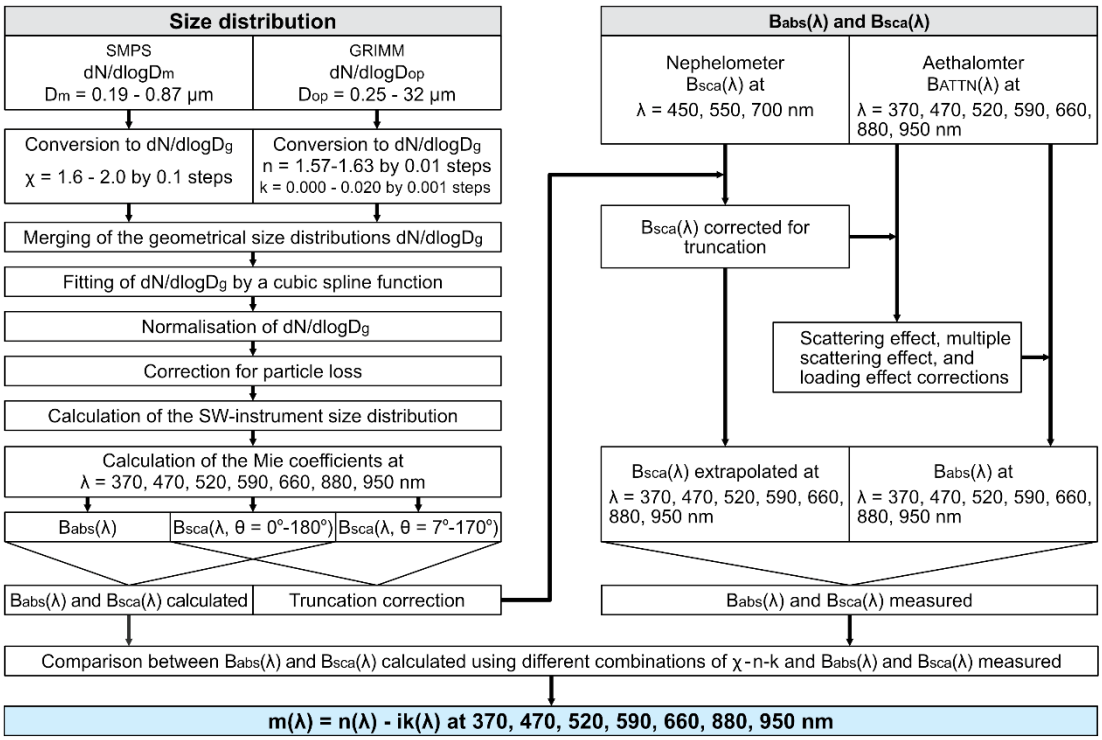

Figure 5.1: Schematic diagram of the method used to retrieve the SW complex refractive index (m = n - ik) of Icelandic dust from 370 to 950 nm.

The particle number size distribution of dust aerosols was measured using a scanning mobility particle sizer (SMPS) (TSI Inc., DMA model 3080, CPC model 3772; 2.0 and 0.2 L min^{-1} sheath–aerosol flow rates; 3 min time resolution), and two optical particle counters (OPCs), GRIMM (Grimm Inc., model 1.109; 655 nm operating wavelength; 1.2 L min^{-1} flow rate; 6 s time resolution) and SkyGRIMM (Grimm Inc., model 1.129; 655 nm operating wavelength; 1.2 L min^{-1} flow rate; 6 s time resolution). The SMPS measured the particle number concentration in the electrical mobility diameter (D_m) range from 0.019 to 0.870 µm. GRIMM and SkyGRIMM measured the particle number concentration in the optical-equivalent diameter (D_{op}) range from 0.25 to 32 µm. SMPS and SkyGRIMM were located at the bottom of the chamber, while the GRIMM was installed at the top of the chamber to verify that the concentration of dust aerosols in the chamber was spatially uniform.

The scattering coefficient β_{sca} of the suspended particles was measured by a three-wavelength integrating nephelometer (TSI Inc., model 3563; operating at 450, 550, and 700 nm; 2 L min^{-1} flow rate, 2 s time resolution). The absorption coefficient β_{abs} was measured by a seven-wavelength aethalometer (Magee

Sci., model AE31; operating at 370, 470, 520, 590, 660, 880, and 950 nm; 2 L min^{-1} flow rate, 2 min time resolution). Dust aerosol samples were also collected using custom-made filter samplers as in Caponi et al. (2017). The samplers were set up for 1 to 3 hours, each with a flow rate of 7 L min^{-1}. The collected filter samples were then analyzed offline to determine the chemical properties of the suspended particles as described in Baldo et al. (2020).

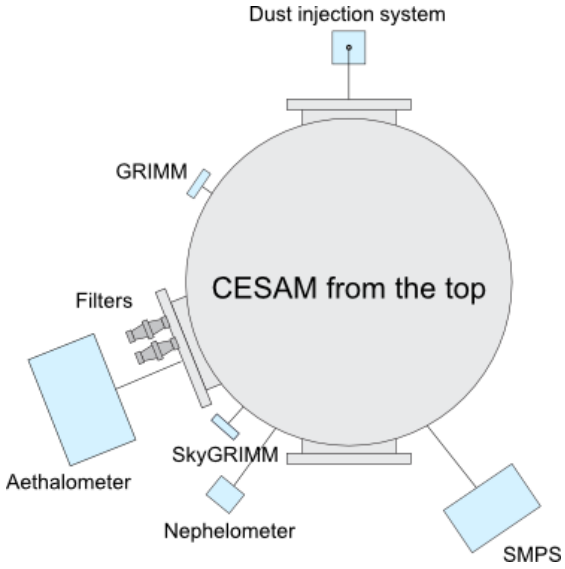

Figure 5.2: Schematic diagram of the CESAM set up for the experiments on the Icelandic dust.

A particle-free N_2/O_2 mixture was continuously injected into the chamber to balance the proportion of air flow sampled by the different instruments. The sampling system consisted of a stainless-steel tube (~ 14-58 cm length, 9.5 mm diameter) located inside the chamber extracting air. For some instruments, conductive silicone tubing (TSI Inc., ~ 30-65 cm length, 5 mm diameter) was also used as an external connection between the chamber and the instrument. The sampling lines were designed to be as straight and direct as possible to minimize particle loss. The total length of the sampling line varied depending on the instrument, 100 cm for the nephelometer, 86 cm for the aethalometer, 79 cm for the SMPS, 58 cm for the SkyGRIMM and the aerosol filter samplers, and 14 cm for the GRIMM. All experiments were conducted at ambient temperature and relative humidity < 2 %. The chamber was manually cleaned between experiments with different samples to avoid any cross-contaminations. The background mass concentrations of dust aerosol in the chamber varied from 0.1 to 3.0 µg m^{-3}.

5.3.2 Measurements of the aerosol size distribution

To allow the comparison of measurements from different instruments, all data were averaged over 12-min intervals from the start of the filter sampling. To ensure that the concentration of dust aerosols in the chamber was spatially uniform, the measurements collected before 30 min from the injection peak were excluded from the data analysis. The percentage difference between the total particle number concentrations in the size range measured by GRIMM and SkyGRIMM was < 10% for the samples D3 and MIR45, < 5% for the samples Land1 and Maeli2, and < 2% for the sample H55 suggesting that homogeneous conditions were obtained during the experiments.

The aerosol size distribution was obtained by combining the measurements from SMPS and GRIMM into a single geometrical size distribution. Several corrections were applied to the SMPS and GRIMM measurements because of the differences in operating principles and diameter definitions between the instruments.

The SMPS measures the size distribution of submicron particles. The operating principle of the SMPS is the balance between the electrical force on a charged particle due to a constant electric field and the drag force experienced by that particle at terminal velocity which is used to derive the particle size (DeCarlo et al., 2004; Hinds, 1999; Wendisch and Brenguier, 2013). The SMPS is composed of a differential mobility analyzer (DMA) and a condensation particle counter (CPC). The particles are first charged to a well-defined charge distribution and classified by the DMA according to their electrical mobility (the velocity of the charged particles per unit electric field) (Hinds, 1999; Wendisch and Brenguier, 2013). Then, the particles are counted by the CPC. In the CPC, the particles are exposed to a supersaturated vapor and act as vapor condensation nuclei growing from a few nanometers to several micrometers. Subsequently, a detector counts the pulse of light scattered by the enlarged particles (Hinds, 1999; Wendisch and Brenguier, 2013). The relationship between the electrical mobility diameter D_m (the diameter of a single-charged spherical particle with the same terminal velocity in a constant electric field as the single-charged particle under consideration), as measured by the SMPS and the volume-equivalent diameter D_g (the diameter of a spherical particle of the same volume as the particle under

consideration) is described by Equation (1) (DeCarlo et al., 2004; Kulkarni et al., 2011; Wendisch and Brenguier, 2013):

$$D_g = \frac{D_m}{\chi} \cdot \frac{C_c(D_g)}{C_c(D_m)} \quad (1)$$

where χ is the dynamic shape factor, C_c is the Cunningham slip correction factor assuming a mean free path of 66 nm (air conditions) (Hinds, 1999):

$$D_{g\text{-}m} > 100 \text{ nm}, \qquad C_c(D_{g\text{-}m}) = 1 + \frac{66}{D_{g\text{-}m}} \cdot 2.52 \quad (2)$$

$$D_{g\text{-}m} \leq 100 \text{ nm}, \qquad C_c(D_{g\text{-}m}) = 1 + \frac{66}{D_{g\text{-}m}} \cdot (2.34 + 1.05 \cdot e^{-0.39 \cdot \frac{D_{g\text{-}m}}{66}}) \quad (3)$$

where $D_{g\text{-}m}$ represents the volume-equivalent diameter (D_g) or the electrical mobility diameter D_m.

The OPCs measure the size distribution across a wide range of sizes including submicron and supermicron particles. The OPC operating principle is the dependence of angular light scattering on particle size (Hinds, 1999; Wendisch and Brenguier, 2013). The aerosol particles are illuminated with monochromatic light and the intensity of the scattered light is collected over a certain range of angles. The signal measured by the instrument is converted into the single-particle scattering cross-section (C_{sca}) using a scale factor based on the calibration with standard reference non-absorbing particles, generally polystyrene latex spheres (PSL) (Wendisch and Brenguier, 2013). C_{sca} is related to the particle size and is the product of the particle physical cross-sectional area (A) and scattering efficiency (Q_{sca}), which quantifies the scattering ability of particles (Seinfeld and Pandis, 2016). C_{sca} is calculated for the reference particles by applying the Mie theory given the size, complex refractive index, laser operating wavelength, and collection angle (Wendisch and Brenguier, 2013).

The particle size measured by OPC instruments is referred to as optical-equivalent diameter D_{op}, the diameter of a spherical particle with a given complex refractive index which has the same scattering

efficiency and cross-sectional area as the particle under consideration. The complex refractive index, m = n - ik, links the particle chemical composition and optical properties, with the real part n defining the scattering properties and the imaginary part k the absorption properties (Wendisch and Brenguier, 2013). However, the complex refractive index of the reference material is likely to be different from that of natural aerosols. In addition, the aerosol particles may not be spheres, and aspherical particles have considerably different optical properties from spherical dust (e.g., Nousiainen and Kandler, 2015). As a result, the aerosol size distribution determined by OPC instruments could not correspond to the geometrical size distribution.

In this study, the morphology of Icelandic dust particles was not measured, but previous research observed that the particles can be irregular and present high porosity (Butwin et al., 2020; Richards-Thomas et al., 2020). In particular, the results of Butwin et al. (2020) indicated that the morphological characteristics of Icelandic dust particles equal or less than 20 µm in diameter tend to be similar to those of mineral dust from global source regions, while larger particles exhibited morphological properties of volcanic ash. In this study, since the particle size distribution effectively measured by the GRIMM corresponds to around the PM_{20} fraction as subsequently explained in section 5.3.2.3, we can assume Icelandic dust particles having similar morphological properties as typical mineral dust particles which largely exhibit irregular shapes (Huang et al., 2021). Here, the uncertainty arising from the use of the Mie theory was not estimated, but previous studies found that not accounting for dust aerosol asphericity in the conversion from D_{op} to D_g can underestimate coarse sizes (Formenti et al., 2021; Huang et al., 2021) because of the larger C_{sca} calculated for aspherical particles than for the volume-equivalent spheres, and this effect is higher with increasing dust imaginary index (Huang et al., 2021).

The volume-equivalent diameter D_g of natural aerosols can be retrieved using the complex refractive index of the examined aerosol with varying the particle size to obtain the same (or closest) C_{sca} as that calculated using D_{op} (Formenti et al., 2021). However, the C_{sca} is not often a linear or monotonic function of the particle diameter due to the oscillation of the scattering phase function calculate by Mie theory. As a result, for a specific complex refractive index and D_{op}, more than one D_g may correspond to the

same C_{sca} as that calculated from D_{op}, which consequently has multiple solutions (e.g., Formenti et al., 2021; Rosenberg et al., 2012; Walser et al., 2017; Wendisch and Brenguier, 2013). Although the best solution is typically to choose D_g close to D_{op}, this may not be always feasible. For the GRIMM, increasing the imaginary index, the scattering cross-section curve tends to become flat at around 1 μm as shown in Figure 2 of Formenti et al. (2021). This determines large uncertainty when calculating the volume-equivalent diameters of light-absorbing aerosols in the range between 0.6 and 2 μm (Formenti et al., 2021). Consequently, increasing the value of D_{op} does not always correspond to increasing D_g, which may produce negative or very small $dlogD_g = logD_{g2} - logD_{g1}$, where D_{g1} and D_{g2} are the lower and upper cut-off diameters of each size range. This generates unusual spikes in the calculated geometrical size distributions $dN/dlogD_g$. Two common strategies to address this issue are widening or grouping the OPC bin size (Johnson and Osborne, 2011) or fitting the corrected D_g curve (Hand and Kreidenweis, 2002; Johnson et al., 2008).

5.3.2.1 Calculation of the SMPS and GRIMM geometrical size distributions

To combine SMPS and GRIMM measurements, first, the SMPS particle number concentration $dN/dlogD_m$ and GRIMM particle number concentration $dN/dlogD_{op}$ were both converted into geometrical size distributions $dN/dlogD_g$ (Figure S1). For the SMPS, the volume-equivalent diameters D_g were retrieved from the mobility diameters D_m using a range of dynamic shape factors χ in Equation (1). The interval of χ values (from 1.6 to 2.0 by 0.1 steps) was selected according to the aspect ratios observed in fine Icelandic dust particles $\leq$ 2.5 μm (Butwin et al., 2020). Iterative calculations were performed to calculate D_g using Equations (1-3).

For the GRIMM optical diameters D_{op}, we used the correction factors calculated by Formenti et al. (2021) by applying the Mie theory and assuming that the particles are homogeneous spheres. We selected a range of potential complex refractive indices with the real part n varying from 1.57 to 1.63 by 0.01 steps and the imaginary index k varying from 0.000 to 0.020 by 0.001 steps. The interval of n and k values was chosen according to the complex refractive index estimated by Zubko et al. (2019) and the initial guess of the complex refractive index of the Icelandic dust samples examined in this study based on the

mineralogical composition (Baldo et al., 2020). Here, the corrected D_g values which return $dlogD_g$ < 0.01 were replaced with the average of the previous and next D_g values.

5.3.2.2 Merging of the SMPS and GRIMM size distributions

The SMPS geometrical size distributions, calculated assuming χ from 1.6 to 2.0 by 0.1 steps, and the GRIMM geometrical size distributions, calculated assuming 147 potential complex refractive indices (n from 1.57 to 1.63 by 0.01 steps, and k from 0.000 to 0.020 by 0.001 steps), were combined in 735 different geometrical size distributions. There is an overlapping interval between the SMPS and GRIMM bin sizes. For simplicity, since the size resolution of the SMPS measurements is higher than that of the GRIMM measurements and because of the good agreement between SMPS and GRIMM in the overlapping region as show in Figure S1, we assumed the SMPS size distribution as a better representative in the overlapping region.

The merged geometrical size distributions were interpolated at a constant dlogDg interval of 1/64 using a fitted cubic smoothing spline. The smooth.spline function from core CRAN R software was used to perform the interpolation following Beddows et al. (2010). Log-normal fitting is also commonly used (e.g., Di Biagio et al., 2019; Di Biagio et al., 2017a; Formenti et al., 2018). To reduce noise in the data, we used the logarithm of the size distribution data for the interpolation. To ensure that the total number of particles before and after interpolation was consistent, the ratio between the total number of particles before and after the fitting was used to normalize the data. The total number of particles was calculated as follows:

$$N_{tot}(D_g) = \int_{D_{g,min}}^{D_{g,max}} \frac{dN(D_g)}{d\log D_g} \cdot d\log D_g \quad (4)$$

5.3.2.3 Particle loss correction

After interpolation, the merged geometrical size distributions were corrected for the particle loss along the sampling lines in order to allow the comparison of measurements from different instruments. The particle loss calculator (PLC) software (von der Weiden et al., 2009) was used to calculate the particle

loss percentage of each instrument. The input parameters for the PLC software included the geometry of the sampling line, the sampling flow rate, the particle density, and the dynamic shape factor χ. The particle bulk density was set to 2.90 ± 0.01 g cm^{-3} as measured using a helium pycnometer for particles ≤ 63 μm (Baldo et al., 2020), a value that is consistent with the results of a recent study by Richards-Thomas et al. (2020). However, from the analysis conducted on larger size fractions (≤ 125 μm) using the water penetration method, Butwin et al. (2020) found an average density value of 2.25 g cm^{-3} in Icelandic dust particles. For each instrument, the particle loss percentage was calculated assuming χ from 1.6 to 2.0 by 0.1 steps.

To retrieve the size distribution of the particles suspended in CESAM, the merged geometrical size distributions were divided into two size ranges which were corrected for particle loss in the sampling systems of SMPS and GRIMM, respectively. The particle size domain was assigned based on the geometrical size distributions of GRIMM and SMPS used to merge the data:

$$\frac{dN(D_g)}{d\log D_g} = \frac{dN(D_{g,SMPS})}{d\log D_{g,SMPS}} + \frac{dN(D_{g,GRIMM})}{d\log D_{g,GRIMM}} \quad (5)$$

For the SMPS, the loss of particles with D_g < 1 μm was less than 5%. For the GRIMM, the particle loss was up to 15% in the range between 1-2.5 μm, below 50% in the range between 2.5-5 μm, and reached 100% at D_g around 20 μm. However, the fraction of particles with diameter > 2.5 μm corresponded to less than 10-14% of the total numbers of particles measured by the GRIMM. Given this, the dominant part of the size distribution was measurable by the GRIMM and the SMPS. The variation in particle loss calculated using the examined χ values was generally below 10%, but over 50% at D_g around 20 μm. The size distributions were corrected as follows:

$$\left[\frac{dN(D_g)}{d\log D_g}\right]_{Corr,SMPS\text{-}GRIMM} = \frac{dN(D_{g,SMPS\text{-}GRIMM})}{d\log D_{g,SMPS\text{-}GRIMM}} \cdot \frac{1}{1 - L(D_{g,SMPS\text{-}GRIMM})} \quad (6)$$

where $dN(D_{g,SMPS\text{-}GRIMM})/dlogD_{g,SMPS\text{-}GRIMM}$ is the size distribution measured by the SMPS or GRIMM, and $L(D_{g,SMPS\text{-}GRIMM})$ is the proportion of particle lost as a function of D_g in the size range measured by the SMPS or GRIMM. Finally, the size distribution of the particles suspended in CESAM was obtained summing up the contributions of the SMPS and GRIMM in their specific size range:

$$\left[\frac{dN(D_g)}{d\log D_g}\right]_{CESAM} = \left[\frac{dN(D_g)}{d\log D_g}\right]_{Corr,SMPS} + \left[\frac{dN(D_g)}{d\log D_g}\right]_{Corr,GRIMM} \quad (7)$$

Subsequently, to retrieve the size distribution behind the inlet of shortwave (SW) instruments, the size distribution of the particles suspended in CESAM was further corrected for particle loss in the sampling systems of the aethalometer and nephelometer. For the aethalometer, the particle loss was below 5% at D_g < 1µm, up to 20% in the range between 1-2.5 µm, below 60% in the range between 2.5-5 µm, and reached 100% at D_g around 9 µm. The variation in particle loss calculated using the examined χ values was generally below 10%, but over 50% at D_g around 9 µm. The percentage difference between the loss correction estimated for the aethalometer and that obtained for the nephelometer was < 11%. The data were corrected as follows (Di Biagio et al., 2017a):

$$\left[\frac{dN(D_g)}{d\log D_g}\right]_{Aet\text{-}Nep} = \left[\frac{dN(D_g)}{d\log D_g}\right]_{CESAM} \cdot \left(1 - L(D_g)_{Aet\text{-}Nep}\right) \quad (8)$$

where $[dN(D_g)/dlogD_g]_{Aet\text{-}Nep}$ is the size distribution measured by the aethalometer or nephelometer and $L(D_g)_{Aet\text{-}Nep}$ is the particle loss as function of D_g estimated for the two instruments. The size distribution behind the inlet of SW-instruments was calculated as the average between the size distributions of the aethalometer and nephelometer. Ultimately, 735 SW-instrument geometrical size distribution $N_{sw}(D_g)$ were calculated. These were used to correct the absorption and scattering coefficients measured respectively by the aethalometer and nephelometer, and to retrieve the complex refractive index of Icelandic dust. An example of the procedure used to process the size distribution data is shown in Figure S2. Furthermore, two sensitivity simulations were performed to account for the error on the size distribution measurements ($\sqrt{dN(D_g)}$ according to the Poisson statistics), where $k(\lambda)$ and $n(\lambda)$ were

calculated using the observed dN plus or minus 1 SD as the upper and lower limits of the SMPS and GRIMM measurements.

Further uncertainty arises from the use of the Mie theory, which assumes homogeneous spherical particles. The particle morphology was not measured during the experiments, but previous research found that Icelandic dust particles can be irregular and present internal pores (Butwin et al., 2020; Richards-Thomas et al., 2020). We simplified the calculations of the optical properties to allow the comparison with previous studies. Most climate models also assume the dust particles to be spherical which however can affect the calculations of dust impacts (Huang et al., 2020).

5.3.3 Measurements of the spectral scattering coefficient

The aerosol scattering coefficient β_{sca} was measured by the nephelometer at 450, 550, and 700 nm. The nephelometer can only detect scattering angles (θ) from about 7º to 170º rather than from 0º to 180º causing a systematic uncertainty known as angular truncation error (Anderson et al., 1996; Anderson and Ogren, 1998). The truncation correction C_{trunc} for total scattering was estimated as follows:

$$C_{trunc}(\lambda, m, N_{sw}(D_g),) = \frac{\beta_{sca}(\lambda, m, N_{sw}(D_g), 0° - 180°)}{\beta_{sca}(\lambda, m, N_{sw}(D_g), 7° - 170°)} \quad (9)$$

where $\beta_{sca}(\lambda, m, N_{sw}(D_g), 0º\text{-}180º)$ is the scattering coefficient calculated for θ between 0º and 180º, and $\beta_{sca}(\lambda, m, N_{sw}(D_g), 7º\text{-}170º)$ is the scattering coefficient calculated for θ between 7º and 170º. The Python PyMieScatt package (Sumlin et al., 2018) was used to retrieve $\beta_{sca}(\lambda, m, N_{sw}(D_g), 0º\text{-}180º)$ and $\beta_{sca}(\lambda, m, N_{sw}(D_g), 7º\text{-}170º)$ at a given λ by Mie calculation for homogeneous spheres by varying the calculated SW-instrument geometrical size distribution $N_{sw}(D_g)$ and using the corresponding complex refractive index.

For single homogeneous spherical particles, the scattering intensity function $|S(X_s, m, \theta)|^2$ at given θ can be calculated using the Mie theory, where X_s is the size parameter ($X_s = \pi \cdot D_g \cdot \lambda^{-1}$) and m is the complex refractive index of particles of geometrical diameter D_g. The scattering intensity function can be

integrated over θ from 0º to 180º to obtain the single-particle total scattering efficiency (e.g., Anderson et al., 1996; Bohren and Hufmann, 1998):

$$Q_{sca}(\lambda, m, D_g) = \frac{1}{X_s^2} \cdot \int_0^{\pi} |S(X_s, m, \theta)|^2 \cdot \sin\theta \cdot d\theta \quad (10)$$

Finally, β_{sca} can be calculated as the integral of Q_{sca} over the particle size distribution $N(D_g)$ multiplied by the particle cross sectional area (e.g., Anderson et al., 1996; Bohren and Hufmann, 1998):

$$\beta_{sca}\left(\lambda, m, N(D_g)\right) = \int_{D_{g,min}}^{D_{g,max}} \frac{\pi \cdot D_g^2}{4} \cdot Q_{sca}(\lambda, m, D_g) \cdot \frac{dN(D_g)}{d\log D_g} \cdot d\log D_g \quad (11)$$

In this study, $\beta_{sca}(\lambda, m, N_{sw}(D_g), 0º\text{-}180º)$ was computed at a given λ by the Mie_SD function for polydisperse size distributions in the Python PyMieScatt package by inputting the calculated $N_{sw}(D_g)$ and the corresponding complex refractive index. To determine $\beta_{sca}(\lambda, m, N_{sw}(D_g), 7º\text{-}170º)$, first the angular scattering intensities $|S(X_s, m, \theta)|^2$ for θ between 7º and 170º were computed by the ScatteringFunction angular function, and then used in Equations (10-11) to obtain Q_{sca} and β_{sca}.

Subsequently, the truncation correction defined by Equation (9) was calculated at 450, 550 and 700 nm for each $N_{sw}(D_g)$. Ultimately, the average of the $C_{trunc}(\lambda)$ values obtained for different $N_{sw}(D_g)$ was used to correct the data. C_{trunc} decreased with increasing λ, and with the dust residence time in the chamber following the decrease in the contribution of the coarse fraction to the aerosol size distribution. $C_{trunc}(\lambda)$ was similar for different Icelandic dust samples and varied between 1.3-1.9. These results are comparable to the range of C_{trunc} values (from 1.2 to 1.7) reported by Di Biagio et al. (2019). The uncertainty on $C_{trunc}(\lambda)$ was estimated from the relative standard deviation (RSD) of $C_{trunc}(\lambda)$ obtained for different $N_{sw}(D_g)$. The uncertainty on $C_{trunc}(\lambda)$ was around 7-17%.

The scattering coefficient at a given λ was corrected by multiplying β_{sca} by C_{trunc}. The uncertainty on β_{sca} at 450, 550, and 700 nm was calculated using the error propagation method considering the photon counting and gas calibration uncertainty (5%), the standard deviation (SD) over 12-min intervals, and

the uncertainty on C_{trunc}. The uncertainty on β_{sca} corrected for truncation varied between 9%-19%. Once corrected for truncation, β_{sca} was extrapolated at the aethalometer operating wavelengths (370, 470, 520, 590, 660, 880, and 950 nm) using the scattering Ångström exponent ($å_{sca}$) which was obtained from the power-law fitting of $\beta_{sca}(\lambda)$ versus λ weighted by the inverse of the variance of $\beta_{sca}(\lambda)$. The uncertainty on β_{sca} at 370, 470, 520, 590, 660, 880, and 950 nm was estimated as the quadratic combination of the average error on β_{sca} corrected for truncation and the root-mean-square error (RMSE) of β_{sca} predicted at 450, 550, and 700 nm. The uncertainty on β_{sca} predicted was 11%-18%. β_{sca} values were reported in Mm^{-1}.

5.3.4 Measurements of the spectral absorption coefficient

The aerosol absorption coefficient β_{abs} was measured by the aethalometer at 370, 470, 520, 590, 660, 880, and 950 nm. The aethalometer measures attenuation (ATTN) of light passing through an aerosol-laden quartz filter, which is then converted into the attenuation coefficient (e.g., Weingartner et al., 2003):

$$\mathrm{ATTN} = \ln\frac{I_0}{I} \tag{12}$$

where I_0 is the intensity of light passing through the blank portion of the filter, and I is the intensity of light passing through the loaded filter.

$$\beta_{\mathrm{ATTN}}(\lambda) = \frac{\Delta\mathrm{ATTN}(\lambda)}{\Delta t}\cdot\frac{A}{V} \tag{13}$$

where β_{ATTN} is the attenuation coefficient (m^{-1}), A is the area of the aerosol collection spot (0.00005 ± 0.001 m^2) and V is the sampling flow rate (0.002 m^3 min^{-1}). ΔATTN ($ATTN_n - ATTN_{n-1}$) was calculated for n^{th} measurements over 2-min time intervals (Δt) which is the time resolution of the aethalometer.

β_{ATTN} contains the contributions of light absorption and scattering by the aerosol particles deposited on the filter and by the filter material itself. The aerosol absorption coefficient was obtained by correcting β_{ATTN} for measurements artefacts according to the correction scheme from Collaud Coen et al. (2010):

$$\beta_{abs}(\lambda) = \frac{\beta_{ATTN}(\lambda) - \alpha(\lambda) \cdot \beta_{sca}(\lambda)}{R(\lambda) \cdot C_{ref}(\lambda)} \quad (14)$$

where $\alpha(\lambda)\beta_{sca}(\lambda)$ is the scattering effect correction. $\beta_{sca}(\lambda)$ is the scattering coefficient weighted by the $\alpha(\lambda)$ parameter. This term represents the scattered radiation by the aerosol particles deposited on the filter and miscounted as attenuation. $C_{ref}(\lambda)$ is the multiple scattering effect correction, representing multiple scattering by the filter fibers. $R(\lambda)$ is the loading effect correction, which accounts for the reduced aethalometer response with time due to light-absorbing particles accumulating on the filter.

The parameter $\alpha(\lambda)$ was calculated using the formula from Arnott et al. (2005):

$$\alpha(\lambda) = A^{(d-1)} \cdot c \cdot \lambda^{-\mathring{a}_{sca} \cdot (d-1)} \quad (15)$$

where A and $\mathring{a}_{sca}$ were obtained from the power-law fitting of $\beta_{sca}(\lambda)$ (m^{-1}) versus λ (nm) weighted by the inverse of the variance of $\beta_{sca}(\lambda)$. The scattering coefficient $\beta_{sca}(\lambda)$ measured by the nephelometer, corrected for truncation, and extrapolated at the aethalometer wavelengths was used in the calculation. We assumed $c = 3.29 \cdot 10^{-4}$ and $d = 0.564$ as reported in Collaud Coen et al. (2010).

The obtained $\alpha(\lambda)$ increased with time as the particles were accumulating on the filter. Different λ showed similar values of the α parameters. In the Icelandic dust samples, $\alpha(\lambda)$ ranged from around 0.005 to 0.02, which is within the range (0.002 to 0.02) reported by Di Biagio et al. (2019) for mineral dust. The uncertainty on $\alpha(\lambda)$ varied between 17%-76% and was estimated by the error propagation through Equation (15) considering the uncertainty on the fitted parameters A and $\mathring{a}_{sca}$. The uncertainty on $\alpha(\lambda)$ was 35%-76% for the samples D3 and MIR45 which showed the largest errors on the fitted parameters, 29%-45% for the samples Maeli2 and H55, and 17%-27% for the sample Land1.

The multiple scattering effect correction C_{ref} was extrapolated at 370, 470, 520, 590, 660, 880, and 950 nm by the linear regression of C_{ref} at 450 and 660 nm estimated for mineral dust by Di Biagio et al. (2017b). C_{ref} varied from 4.3 at 370 nm to 3.3 at 950 nm. The uncertainty on C_{ref} determined by Di Biagio et al. (2017b) was 10%.

The loading effect correction R(λ) was calculated using the formula from Collaud Coen et al. (2010):

$$R(\lambda) = \left(\frac{1}{f(\lambda)} - 1\right) \cdot \frac{ATTN(\lambda)\%}{50\%} + 1 \quad (16)$$

where f(λ) depends on the aerosol absorption properties and is a function of SSA(λ):

$$f(\lambda) = a\left(1 - SSA(\lambda)\right) + 1 \quad (17)$$

We assumed a = 0.74 as reported in Collaud Coen et al. (2010). As an initial guess for R(λ), the single scattering albedo in Equation (17) was estimated using $\beta_{sca}(\lambda)$ measured by the nephelometer, corrected for truncation, and extrapolated at the aethalometer wavelengths, and $\beta_{abs}(\lambda)^*$ which is the absorption coefficient corrected only for the scattering effect (Di Biagio et al., 2019):

$$\beta_{abs}(\lambda)^* = \beta_{ATTN}(\lambda) - \alpha(\lambda) \cdot \beta_{sca}(\lambda) \quad (18)$$

$$SSA(\lambda)^* = \frac{\beta_{sca}(\lambda)}{\beta_{sca}(\lambda) + \beta_{abs}(\lambda)^*} \quad (19)$$

R(λ) increased with λ but decreased with time as particles were loaded onto a new filter. R(λ) obtained after the second iteration varied between 0.7 and 1 in different Icelandic dust samples which is within the range reported by Di Biagio et al. (2019) for mineral dust, from 0.5 to 1. The uncertainty on R(λ) was also estimated by applying the error propagation method and was generally ≤ 10% but varied between 10%-50% within the first 10 min that the particles were loaded onto a new filter.

The uncertainty on $\beta_{abs}(\lambda)$ corrected according to Equation (14) was calculated using the error propagation method considering the uncertainty on $\alpha(\lambda)$, $\beta_{sca}(\lambda)$, C_{ref}, and $R(\lambda)$. The uncertainty on $\beta_{abs}(\lambda)$ as 2-min intervals varied between 25%-78%. Ultimately, $\beta_{abs}(\lambda)$ was averaged over 12-min intervals, and the final uncertainty was calculated as the quadratic combination of SD and the average systematic error over 12-min intervals. The uncertainty on $\beta_{abs}(\lambda)$ as 12-min intervals varied between 27%-75%. $\beta_{abs}(\lambda)$ values were reported in Mm^{-1}.

5.3.5 Calculation of the aerosol spectral single scattering albedo

The scattering coefficient $\beta_{sca}(\lambda)$ and absorption coefficient $\beta_{abs}(\lambda)$ obtained from the nephelometer and aethalometer measurements were used to calculate 12-min average values of the extinction coefficient $\beta_{ext}(\lambda)$ in Mm^{-1} at 370, 470, 520, 590, 660, 880, and 950 nm:

$$\beta_{ext}(\lambda) = \beta_{sca}(\lambda) + \beta_{abs}(\lambda) \quad (20)$$

The single scattering albedo SSA(λ) was also calculated at a 12-min resolution:

$$SSA(\lambda) = \frac{\beta_{sca}(\lambda)}{\beta_{sca}(\lambda)+\beta_{abs}(\lambda)} \quad (21)$$

The uncertainty on $\beta_{ext}(\lambda)$ was 10%-17%, while the uncertainty on SSA(λ) varied between 15%-25%, which were estimated by the error propagation through Equation (20) and Equation (21), respectively, considering the uncertainty on $\beta_{sca}(\lambda)$ and $\beta_{abs}(\lambda)$.

In addition, the experiment-averaged single scattering albedo SSA_{avg} at 370, 470, 520, 590, 660, 880, and 950 nm was retrieved from the slope (m_{RMA}) of the linear regression between $\beta_{sca}(\lambda)$ and $\beta_{abs}(\lambda)$ starting from 30 min after the dust injection peak to 2.5 h (Di Biagio et al., 2019; Moosmuller et al., 2012):

$$SSA_{avg}(\lambda) = \left(1 + \frac{1}{m_{RMA}(\lambda)}\right)^{-1} \quad (22)$$

The linear fitting was performed using the reduced major axis (RMA) regression. The linear fitting was performed using the reduced major axis (RMA) regression, because both variables (x and y) come from measurements and are subject to errors (Ayers, 2001; Smith, 2009). Overall, a strong correlation between $\beta_{sca}(\lambda)$ and $\beta_{abs}(\lambda)$ was observed ($R^2 > 0.99$). The uncertainty on $SSA_{avg}(\lambda)$ calculated considering the error on m_{RMA} in Equation (22) was $\leq 8\%$.

5.3.6 Retrieval of the spectral complex refractive index

The absorption coefficient and scattering coefficient were also computed using the size distribution data as described in Section 5.3.3. hereinafter referred to as $\beta_{abs,model}(\lambda)$ and $\beta_{sca,model}(\lambda)$, respectively. The SW-instrument geometrical size distributions $N_{sw}(D_g)$ obtained using the 735 different combinations of the input parameters (X, n, and k) values generated an equal number of $\beta_{abs,model}(\lambda)$ and $\beta_{sca,model}(\lambda)$ scenarios.

The complex refractive index at 370, 470, 520, 590, 660, 880, and 950 nm was determined through the comparison between $\beta_{abs,model}(\lambda)$ and $\beta_{sca,model}(\lambda)$ and the Mie coefficients estimated from the nephelometer and aethalometer measurements hereinafter referred to as $\beta_{abs,meas}(\lambda)$ and $\beta_{sca,meas}(\lambda)$. The modelled and measured Mie coefficients were both calculated with a temporal resolution of 12 min.

The complex refractive index was retrieved at a 12-min resolution by comparing $\beta_{abs,meas}(\lambda)$ and $\beta_{sca,meas}(\lambda)$ with $\beta_{abs,model}(\lambda)$ and $\beta_{sca,model}(\lambda)$ at individual time points throughout the time series. For each $\beta_{abs,model}(\lambda)$ and $\beta_{sca,model}(\lambda)$ scenario, we estimated the model error as the percentage difference (%diff) respectively with $\beta_{abs,meas}(\lambda)$ and $\beta_{sca,meas}(\lambda)$. To account for the uncertainty on $\beta_{abs,meas}(\lambda)$ and $\beta_{sca,meas}(\lambda)$, we used $\beta_{abs,meas}(\lambda) \pm 1$ SD and $\beta_{sca,meas}(\lambda) \pm 1$ SD as the upper and lower limits of the measurements. We selected $\beta_{abs,model}(\lambda)$ and $\beta_{sca,model}(\lambda)$ scenarios with the lowest model error corresponding to 0.1-0.5 quantile of %diff. Subsequently, the results for $\beta_{abs,meas}(\lambda) \pm 1$ SD and $\beta_{sca,meas}(\lambda) \pm 1$ SD were examined, and only the $\beta_{abs,model}(\lambda)$ and $\beta_{sca,model}(\lambda)$ scenarios common to all six datasets were kept. $k(\lambda)$ and $n(\lambda)$ were

retrieved from the selected scenarios. Since the comparison between modelled and measured Mie coefficients resulted in multiple solutions for k(λ) and n(λ), we calculated the mean of the k solutions and of the n solutions, which showed an uncertainty up to 99% for k(λ) and < 3% for n(λ).

In addition, the experiment-averaged complex refractive index at 370, 470, 520, 590, 660, 880, and 950 nm was determined based on the linear fit between $\beta_{abs,meas}(\lambda)$ and $\beta_{abs,model}(\lambda)$, and $\beta_{sca,meas}(\lambda)$ and $\beta_{sca,model}(\lambda)$ starting from 30 min after the dust injection peak to 2.5 h. To retrieve the experiment-averaged real index $n_{avg}(\lambda)$ and imaginary index $k_{avg}(\lambda)$, we updated the method applied to determine k(λ) and n(λ) at a 12-min resolution. We selected only the model estimates which showed a high correlation with observations (R^2>0.70). The modelled and measured Mie coefficients were then compared based on the RMSE instead of using the %diff at individual time points. The uncertainty on $k_{avg}(\lambda)$ was up to 99%, while the uncertainty on $n_{avg}(\lambda)$ was < 2%.

5.4 Results

5.4.1 Aerosol size distribution and effective diameter

Figure S1 shows some examples of the geometrical size distributions of particles obtained using different dynamic shape factors and complex refractive indices.

For spherical particles (χ = 1 and $D_m = D_g$), the D_g range measured by the SMPS was from 0.019 μm to 0.87 μm. For non-spherical particles (χ>1), D_g decreased with increasing χ as defined by Equation (1). In this study, χ was varied between 1.6 and 2.0 by 0.1 steps. After the conversion of D_m to D_g, the D_g range for the SMPS was around 0.015-0.58 for χ= 1.6, 0.015-0.56 for χ= 1.7, 0.014-0.53 for χ= 1.8, 0.014-0.51 for χ= 1.9, 0.013-0.49 for χ= 2.0.

The D_g range measured by the GRIMM was from 0.25 μm to 32 μm assuming the complex refractive index of PSL reference particles (n = 1.59 and k = 0.000). The complex refractive indices examined in this study included n from 1.57 to 1.63 by 0.01 steps and k from 0.000 to 0.020 by 0.001 steps. The correction factors used to convert D_{op} into D_g had a considerable impact on D_g > 0.6 μm. D_g increased with k, while there was no correlation between D_g and n, which mainly affected D_g around 1 μm. The

variation of the length of the GRIMM D_g intervals showed the same pattern for different n and was driven by k. The minimum D_g varied between around 0.24-0.25 µm. For $k \leq 0.003$, the maximum D_g sharply increased with k from 31.5-32.5 µm to 85.6-90.4 µm. For $k > 0.003$, the maximum D_g showed only a small variation reaching up to around 94 µm (Figure S3).

The overlapping interval between the SMPS and GRIMM data was reduced with increasing χ. The GRIMM size distributions tend to spread out between 0.6-2 µm (Figure S1) consequently reducing the smoothness of the fitted size distributions within this size range which is likely due to the larger uncertainty in the correction factors at these D_g values (Formenti et al., 2021). After correcting the data for the loss along the instrument sampling lines, the size distribution of the particles suspended in CESAM was in the D_g range up to 20 µm, while the size distribution behind the inlet of SW-instruments was in the D_g range up to 9 µm.

The effective diameter (D_{eff}) can be used as a measure of the aerosol size distribution as defined by the following equation (Hansen, 1971):

$$D_{eff} = \frac{\int_{D_{g,min}}^{D_{g,max}} D_g^3 \cdot \frac{dN(D_g)}{d\log D_g} \cdot d\log D_g}{\int_{D_{g,min}}^{D_{g,max}} D_g^2 \cdot \frac{dN(D_g)}{d\log D_g} \cdot d\log D_g} \quad (23)$$

D_{eff} differs from the simple mean diameter because the particle surface area was included as a weight factor. Since light scattering is proportional to the particle surface area, D_{eff} is relevant for describing the scattering properties of size distributions (Hansen, 1971). D_{eff} was calculated for the aerosol fine fractions ($D_g \leq 1$ µm) and coarse fractions ($D_g > 1$ µm) by varying the input parameters χ, n, and k in the examined ranges. Overall, the effective diameter of the coarse fraction ($D_{eff,coarse}$) showed a strong positive correlation with k (R^2 = 0.6-0.8), while the correlation between $D_{eff,coarse}$ and χ or n was low (R^2 < 0.1). The correlation between the effective diameter of the fine fraction ($D_{eff,fine}$) and the input parameters was also low. Figure S4 shows an example of the comparison between D_{eff} calculated using the SW-Instruments size distributions and the input parameters χ, n, and k.

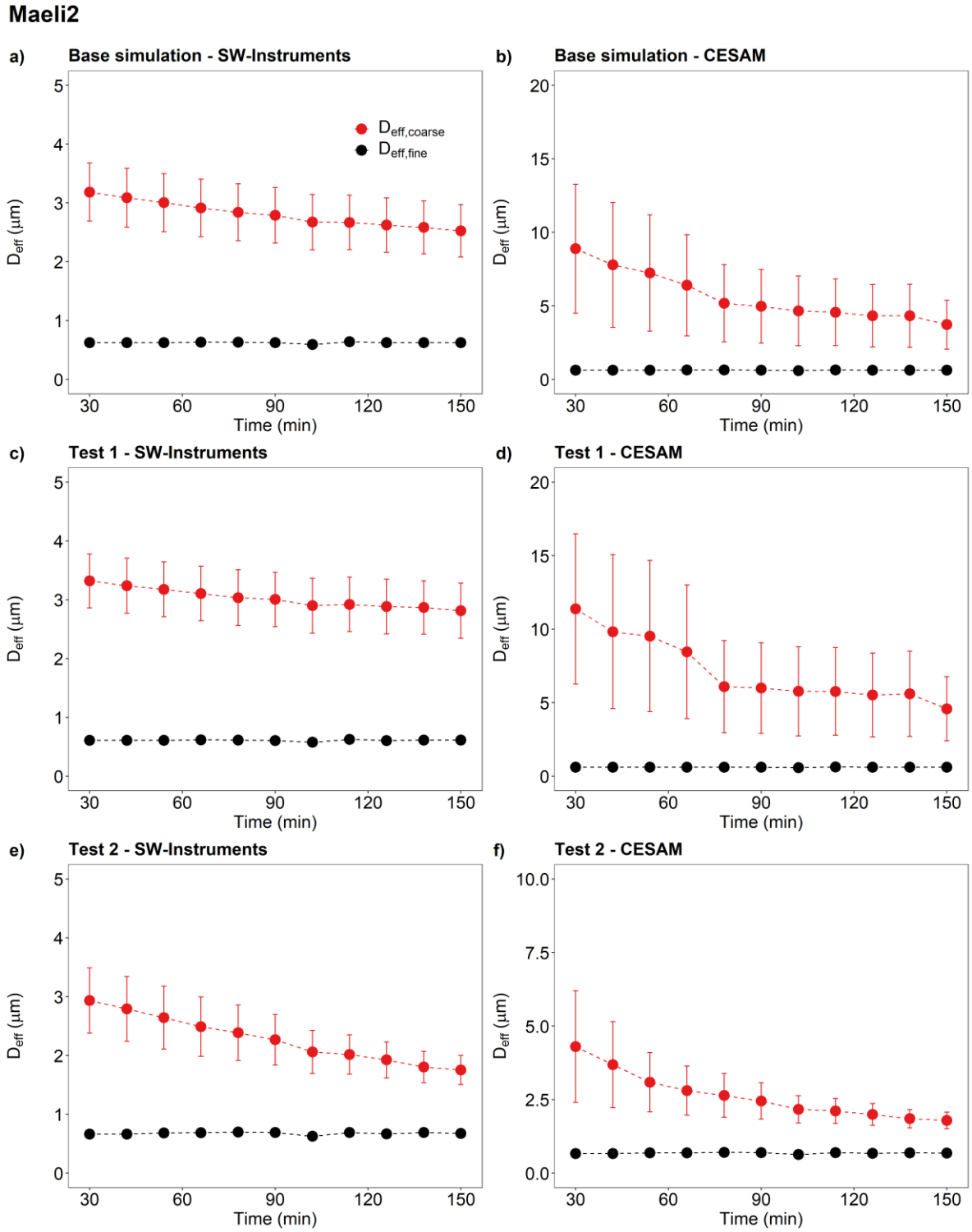

Figure 5.3: Effective diameters D_{eff} of dust particles behind the inlet of SW instruments and in CESAM from 30 min after the injection peak to 2.5 h. a-b) Base simulation; c-d) Test 1; e-f) Test 2. D_{eff} was calculated for particles > 1 µm ($D_{eff,coarse}$) and ≤ 1 µm ($D_{eff,fine}$). Data were reported as 12-min average. Sample ID: Maeli2.

Here, D_{eff} was reported as the average of the D_{eff} values obtained using different χ-n-k combinations. We assumed the RSD of the results as the uncertainty on D_{eff}. $D_{eff,coarse}$ decreased with time due to the rapid deposition of the largest particles in the chamber. In different Icelandic dust samples, $D_{eff,coarse}$ behind the inlet of SW instruments varied from ~3.1-3.5 μm after around 30 min from the injection peak to 2.5-2.7 μm after around 2.5 h from the injection peak. For the particles suspended in CESAM, $D_{eff,coarse}$ varied from 8.4-11 μm (30 min after the injection peak) to 3.7-4.4 μm (2.5 h after the injection peak). $D_{eff,fine}$ remained relatively constant over the duration of the experiments varying between 0.5-0.7 μm in different samples. The uncertainty on $D_{eff,coaurse}$ was < 14%-19% for the SW-instruments, and 44%-56% for the particles suspended in CESAM, while the uncertainty on $D_{eff,fine}$ was less than 3%. Figure 5.3 shows an example of the comparison between D_{eff} calculated for the SW-Instruments and D_{eff} calculated for the particles suspended in CESAM. The D_{eff} results from the sensitivity studies to account for the error on the SMPS and GRIMM measurements were consistent within the uncertainties with the results from the base simulation. In sensitivity Test 1, calculations were performed using the SMPS and GRIMM data plus 1SD uncertainty. In Test 2, we used the SMPS and GRIMM data minus 1SD uncertainty. The difference between the D_{eff} results from the sensitivity studies and D_{eff} from the base simulation was not significant because it was less than three times the square root of the sum of their squared uncertainties. For the SW-instruments, $D_{eff,coarse}$ decreased from ~3.3-3.6 μm (30 min after the injection peak) to 2.8-3.0 μm (2.5 h min after the injection peak) in Test 1, and from 2.8-3.3 (30 min after the injection peak) to 1.4-1.9 (2.5 h min after the injection peak) in Test 2. For the particles suspended in CESAM, $D_{eff,coarse}$ decreased from ~10-12 μm (30 min after the injection peak) to 4.6-5.7 μm (2.5 h min after the injection peak) in Test 1, and from 3.3-5.8 (30 min after the injection peak) to 1.6-2.0 (2.5 h min after the injection peak) in Test 2. The uncertainty on $D_{eff,coarse}$ was 12%-17% in Test 1 and 9%-22% in Test 2 for the SW-Instruments, and 41%-55% in Test 1 and 9%-50% in Test 2 for the particles suspended in CESAM. $D_{eff,fine}$ results were not considerably affected in the sensitivity studies.

5.4.2 Spectral extinction and absorption coefficients, single scattering albedo, and complex refractive index

Figure 5.4 shows a typical example of the spectral extinction coefficient $\beta_{ext}(\lambda)$, absorption coefficient $\beta_{abs}(\lambda)$, and single scattering albedo SSA(λ) at 12-min resolution obtained for Icelandic dust. $\beta_{ext}(\lambda)$ and $\beta_{abs}(\lambda)$ decreased with λ, the largest variation being observed between 370 and 590 nm. On the other hand, SSA(λ) increased with λ. $\beta_{ext}(\lambda)$ and $\beta_{abs}(\lambda)$ decreased with time, while SSA(λ) was relatively constant. $\beta_{ext}(\lambda)$, $\beta_{abs}(\lambda)$ and SSA(λ) results from the sensitivity studies were consistent within their uncertainty with the results of the base simulation (Figure 5.4).

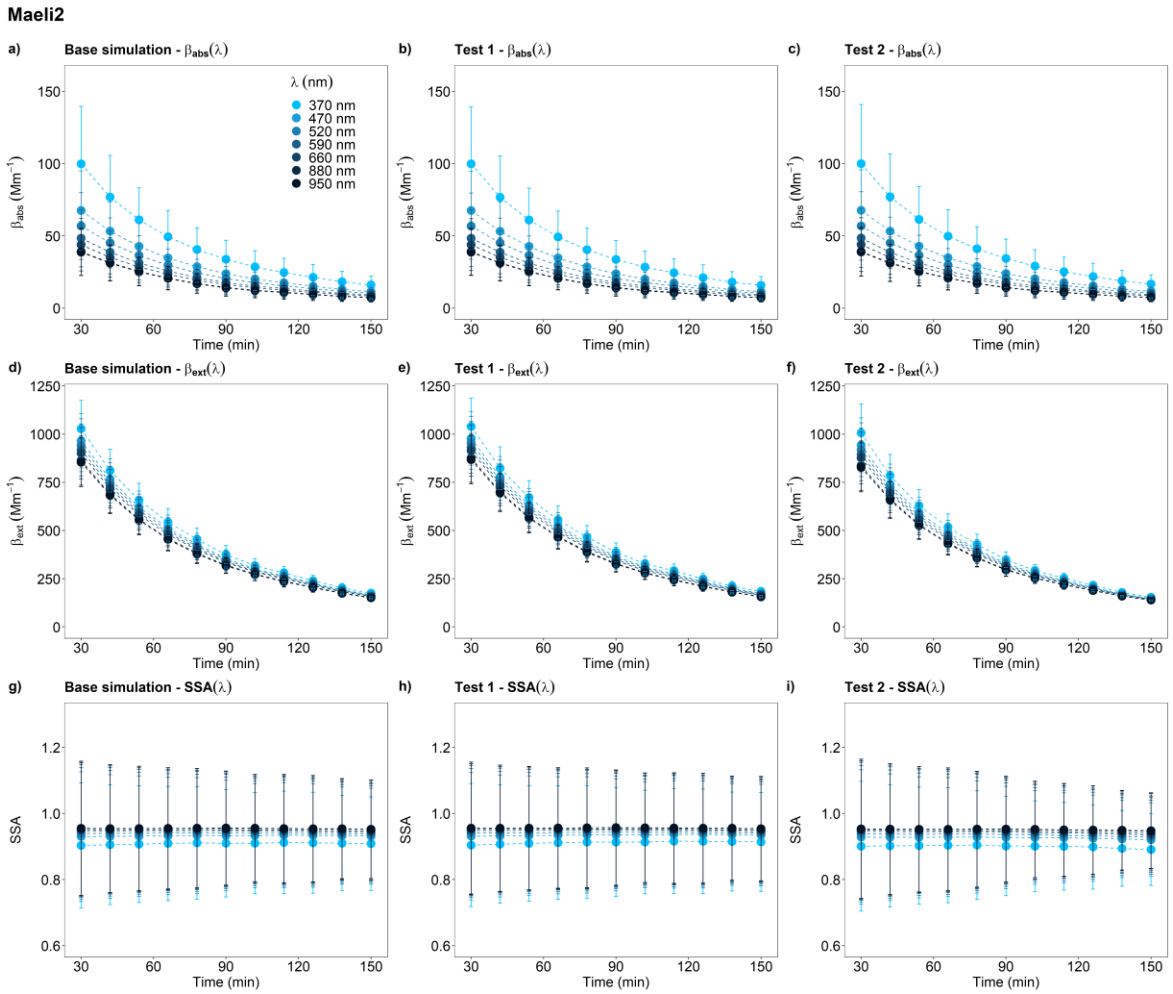

Figure 5.4: Extinction coefficient $\beta_{ext}(\lambda)$, absorption coefficient $\beta_{abs}(\lambda)$, and single scattering albedo SSA(λ) at λ = 370, 470, 520, 590, 660, 880, 950 nm, from 30 min after the injection peak to 2.5 h. a-c) Base simulation; d-f) Test 1; g-i) Test 2. Data were reported as 12-min average. Sample ID: Maeli2.

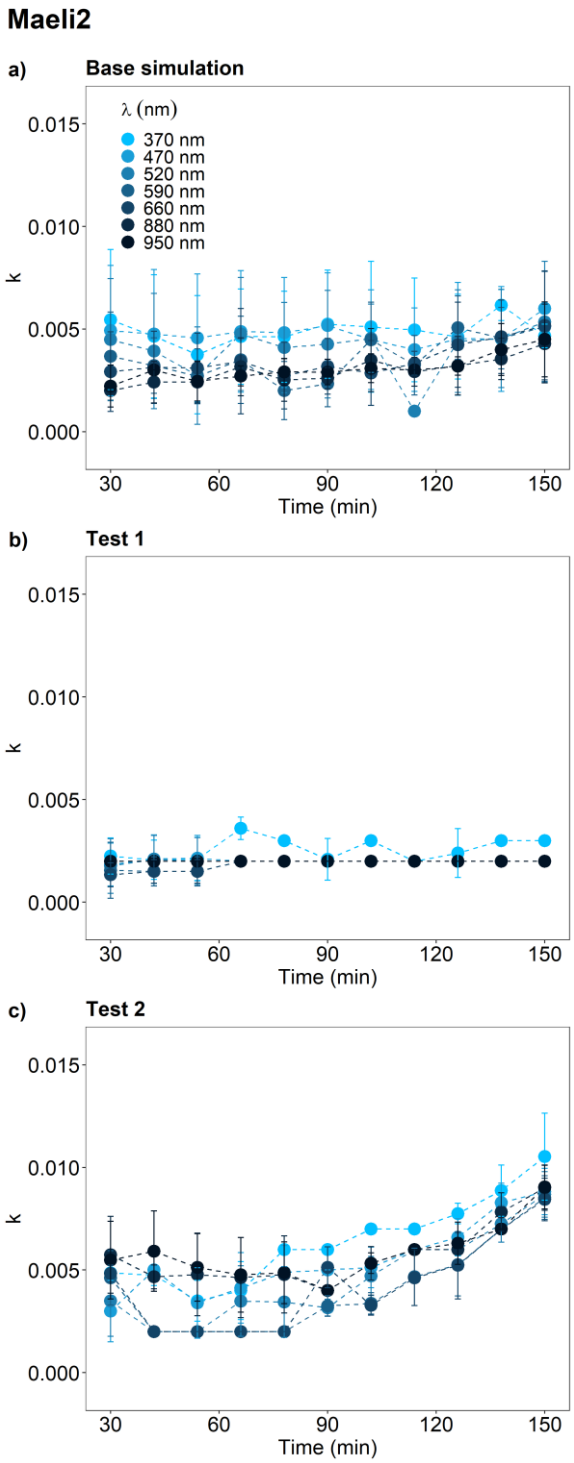

Figure 5.5: Imaginary part of the complex refractive index k(λ) at λ = 370, 470, 520, 590, 660, 880, 950 nm, from 30 min after the injection peak to 2.5 h. a) Base simulation; b) Test 1; c) Test 2. Data were retrieved at 12-min resolution. Sample ID: Maeli2.

The real part of the refractive index n(λ) did not show a dependence on λ and time. n(λ) varied within the range of the examined n values (from 1.57 to 1.63 by 0.01 steps) with an uncertainty of < 3% in the base simulation, Test 1 and Test 2. For the imaginary part of the refractive index k(λ), the data with 12-min resolution were too noisy to identify a clear relationship with time or λ. In Test 1, k(λ) was almost constant with time and λ. In Test 2, k did not show a clear dependence on λ. For the sample MIR45, k(λ) exhibited an increasing trend over time. For D3 and Maeli2, k(λ) increased after around 1.5 h from the dust injection peak. For H55 and Land1, k(λ) did not show a temporal trend. Figure 5.5 reports an example of the imaginary index of Icelandic dust at 12-min resolution. The uncertainty on k(λ) at 12-min resolution varied up to 99% in the base simulation, 198% in Test 1, and 79% in Test 2.

The experiment-averaged single scattering albedo SSA_{avg} increased with λ from 370 to 590 nm, while it was relatively constant between 590 and 950 nm (Figure 5.6). $SSA_{avg}(\lambda)$ varied from 0.93 at 370 nm to 0.96 at 950 nm for the sample D3, from 0.94 to 0.96 for H55, from 0.91 to 0.96 for Land 1, from 0.90 to 0.95 for Maeli2, and from 0.90 to 0.94 for MIR45 (Table 5.1). The uncertainty on $SSA_{avg}(\lambda)$ was ≤ 8%. The $SSA_{avg}(\lambda)$ results from the sensitivity studies were consistent within their uncertainty with the results of the base simulation (Table S1).

Figure 5.7 shows the experiment-averaged imaginary index $k_{avg}(\lambda)$ of different Icelandic dust samples. k_{avg} decreased with λ, and varied from 0.006 at 370 nm to 0.002 at 950 nm for the sample D3, from 0.005 to 0.003 for H55, Land1, and Maeli2, and from 0.005 to 0.003 for MIR45 (Table S2). In Test 1, $k_{avg}(\lambda)$ varied between 0.003 and 0.001 for H55 and Land1, while it was constant at around 0.002 for Maeli2 and MIR45. For the sample D3, $k_{avg}(\lambda)$ was 0.002 at 370 nm and around 0.001 for all the other λ (Table S2). In Test 2, k_{avg} increased with λ from 0.002 at 370 nm to 0.007 at 950 nm for the sample H55. For all the other Icelandic dust samples, the relationship between k_{avg} and λ was not monotonic. k_{avg} varied in the range between 0.002-0.007 for D3, 0.003-0.006 for Land1, 0.002-0.005 for Maeli2, and 0.005-0.007 for MIR45 (Table S2). The uncertainty on $k_{avg}(\lambda)$ was generally < 85% in the base simulation and Test 1, and < 70% in Test 2.

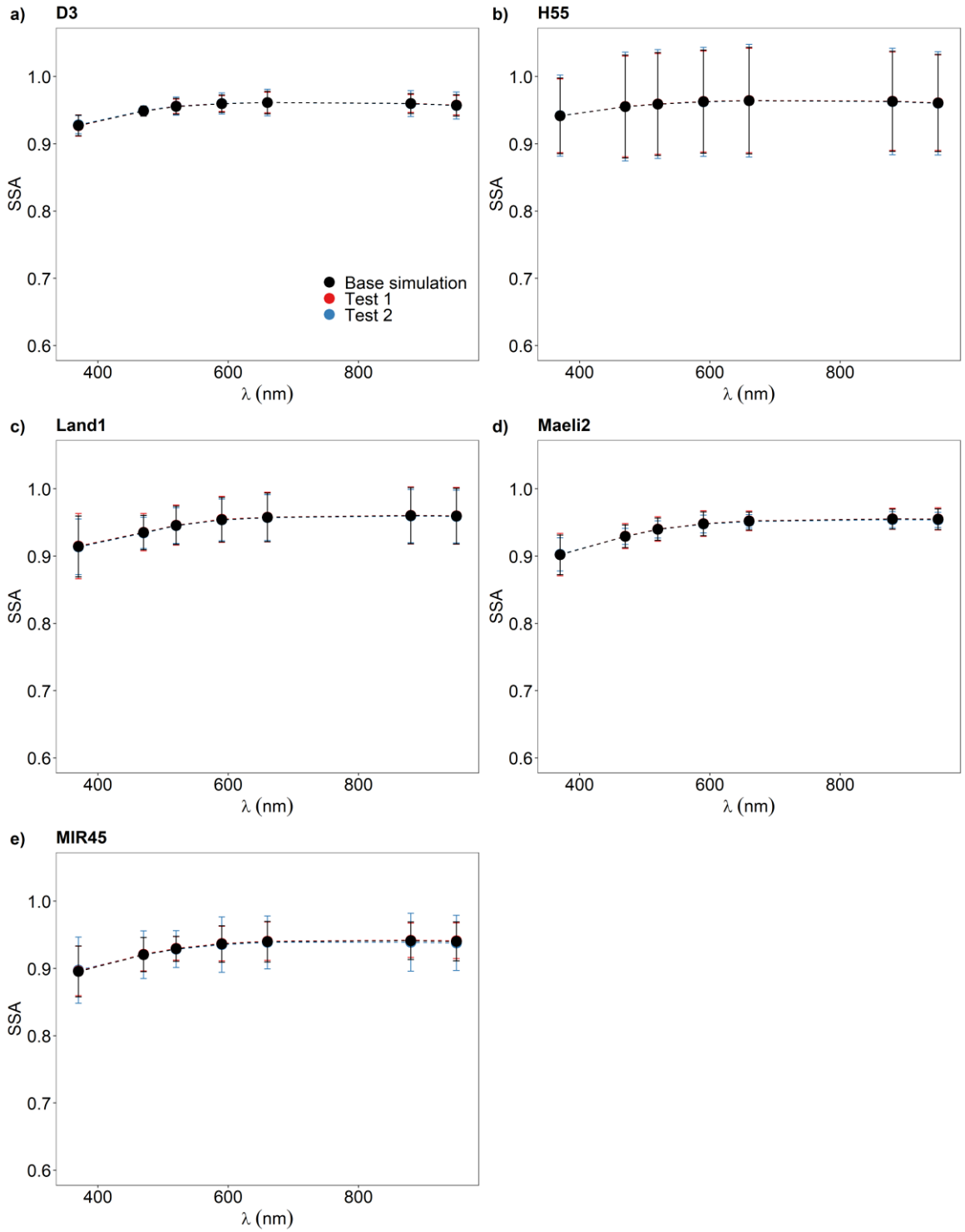

Figure 5.6: Experiment-averaged single scattering albedo $SSA_{avg}(\lambda)$ at λ = 370, 470, 520, 590, 660, 880, 950 nm of Icelandic dust samples for the base simulation (Table 5.1). $SSA_{avg}(\lambda)$ results from the base simulation are consistent with the results from Test 1 and Test 2 (see Table S1).

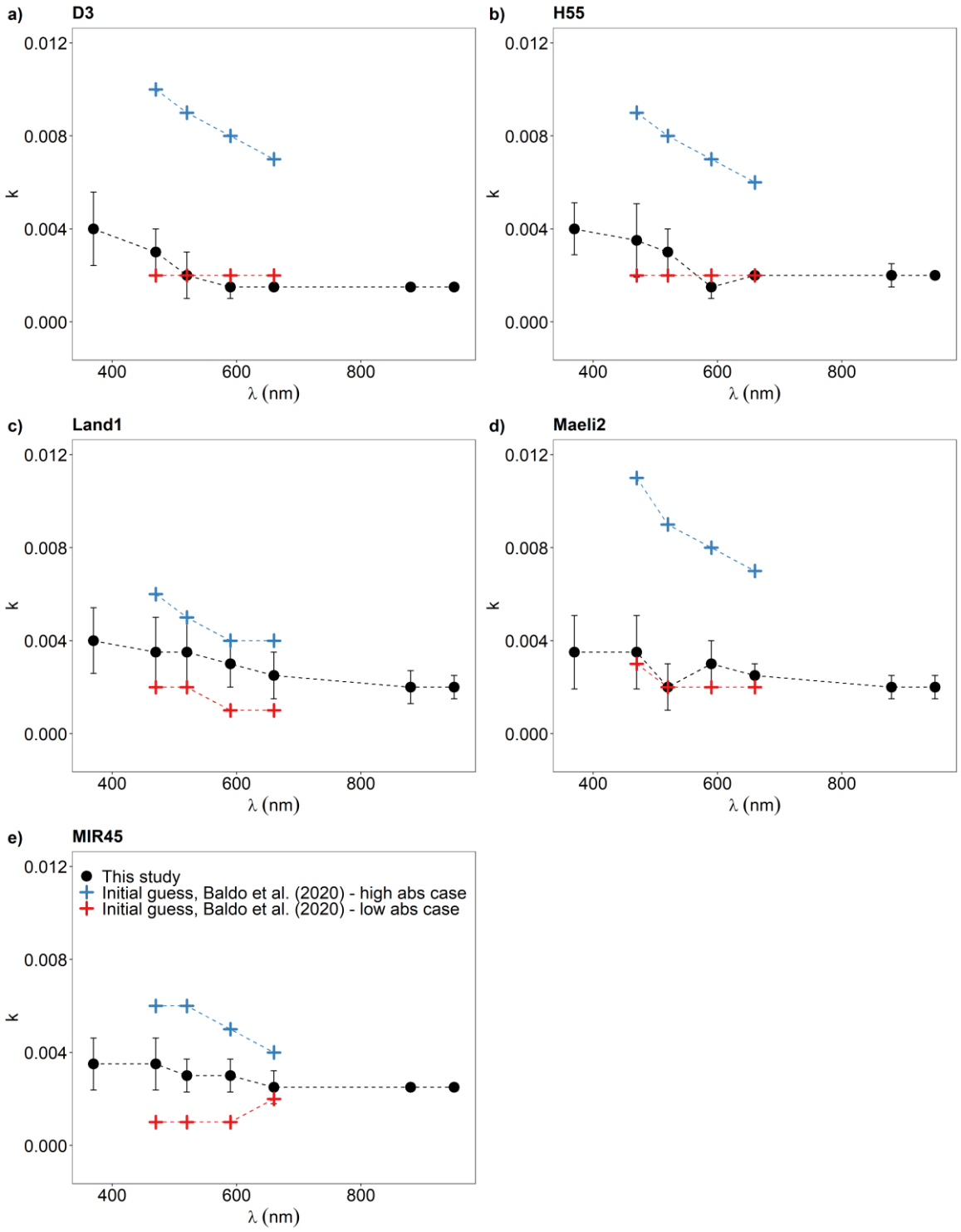

Figure 5.7: Comparison between the experiment-averaged imaginary index $k_{avg}(\lambda)$ at λ = 370, 470, 520, 590, 660, 880, 950 nm of Icelandic dust (Table 5.2) and the initial estimates by Baldo et al. (2020) based on the mineralogical composition (low and high absorption case).

The experiment-averaged real index $n_{avg}(\lambda)$ was not dependent on λ. $n_{avg}(\lambda)$ varied in the range between 1.59-1.62 in the base simulation, 1.58-1.61 in Test 1, and 1.57-1.63 in Test 2 (Table S3). Overall, the uncertainty on $n_{avg}(\lambda)$ was < 2%.

5.5 Discussion

The Icelandic dust samples examined in this study showed similar spectral optical properties. The spectral single scattering albedo and the imaginary index, which quantify respectively the proportion of scattering to the total extinction and absorption of aerosol particles, showed opposite trends. $SSA_{avg}(\lambda)$ increased from 0.90-0.94 at 370 nm to 0.94-0.96 at 950 nm in different samples (Table 5.1), while $k_{avg}(\lambda)$ decreased from 0.005-0.006 at 370 nm to 0.002-0.003 at 950 nm in the base simulation (Table S2). Absorption by mineral dust is highest in the UV-visible spectrum (around 15%) and decreases towards the near-infrared to around 2% (Di Biagio et al., 2019), in particular the presence of iron oxide minerals which have specific absorption bands in the UV-visible spectrum (Caponi et al., 2017; Derimian et al., 2008; Di Biagio et al., 2019; Dubovik et al., 2002; Engelbrecht et al., 2016; Formenti et al., 2014; Lafon et al., 2006; Moosmuller et al., 2012; Redmond et al., 2010).

$k_{avg}(\lambda)$ was sensitive to the size distribution. In Test 1, k_{avg} variation with respect to λ was less evident (Table S2). In Test 2, k_{avg} increased with λ for the sample H55, while k_{avg} dependence on λ was not monotonic for the other Icelandic dust samples (Table S2). Overall, $k_{avg}(\lambda)$ estimates from Test 1 were lower than the base simulation and Test 2 (Table S2). Table S4 reports a summary of the comparison between $SSA_{avg}(\lambda)$ calculated using the measured Mie coefficients and the experiment-averaged single scattering albedo retrieved using the complex refractive indices obtained for the base simulation, Test 1, and Test 2. Although the RMSE values were generally low, the correlation between the measured and modelled single scattering albedo tend to be higher in the base simulation and Test 1 compared to Test 2 (Table S4). Di Biagio et al. (2019) chose to average the k values from all three scenarios. Here the increase of k with wavelength in Test 2 is hard to explain, suggesting that Test 2 results are not realistic. Based on this, we chose to combine the results from the base simulation and Test 1 to obtain a single set of values for the imaginary part (Table 5.2) and real part (Table 5.3) of the complex refractive index. In

Table 5.2, $k_{avg}(\lambda)$ decreased from 0.004 at 370 nm to 0.002-0.003 at 950 nm in different samples, while $n_{avg}(\lambda)$ was 1.60-1.61 in Table 5.3.

The complex refractive index of Icelandic dust was retrieved based on the comparison between β_{ext} measured and β_{ext} computed using the particle size distribution behind the inlet of SW-instruments. The sensitivity simulations mainly affected particles > 1 µm. $D_{eff,coarse}$ behind the inlet of SW-instruments decreased from around 3.1-3.5 µm (30 min after the injection peak) to 2.5-2.7 µm (2.5 h min after the injection peak) in the base simulation, from 3.3-3.6 µm to 2.8-3.0 µm in Test 1, and from 2.8-3.3 µm to 1.4-1.9 µm in Test 2. The results from the base simulation and Test 1 were consistent with previous measurements of the size distribution of dust aerosols conducted at CESAM, where $D_{eff,coarse}$ behind the inlet of SW-instruments varied from 3-4 µm to 2-3 µm (Di Biagio et al., 2019). The results of $D_{eff,coarse}$ from Test 2 were slightly lower than the range of values reported by Di Biagio et al. (2019). It was not possible to define a clear relationship between $D_{eff,coarse}$ and SSA(λ) or k(λ). SSA(λ) was almost constant with time, while k(λ) results at a 12-min resolution were noisier. As a result, the slope of the regression line between $D_{eff,coarse}$ and SSA(λ) or k(λ) was close to zero and the relationship between these parameters mainly depended on the intercept values.

Table 5.1: Experiment-averaged single scattering albedo $SSA_{avg}(\lambda)$ ± estimated uncertainty at λ = 370, 470, 520, 590, 660, 880, 950 nm of Icelandic dust for the base simulation. $SSA_{avg}(\lambda)$ results from the base simulation are consistent with the results from Test 1 and Test 2 (see Table S1).

Sample ID	$SSA_{avg}(\lambda)$						
	370 nm	470 nm	520 nm	590 nm	660 nm	880 nm	950 nm
D3	0.93 ± 0.02	0.95 ± 0.01	0.96 ± 0.01	0.96 ± 0.01	0.96 ± 0.02	0.96 ± 0.01	0.96 ± 0.02
H55	0.94 ± 0.06	0.96 ± 0.08	0.96 ± 0.08	0.96 ± 0.08	0.96 ± 0.08	0.96 ± 0.07	0.96 ± 0.07
Land1	0.91 ± 0.05	0.94 ± 0.03	0.95 ± 0.03	0.95 ± 0.03	0.96 ± 0.04	0.96 ± 0.04	0.96 ± 0.04
Maeli2	0.90 ± 0.03	0.93 ± 0.02	0.94 ± 0.02	0.95 ± 0.02	0.95 ± 0.01	0.96 ± 0.01	0.95 ± 0.02
MIR45	0.90 ± 0.04	0.92 ± 0.03	0.93 ± 0.02	0.94 ± 0.03	0.94 ± 0.03	0.94 ± 0.03	0.94 ± 0.03

Table 5.2: Experiment-averaged imaginary index $k_{avg}(\lambda)$ ± estimated uncertainty at λ = 370, 470, 520, 590, 660, 880, 950 nm of Icelandic dust. $k_{avg}(\lambda)$ data are the mean of the results of the base simulation and Test 1 in Table S2.

Sample ID	$k_{avg}(\lambda)$						
	370 nm	470 nm	520 nm	590 nm	660 nm	880 nm	950 nm
D3	0.004 ± 0.002	0.003 ± 0.001	0.002 ± 0.001	0.002 ± 0.001	0.002 ± 0	0.002 ± 0	0.002 ± 0
H55	0.004 ± 0.001	0.004 ± 0.002	0.003 ± 0.001	0.002 ± 0.001	0.002 ± 0	0.002 ± 0.001	0.002 ± 0
Land1	0.004 ± 0.001	0.004 ± 0.002	0.004 ± 0.002	0.003 ± 0.001	0.003 ± 0.001	0.002 ± 0.001	0.002 ± 0.001
Maeli2	0.004 ± 0.002	0.004 ± 0.002	0.002 ± 0.001	0.003 ± 0.001	0.003 ± 0.001	0.002 ± 0	0.002 ± 0.001
MIR45	0.004 ± 0.001	0.004 ± 0.001	0.003 ± 0.001	0.003 ± 0.001	0.003 ± 0.001	0.003 ± 0	0.003 ± 0

Table 5.3: Experiment-averaged real index $n_{avg}(\lambda)$ ± estimated uncertainty at λ = 370, 470, 520, 590, 660, 880, 950 nm of Icelandic dust. $n_{avg}(\lambda)$ data are the mean of the results of the base simulation and Test 1 in Table S3.

Sample ID	$n_{avg}(\lambda)$						
	370 nm	470 nm	520 nm	590 nm	660 nm	880 nm	X950 nm
D3	1.60 ± 0.01	1.60 ± 0.01	1.60 ± 0.01	1.60 ± 0.01	1.60 ± 0.02	1.60 ± 0.02	1.60 ± 0.01
H55	1.60 ± 0.01	1.60 ± 0.01	1.60 ± 0.01	1.60 ± 0.01	1.61 ± 0.02	1.60 ± 0.01	1.60 ± 0
Land1	1.60 ± 0.01	1.60 ± 0.01	1.60 ± 0.01	1.60 ± 0.01	1.61 ± 0.01	1.60 ± 0.01	1.61 ± 0.01
Maeli2	1.60 ± 0.01	1.60 ± 0.01	1.60 ± 0.02	1.61 ± 0.01	1.60 ± 0.01	1.61 ± 0.01	1.61 ± 0.01
MIR45	1.60 ± 0.01	1.60 ± 0.01	1.60 ± 0.01	1.60 ± 0.01	1.61 ± 0.01	1.60 ± 0.01	1.60 ± 0.01

5.5.1 Spectral complex refractive index and single scattering albedo of Icelandic dust comparison with the literature data, volcanic ash, and low-latitude dust

Currently, only a limited number of studies have investigated the optical properties of Icelandic dust. An initial estimates of the complex refractive index of the Icelandic dust samples examined in this study was provided by Baldo et al. (2020), where the real and imaginary part of the complex refractive index were retrieved using the volume-averaged mineralogical composition estimated from the same experiments at CESAM and by applying reference complex refractive indices of individual minerals. The real part of the volume-averaged refractive index ranged from 1.57-1.63 between 470 and 660 nm.

The imaginary part of the volume-averaged refractive index was sensitive to the reference refractive indices of magnetite applied in the calculations, and k(λ) varied up to 1 order of magnitude in different absorption scenarios. In the high absorption case, k decreased from 0.006-0.01 at 470 nm to 0.004-0.007 at 660 nm in different samples, while k(λ) was between 0.001 and 0.003 in the low absorption case (Baldo et al., 2020). In Zubko et al. (2019), the complex refractive index of Icelandic dust was retrieved based on the measurements of the angular scattered-light intensity and degree of linear polarization of aerosol particles generated from volcanic sand from the Mýrdalssandur area in Iceland. They estimated a value of 1.60 for n and 0.01 for k at 647 nm.

In this study, $n_{avg}(\lambda)$ (Table 5.3) was comparable with the initial estimate (Baldo et al., 2020). $k_{avg}(\lambda)$ results (Table 5.2 and Figure 5.7) were within or at the lower end of the range of $\tilde{k}(\lambda)$ values estimated by Baldo et al. (2020). k_{avg} at 660 nm was 0.002-0.003 (Table 5.2) in different samples, which is 3-5 times lower than the value reported by Zubko et al. (2019) at 647 nm. $k_{avg}(\lambda)$ was higher than the imaginary index of volcanic ash from Iceland (Deguine et al., 2020; Reed et al., 2017). Laboratory measurements showed that the imaginary index of Icelandic ash was close to 0 in the UV-visible spectrum and tend to increase towards the near-infrared region (Deguine et al., 2020; Reed et al., 2017).

In Figure 5.8, the imaginary index of Icelandic dust was compared to the imaginary indices of low-latitude mineral dust from major dust source regions such as northern Africa-Sahara, Sahel and Eastern Asia (Di Biagio et al., 2019), which were obtained from laboratory measurements of suspended particles. The imaginary index of Icelandic dust was comparable to that of typical low-latitude dust between 370-590 nm but tend to be higher than low-latitude dust between 660 and 950. The imaginary index decreased from around 0.002-0.005 at 370 nm to 0.001 at 950 nm for northern African-Saharan dust, from 0.001-0.009 at 370 nm to 0.0003-0.002 at 950 nm for mineral dust from the Sahel, and from 0.002-0.004 at 370 nm to 0.0005-0.001 at 950 nm for eastern Asian dust (Di Biagio et al., 2019). In the spectral range between 370 and 590 nm, the difference of $k_{avg}(\lambda)$ in Table 5.2 with the spectral imaginary indices of northern African-Saharan dust, mineral dust from the Sahel, and eastern Asian dust was less than three times the square root of the sum of their squared uncertainties. The largest differences between

Icelandic dust and low-latitude dust were observed from 660 to 950 nm. In particular, at these wavelengths, the imaginary indices of the samples D3 and MIR45, representative of the two major dust hotspots in Iceland (e.g., Arnalds et al., 2016), were 2-5 times higher than the imaginary indices of mineral dust from Morocco, Libya, and Algeria in northern Africa-Sahara, and the Taklimakan desert in eastern Asia, and 5-8 times higher than the imaginary indices of mineral dust from the Bodele depression in the Sahel.

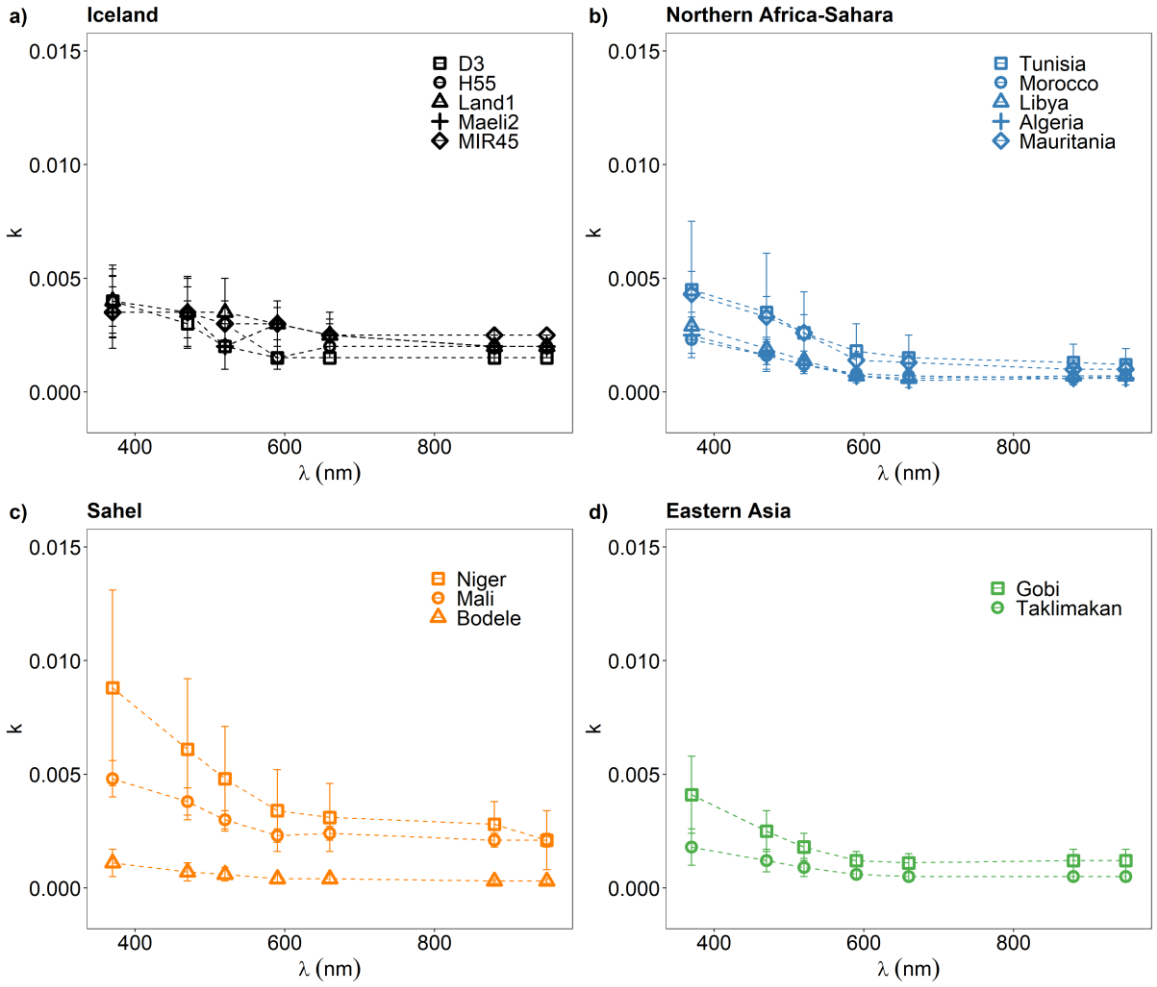

Figure 5.8: Comparison between the experiment-averaged imaginary index $k_{avg}(\lambda)$ at λ = 370, 470, 520, 590, 660, 880, 950 nm of a) Icelandic dust (Table 5.2) and mineral dust from major dust source regions at low-latitude (Di Biagio et al., 2019), b) northern Africa-Sahara, c) Sahel, and d) Eastern Asia.

The single scattering albedo of Icelandic dust (Table 5.1 and Figure 5.6) was comparable to that of low-latitude dust (Di Biagio et al., 2019). $SSA_{avg}(\lambda)$ was consistent for different sensitivity simulations and increased from 0.90-0.94 at 370 nm to 0.94-0.96 at 950 nm in different Icelandic samples.

The single scattering albedo of Icelandic ash was also rather similar to that of Icelandic dust and low-latitude dust. During the 2010 eruptions of Eyjafjallajökull, the single scattering albedo of a volcanic ash plume over France (17 April 2010) varied from 0.81 at 440 nm to 0.92 at 870 nm from Aerosol Robotic Network (AERONET) observations (Derimian et al., 2012), whereas the single scattering albedo derived from AERONET measurements over Spain and Portugal (6-12 May 2010) was 0.95 at 440 nm but slightly decreased with wavelength (Toledano et al., 2012). However, the imaginary index resulting from direct measurements of the Eyjafjallajökull plume in 2010 (e.g., Bukowiecki et al., 2011; Derimian et al., 2012; Weinzierl et al., 2012) is considerably different from the results of laboratory measurements conducted on re-suspended samples where $k(\lambda)$ was close to 0 (Deguine et al., 2020; Reed et al., 2017). In Derimian et al. (2012), the imaginary index of Eyjafjallajökull ash varied from around 0.015 at 440 nm to 0.008 at 870 nm, and Weinzierl et al. (2012) reported similar results, whereas Bukowiecki et al. (2011) reported an average value of 0.02 between 450-700 nm. The difference between observational data and laboratory measurements could be due to different methods used and/or the change of the physical-chemical properties of volcanic ash plumes during atmospheric transport.

5.5.2 Optical properties and mineralogy

The chemical and mineralogical composition of the Icelandic dust samples examined in this study was determined by Baldo et al. (2020). Icelandic dust showed a basaltic composition, with relatively high total Fe content varying from around 11 wt% in the sample H55 to 13% in MIR45. The samples were primarily composed of amorphous basaltic materials ranging from 8 wt % in H55 to 60 wt %–90 wt % in the other Icelandic dust. MIR45 had the highest proportion of amorphous glass. The magnetite fraction (1 wt%–2 wt %) was considerably higher than in low-latitude dust contributing to 7 %–15 % of total Fe. Fe oxide minerals accounted for 9%-20% of the total Fe, while most of the iron was contained in other mineral phases (e.g., pyroxene, feldspars and olivine) and in the amorphous glass (Baldo et al.,

2020). Di Biagio et al. (2019) found a linear relationship between the spectral single scattering albedo and the imaginary index and the mass concentrations of total Fe and Fe oxides. In this study, the sample size was too small to reach statistical significance, and the values of $SSA_{avg}(\lambda)$ and $k_{avg}(\lambda)$ were similar among different samples and did not show a clear pattern (Figures 5.6-5.8). In addition, since amorphous basaltic material is dominant, we do not expect a good correlation. In Figure 5.7, $k_{avg}(\lambda)$ results tend to be closer to the volume-averaged imaginary indices calculated by Baldo et al. (2020) assuming the spectral refractive index of magnetite from Querry (1985) than to the values predicted using the refractive index of magnetite from Huffman and Stapp (1973). This suggest that dataset the from Querry (1985) may be more representative of the complex refractive index of magnetite in Icelandic dust, and that magnetite may be a major mineral contributing to light absorption in particular between 660 and 950 nm.

5.6 Implications for the radiative effect

Here, we provide for the first time a dataset with the spectral SW single scattering albedo and complex refractive index of mineral dust from five major dust hotspots in Iceland. Although the mineralogical composition of Icelandic dust differs considerably from that of mineral dust sourced in arid and semiarid regions at low latitudes such northern Africa and eastern Asia, their spectral optical properties between 370 and 590 nm seem to be rather similar. However, in Icelandic dust, absorption between 660 and 950 nm can be 2-8 times higher than several low-latitude dust.

Icelandic dust can reach several kilometers in altitude (Dagsson-Waldhauserova et al., 2019; Groot Zwaaftink et al., 2017) and be transported over long distances to the high Arctic (Baddock et al., 2017; Groot Zwaaftink et al., 2017; Groot Zwaaftink et al., 2016; Moroni et al., 2018; Prospero et al., 2012). Kylling et al. (2018) estimated that Icelandic dust produces a positive direct radiative forcing in the Arctic via dust-radiation interaction and deposition onto snow and ice, based on calculations assuming the same optical properties as for typical low-latitude dust. The imaginary index of mineral dust was around 0.002 at 555 nm. This assumed k at the lower end of the range of estimates between 520 and 590 nm in Icelandic dust (0.002-0.004). Our analysis indicate that Icelandic dust can absorb more solar

radiation between 660 and 950 nm than dust from northern Africa and eastern Asia. These new findings suggest that the positive direct radiative forcing of Icelandic dust in the Arctic may be stronger than previous estimates.

5.7 References

Achterberg, E. P., Moore, C. M., Henson, S. A., Steigenberger, S., Stohl, A., Eckhardt, S., Avendano, L. C., Cassidy, M., Hembury, D., Klar, J. K., Lucas, M. I., Macey, A. I., Marsay, C. M., and Ryan-Keogh, T. J.: Natural iron fertilization by the Eyjafjallajökull volcanic eruption, Geophys. Res. Lett., 40, 921-926, doi: 10.1002/grl.50221, 2013.

Achterberg, E. P., Steigenberger, S., Marsay, C. M., LeMoigne, F. A. C., Painter, S. C., Baker, A. R., Connelly, D. P., Moore, C. M., Tagliabue, A., and Tanhua, T.: Iron Biogeochemistry in the High Latitude North Atlantic Ocean, Sci. Rep., 8, 1283, doi: 10.1038/s41598-018-19472-1, 2018.

Anderson, T. L., Covert, D. S., Marshall, S. F., Laucks, M. L., Charlson, R. J., Waggoner, A. P., Ogren, J. A., Caldow, R., Holm, R. L., Quant, F. R., Sem, G. J., Wiedensohler, A., Ahlquist, N. A., and Bates, T. S.: Performance Characteristics of a High-Sensitivity, Three-Wavelength, Total Scatter/Backscatter Nephelometer, Journal of Atmospheric and Oceanic Technology, 13, 967-986, doi: 10.1175/1520-0426(1996)013<0967:Pcoahs>2.0.Co;2, 1996.

Anderson, T. L., and Ogren, J. A.: Determining Aerosol Radiative Properties Using the TSI 3563 Integrating Nephelometer, Aerosol Sci. Tech., 29, 57-69, doi: 10.1080/02786829808965551, 1998.

Arnalds, O., Olafsson, H., and Dagsson-Waldhauserova, P.: Quantification of iron-rich volcanogenic dust emissions and deposition over the ocean from Icelandic dust sources, Biogeosciences, 11, 6623-6632, doi: 10.5194/bg-11-6623-2014, 2014.

Arnalds, O., Dagsson-Waldhauserova, P., and Olafsson, H.: The Icelandic volcanic aeolian environment: Processes and impacts — A review, Aeolian Res., 20, 176-195, doi: 10.1016/j.aeolia.2016.01.004, 2016.

Arnott, W. P., Hamasha, K., Moosmüller, H., Sheridan, P. J., and Ogren, J. A.: Towards Aerosol Light-Absorption Measurements with a 7-Wavelength Aethalometer: Evaluation with a Photoacoustic Instrument and 3-Wavelength Nephelometer, Aerosol Sci. Tech., 39, 17-29, doi: 10.1080/027868290901972, 2005.

Ayers, G. P.: Comment on regression analysis of air quality data, Atmos. Environ., 35, 2423-2425, doi: doi.org/10.1016/S1352-2310(00)00527-6, 2001.

Baddock, M. C., Mockford, T., Bullard, J. E., and Thorsteinsson, T.: Pathways of high-latitude dust in the North Atlantic, Earth Planet. Sci. Lett., 459, 170-182, doi: 10.1016/j.epsl.2016.11.034, 2017.

Baldo, C., Formenti, P., Nowak, S., Chevaillier, S., Cazaunau, M., Pangui, E., Di Biagio, C., Doussin, J. F., Ignatyev, K., Dagsson-Waldhauserova, P., Arnalds, O., MacKenzie, A. R., and Shi, Z.: Distinct chemical and mineralogical composition of Icelandic dust compared to northern African and Asian dust, Atmos. Chem. Phys., 20, 13521-13539, doi: 10.5194/acp-20-13521-2020, 2020.

Beddows, D. C. S., Dall'osto, M., and Harrison, R. M.: An Enhanced Procedure for the Merging of Atmospheric Particle Size Distribution Data Measured Using Electrical Mobility and Time-of-Flight Analysers, Aerosol Sci. Tech., 44, 930-938, doi: 10.1080/02786826.2010.502159, 2010.

Bohren, C. F., and Hufmann, D. R.: Absorption and Scattering by a Sphere, in: Absorption and Scattering of Light by Small Particles, 82-129, 1998.

Boy, M., Thomson, E. S., Acosta Navarro, J.-C., Arnalds, O., Batchvarova, E., Bäck, J., Berninger, F., Bilde, M., Brasseur, Z., Dagsson-Waldhauserova, P., Castarède, D., Dalirian, M., de Leeuw, G., Dragosics, M., Duplissy, E.-M., Duplissy, J., Ekman, A. M. L., Fang, K., Gallet, J.-C., Glasius, M., Gryning, S.-E., Grythe, H., Hansson, H.-C., Hansson, M., Isaksson, E., Iversen, T., Jonsdottir, I., Kasurinen, V., Kirkevåg, A., Korhola, A., Krejci, R., Kristjansson, J. E., Lappalainen, H. K., Lauri, A., Leppäranta, M., Lihavainen, H., Makkonen, R., Massling, A., Meinander, O., Nilsson, E. D., Olafsson, H., Pettersson, J. B. C., Prisle, N. L., Riipinen, I., Roldin, P., Ruppel, M., Salter, M., Sand, M., Seland, Ø., Seppä, H., Skov, H., Soares, J., Stohl, A., Ström, J., Svensson, J., Swietlicki, E., Tabakova, K., Thorsteinsson, T., Virkkula, A., Weyhenmeyer, G. A., Wu, Y., Zieger, P., and Kulmala, M.: Interactions between the atmosphere, cryosphere, and ecosystems at northern high latitudes, Atmos. Chem. Phys., 19, 2015-2061, doi: 10.5194/acp-19-2015-2019, 2019.

Bukowiecki, N., Zieger, P., Weingartner, E., Juranyi, Z., Gysel, M., Neininger, B., Schneider, B., Hueglin, C., Ulrich, A., Wichser, A., Henne, S., Brunner, D., Kaegi, R., Schwikowski, M., Tobler, L., Wienhold, F. G., Engel, I., Buchmann, B., Peter, T., and Baltensperger, U.: Ground-based and airborne in-situ measurements of the Eyjafjallajökull volcanic aerosol plume in Switzerland in spring 2010, Atmos. Chem. Phys., 11, 10011-10030, doi: 10.5194/acp-11-10011-2011, 2011.

Bullard, J. E., Baddock, M., Bradwell, T., Crusius, J., Darlington, E., Gaiero, D., Gasso, S., Gisladottir, G., Hodgkins, R., McCulloch, R., McKenna-Neuman, C., Mockford, T., Stewart, H., and Thorsteinsson, T.: High-latitude dust in the Earth system, Rev. Geophys., 54, 447-485, doi: 10.1002/2016rg000518, 2016.

Butwin, M. K., Pfeffer, M. A., von Löwis, S., Støren, E. W. N., Bali, E., and Thorsteinsson, T.: Properties of dust source material and volcanic ash in Iceland, Sedimentology, 67, 3067-3087, doi: 10.1111/sed.12734, 2020.

Caponi, L., Formenti, P., Massabo, D., Di Biagio, C., Cazaunau, M., Pangui, E., Chevaillier, S., Landrot, G., Andreae, M. O., Kandler, K., Piketh, S., Saeed, T., Seibert, D., Williams, E., Balkanski, Y., Prati, P., and Doussin, J. F.: Spectral- and size-resolved mass absorption efficiency of mineral dust aerosols in the shortwave spectrum: a simulation chamber study, Atmos. Chem. Phys., 17, 7175-7191, doi: 10.5194/acp-17-7175-2017, 2017.

Collaud Coen, M., Weingartner, E., Apituley, A., Ceburnis, D., Fierz-Schmidhauser, R., Flentje, H., Henzing, J. S., Jennings, S. G., Moerman, M., Petzold, A., Schmid, O., and Baltensperger, U.: Minimizing light absorption measurement artifacts of the Aethalometer: evaluation of five correction algorithms, Atmos. Meas. Tech., 3, 457-474, doi: 10.5194/amt-3-457-2010, 2010.

Cook, J. M., Tedstone, A. J., Williamson, C., McCutcheon, J., Hodson, A. J., Dayal, A., Skiles, M., Hofer, S., Bryant, R., McAree, O., McGonigle, A., Ryan, J., Anesio, A. M., Irvine-Fynn, T. D. L., Hubbard, A., Hanna, E., Flanner, M., Mayanna, S., Benning, L. G., van As, D., Yallop, M., McQuaid, J. B., Gribbin, T., and Tranter, M.: Glacier algae accelerate melt rates on the south-western Greenland Ice Sheet, Cryosphere, 14, 309-330, doi: 10.5194/tc-14-309-2020, 2020.

Dagsson-Waldhauserova, P.: Variability, origin and physical characteristics of dust aerosol in Iceland (PhD dissertation), Faculty of Physical Sciences Agricultural University of Iceland, Reykjavik, 163 pp., 2014.

Dagsson-Waldhauserova, P., and Meinander, O.: Editorial: Atmosphere—Cryosphere Interaction in the Arctic, at High Latitudes and Mountains With Focus on Transport, Deposition, and Effects of Dust, Black Carbon, and Other Aerosols, Front. Earth Sci., 7, 337, doi: 10.3389/feart.2019.00337, 2019.

Dagsson-Waldhauserova, P., Renard, J.-B., Olafsson, H., Vignelles, D., Berthet, G., Verdier, N., and Duverger, V.: Vertical distribution of aerosols in dust storms during the Arctic winter, Sci. Rep., 9, 16122, doi: 10.1038/s41598-019-51764-y, 2019.

Dai, A., Luo, D., Song, M., and Liu, J.: Arctic amplification is caused by sea-ice loss under increasing CO2, Nat. Commun., 10, 121, doi: 10.1038/s41467-018-07954-9, 2019.

DeCarlo, P. F., Slowik, J. G., Worsnop, D. R., Davidovits, P., and Jimenez, J. L.: Particle Morphology and Density Characterization by Combined Mobility and Aerodynamic Diameter Measurements. Part 1: Theory, Aerosol Sci. Tech., 38, 1185-1205, doi: 10.1080/027868290903907, 2004.

Deguine, A., Petitprez, D., Clarisse, L., Guðmundsson, S., Outes, V., Villarosa, G., and Herbin, H.: Complex refractive index of volcanic ash aerosol in the infrared, visible, and ultraviolet, Appl. Opt., 59, 884-895, doi: 10.1364/AO.59.000884, 2020.

Derimian, Y., Karnieli, A., Kaufman, Y. J., Andreae, M. O., Andreae, T. W., Dubovik, O., Maenhaut, W., and Koren, I.: The role of iron and black carbon in aerosol light absorption, Atmos. Chem. Phys., 8, 3623-3637, doi: 10.5194/acp-8-3623-2008, 2008.

Derimian, Y., Dubovik, O., Tanre, D., Goloub, P., Lapyonok, T., and Mortier, A.: Optical properties and radiative forcing of the Eyjafjallajökull volcanic ash layer observed over Lille, France, in 2010, J. Geophys. Res.-Atmos, 117, D00U25, doi: 10.1029/2011jd016815, 2012.

Di Biagio, C., Formenti, P., Balkanski, Y., Caponi, L., Cazaunau, M., Pangui, E., Journet, E., Nowak, S., Caquineau, S., Andreae, M. O., Kandler, K., Saeed, T., Piketh, S., Seibert, D., Williams, E., and Doussin, J. F.: Global scale variability of the mineral dust long-wave refractive index: a new dataset of in situ measurements for climate modeling and remote sensing, Atmos. Chem. Phys., 17, 1901-1929, doi: 10.5194/acp-17-1901-2017, 2017a.

Di Biagio, C., Formenti, P., Cazaunau, M., Pangui, E., Marchand, N., and Doussin, J. F.: Aethalometer multiple scattering correction C-ref for mineral dust aerosols, Atmos. Meas. Tech., 10, 2923-2939, doi: 10.5194/amt-10-2923-2017, 2017b.

Di Biagio, C., Formenti, P., Balkanski, Y., Caponi, L., Cazaunau, M., Pangui, E., Journet, E., Nowak, S., Andreae, M. O., Kandler, K., Saeed, T., Piketh, S., Seibert, D., Williams, E., and Doussin, J. F.: Complex refractive indices and single-scattering albedo of global dust aerosols in the shortwave spectrum and relationship to size and iron content, Atmos. Chem. Phys., 19, 15503-15531, doi: 10.5194/acp-19-15503-2019, 2019.

Dragosics, M., Meinander, O., Jónsdóttír, T., Dürig, T., De Leeuw, G., Pálsson, F., Dagsson-Waldhauserová, P., and Thorsteinsson, T.: Insulation effects of Icelandic dust and volcanic ash on snow and ice, Arab. J. Geosci., 9, 126, doi: 10.1007/s12517-015-2224-6, 2016.

Dubovik, O., Holben, B., Eck, T. F., Smirnov, A., Kaufman, Y. J., King, M. D., Tanre, D., and Slutsker, I.: Variability of absorption and optical properties of key aerosol types observed in worldwide locations, Journal of the Atmospheric Sciences, 59, 590-608, doi: 10.1175/1520-0469(2002)059<0590:voaaop>2.0.co;2, 2002.

Engelbrecht, J. P., Moosmuller, H., Pincock, S., Jayanty, R. K. M., Lersch, T., and Casuccio, G.: Technical note: Mineralogical, chemical, morphological, and optical interrelationships of mineral dust re-suspensions, Atmos. Chem. Phys., 16, 10809-10830, doi: 10.5194/acp-16-10809-2016, 2016.

Formenti, P., Caquineau, S., Chevaillier, S., Klaver, A., Desboeufs, K., Rajot, J. L., Belin, S., and Briois, V.: Dominance of goethite over hematite in iron oxides of mineral dust from Western Africa: Quantitative partitioning by X-ray absorption spectroscopy, J. Geophys. Res.-Atmos, 119, 12740-12754, doi: 10.1002/2014jd021668, 2014.

Formenti, P., Mbemba Kabuiku, L., Chiapello, I., Ducos, F., Dulac, F., and Tanré, D.: Aerosol optical properties derived from POLDER-3/PARASOL (2005–2013) over the western Mediterranean Sea – Part 1: Quality assessment with AERONET and in situ airborne observations, Atmos. Meas. Tech., 11, 6761-6784, doi: 10.5194/amt-11-6761-2018, 2018.

Formenti, P., Di Biagio, C., Huang, Y., Kok, J., Mallet, M. C., Boulanger, D., and Cazaunau, M.: Look-up tables resolved by complex refractive index to correct particle sizes measured by common research-grade optical particle counters, Atmos. Meas. Tech. Discuss., doi: 10.5194/amt-2021-403, 2021.

Groot Zwaaftink, C. D., Grythe, H., Skov, H., and Stohl, A.: Substantial contribution of northern high-latitude sources to mineral dust in the Arctic, J. Geophys. Res.-Atmos, 121, 13678-13697, doi: 10.1002/2016jd025482, 2016.

Groot Zwaaftink, C. D., Arnalds, O., Dagsson-Waldhauserova, P., Eckhardt, S., Prospero, J. M., and Stohl, A.: Temporal and spatial variability of Icelandic dust emissions and atmospheric transport, Atmos. Chem. Phys., 17, 10865-10878, doi: 10.5194/acp-17-10865-2017, 2017.

Hand, J. L., and Kreidenweis, S. M.: A New Method for Retrieving Particle Refractive Index and Effective Density from Aerosol Size Distribution Data, Aerosol Sci. Tech., 36, 1012-1026, doi: 10.1080/02786820290092276, 2002.

Hansen, J. E.: Multiple Scattering of Polarized Light in Planetary Atmospheres Part II. Sunlight Reflected by Terrestrial Water Clouds, J. Atmos. Sci., 28, 1400-1426, doi: 10.1175/1520-0469(1971)028<1400:Msopli>2.0.Co;2, 1971.

Hinds, W. C.: Aerosol Technology : Properties, Behavior, and Measurement of Airborne Particles, John Wiley & Sons, Incorporated, Somerset, UNITED STATES, 1999.

Huang, Y., Kok, J. F., Kandler, K., Lindqvist, H., Nousiainen, T., Sakai, T., Adebiyi, A., and Jokinen, O.: Climate Models and Remote Sensing Retrievals Neglect Substantial Desert Dust Asphericity, Geophys. Res. Lett., 47, e2019GL086592, doi: 10.1029/2019GL086592, 2020.

Huang, Y., Adebiyi, A. A., Formenti, P., and Kok, J. F.: Linking the Different Diameter Types of Aspherical Desert Dust Indicates That Models Underestimate Coarse Dust Emission, Geophys. Res. Lett., 48, e2020GL092054, doi: doi.org/10.1029/2020GL092054, 2021.

Huffman, D. R., and Stapp, J. L.: Optical measurements on solids of possible interstellar importance, in: Interstellar dust and related topics, Springer, 297-301, 1973.

Johnson, B. T., Osborne, S. R., Haywood, J. M., and Harrison, M. A. J.: Aircraft measurements of biomass burning aerosol over West Africa during DABEX, J. Geophys. Res.-Atmos, 113, D00C06, doi: 10.1029/2007JD009451, 2008.

Johnson, B. T., and Osborne, S. R.: Physical and optical properties of mineral dust aerosol measured by aircraft during the GERBILS campaign, Quarterly Journal of the Royal Meteorological Society, 137, 1117-1130, doi: 10.1002/qj.777, 2011.

Kulkarni, P., Baron, P. A., and Willeke, K.: Aerosol Measurement : Principles, Techniques, and Applications, John Wiley & Sons, Incorporated, Hoboken, UNITED STATES, 2011.

Kylling, A., Zwaaftink, C. D. G., and Stohl, A.: Mineral Dust Instantaneous Radiative Forcing in the Arctic, Geophys. Res. Lett., 45, 4290-4298, doi: 10.1029/2018gl077346, 2018.

Lafon, S., Sokolik, I. N., Rajot, J. L., Caquineau, S., and Gaudichet, A.: Characterization of iron oxides in mineral dust aerosols: Implications for light absorption, J. Geophys. Res.-Atmos, 111, D21207, doi: 10.1029/2005jd007016, 2006.

McCutcheon, J., Lutz, S., Williamson, C., Cook, J. M., Tedstone, A. J., Vanderstraeten, A., Wilson, S. A., Stockdale, A., Bonneville, S., Anesio, A. M., Yallop, M. L., McQuaid, J. B., Tranter, M., and

Benning, L. G.: Mineral phosphorus drives glacier algal blooms on the Greenland Ice Sheet, Nat. Commun., 12, 570, doi: 10.1038/s41467-020-20627-w, 2021.

Meinander, O., Kontu, A., Virkkula, A., Arola, A., Backman, L., Dagsson-Waldhauserová, P., Järvinen, O., Manninen, T., Svensson, J., de Leeuw, G., and Leppäranta, M.: Brief communication: Light-absorbing impurities can reduce the density of melting snow, Cryosphere, 8, 991-995, doi: 10.5194/tc-8-991-2014, 2014.

Meinander, O., Dagsson-Waldhauserova, P., and Arnalds, O.: Icelandic volcanic dust can have a significant influence on the cryosphere in Greenland and elsewhere, Polar Res., 35, 31313, doi: 10.3402/polar.v35.31313, 2016.

Möller, R., Möller, M., Kukla, P. A., and Schneider, C.: Impact of supraglacial deposits of tephra from Grímsvötn volcano, Iceland, on glacier ablation, J. Glaciol., 62, 933-943, doi: 10.1017/jog.2016.82, 2016.

Möller, R., Möller, M., Kukla, P. A., and Schneider, C.: Modulation of glacier ablation by tephra coverage from Eyjafjallajökull and Grimsvötn volcanoes, Iceland: an automated field experiment, Earth Syst. Sci. Data, 10, 53-60, doi: 10.5194/essd-10-53-2018, 2018.

Moosmuller, H., Engelbrecht, J. P., Skiba, M., Frey, G., Chakrabarty, R. K., and Arnott, W. P.: Single scattering albedo of fine mineral dust aerosols controlled by iron concentration, J. Geophys. Res.-Atmos, 117, D11210, doi: 10.1029/2011jd016909, 2012.

Moroni, B., Arnalds, O., Dagsson-Waldhauserova, P., Crocchianti, S., Vivani, R., and Cappelletti, D.: Mineralogical and Chemical Records of Icelandic Dust Sources Upon Ny-angstrom lesund (Svalbard Islands), Front. Earth Sci., 6, UNSP 187, doi: 10.3389/feart.2018.00187, 2018.

Morrison, H., de Boer, G., Feingold, G., Harrington, J., Shupe, M. D., and Sulia, K.: Resilience of persistent Arctic mixed-phase clouds, Nat. Geosci., 5, 11-17, doi: 10.1038/ngeo1332, 2012.

Murray, B. J., Carslaw, K. S., and Field, P. R.: Opinion: Cloud-phase climate feedback and the importance of ice-nucleating particles, Atmos. Chem. Phys., 21, 665-679, doi: 10.5194/acp-21-665-2021, 2021.

Nousiainen, T., and Kandler, K.: Light scattering by atmospheric mineral dust particles, in: Light Scattering Reviews 9: Light Scattering and Radiative Transfer, edited by: Kokhanovsky, A. A., Springer Berlin Heidelberg, Berlin, Heidelberg, 3-52, 2015.

Peltoniemi, J. I., Gritsevich, M., Hakala, T., Dagsson-Waldhauserova, P., Arnalds, O., Anttila, K., Hannula, H. R., Kivekas, N., Lihavainen, H., Meinander, O., Svensson, J., Virkkula, A., and de Leeuw, G.: Soot on Snow experiment: bidirectional reflectance factor measurements of contaminated snow, Cryosphere, 9, 2323-2337, doi: 10.5194/tc-9-2323-2015, 2015.

Prospero, J. M., Bullard, J. E., and Hodgkins, R.: High-Latitude Dust Over the North Atlantic: Inputs from Icelandic Proglacial Dust Storms, Science, 335, 1078-1082, doi: 10.1126/science.1217447, 2012.

Magnetite, Refractive index database, available at https://refractiveindex.info/?shelf=main&book=Fe3O4& (last access: 02 January 2020), 1985.

Redmond, H. E., Dial, K. D., and Thompson, J. E.: Light scattering and absorption by wind blown dust: Theory, measurement, and recent data, Aeolian Res., 2, 5-26, doi: 10.1016/j.aeolia.2009.09.002, 2010.

Reed, B. E., Peters, D. M., McPheat, R., Smith, A. J. A., and Grainger, R. G.: Mass extinction spectra and size distribution measurements of quartz and amorphous silica aerosol at 0.33-19 mu m compared to modelled extinction using Mie, CDE, and T-matrix theories, J. Quant. Spectrosc. Ra., 199, 52-65, doi: 10.1016/j.jqsrt.2017.05.011, 2017.

Richards-Thomas, T., McKenna-Neuman, C., and Power, I. M.: Particle-scale characterization of volcaniclastic dust sources within Iceland, Sedimentology, 68, 1137-1158, doi: 10.1111/sed.12821, 2020.

Rosenberg, P. D., Dean, A. R., Williams, P. I., Dorsey, J. R., Minikin, A., Pickering, M. A., and Petzold, A.: Particle sizing calibration with refractive index correction for light scattering optical particle counters and impacts upon PCASP and CDP data collected during the Fennec campaign, Atmos. Meas. Tech., 5, 1147-1163, doi: 10.5194/amt-5-1147-2012, 2012.

Sanchez-Marroquin, A., Arnalds, O., Baustian-Dorsi, K. J., Browse, J., Dagsson-Waldhauserova, P., Harrison, A. D., Maters, E. C., Pringle, K. J., Vergara-Temprado, J., Burke, I. T., McQuaid, J. B., Carslaw, K. S., and Murray, B. J.: Iceland is an episodic source of atmospheric ice-nucleating particles relevant for mixed-phase clouds, Sci. Adv., 6, doi: 10.1126/sciadv.aba8137, 2020.

Seinfeld, J. H., and Pandis, S. N.: Atmospheric chemistry and physics: from air pollution to climate change, John Wiley & Sons, 2016.

Serreze, M. C., and Barry, R. G.: Processes and impacts of Arctic amplification: A research synthesis, Glob. Planet. Change, 77, 85-96, doi: 10.1016/j.gloplacha.2011.03.004, 2011.

Smith, R. J.: Use and misuse of the reduced major axis for line-fitting, American Journal of Physical Anthropology, 140, 476-486, doi: doi.org/10.1002/ajpa.21090, 2009.

Sokolik, I. N., and Toon, O. B.: Incorporation of mineralogical composition into models of the radiative properties of mineral aerosol from UV to IR wavelengths, J. Geophys. Res.-Atmos, 104, 9423-9444, doi: 10.1029/1998jd200048, 1999.

Sumlin, B. J., Heinson, W. R., and Chakrabarty, R. K.: Retrieving the aerosol complex refractive index using PyMieScatt: A Mie computational package with visualization capabilities, Journal of Quantitative Spectroscopy and Radiative Transfer, 205, 127-134, doi: 10.1016/j.jqsrt.2017.10.012, 2018.

Toledano, C., Bennouna, Y., Cachorro, V., de Galisteo, J. P. O., Stohl, A., Stebel, K., Kristiansen, N. I., Olmo, F. J., Lyamani, H., Obregon, M. A., Estelles, V., Wagner, F., Baldasano, J. M., Gonzalez-Castanedo, Y., Clarisse, L., and de Frutos, A. M.: Aerosol properties of the Eyjafjallajökull ash derived from sun photometer and satellite observations over the Iberian Peninsula, Atmos. Environ., 48, 22-32, doi: 10.1016/j.atmosenv.2011.09.072, 2012.

Vergara-Temprado, J., Miltenberger, A. K., Furtado, K., Grosvenor, D. P., Shipway, B. J., Hill, A. A., Wilkinson, J. M., Field, P. R., Murray, B. J., and Carslaw, K. S.: Strong control of Southern Ocean cloud reflectivity by ice-nucleating particles, P. Natl. Acad. Sci. USA, 115, 2687-2692, doi: 10.1073/pnas.1721627115, 2018.

von der Weiden, S. L., Drewnick, F., and Borrmann, S.: Particle Loss Calculator – a new software tool for the assessment of the performance of aerosol inlet systems, Atmos. Meas. Tech., 2, 479-494, doi: 10.5194/amt-2-479-2009, 2009.

Walser, A., Sauer, D., Spanu, A., Gasteiger, J., and Weinzierl, B.: On the parametrization of optical particle counter response including instrument-induced broadening of size spectra and a self-consistent evaluation of calibration measurements, Atmos. Meas. Tech., 10, 4341-4361, doi: 10.5194/amt-10-4341-2017, 2017.

Wang, J., Doussin, J. F., Perrier, S., Perraudin, E., Katrib, Y., Pangui, E., and Picquet-Varrault, B.: Design of a new multi-phase experimental simulation chamber for atmospheric photosmog, aerosol and cloud chemistry research, Atmos. Meas. Tech., 4, 2465-2494, doi: 10.5194/amt-4-2465-2011, 2011.

Weingartner, E., Saathoff, H., Schnaiter, M., Streit, N., Bitnar, B., and Baltensperger, U.: Absorption of light by soot particles: determination of the absorption coefficient by means of aethalometers, J. Aerosol Sci., 34, 1445-1463, doi: 10.1016/S0021-8502(03)00359-8, 2003.

Weinzierl, B., Sauer, D., Minikin, A., Reitebuch, O., Dahlkotter, F., Mayer, B., Emde, C., Tegen, I., Gasteiger, J., Petzold, A., Veira, A., Kueppers, U., and Schumann, U.: On the visibility of airborne volcanic ash and mineral dust from the pilot's perspective in flight, Phys. Chem. Earth, 45-46, 87-102, doi: 10.1016/j.pce.2012.04.003, 2012.

Wendisch, M., and Brenguier, J.-L.: Airborne Measurements for Environmental Research : Methods and Instruments, John Wiley & Sons, Incorporated, Somerset, GERMANY, 2013.

Wittmann, M., Zwaaftink, C. D. G., Schmidt, L. S., Gudmundsson, S., Palsson, F., Arnalds, O., Björnsson, H., Thorsteinsson, T., and Stohl, A.: Impact of dust deposition on the albedo of Vatnajökull ice cap, Iceland, Cryosphere, 11, 741-754, doi: 10.5194/tc-11-741-2017, 2017.

Zubko, N., Munoz, O., Zubko, E., Gritsevich, M., Escobar-Cerezo, J., Berg, M. J., and Peltoniemi, J.: Light scattering from volcanic-sand particles in deposited and aerosol form, Atmos. Environ., 215, 116813, doi: 10.1016/j.atmosenv.2019.06.051, 2019.

CHAPTER 6: CONCLUSIONS AND FUTURE RESEARCH

6.1 Summary and conclusions

The overall aim of this thesis was to determine the chemical and physical properties of important sources of aerosol Fe such as CFA particles and Icelandic dust. The specific research objectives were: (1) To determine the Fe dissolution kinetic of CFA under simulated acidic processing. (2) To determine the mineralogical and optical properties of Icelandic dust.

This thesis focused on three major sources of uncertainty in estimating the impacts of aerosol Fe on climate including the fractional Fe solubility, Fe mineralogy, and optical properties of aerosols, which were identified in Chapter 1.

Chapter 2 reviewed observations and laboratory measurements of pyrogenic Fe in aerosols.

Chapter 3 presented the experimental results of Fe dissolution kinetics of CFA samples under simulated acidic processing. More specifically, the effect of the ionic strength on the Fe dissolution at low pH and in the presence of oxalate was examined. The high ionic strength enhanced the proton-promoted Fe dissolution of CFA at low pH (2-3) but suppressed the oxalate-promoted Fe dissolution, which was not considered in previous research. However, the Fe dissolution behavior varied depending on the type of CFA. CFA samples dissolved up to 7 times faster than a Saharan dust precursor at similar experimental conditions. The high Fe solubility of CFA was partly explained by the complete dissolution of highly reactive amorphous Fe, but the modelled dissolution kinetics suggest that magnetite may also dissolve relatively rapidly at low pH. The experimental results were used to develop a 3-step dissolution scheme for the proton- and oxalate- promoted Fe dissolution of CFA at high ionic strength which was implemented into the global atmospheric chemical transport model IMPACT. The revised model was

validated against observations of aerosol Fe solubility over the Bay of Bengal and showed a better agreement.

Chapter 4 and Chapter 5 described respectively the mineralogical and optical properties of Icelandic dust in comparison to typical low-latitude dust and discussed potential impacts of Icelandic dust on climate in high latitude regions. The experimental results showed that the mineralogical composition of Icelandic dust differs considerably from that of northern African and Asian dust. Icelandic dust is primarily composed of amorphous basaltic material and has a relatively high total Fe and magnetite content and low degree of chemical weathering. The Fe solubility of Icelandic dust was comparable to that of northern African dust at pH 4.7 but was significantly higher at pH 2. The spectral optical properties of Icelandic dust were rather similar to those of low-latitude dust samples between 370 and 590 nm, but Icelandic dust exhibited a stronger absorptive capacity in the near-infrared region than most of the dust samples sourced in northern Africa and eastern Asia. Our analysis indicate that magnetite may be a major contribution to light absorption in Icelandic dust particularly between 660 and 950 nm. Based on these differences, we concluded that Icelandic dust may have a stronger positive radiative forcing on climate than previous estimates which were based on calculations assuming the same optical properties as for low-latitude dust. Furthermore, Icelandic dust contributes to the atmospheric deposition of dissolved Fe and can impact biogeochemical cycles in the North Atlantic Ocean.

This work has contributed to reducing the uncertainty in predicting the impacts of aerosol Fe on climate and biogeochemical systems in two ways: (1) By defining a 3-step dissolution scheme for the proton- and oxalate- promoted Fe dissolution of coal combustion sources under more realistic conditions which can be implemented in global modelling to estimate the deposition fluxes of aerosol dissolved Fe to the ocean. (2) By building a new dataset on the chemical composition, mineralogy, Fe speciation, fractional Fe solubility, size distribution, and optical properties of Icelandic dust which can be used to estimate the deposition fluxes of aerosol dissolved Fe to the North Atlantic Ocean and to determine the radiative impact of Icelandic dust and its role on Arctic climate. Ultimately, we highlighted the role of magnetite in the chemical and optical properties of pyrogenic Fe and mineral dust.

6.2 Future research

This thesis provided an estimate of the optical properties of Icelandic dust, but calculation can be improved in the future by applying different modelling approaches which account for the particle asphericity (e.g., Nousiainen and Kandler, 2015). The measurements of the longwave optical properties of Icelandic dust conducted at CESAM will provide further insight into the radiative effect of Icelandic dust and its contribution to Arctic warming. The complex refractive index of volcanic ash samples measured by Deguine et al. (2020) showed a main absorption band between 8-12 μm and centered at around 10 μm. This absorption feature was linked to amorphous silicate which is a major component of volcanic ash (Deguine et al., 2020). On the other hand, the absorption properties of Saharan dust in the infrared region are closely related to the content of principal mineral components including calcite, quartz, and clays (e.g., Di Biagio et al., 2017; Sokolik and Toon, 1999). Calcite absorption band peaks at around 7 and 11.4 μm, while absorption in the range between 8 and 14 μm is determined by the relative abundance of quartz and clays (Di Biagio et al., 2017; Sokolik and Toon, 1999). Since Icelandic dust is primarily composed of amorphous silicate while calcite and clay minerals were not observed in the samples analyzed in this study, Icelandic dust and Saharan dust may have some common features related to the quartz absorption band.

More research is still needed to improve Fe emission, transport, and deposition and reduce the uncertainty in the predicted fluxes of aerosol Fe. Emission inventories can be improved by a comprehensive characterization of Fe species in pyrogenic Fe sources such as size distribution, total Fe content, Fe mineralogy, and fractional Fe solubility. Further work is needed to determine the ligand-promoted and photo-reductive Fe dissolution of aerosols under more realistic conditions for example at high ionic strength and in the presence of oxalate, but also other organic ligands such as siderophore and humic like substant (HULIS) which are present in aerosols. To determine the Fe mineralogy at emission and after atmospheric processing is also necessary to better understand the links between Fe solubility and Fe mineralogy.

More research is also needed to quantify the content of magnetite and other iron oxide minerals in aerosols and their microphysical properties such as size distribution, morphology, mixing states and optical properties as these are the major factors controlling their radiative effect, and may also affect the bio-accessibility of deposited Fe for marine ecosystems.

Future research should focus on biomass burning emissions which may play a key role in determining the aerosol Fe solubility in the Southern Ocean (Ito et al., 2020; Perron et al., 2020), and metal smelting emissions as a major source of pyrogenic magnetite in aerosols (Li et al., 2021; Rathod et al., 2020).

6.3 References

Di Biagio, C., Formenti, P., Balkanski, Y., Caponi, L., Cazaunau, M., Pangui, E., Journet, E., Nowak, S., Caquineau, S., Andreae, M. O., Kandler, K., Saeed, T., Piketh, S., Seibert, D., Williams, E., and Doussin, J. F.: Global scale variability of the mineral dust long-wave refractive index: a new dataset of in situ measurements for climate modeling and remote sensing, Atmos. Chem. Phys., 17, 1901-1929, doi: 10.5194/acp-17-1901-2017, 2017.

Ito, A., Perron, M. M. G., Proemse, B. C., Strzelec, M., Gault-Ringold, M., Boyd, P. W., and Bowie, A. R.: Evaluation of aerosol iron solubility over Australian coastal regions based on inverse modeling: implications of bushfires on bioaccessible iron concentrations in the Southern Hemisphere, Prog. Earth Planet. Sci., 7, 42, doi: 10.1186/s40645-020-00357-9, 2020.

Li, S., Zhang, B., Wu, D., Li, Z., Chu, S.-Q., Ding, X., Tang, X., Chen, J., and Li, Q.: Magnetic Particles Unintentionally Emitted from Anthropogenic Sources: Iron and Steel Plants, Environ. Sci. Technol. Lett., 8, 295-300, doi: 10.1021/acs.estlett.1c00164, 2021.

Nousiainen, T., and Kandler, K.: Light scattering by atmospheric mineral dust particles, in: Light Scattering Reviews 9: Light Scattering and Radiative Transfer, edited by: Kokhanovsky, A. A., Springer Berlin Heidelberg, Berlin, Heidelberg, 3-52, 2015.

Perron, M. M. G., Proemse, B. C., Strzelec, M., Gault-Ringold, M., Boyd, P. W., Rodriguez, E. S., Paull, B., and Bowie, A. R.: Origin, transport and deposition of aerosol iron to Australian coastal waters, Atmos. Environ., 228, 117432, doi: 10.1016/j.atmosenv.2020.117432, 2020.

Rathod, S. D., Hamilton, D. S., Mahowald, N. M., Klimont, Z., Corbett, J. J., and Bond, T. C.: A Mineralogy ‐ Based Anthropogenic Combustion ‐ Iron Emission Inventory, J. Geophys. Res.-Atmos, 125, e2019JD032114, doi: 10.1029/2019jd032114, 2020.

Sokolik, I. N., and Toon, O. B.: Incorporation of mineralogical composition into models of the radiative properties of mineral aerosol from UV to IR wavelengths, J. Geophys. Res.-Atmos, 104, 9423-9444, doi: 10.1029/1998jd200048, 1999.

Supporting information (SI)

SI Chapter 3

Table S1: Summary of the Fe dissolution experiments conducted in this study. A particles/liquid ratio of 1 g L^{-1} was used at different experimental conditions. The molar concentrations of H_2SO_4, $H_2C_2O_4$ and $(NH_4)_2SO_4$ in the experiment solutions are reported (mol L^{-1}). The molar concentration and activity (a) of H^+ and the solution pH before adding the samples (i) and at the end of the experiments (f) were calculated using the E-AIM model III for aqueous solution (Wexler and Clegg, 2002). The estimated buffered H^+ is ~0.008 M for Krakow ash, ~0.0007 M for Aberthaw/Shandong ash, ~0.004 M for Libyan dust end member (the procedure used to calculate the sample buffer capacity is reported in section 2.2). The final pH (pH_f) accounts for the buffer capacity of the CFA samples. For the experiment solutions with no $(NH_4)_2SO_4$, the initial pH (pH_i) and pH_f were also measured

	Exp.	$[H_2SO_4]$	$[(NH_4)_2SO_4]$	$[H_2C_2O_4]$	Model estimates						Measured pH	
					$[H^+]_i$	$[H^+]_f$	$a(H^+)_i$	$a(H^+)_f$	pH_i	pH_f	pH_i	pH_f
Krakow ash	Exp 1	0.01	-	-	0.016	0.009	0.86	0.86	1.9	2.1	1.9	2.1
	Exp 2	0.05	1	-	0.031	0.029	0.29	0.29	2.0	2.1	0.0	-
	Exp 3	0.05	1	0.01	0.035	0.032	0.29	0.29	2.0	2.0	0.0	-
	Exp 4	0.01	-	0.01	0.023	0.016	0.86	0.85	1.7	1.9	1.7	1.9
	Exp 1	0.005	-	-	0.008	0.002	0.89	0.88	2.1	2.7	2.2	2.6
	Exp 2	0.01	1	-	0.006	0.004	0.28	0.28	2.8	3.0	0.0	-
	Exp 3	0.005	1	0.01	0.007	0.005	0.28	0.28	2.7	2.9	0.0	-
	Exp 5	0.1	-	0.03	0.138	0.131	0.76	0.76	1.0	1.0	1.1	1.1
	Exp 6	0.25	0.5	0.03	0.189	0.186	0.49	0.49	1.0	1.0	0.0	-
	Exp 7	0.35	1	0.03	0.252	0.249	0.39	0.39	1.0	1.0	0.0	-
	Exp 8	0.4	1.5	0.03	0.285	0.282	0.33	0.33	1.0	1.0	0.0	-
Aberthaw ash	Exp 1	0.005	-	-	0.008	0.008	0.89	0.89	2.1	2.2	2.1	2.3
	Exp 2	0.05	1	-	0.031	0.031	0.29	0.29	2.0	2.0	0.0	-
	Exp 3	0.05	1	0.01	0.035	0.034	0.29	0.29	2.0	2.0	0.0	-

	Exp 4	0.002	-	0.01	0.012	0.011	0.90	0.90	2.0	2.0	2.0	2.1
	Exp 1	0.001	-	-	0.002	0.001	0.94	0.94	2.8	2.9	2.8	3.1
	Exp 2	0.005	1	-	0.003	0.003	0.28	0.28	3.1	3.1	0.0	-
Shandong ash	Exp 1	0.005	-	-	0.008	0.008	0.89	0.89	2.1	2.2	2.1	2.2
	Exp 2	0.05	1	-	0.031	0.031	0.29	0.29	2.0	2.0	0.0	-
	Exp 3	0.05	1	0.01	0.035	0.034	0.29	0.29	2.0	2.0	0.0	-
	Exp 4	0.002	-	0.01	0.012	0.011	0.90	0.90	2.0	2.0	2.0	2.0
	Exp 1	0.001	-	-	0.002	0.001	0.94	0.94	2.8	2.9	2.8	3.1
	Exp 2	0.005	1	-	0.003	0.003	0.28	0.28	3.1	3.1	0.0	-
Libyan dust	Exp 1	0.01	-	-	0.016	0.012	0.86	0.86	1.9	2.0	1.9	2.0
	Exp 2	0.05	1	-	0.031	0.030	0.29	0.29	2.0	2.1	0.0	-
	Exp 3	0.05	1	0.01	0.035	0.033	0.29	0.29	2.0	2.0	0.0	-
	Exp 4	0.005	-	0.01	0.016	0.012	0.88	0.87	1.9	2.0	1.9	2.0

Table S2: Percentages of ascorbate Fe (FeA), dithionite Fe (FeD), magnetite Fe (FeM), and total Fe (FeT) in the Arizona Test Dust (ATD, Power Technology, Inc.). to the total dust mass (wt%). For each type of extracted Fe, the standard deviation (sd) and number of replicates (n) is reported.

Fe species	wt%	sd	n
FeA	0.057	0.002	7
FeD	0.394	0.045	7
FeM	0.047	0.006	7
FeT	3.501	0.056	3

Table S3: Summary of the molar concentration in mol L^{-1} and activity (a) of total oxalate ions, $C_2O_4^{2-}$, and $HC_2O_4^-$ in the experiment solutions calculated using the E-AIM model III for aqueous solution (Wexler and Clegg, 2002). A comprehensive description of the experimental conditions is provided in Table S1. pHf is the calculated final pH in the experiment solutions.

Sample	Exp.	pH_f	$[oxalate]_{total}$	$[C_2O_4^{2-}]$	$a(C_2O_4^{2-})$	$[HC_2O_4^-]$	$a(HC_2O_4^-)$
Krakow ash	Exp 3	2.0	0.009	0.00071	0.04	0.009	0.55
Krakow ash	Exp 4	1.9	0.008	0.00006	0.49	0.008	0.86
Krakow ash	Exp 3	2.9	0.010	0.00343	0.04	0.006	0.54
Krakow ash	Exp 5	1.0	0.012	0.00002	0.22	0.012	0.79
Krakow ash	Exp 6	1.0	0.015	0.00010	0.06	0.015	0.64
Krakow ash	Exp 7	1.0	0.015	0.00015	0.04	0.015	0.65
Krakow ash	Exp 8	1.0	0.015	0.00022	0.03	0.015	0.68
Aberthaw ash	Exp 3	2.0	0.009	0.00066	0.04	0.009	0.56
Aberthaw ash	Exp 4	2.0	0.009	0.00007	0.60	0.009	0.90
Shandong ash	Exp 3	2.0	0.009	0.00066	0.04	0.009	0.56
Shandong ash	Exp 4	2.0	0.009	0.00007	0.60	0.009	0.90
Libyan dust	Exp 3	2.0	0.009	0.00068	0.04	0.009	0.56
Libyan dust	Exp 4	2.0	0.008	0.00006	0.55	0.008	0.88

Table S4: Modelled mass concentration of total Fe in $PM_{2.5}$ aerosol particles (ng m^{-3}) over the Bay of Bengal from 27 December 2008 to 26 January 2009. Observations are reported in Bikkina et al. (2020). The concentrations of total Fe were calculated along the cruise tracks in the North Bay of Bengal (27 December 2008 - 10 January 2009) and the South Bay of Bengal (11-26 January 2009) using the IMPACT model. The total Fe emissions from anthropogenic combustion sources (ANTHRO) and biomass burning (BB) were estimated using the emission inventory of (Ito et al., 2018), whereas Fe emissions from mineral dust sources (DUST) were dynamically simulated (Ito et al., 2021).

Date	DUST	ANTHRO	BB	Total Fe
27/12/2008	20.7	11.1	0.2	31.9
28/12/2008	56.8	12.8	0.4	70.0
29/12/2008	71.2	10.7	0.4	82.4
30/12/2008	48.5	11.7	0.5	60.7
31/12/2008	55.3	17.1	0.6	73.0
01/01/2009	65.4	25.2	0.7	91.3
02/01/2009	69.2	33.5	0.7	103.4
03/01/2009	66.8	33.4	0.6	100.8
04/01/2009	48.0	19.1	0.5	67.7
05/01/2009	18.1	9.2	0.4	27.8
06/01/2009	6.5	7.0	0.3	13.9
07/01/2009	36.3	18.9	0.4	55.6
08/01/2009	31.1	14.9	0.4	46.4
09/01/2009	13.9	6.4	0.5	20.8
10/01/2009	3.4	27.9	1.9	33.2
11/01/2009	7.2	35.2	3.8	46.3
12/01/2009	5.6	21.4	3.5	30.5
13/01/2009	3.3	13.6	5.4	22.3
14/01/2009	3.3	15.0	7.0	25.2
15/01/2009	4.2	25.7	4.9	34.8
16/01/2009	4.6	24.3	6.1	35.0
17/01/2009	2.9	15.5	6.4	24.8
18/01/2009	2.0	9.5	4.7	16.1
19/01/2009	1.1	3.4	2.2	6.7
20/01/2009	1.0	4.3	3.9	9.2
21/01/2009	2.3	9.4	2.7	14.3
22/01/2009	2.5	8.7	2.1	13.2

23/01/2009	1.1	4.2	4.3	9.6
24/01/2009	0.7	2.4	5.0	8.1
25/01/2009	0.6	2.9	9.5	13.1
26/01/2009	0.4	2.5	8.2	11.2

Table S5: Modelled Fe solubility in $PM_{2.5}$ aerosol particles (Fe%) over the Bay of Bengal from 27 December 2008 to 26 January 2009. Observations are reported in Bikkina et al. (2020). The aerosol Fe solubility were calculated along the cruise tracks in the North Bay of Bengal (27 December 2008 - 10 January 2009) and the South Bay of Bengal (11-26 January 2009) using the IMPACT model. In Test 0, we run the model without upgrades (Ito et al., 2021) and applying the proton-promoted, oxalate-promoted, and photoinduced dissolution schemes for combustion aerosols in Table S6 (Ito, 2015). The proton + oxalate dissolution scheme (Table 1) was applied in Test 1 and 3, while proton-promoted dissolution is used for Test 2. We adopted the base mineralogy for anthropogenic Fe emissions (Rathod et al., 2020) in Test 1 and 2. In Test 3, the Fe speciation of Krakow ash was used for all combustion sources.

Date	Test 0	Test 1	Test 2	Test 3
27/12/2008	14.2	17.2	38.0	15.2
28/12/2008	8.8	11.1	21.7	10.6
29/12/2008	6.5	9.3	17.2	9.2
30/12/2008	7.5	12.5	25.1	13.2
31/12/2008	7.5	14.4	29.9	14.6
01/01/2009	8.7	16.2	33.2	16.3
02/01/2009	8.8	15.8	34.1	16.0
03/01/2009	8.8	16.5	37.9	16.0
04/01/2009	8.9	16.1	35.7	16.0
05/01/2009	14.0	18.2	40.4	19.2
06/01/2009	21.6	25.2	58.4	26.6
07/01/2009	12.1	17.7	39.6	17.2
08/01/2009	9.5	16.4	36.0	15.6
09/01/2009	10.5	15.9	33.4	16.3
10/01/2009	19.0	26.7	77.9	31.4
11/01/2009	12.8	24.2	74.2	29.3
12/01/2009	16.3	24.7	81.1	30.0
13/01/2009	25.2	24.0	82.8	30.9
14/01/2009	20.5	23.8	86.8	31.1
15/01/2009	12.8	24.4	89.8	30.0

16/01/2009	15.0	24.4	88.6	30.4
17/01/2009	22.8	26.3	90.7	33.2
18/01/2009	32.0	28.2	91.2	35.3
19/01/2009	47.9	28.8	88.7	35.3
20/01/2009	48.7	30.7	94.5	39.9
21/01/2009	36.5	35.7	88.6	42.0
22/01/2009	37.1	37.8	86.7	41.7
23/01/2009	60.9	37.5	95.3	46.8
24/01/2009	73.0	35.7	97.6	47.3
25/01/2009	66.8	32.7	98.8	46.0
26/01/2009	71.6	34.7	99.2	47.7

Table S6: Constants used to calculate the Fe dissolution rates for fossil fuel combustion aerosols in Ito (2015), and the new dissolution scheme implemented in this study. Note that the dissolution scheme in Ito (2015) was based on laboratory measurements conducted at low ionic strength.

Scheme	Reference	Rate constant - k(pH, T)[a]		m[c]
Proton	Ito (2015)	5.24×10^{-8} exp[E(pH)^{b} × (1/298 – 1/T)]		0.36
Oxalate	Ito (2015)	3.85×10^{-6} exp[E(pH)^{b} × (1/298 – 1/T)]		1
Photoinduced	Ito (2015)	4.10×10^{-6} exp[E(pH)^{b} × (1/298 – 1/T)]		1
Proton	This study	7.61×10^{-6}exp[E(pH)^{b} × (1/298 – 1/T)]	Stage I - Kinetic fast	0.241
		1.91×10^{-7}exp[E(pH)^{b} × (1/298 – 1/T)]	Stage II - Kinetic intermediate	0.195
		2.48×10^{-7}exp[E(pH)^{b} × (1/298 – 1/T)]	Stage III - Kinetic slow	0.843
Proton + Oxalate	This study	5.54×10^{-6}exp[E(pH)^{b} × (1/298 – 1/T)]	Stage I - Kinetic fast	0.209
		1.50×10^{-7}exp[E(pH)^{b} × (1/298 – 1/T)]	Stage II - Kinetic intermediate	0.091
		1.77×10^{-8}exp[E(pH)^{b} × (1/298 – 1/T)]	Stage III - Kinetic slow	0.204

[a]K(pH,T) is the rate constant (moles Fe g^{-1} s^{-1}) for each dissolution scheme.
[b]E(pH) = $-1.56 \times 10^{3} \times$pH + 1.08×10^{4}.
[c]mi is the reaction order with respect to aqueous phase protons.

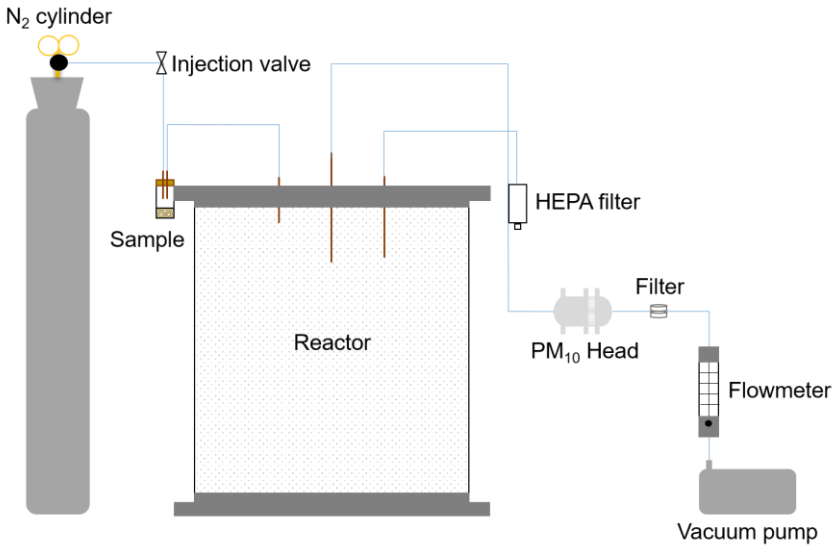

Figure S1: PM_{10} collection system.

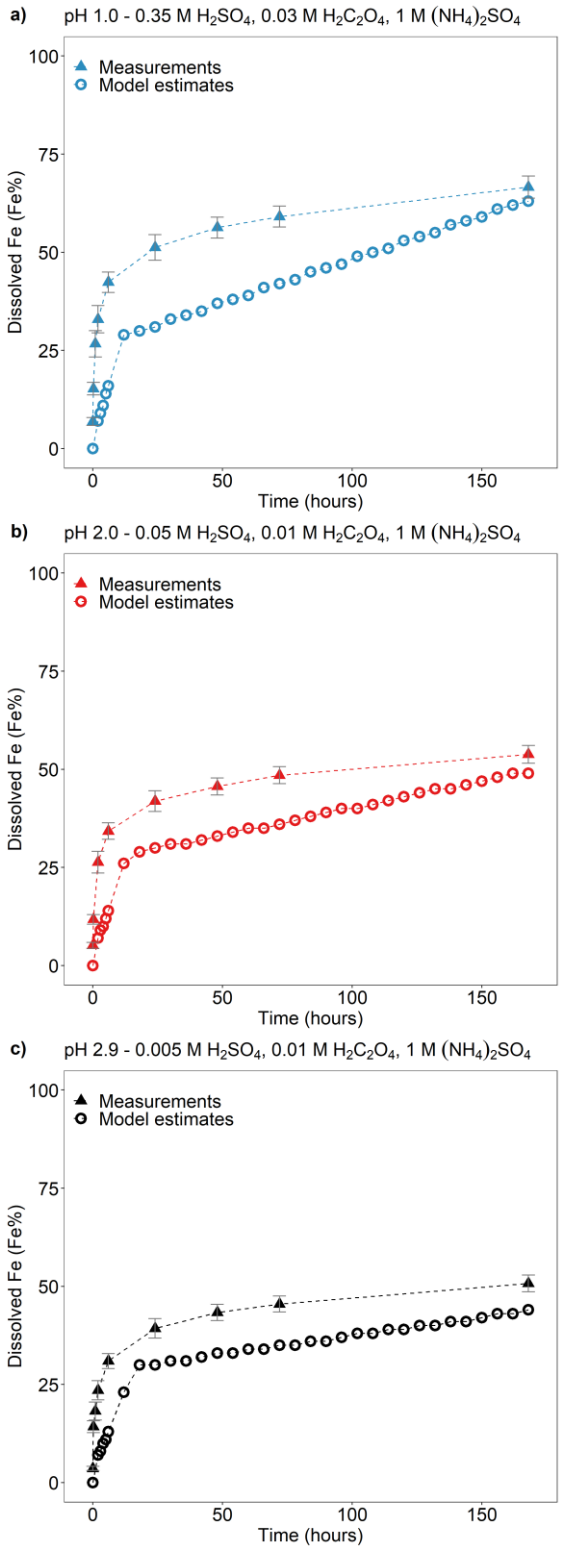

Figure S2: Comparison between the Fe dissolution kinetics of Krakow ash predicted using Eq. (1) and measured in H_2SO_4 solutions a) at pH 1.0 with 0.03 M $H_2C_2O_4$ and 1 M $(NH_4)_2SO_4$, b) at pH 2.0 with 0.01 M $H_2C_2O_4$ and 1 M $(NH_4)_2SO_4$, c) at pH 2.9 with 0.01 M $H_2C_2O_4$ and 1 M $(NH_4)_2SO_4$. The molar concentrations of H_2SO_4, $H_2C_2O_4$ and $(NH_4)_2SO_4$ in the experiment solutions are shown. The final pH of the experiment solutions is also reported, which was calculated using the E-AIM model III for aqueous solution (Wexler and Clegg, 2002) accounting for the buffer capacity of the CFA samples (Experiment 7 at pH 1.0, Experiment 3 at pH 2.0, and Experiment 3 at pH 2.9 in Table S1).

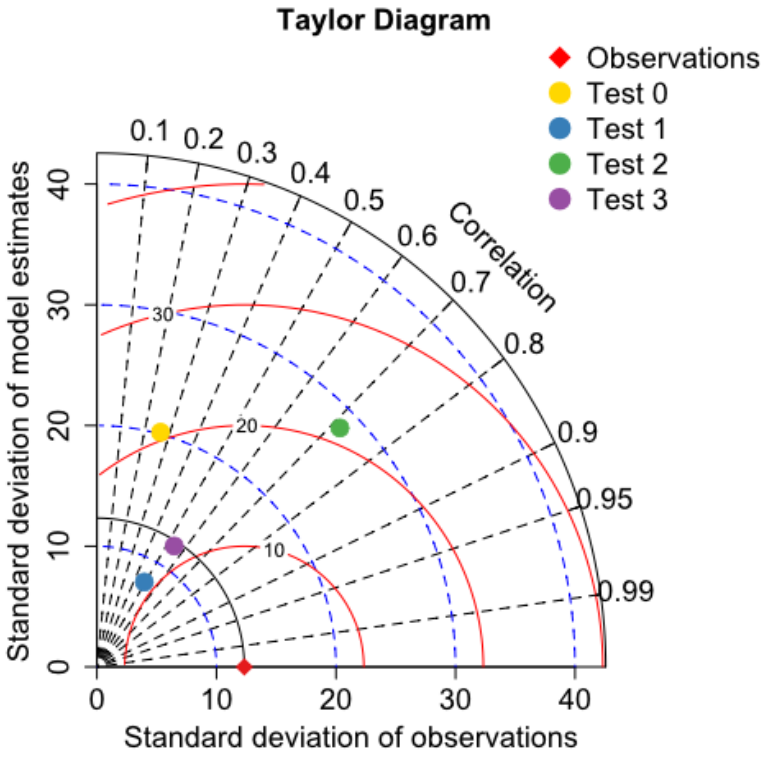

Figure S3: Comparison between observations and model estimates of Fe solubility in $PM_{2.5}$ aerosol particles over the Bay of Bengal from 27 December 2008 to 26 January 2009. Observations are from Bikkina et al. (2020). Model estimates of Test 0, Test 1, Test 2, and Test 3 were calculated along the cruise tracks using the IMPACT model. The Taylor diagram summarizes the statistics for the comparison between observations of aerosol Fe solubility and the different simulations (Test 0-3). The dashed curves in blue indicate the standard deviation values. The curves in red denote the root-mean-squared difference between the observational data and the model predictions (RMSE). The dashed lines in black represent the correlation coefficients.

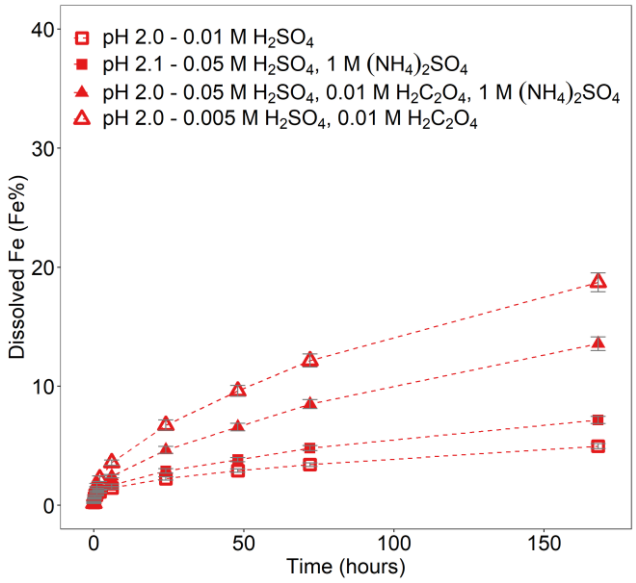

Figure S4: Fe dissolution kinetics of Libyan dust end member in H_2SO_4 solutions at around pH 2 (open rectangles), with 1 M $(NH_4)_2SO_4$ (filled rectangles), with 0.01 M $H_2C_2O_4$ (open triangles), with 0.01 M $H_2C_2O_4$ and 1 M $(NH_4)_2SO_4$ (filled triangles). The molar concentrations of H_2SO_4, $H_2C_2O_4$ and $(NH_4)_2SO_4$ in the experiment solutions are shown. The final pH of the experiment solutions is also reported, which was calculated using the E-AIM model III for aqueous solution (Wexler and Clegg, 2002) accounting for the buffer capacity of the CFA samples (Experiments 1-4 in Table S1). The data uncertainty was estimated using the error propagation formula.

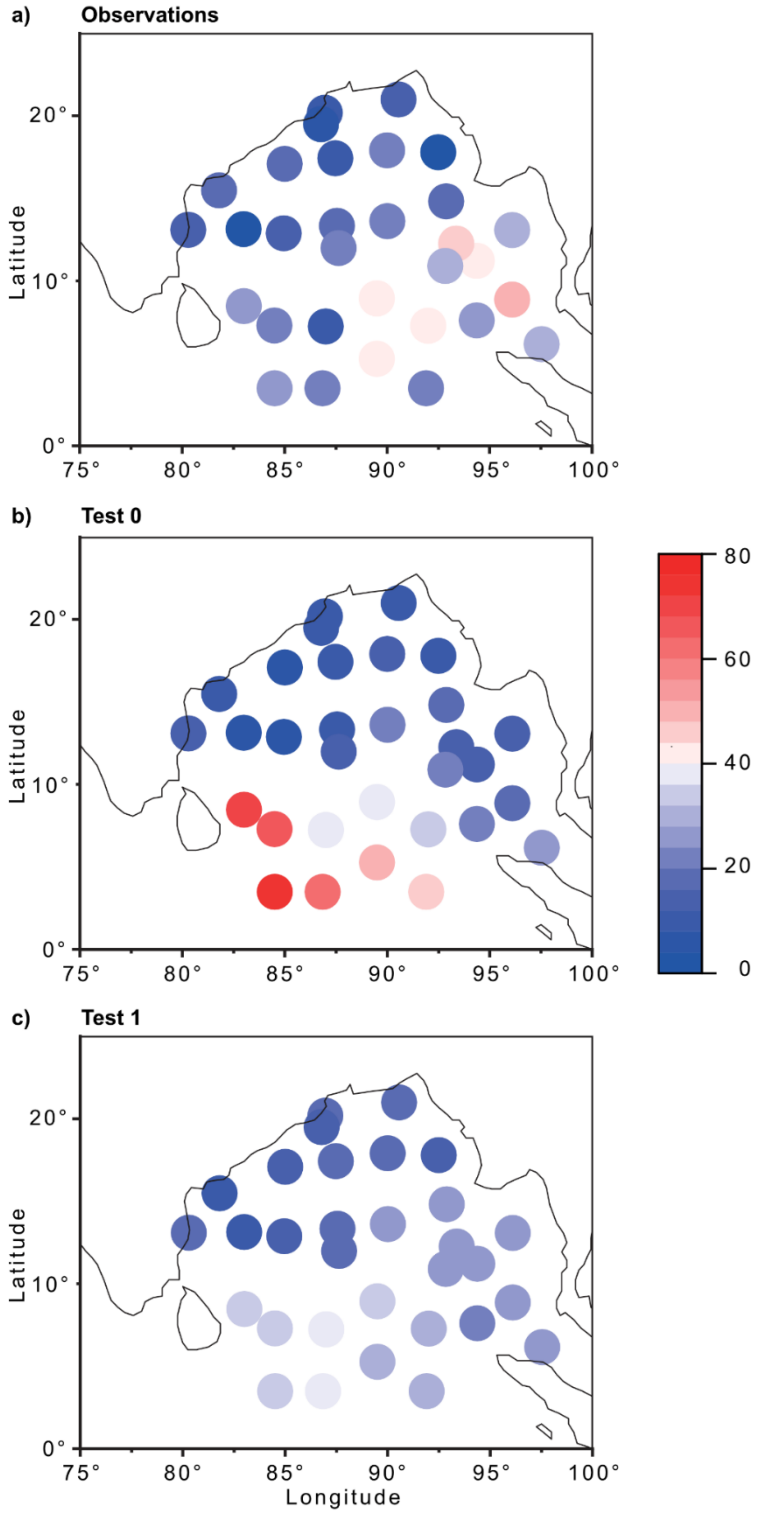

Figure S5: Fe solubility in $PM_{2.5}$ aerosol particles over the Bay of Bengal from 27 December 2008 to 26 January 2009. a) Observations from Bikkina et al. (2020). b-c) Model estimates of Test 0 and Test 1 calculated along the cruise tracks using the IMPACT model. In Test 0, we ran the model without upgrades in the Fe dissolution scheme (Ito et al., 2021) and applying the proton-promoted, oxalate-promoted and photoinduced dissolution schemes for combustion aerosols in Table S6 (Ito, 2015). The proton + oxalate dissolution scheme (Table 1) was applied in Test 1 and we adopted the base mineralogy for anthropogenic Fe emissions (Rathod et al., 2020).

References

Bikkina, S., Kawamura, K., Sarin, M., and Tachibana, E.: ^{13}C Probing of Ambient Photo-Fenton Reactions Involving Iron and Oxalic Acid: Implications for Oceanic Biogeochemistry, ACS Earth Space Chem., 4, 964-976, doi: 10.1021/acsearthspacechem.0c00063, 2020.

Ito, A.: Atmospheric Processing of Combustion Aerosols as a Source of Bioavailable Iron, Environ. Sci. Technol. Lett., 2, 70-75, doi: 10.1021/acs.estlett.5b00007, 2015.

Ito, A., Lin, G. X., and Penner, J. E.: Radiative forcing by light-absorbing aerosols of pyrogenetic iron oxides, Sci. Rep., 8, 7347, doi: 10.1038/s41598-018-25756-3, 2018.

Ito, A., Adebiyi, A. A., Huang, Y., and Kok, J. F.: Less atmospheric radiative heating by dust due to the synergy of coarser size and aspherical shape, Atmos. Chem. Phys., 21, 16869–16891, doi: 10.5194/acp-21-16869-2021, 2021.

Rathod, S. D., Hamilton, D. S., Mahowald, N. M., Klimont, Z., Corbett, J. J., and Bond, T. C.: A Mineralogy‐Based Anthropogenic Combustion‐Iron Emission Inventory, J. Geophys. Res.-Atmos, 125, e2019JD032114, doi: 10.1029/2019jd032114, 2020.

Wexler, A. S., and Clegg, S. L.: Atmospheric aerosol models for systems including the ions H^+, NH_4^+, Na^+, SO_4^{2-}, NO_3^-, Cl^-, Br^-, and H_2O, J. Geophys. Res.-Atmos, 107, 4207, doi: 10.1029/2001JD000451, 2002.

SI Chapter 4

Table S1: Sampling sites.

Dust Hotspot	Location	Sample Code	Latitude / Longitude
Dyngjusandur	NE Iceland	D3	64°50'41.885"N / 16°59'40.78"W
Hagavatn	Central W Iceland	H55	64°28'52.04"N / 20°27'18.81"W
Landeyjarsandur	S Iceland	Land1	63°34'13"N / 20°02'31"W
Mælifellssandur	Central S Iceland	Mæli2	63°48'42.2"N / 19°07'02.5"W
Myrdalssandur	S Iceland	MIR45	63°32'42.08"N / 18°42'14.14"W

Table S2: Complex refractive indexes of the individual minerals used in this study.

Mineral	Reference
Hematite	Longtin et al. (1988)
Hematite	Bedidi and Cervelle (1993)
Goethite	Bedidi and Cervelle (1993)
Magnetite	Querry (1985)
Magnetite	Huffman and Stapp (1973)
Olivine	Fabian et al. (2001)
Augite	Egan and Hilgeman (1979)
Feldspar	Egan and Hilgeman (1979)
Quartz	Khashan and Nasif (2001)
Basaltic glass	Pollack et al. (1973)

Table S3: Amorphous Fe (FeA), dithionite Fe (FeD, Hematite + Goethite), magnetite (FeM), initial Fe solubility (Fe_{isol}) and potential Fe solubility (Fe_{psol}) as extracted-dissolved Fe to total dust mass. The standard deviation (sd) is reported, n = 3. For Fe_{psol}, sd was estimated based on the relative standard deviation obtained for a dust sample from Africa (Libya), n = 7.

Samples	FeA	FeD	FeM	Fe_{isol}	Fe_{psol}
	wt% (sd)	wt% (sd)	wt% (sd)	wt% (sd)	wt% (sd)
D3	0.1 (0.02)	0.44 (0.04)	1.76 (0.26)	0.07 (0.002)	3.35 (0.14)
H55	0.04 (0.004)	0.33 (0.02)	1.5 (0.20)	0.01 (0.001)	1.78 (0.07)
Land1	0.14 (0.03)	0.77 (0.09)	0.87 (0.02)	0.01 (0.001)	2.12 (0.09)
Maeli2	0.18 (0.006)	0.79 (0.03)	1.66 (0.10)	0.03 (0.003)	3.39 (0.14)
MIR45	0.04 (0.001)	0.13 (0.002)	1 (0.06)	0.01 (0.001)	1.75 (0.07)

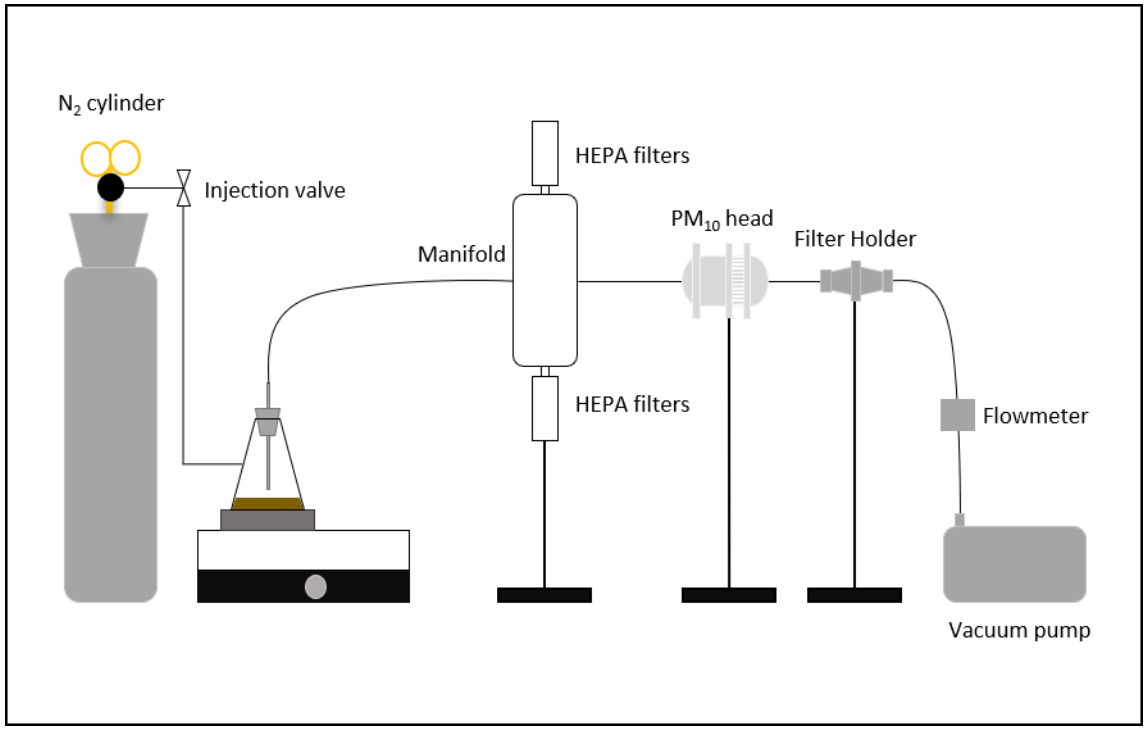

Figure S1: PM_{10} collection system.

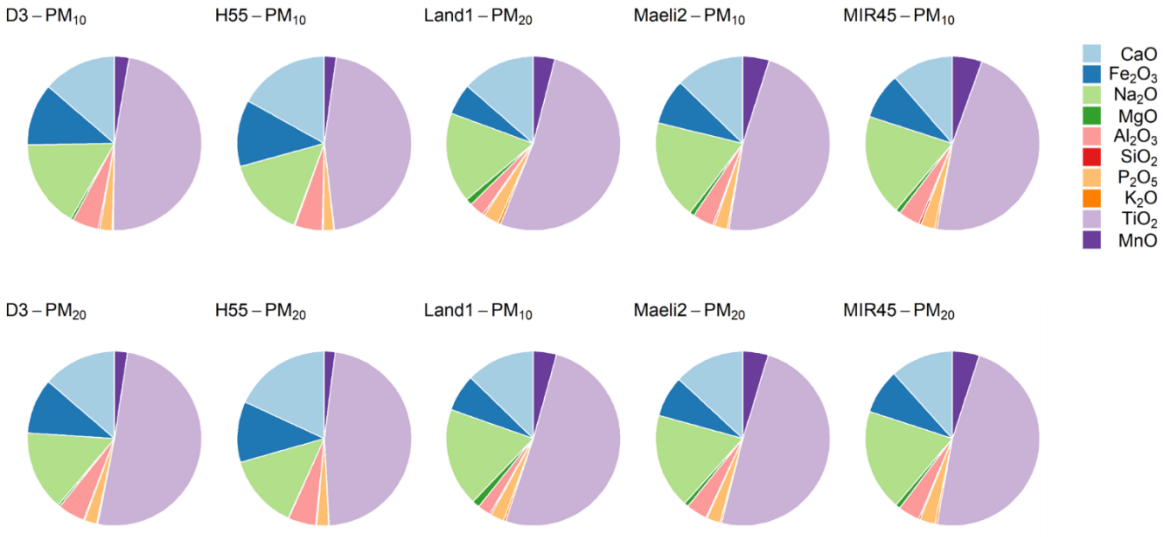

Figure S2: Element oxide mass percentages of PM_{10} (custom-made reactor) and PM_{20} (CESAM chamber). The data uncertainty is ~12%, estimated using the error propagation formula.

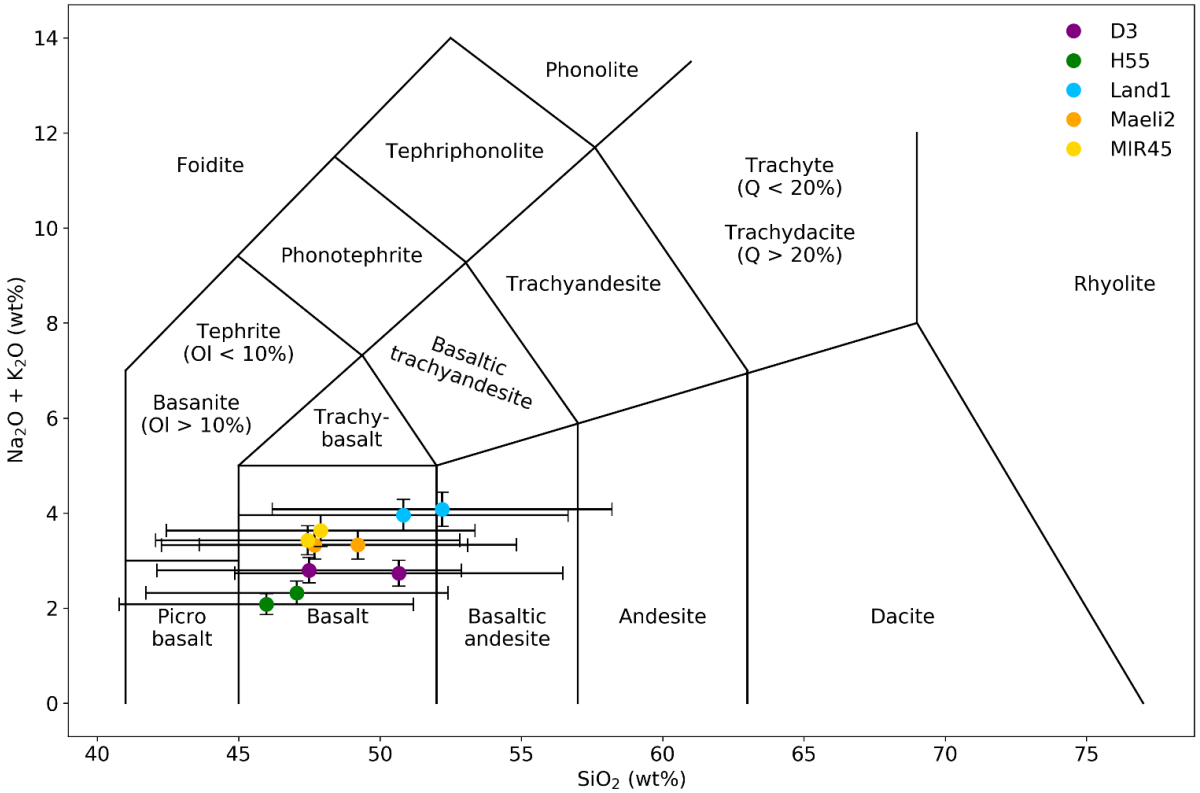

Figure S3: Classification of the dust samples (PM_{10} and PM_{20} fractions) based on the total alkali and silica (TAS) contents from the XRF measurements. The data uncertainty was estimated using the error propagation formula.

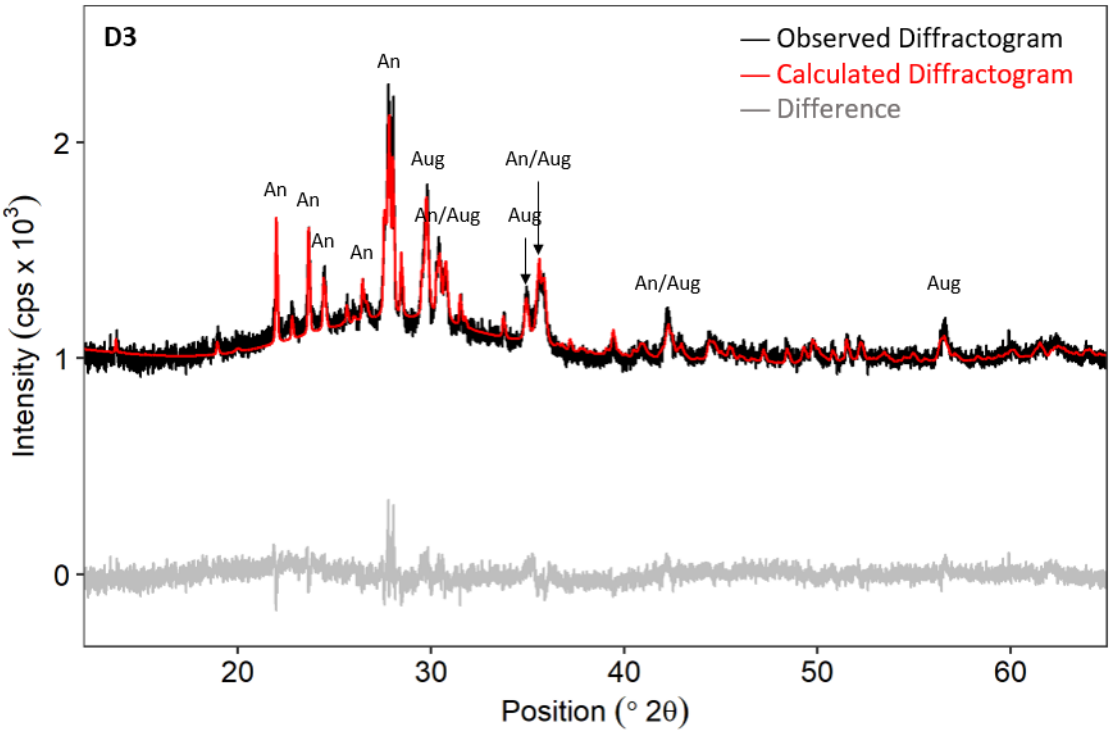

An = Anorthite #98-010-0235, Aug = Augite #98-003-4194

Figure S4: Diffractogram of D3, PM_{10} fraction. The black curve corresponds to the experimental data and the red curve to the model by MAUD software. The grey curve is the difference between the observations and the model.

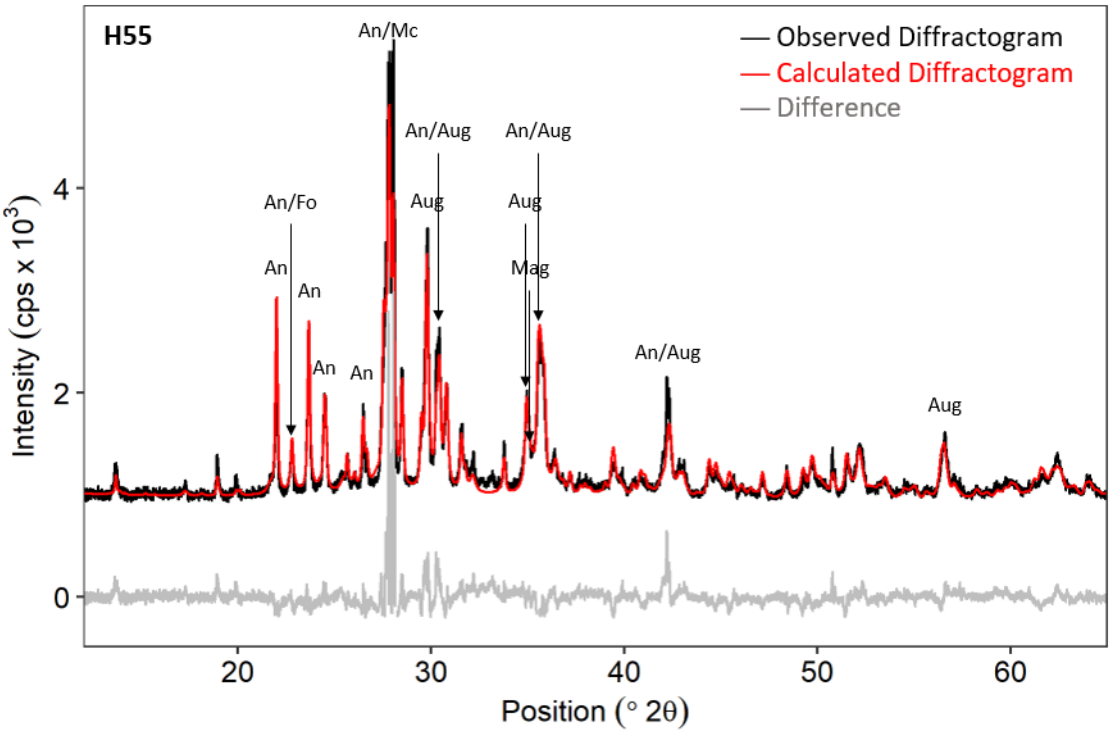

An = Anorthite #98-010-0235, Aug = Augite #98-003-4194, Fo = Forsterite #98-003-4112,
Mag = (Titano)Magnetite #98-016-2356, Mc = Microcline #98-008-3534

Figure S5: Diffractogram of H55, PM_{10} fraction. The black curve corresponds to the experimental data and the red curve to the model by MAUD software. The grey curve is the difference between the observations and the model.

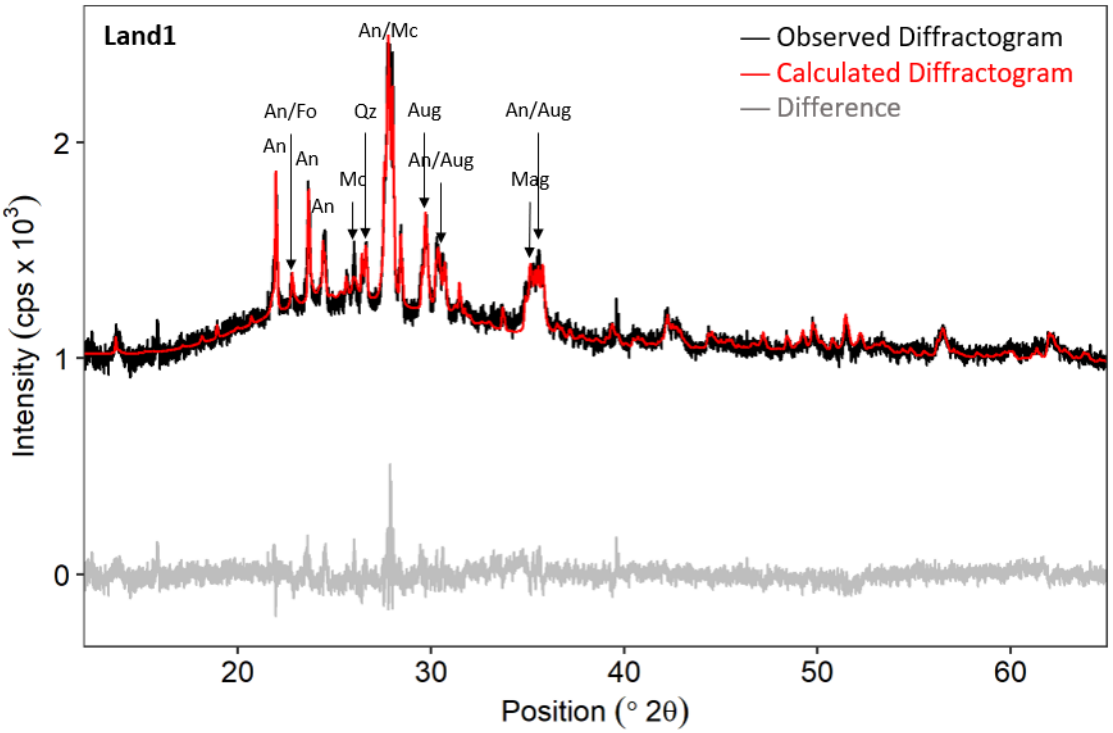

An = Anorthite #98-010-0235, Aug = Augite #98-003-4194, Fo = Forsterite #98-003-4112,
Mag = (Titano)Magnetite #98-016-2356, Mc = Microcline #98-008-3534, Qz = Quartz #98-009-3093

Figure S6: Diffractogram of Land1, PM_{10} fraction. The black curve corresponds to the experimental data and the red curve to the model by MAUD software. The grey curve is the difference between the observations and the model.

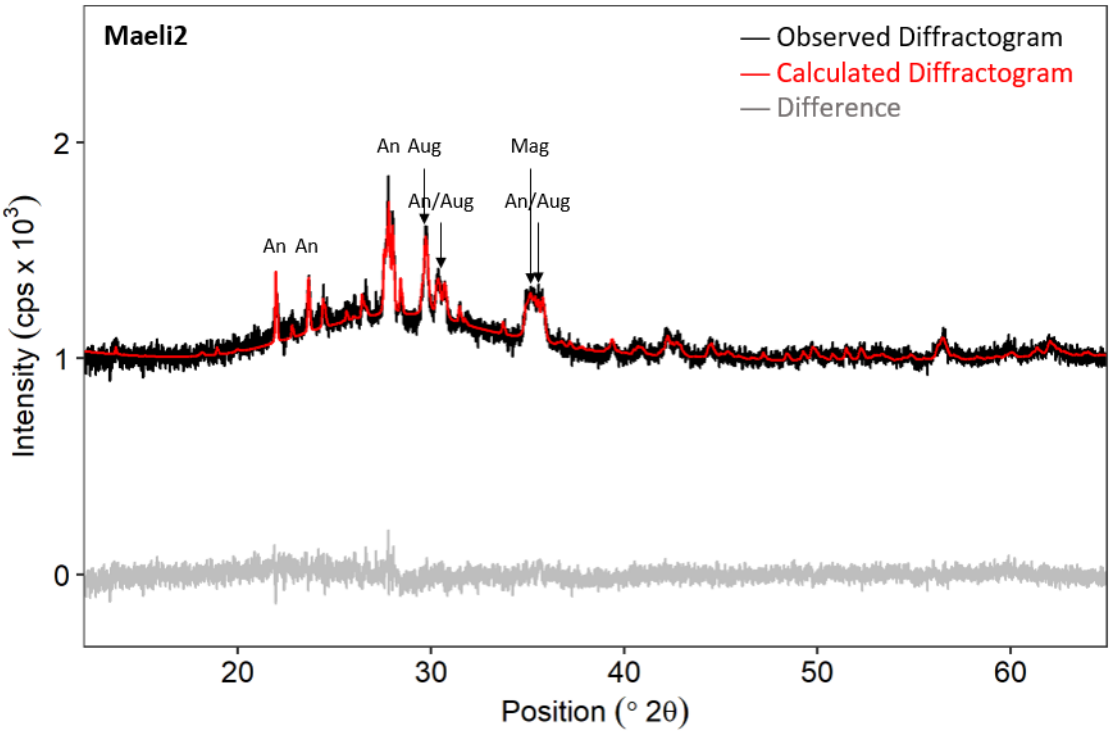

An = Anorthite #98-010-0235, Aug = Augite #98-003-4194, Mag = (Titano)Magnetite #98-016-2356,

Figure S7: Diffractogram of Maeli2, PM_{10} fraction. The black curve corresponds to the experimental data and the red curve to the model by MAUD software. The grey curve is the difference between the observations and the model.

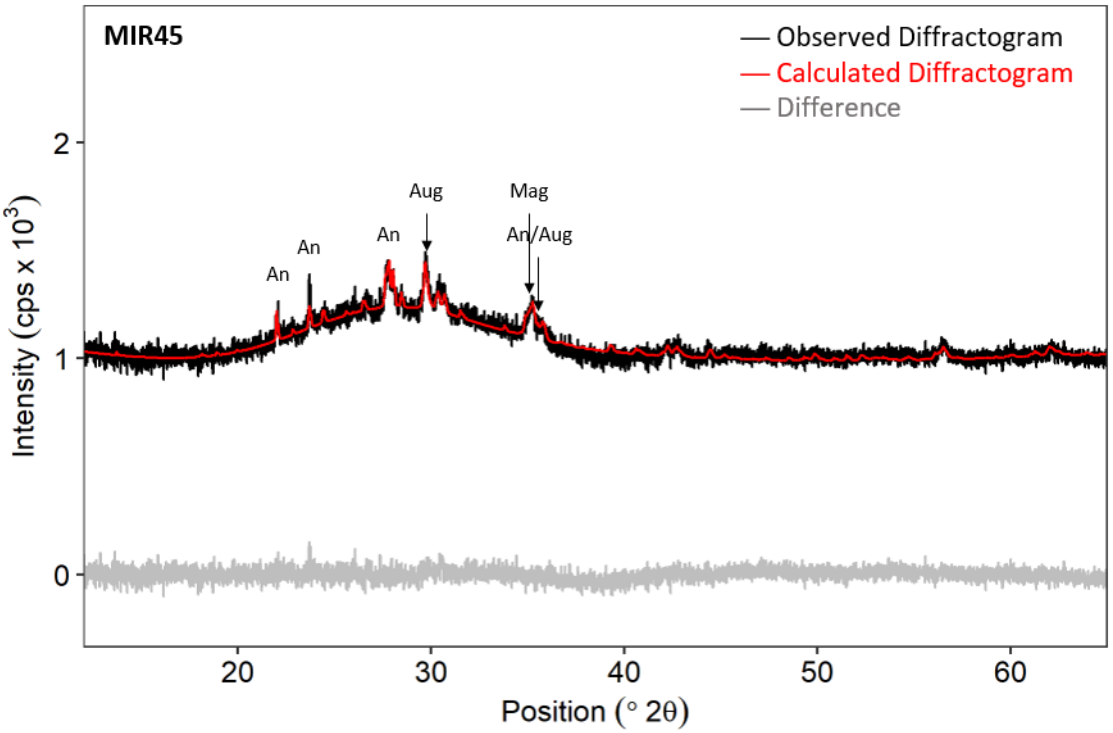

Figure S8: Diffractogram of MIR45, PM_{10} fraction. The black curve corresponds to the experimental data and the red curve to the model by MAUD software. The grey curve is the difference between the observations and the model.

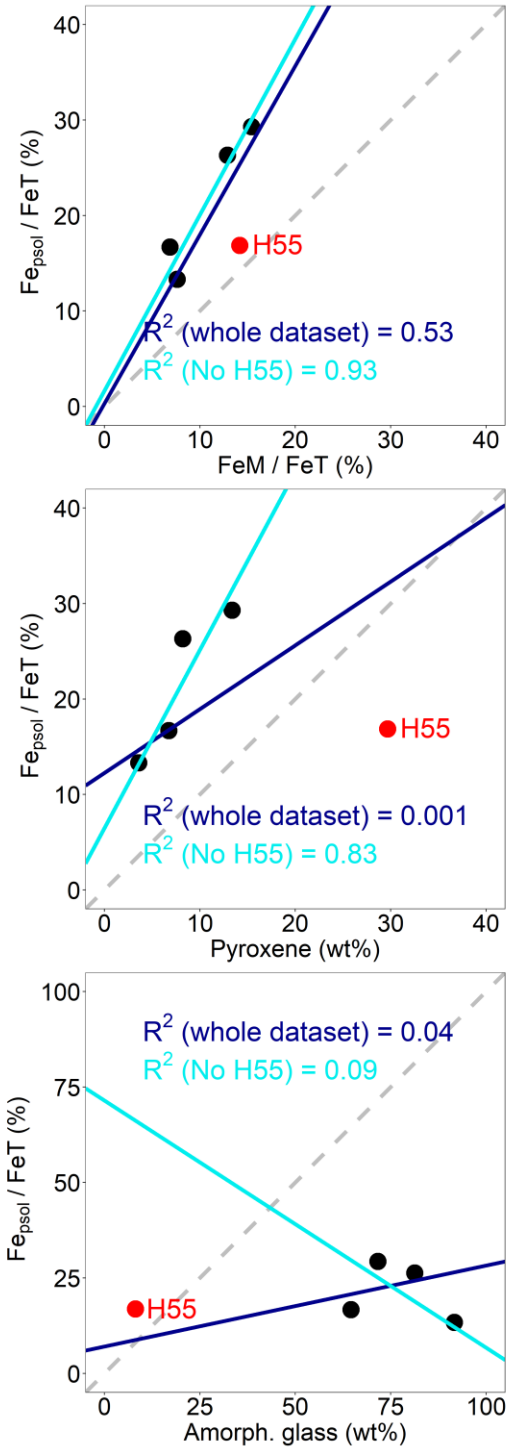

Figure S9: Correlation of Fe_{psol} / FeT (%) with the content of magnetite (FeM / FeT, %), pyroxene (wt%) and amorphous glass (wt%). The regression line in blue was calculated based on the whole dataset. The regression line in light blue was calculated excluding H55 (the dust sample with the lowest amorphous fraction).

References

Bedidi, A., and Cervelle, B.: Light scattering by spherical particles with hematite and goethitelike optical properties: effect of water impregnation, Journal of Geophysical Research: Solid Earth, 98, 11941-11952, doi: 10.1029/93JB00188, 1993.

Egan, W., and Hilgeman, T.: Optical Properties of Inhomogeneous Materials: Applications to Geology, Astronomy, Chemistry and Engineering Academic Press, New York, 1979.

Fabian, D., Henning, Th., Joger, C., Mutschke, H., Dorschner, J., Werhan, O.: Olivine, EODG ARIA, available at http://eodg.atm.ox.ac.uk/ARIA/data?Minerals/Olivine/non-oriented_(Fabian_et_al._2001)/olivine_Fabian_2001.ri (last access: 02 January 2020), 2001.

Huffman, D. R., and Stapp, J. L.: Optical measurements on solids of possible interstellar importance, in: Interstellar dust and related topics, Springer, 297-301, 1973.

Khashan, M. A. and Nasif, A. Y.: Quartz, EODG ARIA, available at http://eodg.atm.ox.ac.uk/ARIA/data?Minerals/Quartz/ (Khashan_and Nassif_2001)/quartz_Khashan_2001.ri (last access: 02 January 2020), 2001.

Longtin, D. R., Shettle, E. P., Hummel, J. R., and Pryce, J. D.: A wind dependent desert aerosol model: Radiative properties, AFGLTR-88-0112, Air Force Geophysics Laboratory, Hanscom AFB, MA, 1988.

Pollack, J. B., Toon, O. B., and Khare, B. N.: Optical properties of some terrestrial rocks and glasses, Icarus, 19, 372-389, 1973.

Querry, M. R.: Magnetite, Refractive index database, available at https://refractiveindex.info/?shelf=main&book=Fe3O4& (last access: 02 January 2020), 1985.

SI Chapter 5

Table S1: Experiment-averaged single scattering albedo $SSA_{avg}(\lambda)$ ± estimated uncertainty at λ = 370, 470, 520, 590, 660, 880, 950 nm of Icelandic dust for the base simulation, Test 1 and Test 2.

Info	Sample ID	$SSA_{avg}(\lambda)$						
		370 nm	470 nm	520 nm	590 nm	660 nm	880 nm	X950 nm
Base simulation	D3	0.93 ± 0.02	0.95 ± 0.01	0.96 ± 0.01	0.96 ± 0.01	0.96 ± 0.02	0.96 ± 0.01	0.96 ± 0.02
Base simulation	H55	0.94 ± 0.06	0.96 ± 0.08	0.96 ± 0.08	0.96 ± 0.08	0.96 ± 0.08	0.96 ± 0.07	0.96 ± 0.07
Base simulation	Land1	0.91 ± 0.05	0.94 ± 0.03	0.95 ± 0.03	0.95 ± 0.03	0.96 ± 0.04	0.96 ± 0.04	0.96 ± 0.04
Base simulation	Maeli2	0.90 ± 0.03	0.93 ± 0.02	0.94 ± 0.02	0.95 ± 0.02	0.95 ± 0.01	0.96 ± 0.01	0.95 ± 0.02
Base simulation	MIR45	0.90 ± 0.04	0.92 ± 0.03	0.93 ± 0.02	0.94 ± 0.03	0.94 ± 0.03	0.94 ± 0.03	0.94 ± 0.03
Test 1	D3	0.93 ± 0.02	0.95 ± 0.01	0.96 ± 0.01	0.96 ± 0.01	0.96 ± 0.02	0.96 ± 0.01	0.96 ± 0.01
Test 1	H55	0.94 ± 0.05	0.96 ± 0.07	0.96 ± 0.07	0.96 ± 0.08	0.96 ± 0.08	0.96 ± 0.07	0.96 ± 0.07
Test 1	Land1	0.91 ± 0.05	0.94 ± 0.03	0.95 ± 0.03	0.95 ± 0.03	0.96 ± 0.04	0.96 ± 0.04	0.96 ± 0.04
Test 1	Maeli2	0.90 ± 0.03	0.93 ± 0.02	0.94 ± 0.02	0.95 ± 0.02	0.95 ± 0.01	0.96 ± 0.02	0.96 ± 0.02
Test 1	MIR45	0.90 ± 0.04	0.92 ± 0.02	0.93 ± 0.02	0.94 ± 0.03	0.94 ± 0.03	0.94 ± 0.03	0.94 ± 0.03
Test 2	D3	0.93 ± 0.01	0.95 ± 0.01	0.96 ± 0.01	0.96 ± 0.02	0.96 ± 0.02	0.96 ± 0.02	0.96 ± 0.02
Test 2	H55	0.94 ± 0.06	0.96 ± 0.08	0.96 ± 0.08	0.96 ± 0.08	0.96 ± 0.08	0.96 ± 0.08	0.96 ± 0.08
Test 2	Land1	0.91 ± 0.04	0.93 ± 0.02	0.95 ± 0.03	0.95 ± 0.03	0.96 ± 0.03	0.96 ± 0.04	0.96 ± 0.04
Test 2	Maeli2	0.90 ± 0.02	0.93 ± 0.01	0.94 ± 0.01	0.95 ± 0.01	0.95 ± 0.01	0.95 ± 0.01	0.95 ± 0.01
Test 2	MIR45	0.90 ± 0.05	0.92 ± 0.04	0.93 ± 0.03	0.94 ± 0.04	0.94 ± 0.04	0.94 ± 0.04	0.94 ± 0.04

Table S2: Experiment-averaged imaginary index $k_{avg}(\lambda)$ ± estimated uncertainty at λ = 370, 470, 520, 590, 660, 880, 950 nm of Icelandic dust for the base simulation, Test 1 and Test 2.

Info	Sample ID	$k_{avg}(\lambda)$						
		370 nm	470 nm	520 nm	590 nm	660 nm	880 nm	X950 nm
Base simulation	D3	0.006 ± 0.003	0.005 ± 0.002	0.003 ± 0.002	0.002 ± 0.001	0.002 ± 0	0.002 ± 0	0.002 ± 0
Base simulation	H55	0.005 ± 0.002	0.005 ± 0.003	0.005 ± 0.002	0.002 ± 0.001	0.003 ± 0	0.002 ± 0	0.002 ± 0
Base simulation	Land1	0.005 ± 0.002	0.005 ± 0.003	0.005 ± 0.003	0.005 ± 0.002	0.004 ± 0.002	0.003 ± 0.001	0.002 ± 0.001
Base simulation	Maeli2	0.005 ± 0.003	0.005 ± 0.003	0.002 ± 0.002	0.004 ± 0.002	0.003 ± 0.001	0.002 ± 0.001	0.002 ± 0.001
Base simulation	MIR45	0.005 ± 0.002	0.005 ± 0.002	0.004 ± 0.001	0.004 ± 0.001	0.003 ± 0.001	0.003 ± 0	0.003 ± 0
Test 1	D3	0.002 ± 0.001	0.001 ± 0	0.001 ± 0	0.001 ± 0	0.001 ± 0	0.001 ± 0	0.001 ± 0
Test 1	H55	0.003 ± 0.001	0.002 ± 0.001	0.001 ± 0	0.001 ± 0	0.001 ± 0	0.002 ± 0.001	0.002 ± 0
Test 1	Land1	0.003 ± 0.002	0.002 ± 0	0.002 ± 0	0.001 ± 0	0.001 ± 0	0.001 ± 0.001	0.002 ± 0
Test 1	Maeli2	0.002 ± 0.001	0.002 ± 0.001	0.002 ± 0	0.002 ± 0	0.002 ± 0	0.002 ± 0	0.002 ± 0
Test 1	MIR45	0.002 ± 0.001	0.002 ± 0.001	0.002 ± 0.001	0.002 ± 0.001	0.002 ± 0.001	0.002 ± 0	0.002 ± 0
Test 2	D3	0.003 ± 0.001	0.002 ± 0	0.002 ± 0	0.002 ± 0	0.004 ± 0.002	0.002 ± 0	0.007 ± 0.002
Test 2	H55	0.002 ± 0	0.004 ± 0.001	0.005 ± 0.001	0.006 ± 0.002	0.007 ± 0	0.006 ± 0.002	0.007 ± 0
Test 2	Land1	0.005 ± 0	0.003 ± 0.001	0.003 ± 0.001	0.003 ± 0.001	0.004 ± 0.002	0.005 ± 0.001	0.006 ± 0.002
Test 2	Maeli2	0.004 ± 0	0.004 ± 0.002	0.002 ± 0.001	0.002 ± 0	0.002 ± 0	0.005 ± 0.001	0.005 ± 0.001
Test 2	MIR45	0.007 ± 0	0.006 ± 0	0.006 ± 0.001	0.005 ± 0	0.005 ± 0	0.006 ± 0	0.006 ± 0

Table S3: Experiment-averaged real index $n_{avg}(\lambda)$ ± estimated uncertainty at λ = 370, 470, 520, 590, 660, 880, 950 nm of Icelandic dust for the base simulation, Test 1 and Test 2.

Info	Sample ID	$n_{avg}(\lambda)$						
		370 nm	470 nm	520 nm	590 nm	660 nm	880 nm	X950 nm
Base simulation	D3	1.60 ± 0.02	1.61 ± 0.02	1.61 ± 0.02	1.61 ± 0.02	1.60 ± 0	1.60 ± 0	1.60 ± 0
Base simulation	H55	1.59 ± 0.02	1.60 ± 0.02	1.62 ± 0.01	1.61 ± 0.02	1.61 ± 0.03	1.60 ± 0	1.60 ± 0
Base simulation	Land1	1.59 ± 0.02	1.59 ± 0.01	1.60 ± 0.02	1.60 ± 0.02	1.61 ± 0.02	1.60 ± 0.02	1.61 ± 0.02
Base simulation	Maeli2	1.59 ± 0.02	1.60 ± 0.02	1.60 ± 0.03	1.61 ± 0.02	1.60 ± 0.02	1.61 ± 0.02	1.61 ± 0.02
Base simulation	MIR45	1.60 ± 0.02	1.60 ± 0.02	1.60 ± 0.02	1.59 ± 0.02	1.60 ± 0.02	1.60 ± 0.02	1.60 ± 0.02
Test 1	D3	1.60 ± 0.02	1.58 ± 0	1.58 ± 0	1.58 ± 0.00	1.60 ± 0.03	1.60 ± 0.03	1.60 ± 0.02
Test 1	H55	1.60 ± 0.02	1.60 ± 0.02	1.58 ± 0	1.59 ± 0.02	1.60 ± 0.02	1.59 ± 0.01	1.60 ± 0
Test 1	Land1	1.60 ± 0.02	1.60 ± 0	1.60 ± 0	1.60 ± 0.02	1.60 ± 0.02	1.60 ± 0.02	1.60 ± 0
Test 1	Maeli2	1.60 ± 0.02	1.60 ± 0.02	1.60 ± 0	1.60 ± 0	1.60 ± 0	1.60 ± 0	1.60 ± 0
Test 1	MIR45	1.60 ± 0.02	1.60 ± 0.02	1.60 ± 0.02	1.60 ± 0.02	1.61 ± 0.02	1.60 ± 0	1.60 ± 0
Test 2	D3	1.60 ± 0.02	1.60 ± 0.02	1.60 ± 0.02	1.59 ± 0.02	1.59 ± 0.02	1.58 ± 0	1.60 ± 0.02
Test 2	H55	1.60 ± 0.02	1.61 ± 0.02	1.62 ± 0.01	1.60 ± 0.02	1.59 ± 0	1.59 ± 0.02	1.63 ± 0
Test 2	Land1	1.62 ± 0.01	1.60 ± 0.02	1.60 ± 0.03	1.61 ± 0.03	1.60 ± 0.03	1.61 ± 0.02	1.60 ± 0.02
Test 2	Maeli2	1.62 ± 0.02	1.61 ± 0.02	1.60 ± 0.02	1.60 ± 0.02	1.60 ± 0.02	1.60 ± 0.02	1.61 ± 0.02
Test 2	MIR45	1.57 ± 0	1.59 ± 0.02	1.60 ± 0.02	1.62 ± 0	1.62 ± 0	1.58 ± 0.02	1.60 ± 0

Table S4: Comparison between SSAavg(λ) calculated using the measured Mie coefficients and the single scattering albedo retrieved using the complex refractive indices from the results of the base simulation, Test 1 and Test 2. The RMA regression slope and intercept are reported, in addition to the R^2 value and RMSE.

Info	Sample ID	Slope	Intercept	R^2	RMSE
Base Simulation	D3	4.75	-3.62	0.84	0.06
Test 1	D3	1.15	-0.13	0.95	0.01
Test 2	D3	2.64	-1.59	0.29	0.04
Base Simulation	H55	6.69	-5.50	0.68	0.07
Test 1	H55	4.46	-3.33	0.95	0.03
Test 2	H55	-3.28	4.03	0.72	0.08
Base Simulation	Land1	2.72	-1.68	0.75	0.06
Test 1	Land1	1.92	-0.87	0.96	0.02
Test 2	Land1	1.62	-0.62	0.43	0.04
Base Simulation	Maeli2	2.49	-1.44	0.79	0.04
Test 1	Maeli2	0.76	0.22	0.88	0.01
Test 2	Maeli2	1.75	-0.72	0.59	0.03
Base Simulation	MIR45	2.46	-1.38	0.89	0.04
Test 1	MIR45	0.81	0.18	0.80	0.01
Test 2	MIR45	2.24	-1.20	0.95	0.05

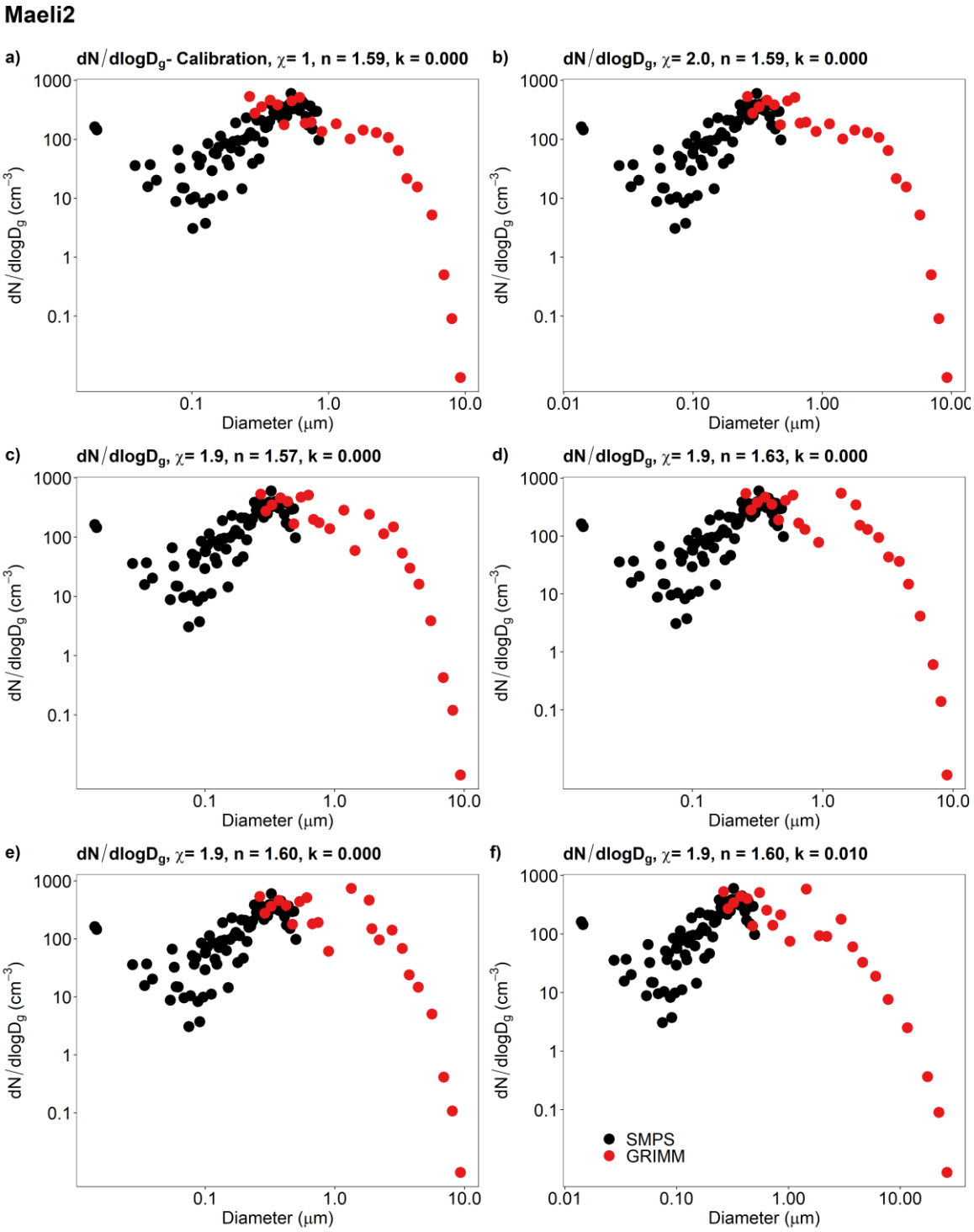

Figure S1: Geometrical size distributions dN/dlogD_g at 30 min after the injection peak a) obtained using the calibration values of χ, n and k, b-f) obtained for different χ-n-k combinations. χ is the dynamic shape factor used to convert the mobility diameter D_m measured by the SMPS into geometrical diameters D_g. n and k are respectively the real and imaginary part of the complex refractive index used to convert the optical diameter D_{op} measured by the GRIMM into D_g. Sample ID: Maeli2.

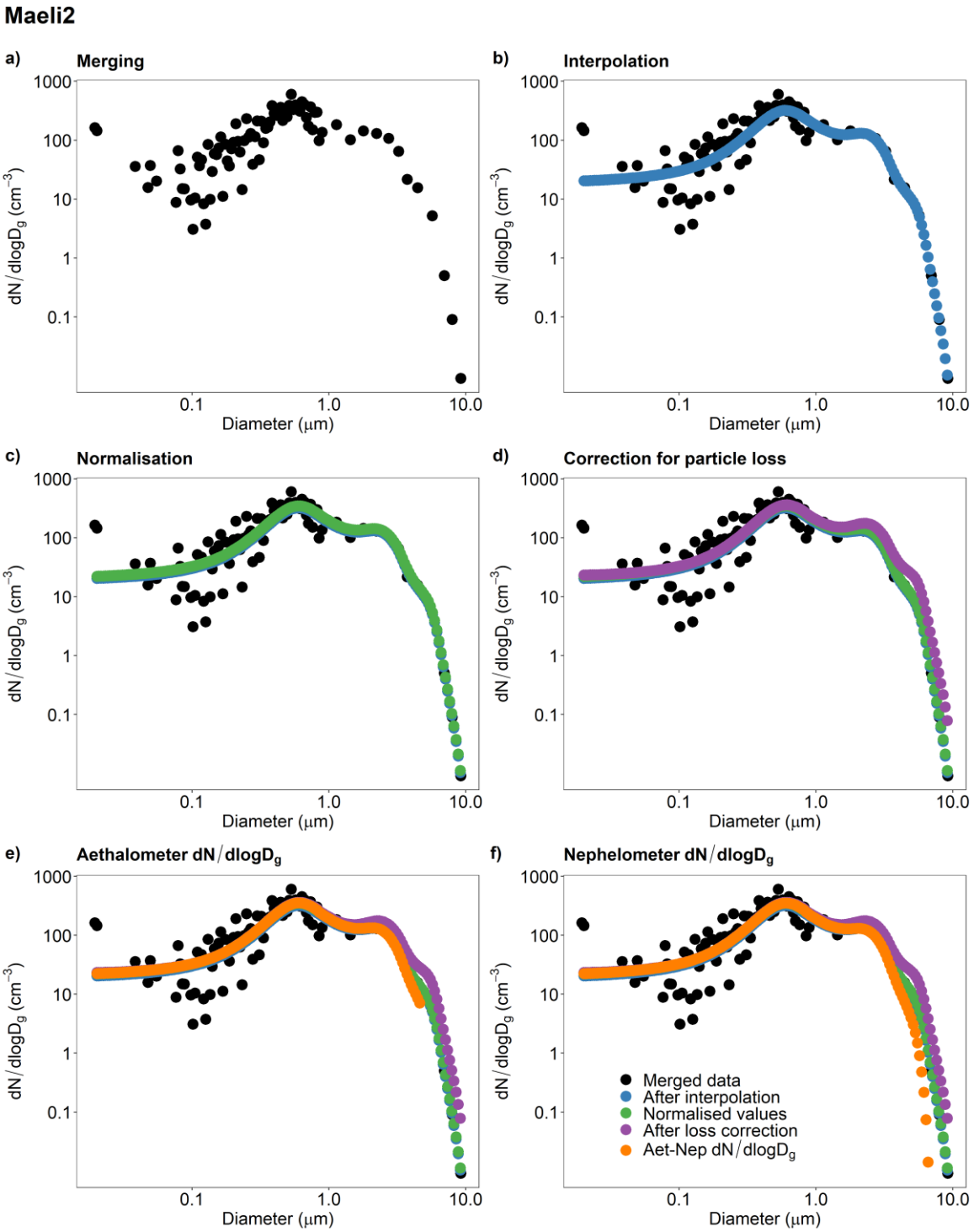

Figure S2: Processing of the size distribution data. The graphs show the geometrical size distributions $dN/dlogD_g$ at 30 min after the injection peak obtained using the calibration values of the parameters χ, n, and k. a) Merging of the geometrical size distributions $dN/dlogD_g$ of SMPS and GRIMM. b) Interpolation of the merged size distribution. c) Normalisation. d) Correction for particle loss to determine the real size distribution in CESAM. Size distribution behind the inlet of the SW-instruments e) aethalometer and f) nephelometer. Sample ID: Maeli2.

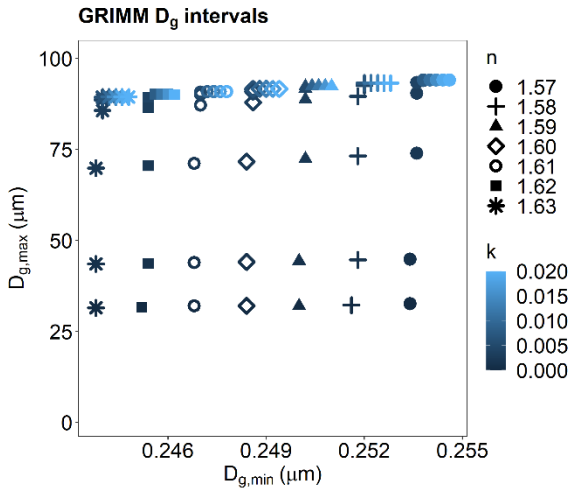

Figure S3: GRIMM D_g intervals. $D_{g,max}$ and $D_{g,min}$ are the upper and lower limit of the D_g intervals. n and k are respectively the real and imaginary part of the complex refractive indices used to convert the optical diameter D_{op} measured by the GRIMM into geometrical diameters D_g.

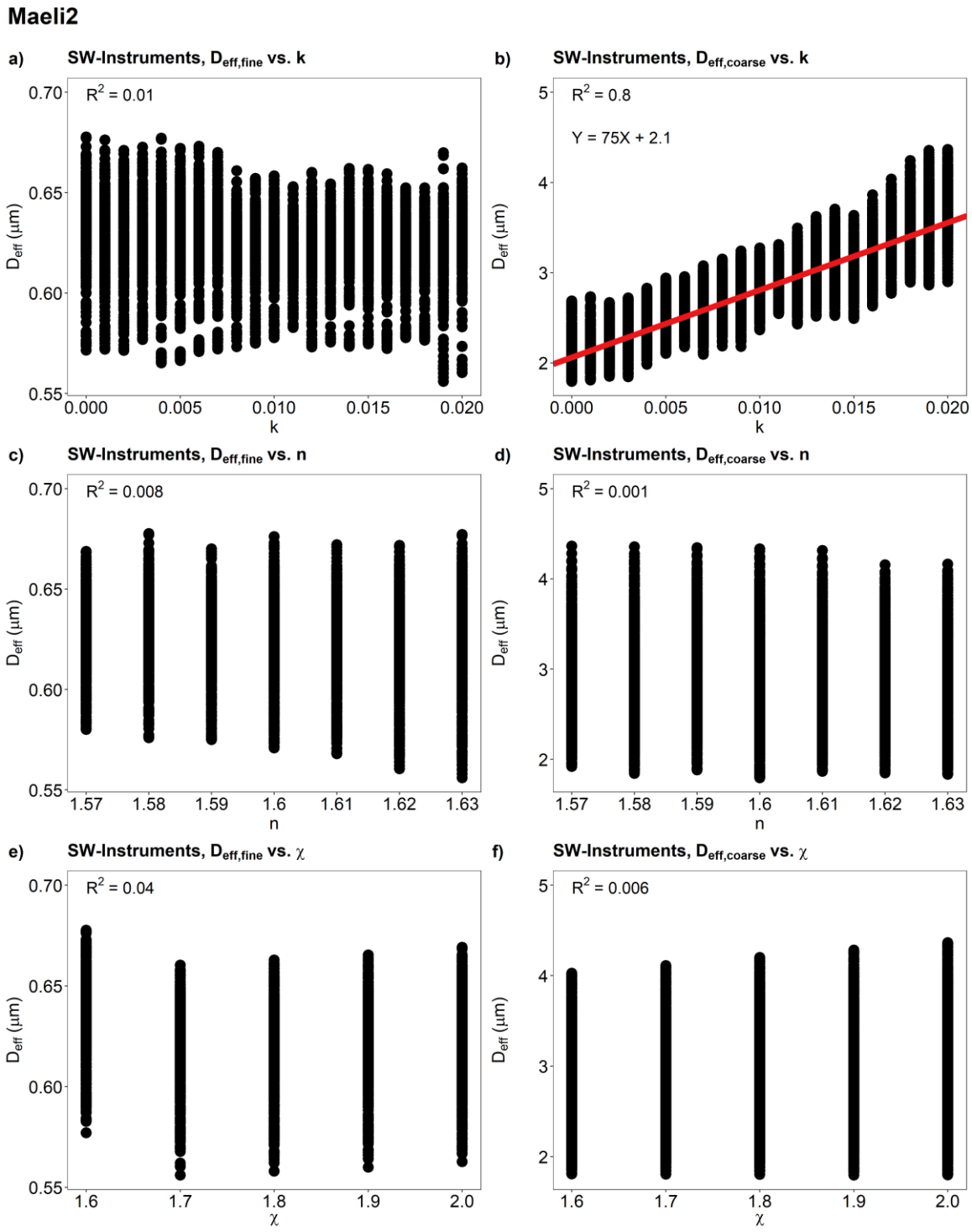

Figure S4: Comparison between the effective diameter of the coarse fractions ($D_{eff,coarse}$) and of the fine fractions ($D_{eff,fine}$) calculated using the SW-Instruments size distributions and the input parameters χ, n, and k.

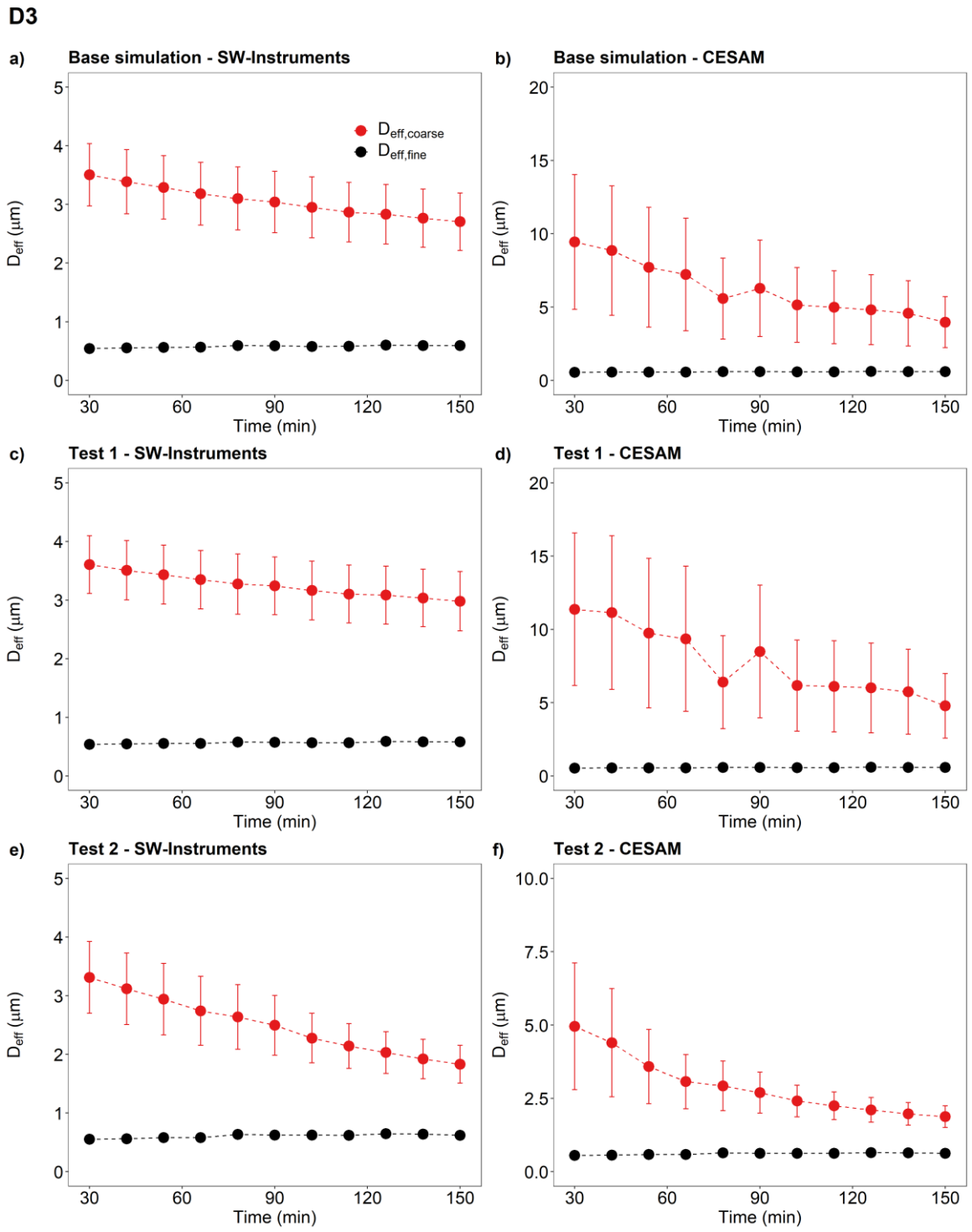

Figure S5: Effective diameters D_{eff} of dust particles behind the inlet of SW instruments and in CESAM, from 30 min after the injection peak to 2.5 h. a-b) Base simulation; c-d) Test 1; e-f) Test 2. D_{eff} was calculated for particles > 1 µm ($D_{eff,coarse}$) and ≤ 1 µm ($D_{eff,fine}$). Data were reported as 12-min average. Sample ID: D3.

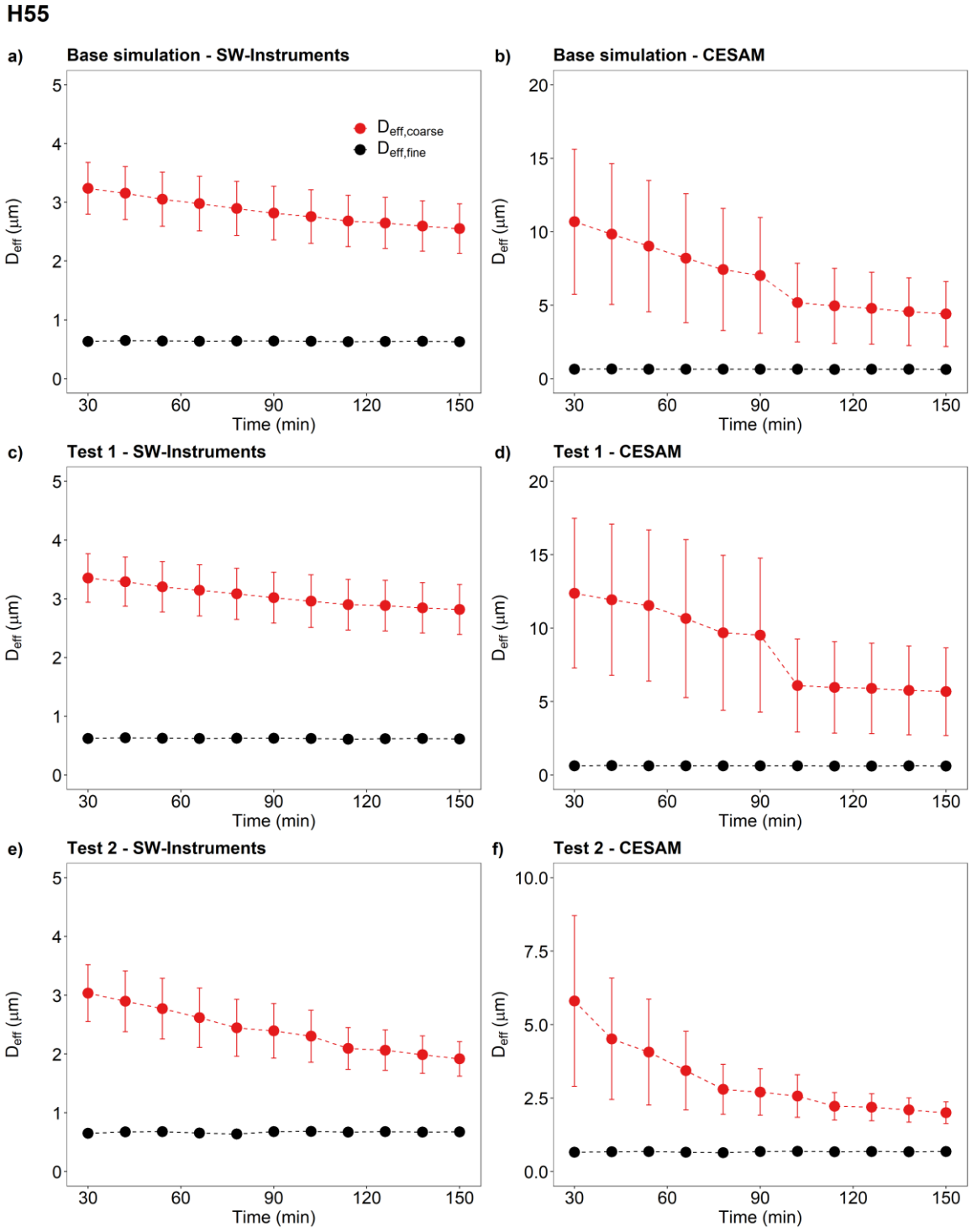

Figure S6: Effective diameters D_{eff} of dust particles behind the inlet of SW instruments and in CESAM, from 30 min after the injection peak to 2.5 h. a-b) Base simulation; c-d) Test 1; e-f) Test 2. D_{eff} was calculated for particles > 1 µm ($D_{eff,coarse}$) and ≤ 1 µm ($D_{eff,fine}$). Data were reported as 12-min average. Sample ID: H55.

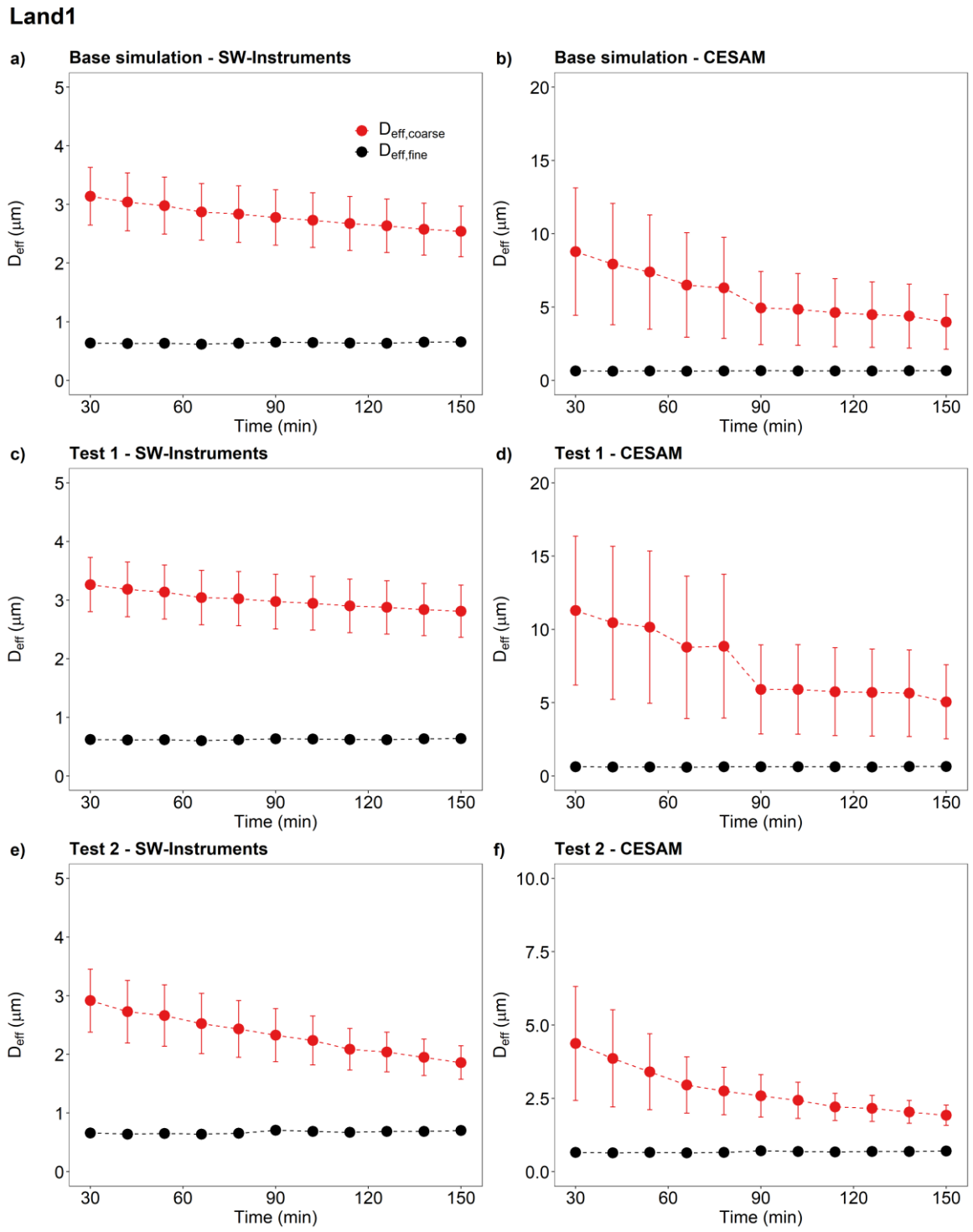

Figure S7: Effective diameters D_{eff} of dust particles behind the inlet of SW instruments and in CESAM, from 30 min after the injection peak to 2.5 h. a-b) Base simulation; c-d) Test 1; e-f) Test 2. D_{eff} was calculated for particles > 1 µm ($D_{eff,coarse}$) and ≤ 1 µm ($D_{eff,fine}$). Data were reported as 12-min average. Sample ID: Land1.

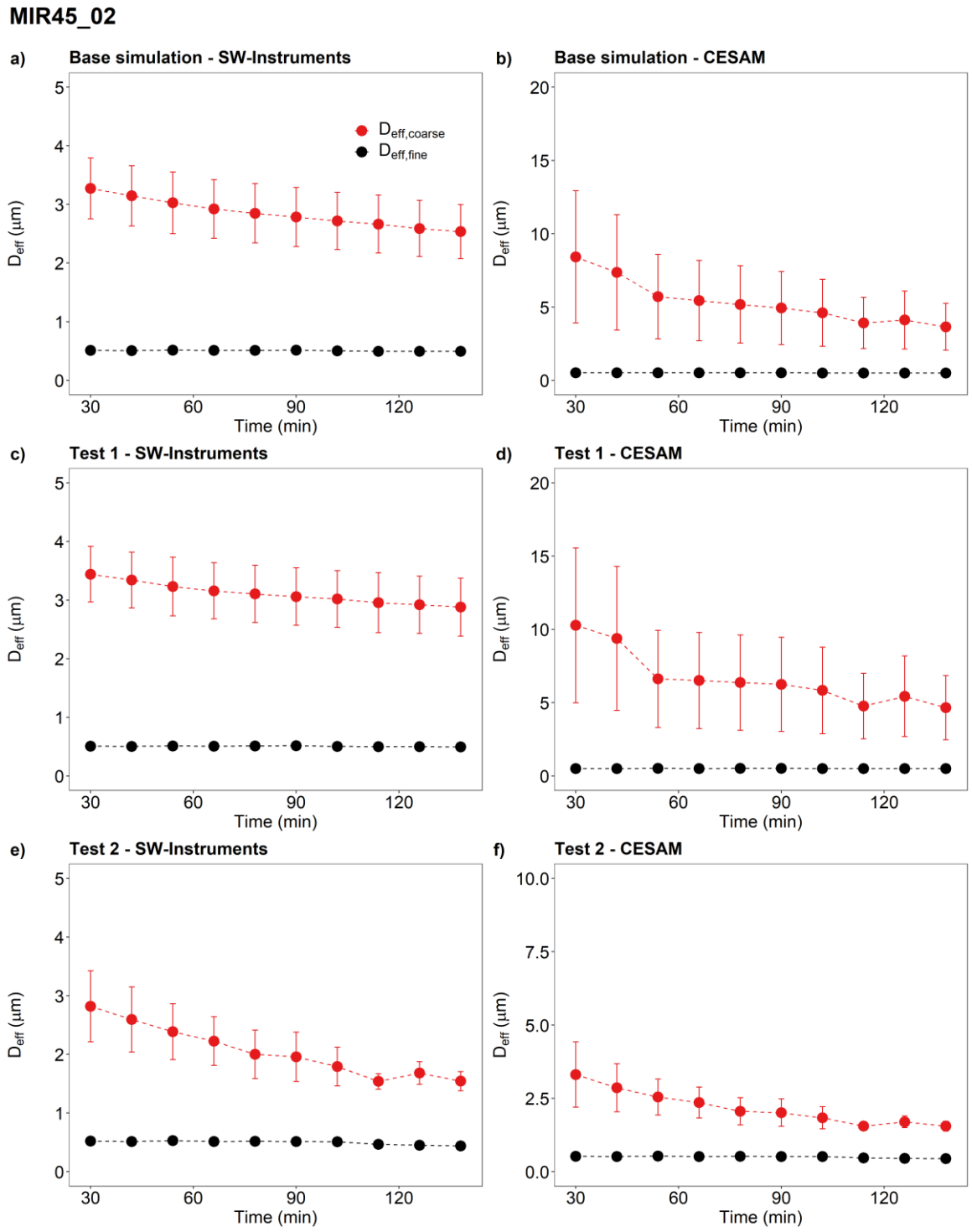

Figure S8: Effective diameters D_{eff} of dust particles behind the inlet of SW instruments and in CESAM, from 30 min after the injection peak to 2.5 h. a-b) Base simulation; c-d) Test 1; e-f) Test 2. D_{eff} was calculated for particles > 1 µm ($D_{eff,coarse}$) and ≤ 1 µm ($D_{eff,fine}$). Data were reported as 12-min average. Sample ID: MIR45.

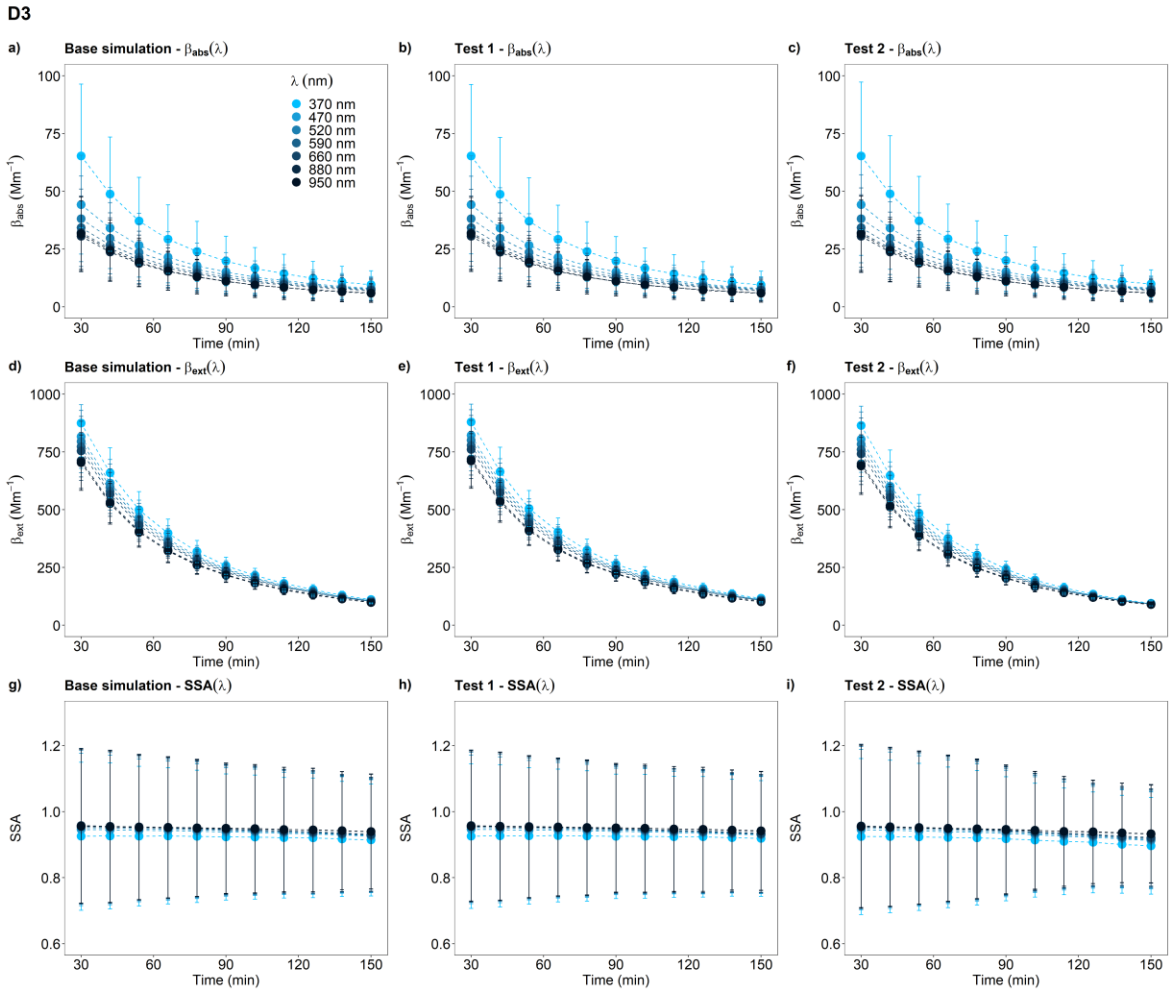

Figure S9: Extinction coefficient $\beta_{ext}(\lambda)$, absorption coefficient $\beta_{abs}(\lambda)$, and single scattering albedo SSA(λ) at λ = 370, 470, 520, 590, 660, 880, 950 nm, from 30 min after the injection peak to 2.5 h. a-c) Base simulation; d-f) Test 1; g-i) Test 2. Data were reported as 12-min average. Sample ID: D3.

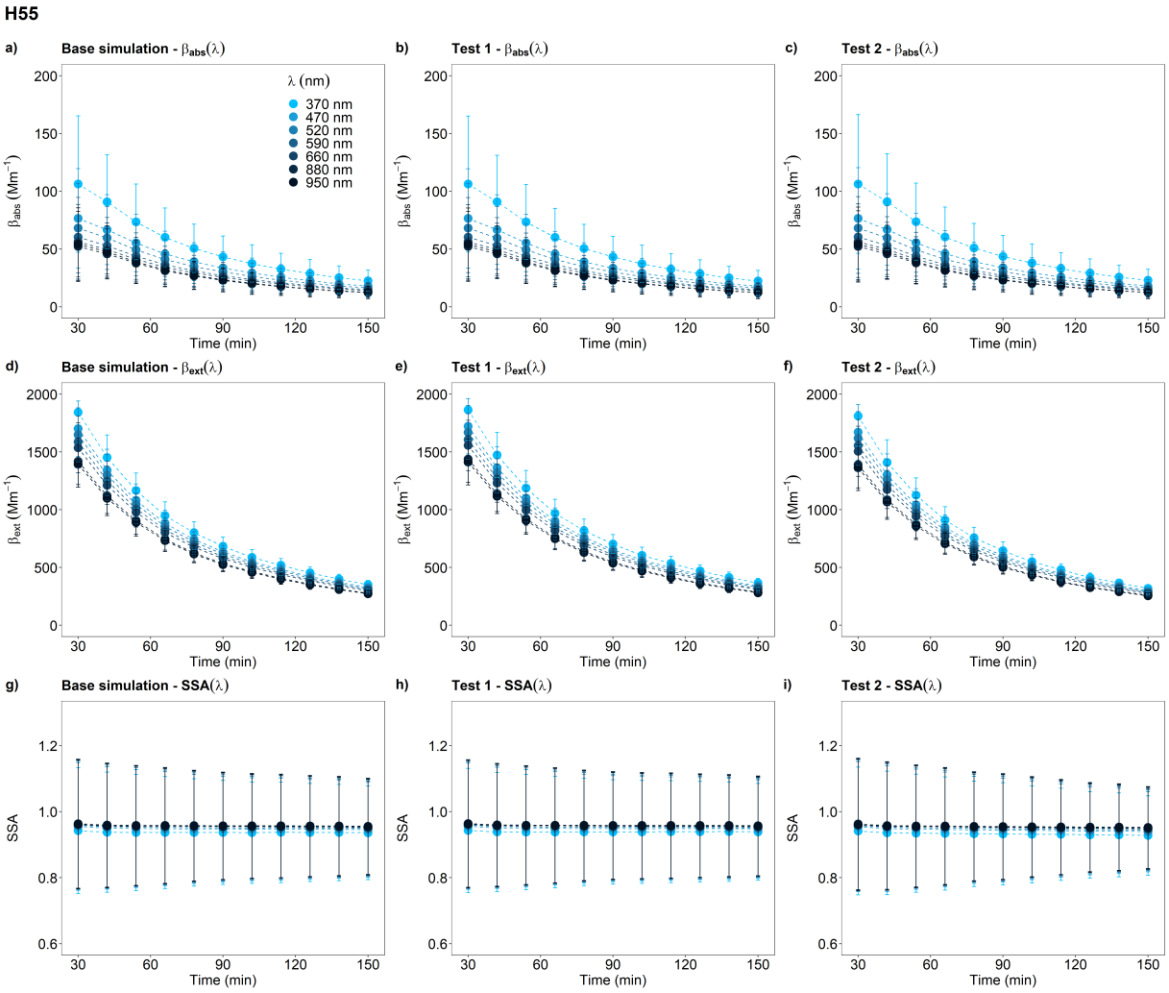

Figure S10: Extinction coefficient $\beta_{ext}(\lambda)$, absorption coefficient $\beta_{abs}(\lambda)$, and single scattering albedo SSA(λ) at λ = 370, 470, 520, 590, 660, 880, 950 nm, from 30 min after the injection peak to 2.5 h. a-c) Base simulation; d-f) Test 1; g-i) Test 2. Data were reported as 12-min average. Sample ID: H55.

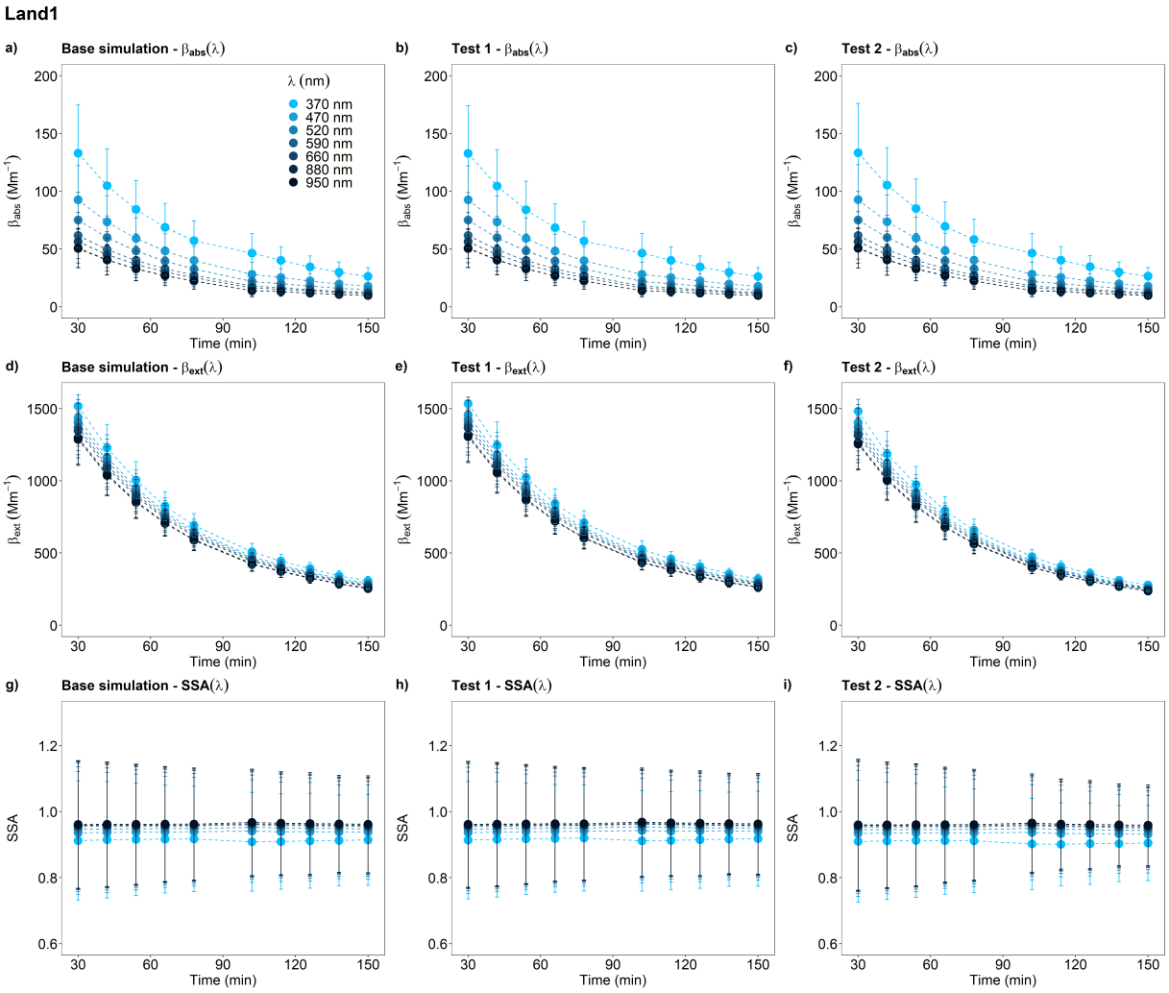

Figure S112: Extinction coefficient $\beta_{ext}(\lambda)$, absorption coefficient $\beta_{abs}(\lambda)$, and single scattering albedo SSA(λ) at λ = 370, 470, 520, 590, 660, 880, 950 nm, from 30 min after the injection peak to 2.5 h. a-c) Base simulation; d-f) Test 1; g-i) Test 2. Data were reported as 12-min average. Sample ID: Land1.

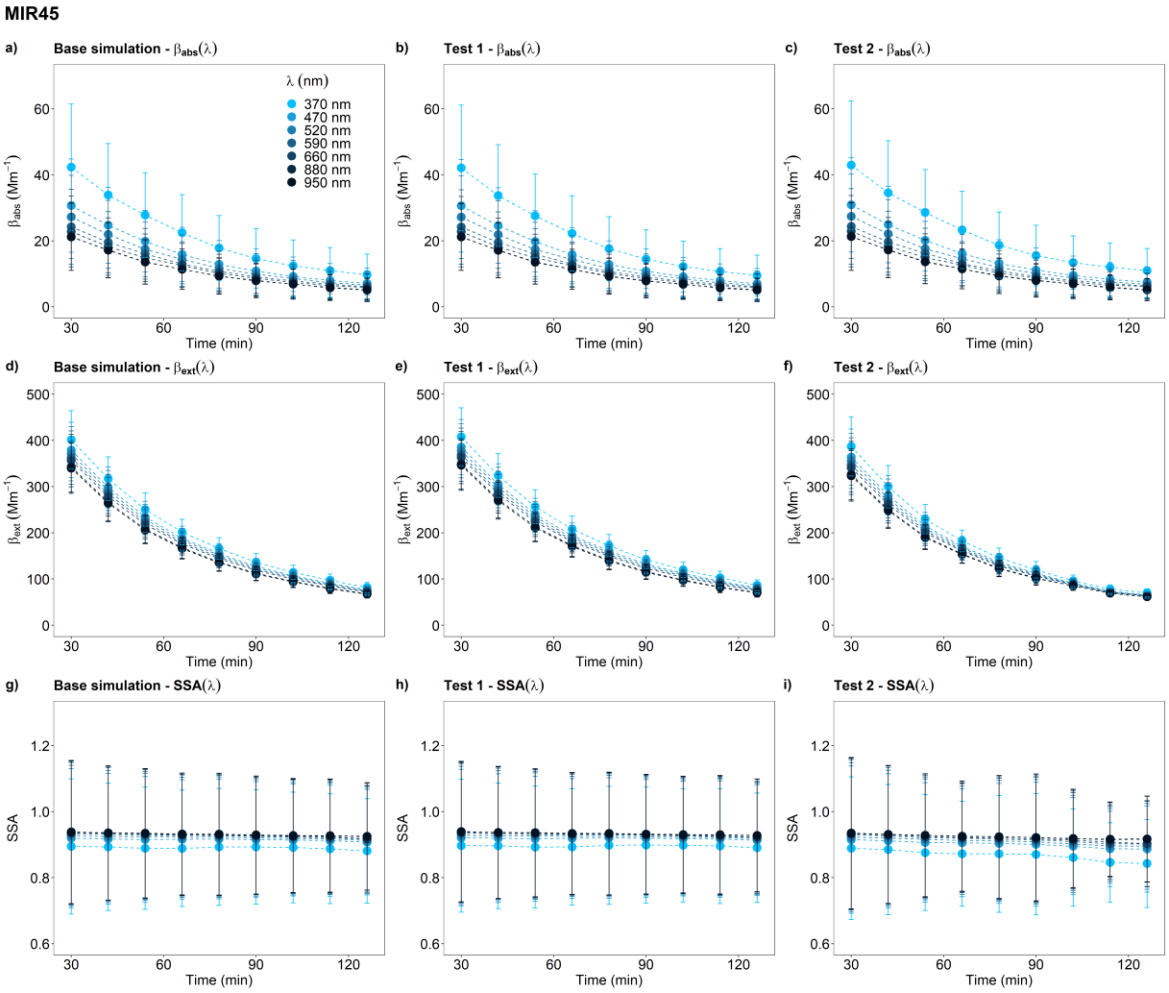

Figure S12: Extinction coefficient $\beta_{ext}(\lambda)$, absorption coefficient $\beta_{abs}(\lambda)$, and single scattering albedo SSA(λ) at λ = 370, 470, 520, 590, 660, 880, 950 nm, from 30 min after the injection peak to 2.5 h. a-c) Base simulation; d-f) Test 1; g-i) Test 2. Data were reported as 12-min average. Sample ID: MIR45.

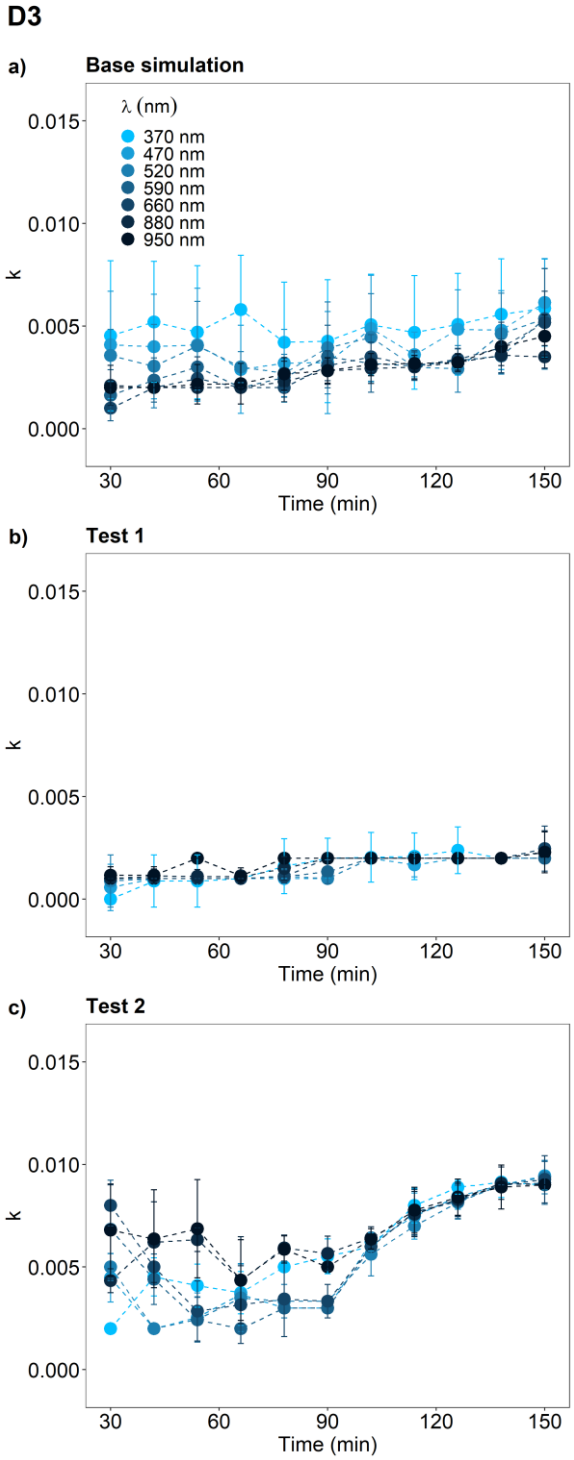

Figure S13: Imaginary part of the complex refractive index k(λ) at λ = 370, 470, 520, 590, 660, 880, 950 nm, from 30 min after the injection peak to 2.5 h. a) Base simulation; b) Test 1; c) Test 2. Data were retrieved at 12-min resolution. Sample ID: D3.

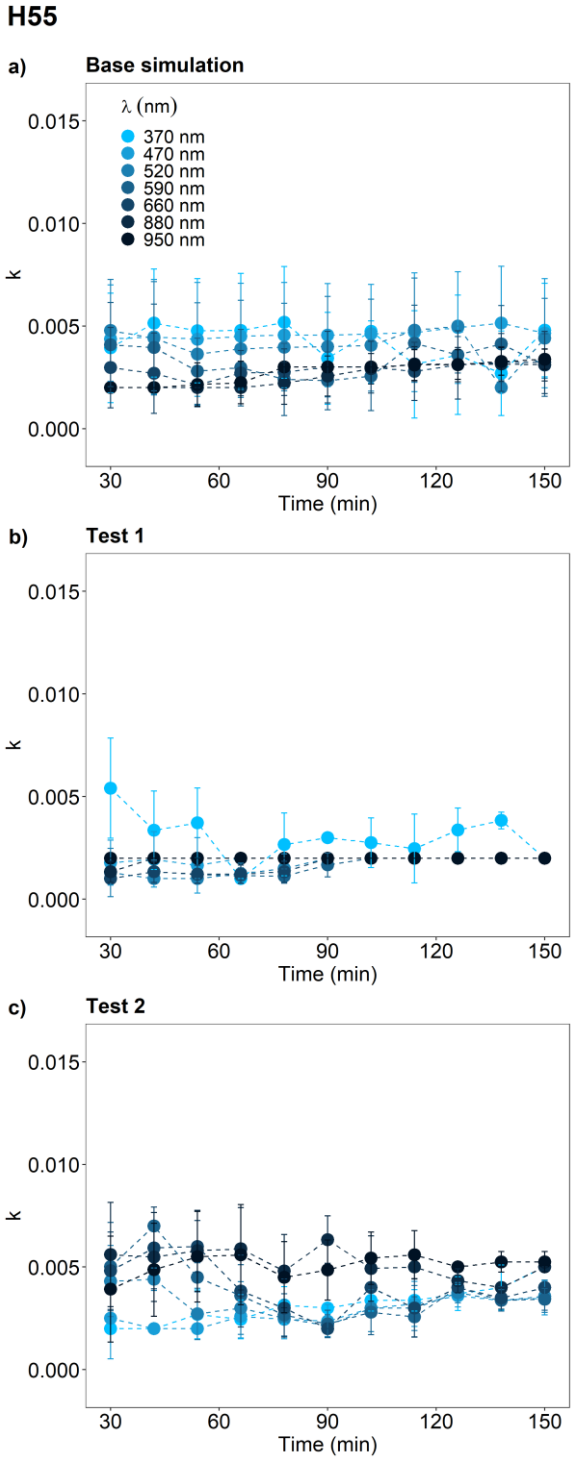

Figure S14: Imaginary part of the complex refractive index k(λ) at λ = 370, 470, 520, 590, 660, 880, 950 nm, from 30 min after the injection peak to 2.5 h. a) Base simulation; b) Test 1; c) Test 2. Data were retrieved at 12-min resolution. Sample ID: H55.

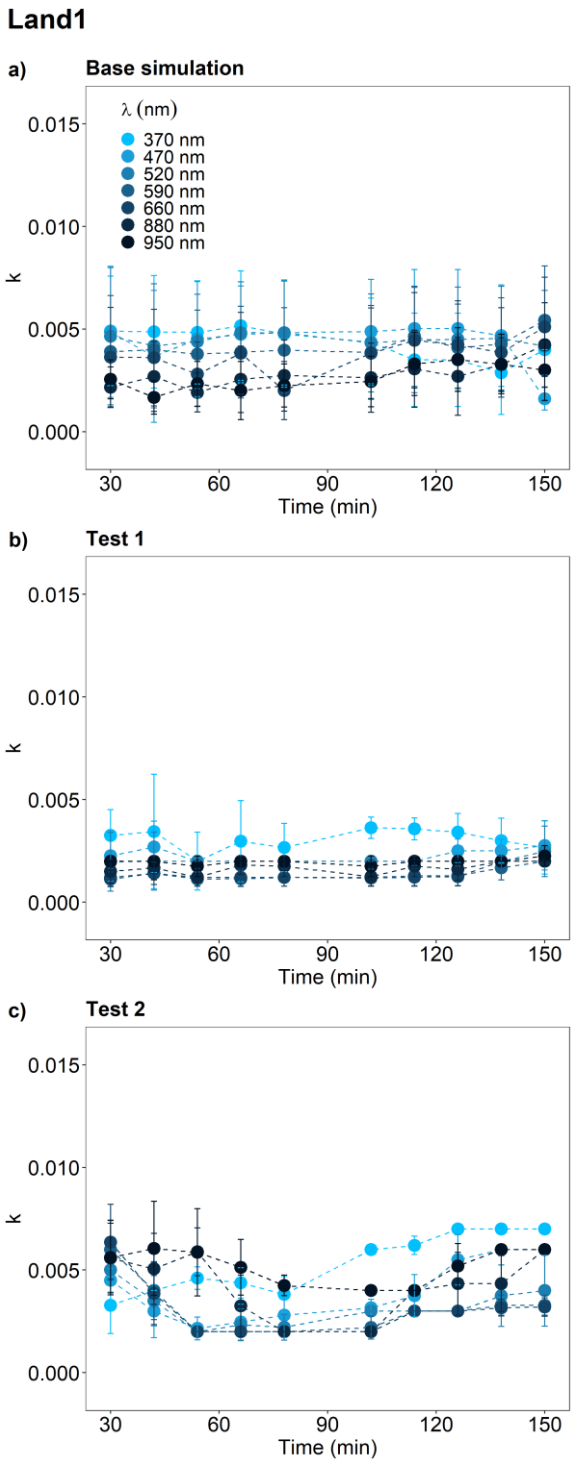

Figure S15: Imaginary part of the complex refractive index k(λ) at λ = 370, 470, 520, 590, 660, 880, 950 nm, from 30 min after the injection peak to 2.5 h. a) Base simulation; b) Test 1; c) Test 2. Data were retrieved at 12-min resolution. Sample ID: Land1.

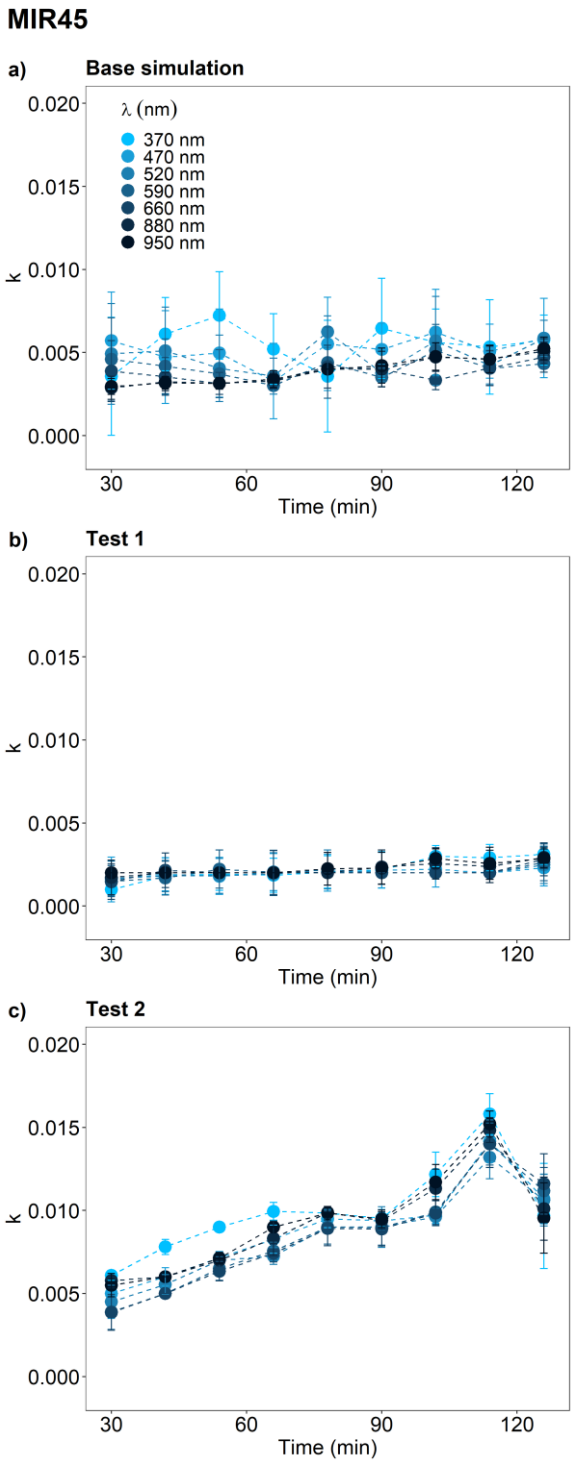

Figure S16: Imaginary part of the complex refractive index k(λ) at λ = 370, 470, 520, 590, 660, 880, 950 nm, from 30 min after the injection peak to 2.5 h. a) Base simulation; b) Test 1; c) Test 2. Data were retrieved at 12-min resolution. Sample ID: MIR45.